35th NOAA Climate Diagnostics and Prediction Workshop
Special Issue


Raliegh, NC

Climate Prediction S&T Digest

December 2010

NWS Science &Technology Infusion Climate Bulletin Supplement

Inside this issue:

NOAA's National Weather Service

Office of Science and Technology
1325 East West Highway
Silver Spring, MD 20910

Climate Prediction Center
5200 Auth Road
Camp Springs, MD 20746

Although the skill of current operational climate prediction is limited and the research on the topic presents many challenges, there are promises of improvement on the horizon. To accelerate advancement in climate services, an effective mechanism of S&T infusion from research to operation for application is much needed. This bulletin has been established to clarify science-related problems and relevant issues identified in operation, helping our partners in the research community to understand which R&D activities are needed to "shoot arrows at the target".

Science and Technology Infusion Climate Bulletin
http://www.nws.noaa.gov/ost/climate/STIP/index.htm

National Weather Service
National Oceanic and Atmospheric Administration
U.S. Department of Commerce

PREFACE

It is with great pleasure that the Climate Prediction Center and the Office of Science and Technology offer you this synthesis of the 35th Climate Diagnostics and Prediction Workshop. The CDPW has become an important institution in the climate prediction community. As is clearly evident in this digest, considerable progress is being made both in our understanding and in our ability to simulate and predict climate. The purpose of this digest is to help ensure that climate research advances are both shared with the broader climate community and also transitioned into operations. This is especially important as NOAA works to enhance climate services both across the agency and with external partners. We hope you find this digest to be both useful and stimulating. And please drop me a note if you have suggestions to improve the digest.

Finally, I would like to thank Dr. Jiayu Zhou of the Office of Science and Technology / NWS, for developing the concept for the digest and seeing it through to completion. This partnership between OST and CPC is an essential element of NOAA climate services.

Wayne Higgins

Wayne Higgins

Director, Climate Prediction Center
National Centers for Environmental Prediction
NOAA's National Weather Service

CONTENTS

Photography by Ed O'Lenic

OVERVIEW

The 35th Annual Climate Diagnostics and Prediction Workshop was held in Raleigh, North Carolina, on 4-7 October 2010. The workshop was hosted by the Cooperative Institute for Climate and Satellites (CICS) and North Carolina State University; and co-sponsored by the Climate Prediction Center (CPC) of the National Centers for Environmental Prediction and National Climatic Data Center (NCDC). The American Meteorological Society is a cooperating sponsor.

A diverse group of about 165 scientists from more than 40 domestic and international institutes gathered to explore current operational climate prediction capabilities, identify opportunities for advances, and discuss new products needed to support regional decision makers.

The workshop addressed the status and prospects for advancing climate monitoring, assessment, and prediction, with emphasis in three major themes:

1) Use of climate data records including satellite data, climatologies for improving climate predictions/predictability, and understanding and attribution of climate variability and its impacts;
2) Improving climate services through development and delivery of climate models, applications, and products in support of adaptation strategies;
3) Improving coastal monitoring and prediction in support of assessing climate impacts in the coastal zone.

This Workshop is continuing to grow and expect to provide a stimulus for further improvements in climate monitoring, diagnostics, prediction, applications and services.

1. RECENT CLIMATE EVENTS

Science and Technology Infusion Climate Bulletin
NOAA's National Weather Service
35th NOAA Annual Climate Diagnostics and Prediction Workshop
Raleigh, NC, 4-7 October 2010

The Rise and Fall of "Drought David": A Review of Recent Drought Events across the United States

Michael Hayes

National Drought Mitigation Center
School of Natural Resources, University of Nebraska-Lincoln, Lincoln, NE

Most people in the United States know that Atlantic and eastern Pacific hurricanes are named. Once named, these storms have the attention of the people in their path, and if they are severe enough, they leave memories of their impact. In contrast, focusing attention on droughts during and after an event has been more difficult and, sometimes, frustrating. This presentation discussed the potential reasons for this difficulty within the larger context of recent drought events and the recent progress toward drought risk management that has taken place in the country.

It is first necessary to understand drought and its characteristics. Drought is a natural hazard. In a list of natural hazards put together by the National Climatic Data Center (NCDC), the "billion dollar" drought events cause as much damage per event as do hurricanes, and this per-event price tag is much higher than that of tornadoes, floods, fires, or winter-related storms (NCDC 2010; http://www.ncdc.noaa.gov/oa/reports/billionz.html). But droughts are different from these other hazards in terms of several key characteristics. First, droughts often have a slow onset and have been called the "creeping phenomenon". Second, unlike the other natural hazards, they lack a universal definition, and drought severity is best described by multiple indicators. Third, the impacts of drought are often non-structural and spread over very large areas. Because of these unique characteristics, two things occur. First, it is often difficult to get attention focused on drought events as they are happening. Second, progress on drought risk management has been slow. As a result, Senator Ben Nelson of Nebraska developed the idea that droughts, like hurricanes, should be named. As early as January 2003, when the U.S. High Plains was in a serious drought situation, Senator Nelson named that drought event "David". Senator Nelson continues to highlight "David" on his website [http://bennelson.senate.gov/issues/rural_security/drought.cfm], in an effort to maintain attention on the drought hazard across the United States.

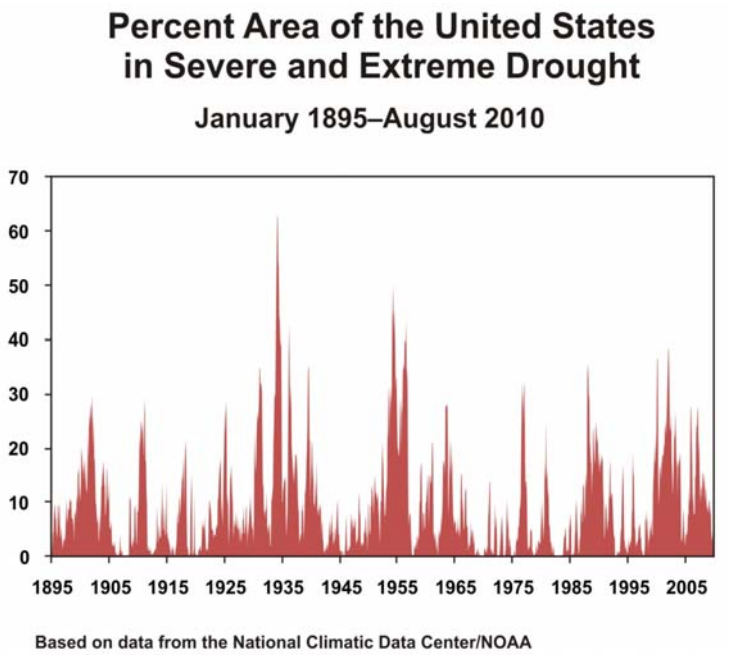

Fig. 1 The percent area of the United States in "severe" to "extreme" drought, as classified by the Palmer Drought Severity Index, between 1895 and 2010. Data provided by the National Climatic Data Center in Asheville, North Carolina.

Droughts have been a normal part of the United States' climate. Figure 1 shows the percent of the United States in either severe or extreme drought, according to the Palmer Drought Severity Index, between 1895 and August 2010. On average, about 14% of the United States is in severe to extreme drought at any one time. The major droughts also stand out in this figure. What has happened is that these major drought events have

Correspondence to: Michael Hayes, National Drought Mitigation Center, School of Natural Resources, University of Nebraska-Lincoln, Lincoln, NE; E-mail: mhayes2@unl.edu

often been “windows of opportunity”. For example, after the 1930s drought, the Soil Conservation Service (now the Natural Resources Conservation Service, NRCS, within USDA) was formed and a new standard for conservation, particularly with agricultural soils, evolved. Thus, in the 1950s drought, soil erosion and dust storms were not as prevalent. Likewise, following the 1950s and 1970s droughts, irrigation evolved in the Plains, and Nebraska is now the number one state in terms of irrigated acres in the country.

Recent drought events have also contributed in part to the development of proactive and innovative drought monitoring and drought risk management strategies. The western drought in 1994 and the drought in the southwest United States in 1995-96 provided some great opportunities. Following a recommendation that was made at a national drought conference in Portland, Oregon, in 1994, the National Drought Mitigation Center was formed in 1995 at the University of Nebraska-Lincoln. The Western Governors’ Association met in 1996, and the Western Drought Coordination Council (WDCC) was formed in 1997. One of the outcomes of the WDCC was a quarterly report named the “Western Climate and Water Status”, which was an important precursor to the U.S. Drought Monitor (USDM) product. Momentum continued and the National Drought Policy Act, forming the National Drought Policy Commission (NDPC), was passed in 1998. The NDPC issued a final report to Congress in 2000 containing multiple recommendations to improve the nation’s drought risk management capability. Finally, the first USDM map was released in August 1999, and this product continues to be issued weekly, providing a standard for current drought assessment and an instrument for policy-related decision making.

Beginning in late 1999, and establishing a stronghold in 2000, drought developed again across large parts of the United States (Figure 1). This drought peaked in 2002, when in July all 50 states had some type of dryness or drought according to the USDM map, with other peaks in 2000, 2004, and 2006. As with the droughts a decade before, this drought resulted in a couple of very important events. In 2001, 2003, and 2005, a National Drought Preparedness Act was introduced in Congress, in part to help implement the recommendations that had been proposed by the NDPC. This act did not pass, likely for numerous reasons each time.

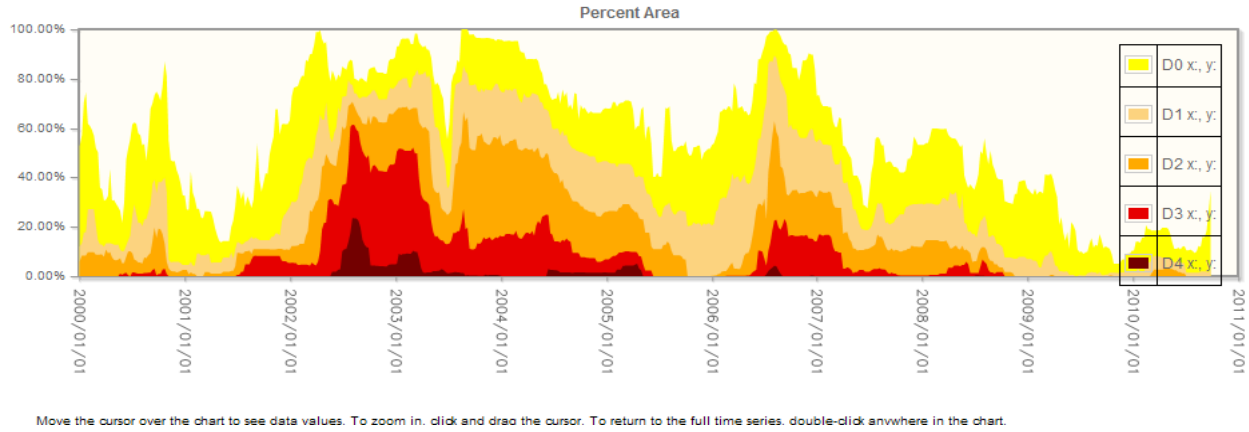

Fig. 2 The percent of the High Plains region in dryness and drought according to the U. S. Drought Monitor map between 2000 and 2010. Categories: D0 (abnormal dryness) is yellow; D1 (moderate drought) is tan; D2 (severe drought) is orange; D3 (extreme drought) is red; and D4 (exceptional drought) is dark red.

In 2004, however, an idea was proposed to the Western Governors’ Association for “Creating a Drought Early Warning System for the 21st Century” (http://www.westgov.org/wga/publicat/nidis.pdf). The outcome, the National Integrated Drought Information System (NIDIS), was passed by Congress in December 2006, and the NIDIS Implementation Plan was released in 2007 (http://www.drought.gov/pdf/NIDIS-IPFinal-June07.pdf). Since 2007, NIDIS has moved forward in a variety of ways. Multiple knowledge assessments and workshops have taken place across the country, and working groups have been established to focus on the issues of 1) a national drought portal, 2) integrated monitoring and assessment, 3) interdisciplinary research, 4) public awareness and education, and 5) engaging the preparedness communities. The approach NIDIS is

taking to address these issues across all the local, state, tribal, and federal agencies dealing with drought and water is to establish pilot projects focused on a region with specific drought-related needs. The three pilot projects that have been established at this point include the Upper Colorado River Basin, the Apalachicola-Chattahoochee-Flint (ACF) River Basin, and California.

In spite of these advancements--all of them resulting from recent drought events--the overall movement toward proactive drought risk management in the United States has been very slow. And this brings us back to "Drought David", and the need to name droughts. The characteristics of drought, described earlier, make it difficult to provide the definition and distinction of a drought event: its beginning, end, and spatial evolution through time. Figure 2 shows a time series for the U.S. Drought Monitor for the High Plains Region between 2000 and 2010. The beginning of the drought is evident before 2000, continuing and building into 2002, lasting through 2006, and waning in 2007 and 2008. One could maybe say that the drought event was "over" in 2009. Therefore, with the purpose of providing a name for this drought event, is "David" then the same event that began in Nebraska in 2000, spread coast-to-coast in 2002, still existed in the High Plains in 2006, ravaged the Southeast in 2007-08, and established pockets of severe drought in Hawaii, California, Texas, and the Upper Midwest in 2009? This illustrates some of the issues that might be faced if names are going to be attached with specific drought events.

One tool that may provide a little guidance and assistance, at least in the identification of the start and end of drought events in a particular location, is the Drought Impact Reporter (DIR), which has been available at the NDMC since 2005 (http://droughtreporter.unl.edu/). Figure 3 shows what the DIR tool looked like on October 5, 2009. At that time, a very serious drought was taking place in southern Texas. If one scrolls over the map on the website with a mouse, the number and type of drought impacts taking place appears. If one clicks on a state, a county-level map appears. The mouse can also be used to highlight the number and type of impacts taking place in each county. Most of the impacts within the DIR database come from newspaper accounts, but partnering with organizations to receive local impact information is also an important objective. In spring 2010, the Community Collaborative Rain, Hail, and Snow (CoCoRaHS) network [http://www.cocorahs.org/] provided the capability to their nearly 15,000 observers across the country to enter drought impacts they are experiencing into the DIR database.

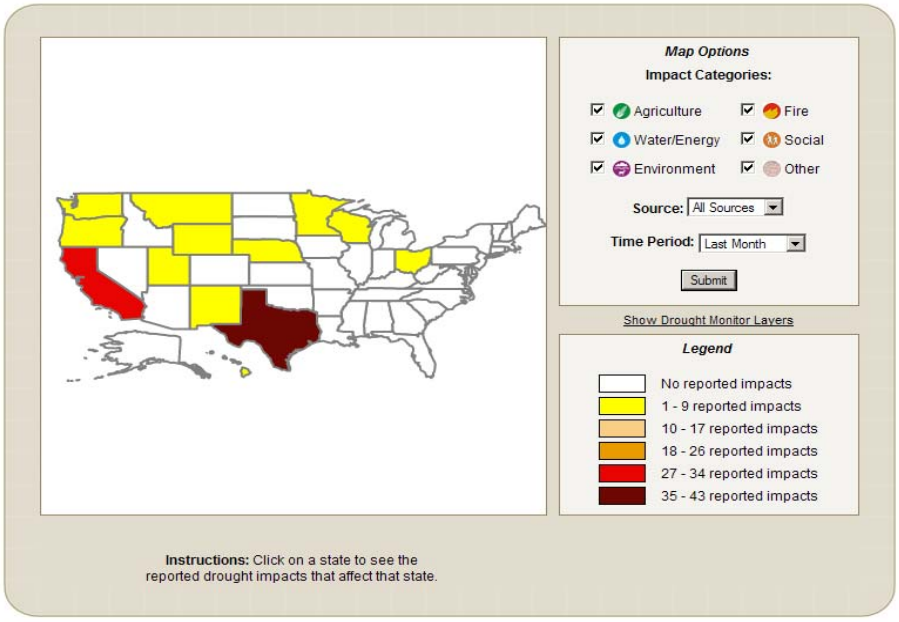

Fig. 3 The Drought Impact Reporter for October 5, 2009.

Figure 4 shows an example of how the U.S. Drought Monitor and the DIR tool can be combined to highlight important drought characteristics. In this case, the drought in Texas is featured with a time series between mid 2007 and early 2010. For the most part, the reported impacts ebb and flow with the drought severity levels, although a rise in impacts during winter 2007-08 precedes a significant increase in severity during the spring 2008. Another interesting feature is that while the D0, D1, and D2 areas significantly reduced in size during 2009 (indicating an improvement in drought conditions for large parts of northern and central Texas), the D3 and D4 areas increased (indicating that the drought was becoming much more severe in

southern Texas) during this same time. The number of reported impacts also reflected the worsening of conditions in southern Texas, and peaked during this time as well.

In the end, although we are unsure about the efficacy of naming this most recent drought "David", what is the legacy of this recent drought? One of the biggest areas of improvement during the past 10 years has been in the area of drought monitoring. In addition to the U.S. Drought Monitor product, multiple other advancements have occurred in drought monitoring, and this trend is expected to continue. NIDIS is also a huge success story of recent years, and the NIDIS efforts and pilot projects hold great promise. There have been successes in terms of proactive risk management activities, in planning for example, particularly at the state and local levels. Recent droughts have highlighted the opportunities that exist in terms of drought prediction, and the drought prediction community is making progress in terms of attribution of various events. In terms of climate change, the recent drought events around the country have provided the opportunity for climatologists to address issues of climate variability and change in areas and to audiences that would otherwise be quite skeptical to these issues. Finally, as 2011 approaches, the developing dryness and drought in the Southeast, combined with the evolving La Nina, provides another opportunity for potential lessons learned and advancements in drought risk management across this region. To address Senator Nelson's concerns, and to focus attention on this drought, should it also be given a name like "David"?

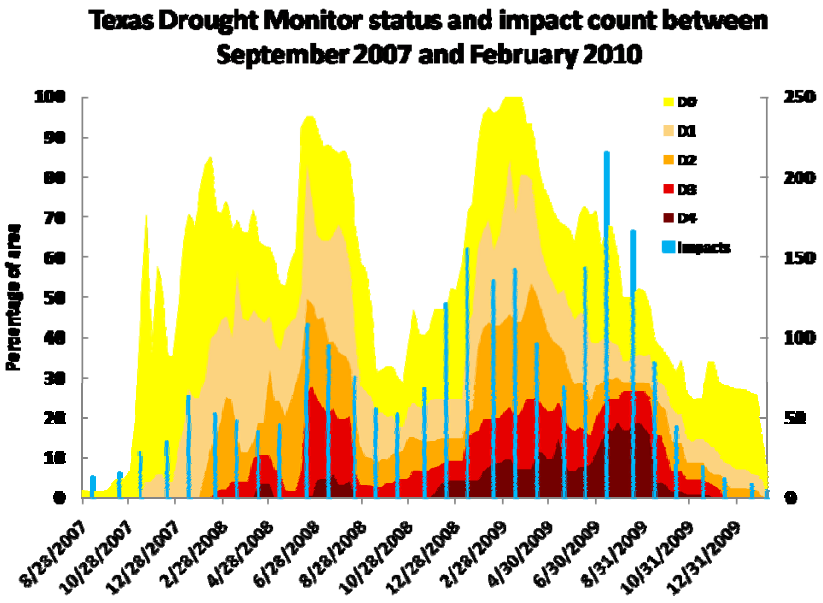

Fig. 4 The severity levels of the U.S. Drought Monitor combined with the number of drought impacts within the NDMC's DIR database for Texas between September 2007 and February 2010.

Science and Technology Infusion Climate Bulletin
NOAA's National Weather Service
35th NOAA Annual Climate Diagnostics and Prediction Workshop
Raleigh, NC, 4-7 October 2010

Extremely Negative Arctic Oscillation Persisting during the Winter 2009/2010 and the Spring 2010

Shingo Ushida

Japan Meteorological Agency

1. Observed extremely negative Arctic Oscillation in the winter 2009/2010

In the boreal winter (Dec.-Feb.) 2009/2010, extremely cold waves hit a lot of areas in the middle latitude of the Northern Hemisphere, especially around Europe, Siberia and the eastern United States where low temperature anomalies persisted during the winter (Figure 1). These cold waves were caused by the extremely negative Arctic Oscillation (AO). The negative AO was characterized with an annular pattern of high-pressure anomalies over the Arctic region and low-pressure anomalies in the middle latitudes. Associated with the negative AO, the polar front jet was weaker than normal and the subtropical jet was stronger than normal (Figure 2).

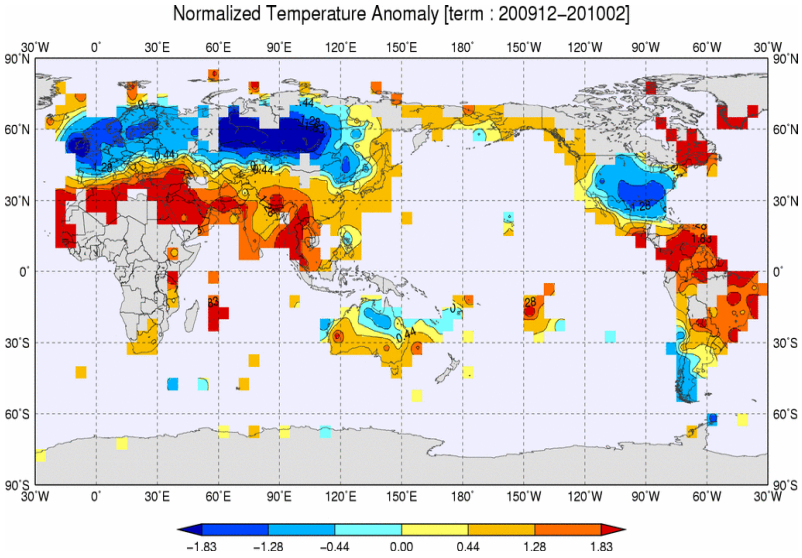

Fig. 1 Normalized surface temperature anomalies in the boreal winter 2009/2010.

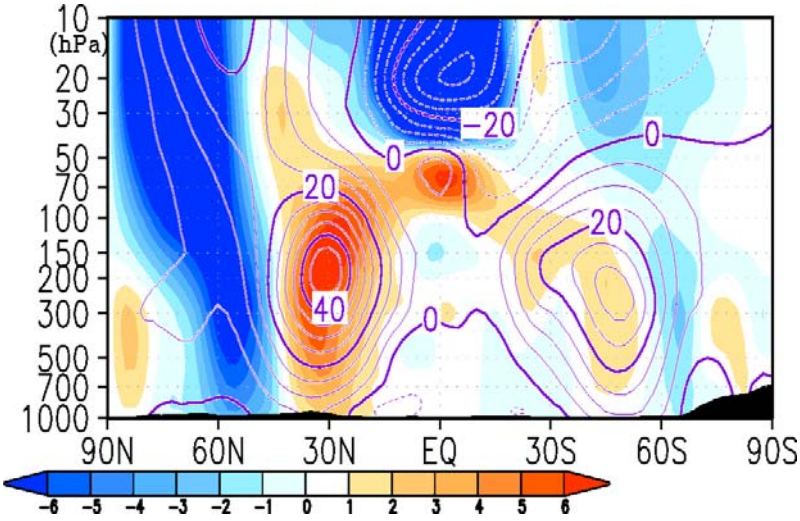

Fig. 2 Vertical-latitude cross-section of zonal-mean zonal wind in the boreal winter 2009/2010. The contours show zonal-mean zonal wind (m/s) and the shading shows its anomaly.

2. Performance of JMA's operational one month forecast

The atmospheric global circulation model (AGCM) which is operated at the Japan Meteorological Agency (JMA) for one month forecast showed the extremely good performance in the boreal winter 2009/2010. It is worthy of mention that the JMA's operational AGCM appropriately predicted the pressure pattern of the negative AO for the third and fourth week (17 – 30 day).

For the last half of February 2010, the anomaly pattern of 500-hPa height predicted by the AGCM was similar to that analyzed by the JMA's climate data assimilation system (Figure 3). The anomaly correlation between the prediction and observation was 0.78. As shown in Section 1, the weak polar jet and strong subtropical jet persisted during the boreal winter in 2009/2010. To examine the contribution of high frequency eddies to the persistence of the anomalous jets, the diagnosis was

Correspondence to: Shingo Ushida, Japan Meteorological Agency; E-mail: ushida@met.kishou.go.jp

made using the E-vector. The left panel of Figure 4 indicates that the subtropical jet was accelerated (divergence of E-vector) by the high frequency eddies with the cycle of less than 10 days over the North Pacific and North Atlantic. On the other hand, easterly wind anomalies in the high latitudes were maintained by the deceleration (convergence of E-vector) of the high frequency eddies. The JMA's operational AGCM was able to appropriately forecast such feedback of the high frequency eddies to the mean flows in the boreal winter 2009/2010 (the right panel of Figure 4). The hindcast experiment of the JMA's operational AGCM shows the model has the ability to predict the contribution of the high frequency eddies to the subtropical jet, in particular when negative AO already appears on the initial day of the prediction (Figure 5).

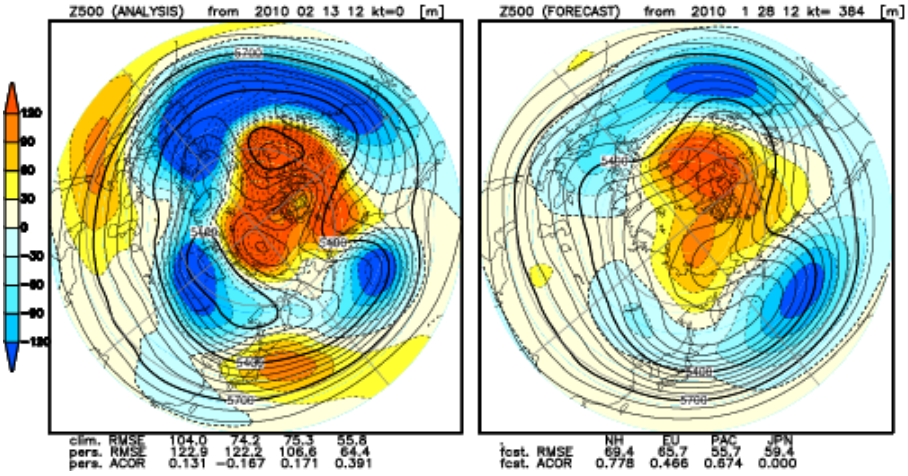

Fig. 3 Analyzed (left) and predicted (right) 500-hPa height and anomaly for 13 – 26 February 2010. The contours show 500-hPa height (m) and the shading shows its anomaly. The right panel is the JMA's operational AGCM prediction for the period from 13 to 26 February 2010 (initial date: 28 January 2010). The left panel is the analysis by the JMA's climate data assimilation system for the same period of time.

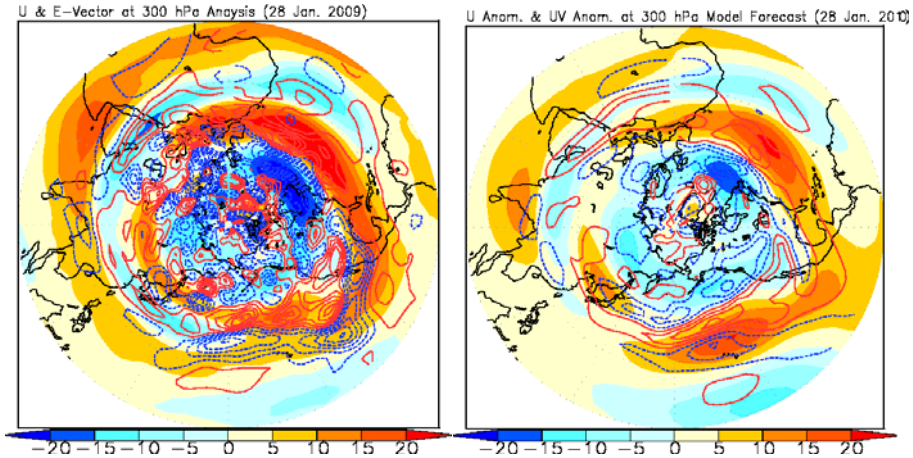

Fig. 4 Analysis (left) and prediction (right) of the divergence of E-vector and zonal wind anomaly at 300-hPa. The contours show the divergence of E-vector (m^2/s^2). The red and blue color shading shows the westerly and easterly wind anomaly (m/s). E-vector was based on the high frequency eddies with the cycle of less than 10 days. The right panel is the prediction by the JMA's operational AGCM, and the left panel is the analysis by the JMA's climate data assimilation system. The time period and initial date are the same as in Figure 3.

3. Summary

From this diagnostic analysis, it was identified that the persistence of the extremely negative AO during the boreal winter 2009/2010 was contributed by the high frequency eddies with cycle of less than 10 days. According to the hindcast results, it was revealed that the JMA's operational AGCM has high skill to predict the maintenance of the negative AO with a couple of weeks lead time after negative AO appeared. However, it is required to improve the AGCM prediction skill for AO evolution of transition from neutral or positive phase to negative phase and vice versa.

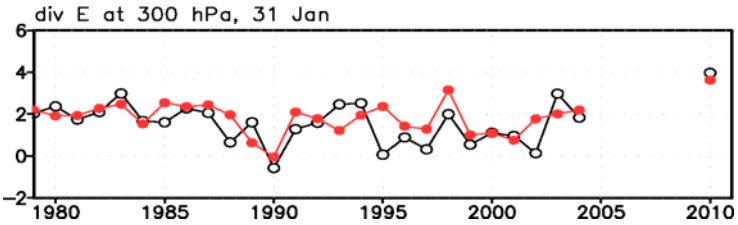

Fig. 5 Time series of zonal mean divergence of E-vector meridionally averaged between 30˚N and 40˚N for the last half of February. The white and red points show the analysis and hindcast (the third and fourth week with initial date of 31 January), respectively. The points for 2010 are the average for 13 – 26 February 2010.

Science and Technology Infusion Climate Bulletin
NOAA's National Weather Service
35th NOAA Annual Climate Diagnostics and Prediction Workshop
Raleigh, NC, 4-7 October 2010

The 2009-10 El Niño and Florida Dry Season Tornadoes: A Reality Check for the Limits of Predictability

Bartlett C. Hagemeyer

NOAA/National Weather Service, Melbourne, Florida

1. Introduction

Extratropical storms can produce various societal impacts during Florida's dry season (1 November – 30 April), including deadly tornado outbreaks, hailstorms, damaging thunderstorm winds, coastal flooding, hazardous marine conditions, strong gradient winds, and both beneficial and flooding rains. The lack of extratropical storms can cause drought and increased wildfire risk.

The author (Hagemeyer 2006 and 2007) has documented a very strong relationship between the phase of the EL Niño Southern Oscillation (ENSO) and the number of extratropical storms affecting Florida during the dry season. He has made forecasts of the number of significant dry season extratropical storms based on ENSO phase since 2002 with considerable success (see Dry Season Forecast for Florida, http://www.srh.noaa.gov/media/mlb/pdfs/Florida_Dry_Season_Forecast.pdf).

The environment necessary for the development of tornadic supercell thunderstorms during the Florida dry season: strong vertical motion and wind shear with plentiful low-level moisture and vertical instability, is typically found only in the warm sectors of extratropical storms (Figure 1, Hagemeyer, 1997). Thus it is not surprising that a strong positive correlation between El Niño and the occurrence of severe weather such as tornadoes, damaging convective wind gusts, and lightning has also been documented by the author (Hagemeyer 1998 and 2000) and others (see for example: La Joie, 2008 and Cook and Schaefer, 2008). However, it is the impact of violent tornadoes that is of most concern.

The two deadliest Florida tornado outbreaks, responsible for 63 deaths, occurred during the recent El Niño winters of 1997-98 and 2006-07. Figure 2 shows the distribution of dry season tornado deaths in peninsular Florida since 1950 by ENSO phase with 90% of the deaths occurring during El Niño's. On a seasonal scale, the greater the number of extratropical storms affecting Florida the greater the chances that one or several of them will produce the sufficient conditions for violent tornadoes. An explicit dry season forecasts of severe weather is not made, however, the Florida NWS offices use the forecast of an El Niño – and the expected increase in storminess and severe weather – to raise awareness of, and preparedness for,

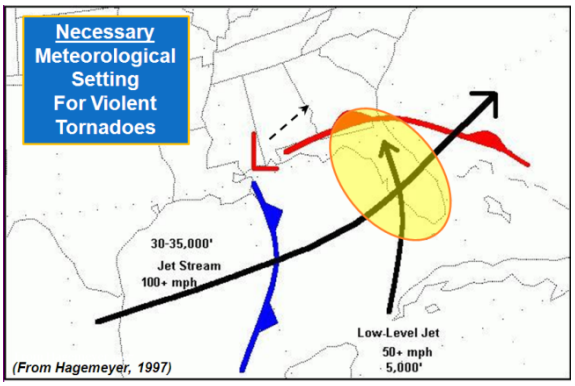

Fig. 1 Conceptual model of favorable synoptic conditions for ≥EF2 tornadoes in the Florida Dry Season (from Hagemeyer 1997).

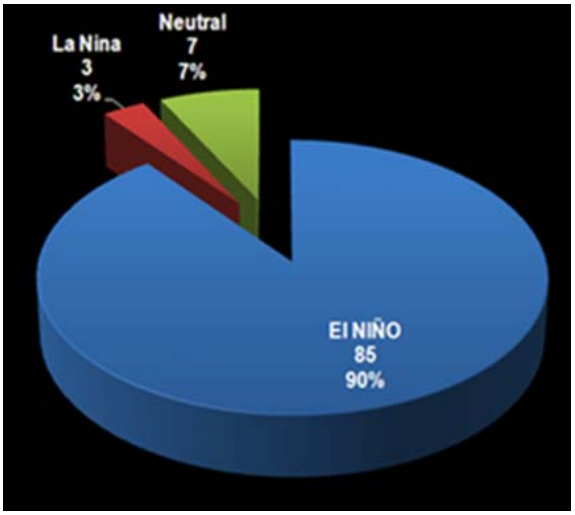

Fig. 2 Peninsular Florida dry season tornado deaths (1950-2008) by ENSO phase (from Hagemeyer *et. al.* 2010).

Correspondence to: Bartlett C. Hagemeyer, NOAA/National Weather Service, Melbourne, Florida;
E-mail: Bart.Hagemeyer@noaa.gov

strong tornadoes in their outreach activities.

As another El Niño developed during the summer of 2009 and was expected to strengthen into winter, NOAA/NWS established an El Niño Communications Campaign Team of which the author was a member. The El Niño impacts graphic developed for educational and outreach use highlighted the "increased chances for severe weather in Florida" for the first time (Figure 3). The Florida NWS offices, in partnership with emergency managers and the media, conducted an unprecedented campaign to prepare the state for the expected increase in severe weather during the upcoming dry season. The goal was to avoid the large loss of life in tornado disasters of the previous El Niño winters.

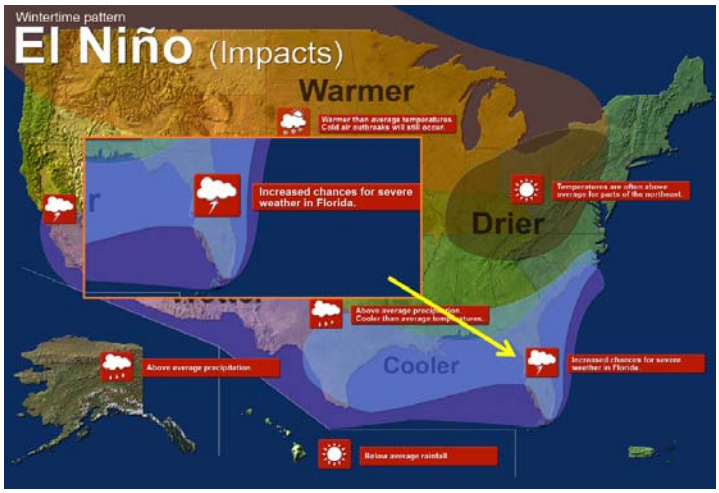

Fig. 3 Graphic of expected winter impacts from the 2009-10 El Niño developed by the NOAA/NWS El Nino Communications Campaign Team.

As expected, the number of extratropical storms affecting Florida was well above normal. Indeed, the 2009-10 El Niño winter tied the record of 18 extratropical storms set during the 1997-1998 El Niño. While the forecast of above normal extratropical storms was accurate, the tornado activity was actually below normal, with only 18 weak tornadoes reported. By contrast, 71 tornadoes, ten of which were strong and violent, occurred during the 1997-98 El Niño dry season. The 2009-10 El Niño dry season was the first since 1972-73 without any severe weather-related fatalities.

Conventional thinking has been that sufficient warm, moist, low-level air would be available during an El Niño winter to produce several significant severe weather outbreaks from passing extratropical cyclones. However, the development of a persistent strong, negative Arctic Oscillation (AO) in late 2009 and early 2010 (L'Heureux *et. al.* 2010 and Cohen *et. al.* 2010) was responsible for significantly modifying the typical impact of El Niño on Florida through frequent incursions of cold continental air masses deep into the southern latitudes, resulting in cold and wet conditions. Indeed, there were two deaths attributed to exposure to cold in Florida. As a result of the deep penetration of the cold air masses, the warm sectors of the majority of the developing extratropical storms that affected Florida were unable to supply enough low-level moisture and instability to fuel the deep convection in a high-shear environment needed to produce significant tornadoes.

The following sections will discuss the 2009-10 El Niño and the implications of the persistent negative AO pattern that likely spared Florida from the impact of violent tornadoes and instead brought record cold spells. The dominance of the negative AO, while rare, raises significant questions regarding the limits of predictability of seasonal impacts based primarily on the ENSO phase and brings into sharp focus the need to improve the prediction of other intraseasonal oscillations such as the AO, the North Atlantic Oscillation (NAO) and the Pacific-North American (PNA) pattern (Hagemeyer and Almeida, 2004) and related blocking phenomena. An expanded version of this paper with detailed case studies and comments on communicating with decision-makers will be included in the preprints for the AMS 23rd Conference on Climate Variability and Change.

2. The impact of the 2009-10 strong El Niño and record negative Arctic Oscilation on Florida

It is well-documented that El Niño has a profound effect on Florida's dry season weather by increasing the strength of the subtropical jet stream and shifting it and the associated storm track southward on average over the Gulf of Mexico and Florida. The Florida Peninsula is ground zero for the impact of increased storminess during El Niño and coincidently has the greatest concentration of old-code manufactured housing units, campgrounds and travel trailer parks in the United States. This convergence of vulnerable housing and

climatic factors favoring violent nocturnal tornadoes has resulted in tragedies during past El Niño winters. A detailed discussion of these issues is contained in Hagemeyer *et al.* 2010.

2.1 Record El Niño jet stream and Florida storminess

To put the 2009-10 El Niño into historical perspective the 250 mb zonal mean wind (U) chart for February and March (typically the peak severe weather season) is compared with the two greatest El Niño's of 1983 and 1998 (Figures 4). The typical bull's-eye of maximum 250 mb U during El Niño is found right over the Florida peninsula in each case. However, the jet stream during 2010 was considerably larger and stronger over Florida than during the two greatest El Niño's on record (55 m/s vs. 50 m/s). The 250 mb jet during early 2010 also showed a significant eastward extension over the Atlantic compared to 1983 and 1998.

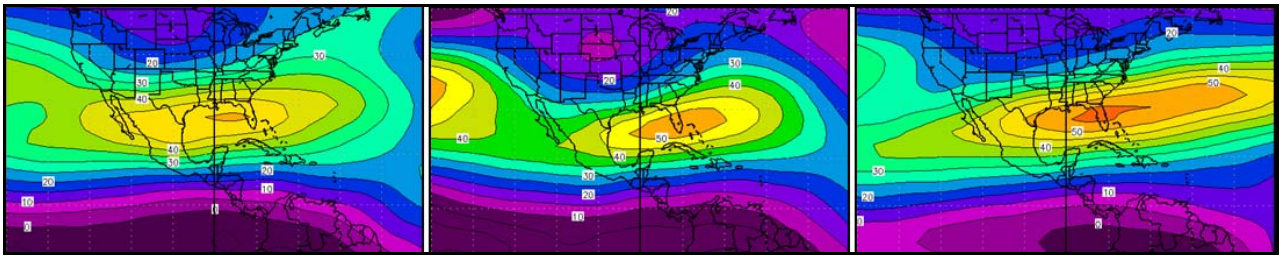

Fig. 4 250 mb zonal mean wind (m/s) for February and March 1998 (left), 1983 (middle), and 2010 (right).

The result of the persistent, strong jet stream was 18 significant extratropical storms affecting Florida, tying the record set in the 1997-98 dry season. Figure 5 shows the daily gridded mean sea level pressure (MSLP) over Florida for the dry season with the temporal location of the 18 storms. Typical of strong El Niño's February and March were exceptionally stormy with a trend of successively deeper storms leading to a "climax low" for the season in mid-March.

At first glance, successive severe weather events might be expected across Florida with the warm Gulf of Mexico providing ample low-level moisture. However, the 2009-10 dry season had a below normal 18 weak (none ≥EF2) tornadoes on 10 days (normal is 22 tornadoes with 3≥EF2) compared to the 1997-98 dry season with 71 tornadoes on 21 days with 10 ≥EF2. The lack of significant severe weather despite the record strength jet stream and number of extratropical storms was a result of the persistent, strongly negative AO.

2.2 Record negative Arctic Oscillation – Below normal temperature and tornadoes

Daily AO values during the Florida dry season plotted against the daily mean temperature for Orlando, Florida and the temporal location of the 10 Florida tornado days are shown on Figure 6. The AO index was negative from the 1st of December through early March, more than half of the dry season. There were two major negative AO events

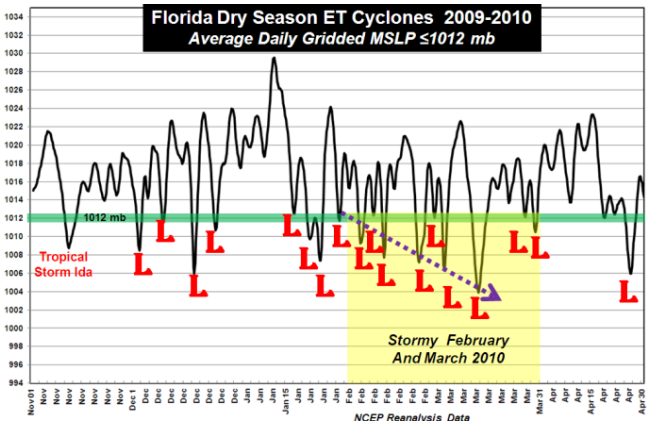

Fig. 5. Average daily dry season MSLP for Florida with the 18 significant extratropical storms (<1012mb) indicated by large red "L's".

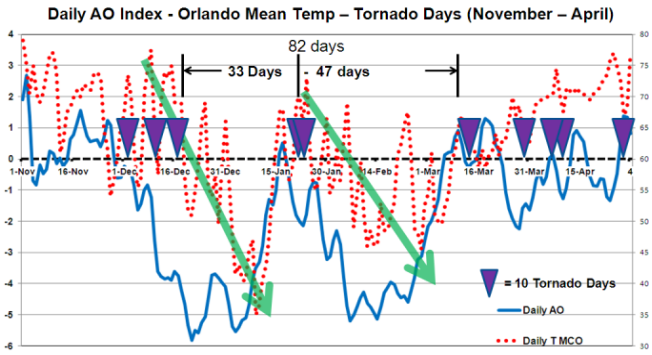

Fig. 6 Daily AO index and Orlando mean temperature from 1 November 2009 through 30 April 2010 with the 10 tornado days indicated.

with just a very brief respite between them in late January. In comparing the daily AO values with Orlando mean temperature it is easy to see the relationship between the leading negative AO pattern and cold weather in Florida. Indeed, Hagemeyer (2007b) noted there was only one way to get sustained cold weather in Florida: the high amplitude meridional trajectory associated with the negative AO pattern.

As the first negative AO event starting in December strengthened, each subsequent extratropical storm and cold front brought reinforcing cold air deep into Florida and beyond. There were 3 weak tornado days during the first half of December with passing extratropical storms which is not unusual. However, as the negative AO strengthened and persisted there were no more tornado days until it briefly abated in mid-January allowing warmer weather to return.

The cold air intrusions associated with the first negative AO event resulted in significantly colder than normal shelf waters by late January, particularly in the northeast Gulf of Mexico (Figure 7), and very cold soil temperatures as far south as the Florida Everglades (Figure 8). In real-time, the author and his colleagues speculated that the cold water could weaken convection with future ET Cyclones in Gulf of Mexico as the dry season progressed.

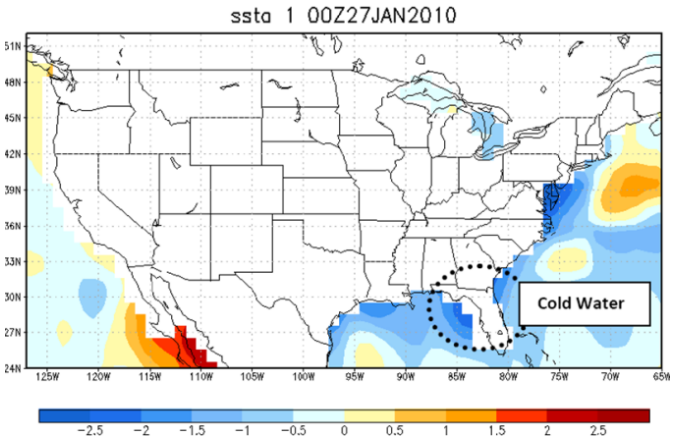

Fig. 7 Sea surface temperature (SST) anomaly for 27 January, 2010.

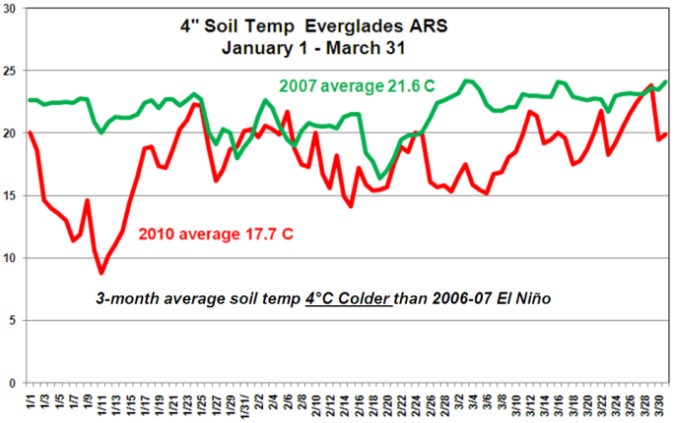

Fig. 8 Soil temperature (°C) from January 1 to March 31 at the Everglades Agricultural Research Station for the 2010 (red) and 2007 (green) El Niño's.

After two weak tornado days during the brief warm period in the second half of January 2010, the strong negative AO pattern returned and reinforcing cold air masses following the passage of strong storms again continually impacted Florida. It would be 47 days until another weak tornado day occurred in mid-March. The total lack of tornadoes in February in an El Niño winter was unprecedented. This second negative AO event insured that the shelf waters of the Gulf of Mexico would not recover to normal through the end of the dry season. The average 4 inch soil temperature from 1 January through 31 March at the Everglades Agricultural Research Center was 17.7°C in 2010 versus 21.6º during the last El Niño in 2007.

Interestingly, as soon as the strong negative AO abated in mid-March, weak tornadoes again occurred with the passing extratropical storms. This illustrates the propensity for strong extratropical cyclones to produce severe weather in Florida. The record negative AO pattern ended in mid-March and the typical seasonal trend of steadily rising temperatures without significant cold air intrusions occurred. However, the cold shelf water and soil temperatures persisted until very late into the dry season. The cumulative effect of the cold weather had a major impact on the ability to develop a warm, moist, unstable airmass in the warm sectors of passing storms to fuel the deep convection needed to produce supercell thunderstorms capable of spawning violent tornadoes. The net result of the frequent incursions of cold air into, and well south of, Florida was the modification of the typical maritime tropical (mT) airmass deep into the tropics. This resulted in a huge positive instability anomaly (more stable +5°K) right over Florida during the peak severe weather season of February and March (Figure 9) that greatly reduced severe local storm potential. The cold weather had a negative societal impact, but the lack of violent tornadoes was a very positive consequence.

3. Concluding renarks: A reality check for the limits of predictability

The author (Hagemeyer 2007a) found that the AO had a significant correlation to jet stream strength over Florida that was additive to the impact of El Nino. In other words, a negative AO would tend to make the jet stream stronger over Florida during an El Niño and presumably increase the chances for stronger extratropical cyclones and severe weather. The record strong, persistent, negative AO pattern indicative of blocking of early 2010 did indeed result in a jet stream of record strength over Florida during the peak severe weather season. However, while not significantly modifying the traditional tracks of extratropical storms up to the point of impacting Florida, the influence of the record negative AO resulted in higher amplitude storms downstream of Florida compared to past El Niño's. This influence can be seen in the significant eastward extension of the jet stream into the Atlantic Ocean east of Florida that is not present in the two greatest El Niño's of 1983 and 1997 (see Figs. 4a-c). This pattern left Florida largely on the cold side of the mean upper level jet circulation. It is perhaps not a coincidence that rare winter tornadoes, stronger than any in Florida, struck both the Bahamas and Bermuda during these unusual mean conditions.

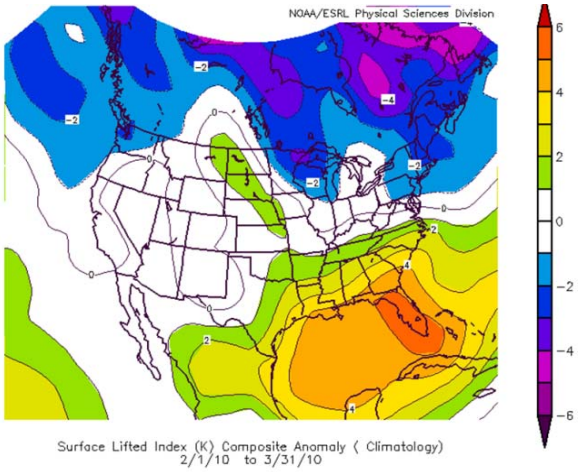

Fig. 9 Composite surface Lifted Index (ºK) anomaly from 1 February through 31 March, 2010.

Historic deadly tornado events in the El Niño's of 1966, 1983, 1998, and 2007 all occurred when the AO was weakly negative. It is a subject ripe for more research, but it is reasonable to conclude that a little bit of negative AO during El Niño's favors increased chances of severe weather in Florida, but a very strong negative AO is a limiting factor. This would be very important information for seasonal preparedness. The reality is that the AO and other *teleconnections* are not reliably predictable beyond a few weeks and a negative AO the likes of the 2009-10 event had never been seen before.

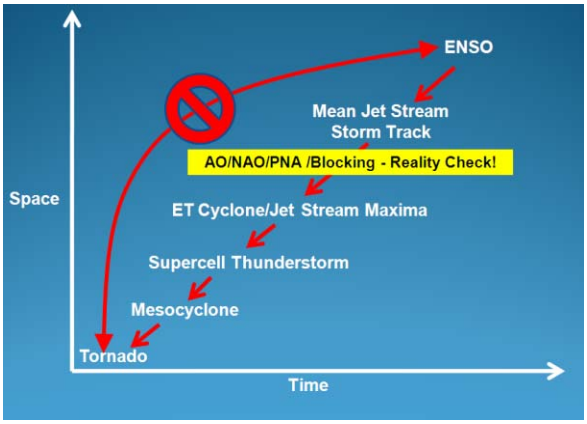

Fig. 10 Simple conceptual predictability considerations for conditions leading to strong tornado development over Florida.

It would, of course, be scientifically incorrect to state that El Niño causes violent tornadoes in the Florida dry season, but it might not be incorrect to say that a strong negative AO can limit them. Figure 10 is a simple conceptual schematic time/space scale diagram illustrating the predictability of tornadoes in Florida. There is a cascade of environmental processes on various scales that must take place to produce a violent tornado in Florida, but there are certain basic requirements that must be met such as the synoptic setting of the warm sector of an extratropical cyclone (Figure1). To this extent El Niño certainly sets the stage for increased severe weather in Florida, but all the various actors from the synoptic scale to the sub-storm scale have to play their parts a certain way.

The rarity of violent killer tornadoes is testament to the difficulty of all the right atmospheric conditions coming together in space and time and striking vulnerable housing. El Niño significantly tilts the odds that this will happen in Florida. While El Niño increase the chances that the necessary conditions for severe weather will be more likely, the repeated cold outbreaks associated with the strong negative AO can mean that sufficient low-level moisture and instability in the warm sectors of extratropical storms is impossible – hence the total lack of tornadoes in February despite record storminess.

How many ≥ EF2 tornadoes would have impacted Florida during the 2009-10 dry season without persistent cold air outbreaks and cooling of land and sea, and would any of them have struck vulnerable housing resulting in fatalities? It is impossible to know. Insight might be gained into this hypothetical question by considering that on the morning of March 29th, 2010 supercell thunderstorms in the warm sector of an extratropical storm caused several strong tornadoes that killed three people on Grand Bahamas Island just east of Florida where all the sufficient atmospheric conditions finally converged in space and time to produce strong tornadoes that intersected with a vulnerable population.

The phases and combinations of ENSO, AO/NAO, PNA, and the MJO can greatly affect the odds off certain extreme weather events occurring in a region such as Florida on a seasonal scale and there would be tremendous benefits to be gained in their reliable prediction. Until significant progress is made in this area the reality check on ENSO-based forecast schemes remains.

References

Cohen, J., J. Foster, M. Barlow, K. Saito, and J. Jones, 2010: Winter 2009–2010: A case study of an extreme Arctic Oscillation event, *Geophys. Res. Lett.*, **37**, L17707, doi:10.1029/2010GL044256.

Cook, A. R., J. T. Schaefer, 2008: The relation of El Niño–Southern Oscillation (ENSO) to winter tornado outbreaks. *Mon. Wea. Rev.*, **136**, 3121–3137.

Hagemeyer, B. C., 1997: An investigation of tornado and thunderstorm deaths in Florida. Presented to the 22nd Annual Meeting of the National Weather Association. Reno, NV (10/97).

—, 1998: Significant extratropical tornado occurrences in Florida during strong El Niño and strong La Niña events. Preprints, 19th Conference on Severe Storms, Amer. Meteor. Soc., Minneapolis, MN, 412-415.

—, 2000: Development of a low pressure index as a proxy for dry season severe weather in Florida and its relationship with ENSO. Preprints, 20th Conference on Severe Local Storms, Amer. Meteor. Soc., Orlando, FL, 439-442.

—, and R.A. Almeida, 2004: Extreme interseasonal and intraseasonal variability of Florida dry season storminess and rainfall and the role of the MJO, PNA, and NAO. Preprints, 15th Symposium on Global Change and Climate Variations, Amer. Meteor. Soc., Seattle, WA, CD-ROM P7.1.

—, 2006: ENSO, PNA and NAO scenarios for extreme storminess, rainfall and temperature variability during the Florida dry season. Preprints, 18th Conference on Climate Variability and Change, Amer. Meteor. Soc., Atlanta, GA, CD -ROM P2.4.

—, 2007a: The relationship between ENSO, PNA, and AO/NAO and extreme storminess, rainfall, and temperature variability during the Florida dry season: thoughts on predictability and attribution, Preprints, 19th Conference on Climate Variability and Change, Amer. Meteor. Soc., San Antonio, TX, CD-ROM JP2.16.

—, 2007b: Attribution of extreme variability of temperature and rainfall in the Florida dry season. NOAA 32nd Annual Climate Diagnostics and Prediction Workshop. Tallahassee, FL (10/07).

—, L. A. Jordan, A. L. Moses, S. M. Spratt, and D. F. Van Dyke, 2010: Climatological, meteorological, and societal implications for the large number of fatalities from central Florida Dry Season tornadoes during El Niño. Preprints, 22nd Conference on Climate Variability and Change. Amer. Meteor. Soc, Atlanta, GA, CD-ROM J4.5.

La Joie, M., and A. Laing, 2008: The influence of the El Niño–Southern Oscillation on cloud-to-ground lightning activity along the Gulf coast. Part I: Lightning climatology. *Mon. Wea. Rev.*, **136**, 2523-2542.

L'Heureux, M., A. Butler, B. Jha, A. Kumar, and W. Wang, 2010: Unusual extremes in the negative phase of the Arctic Oscillation during 2009, *Geophys. Res. Lett.*, **37**, L10704, doi:10.1029/2010GL043338.

2. CLIMATE VARIABILITY

Science and Technology Infusion Climate Bulletin
NOAA's National Weather Service
35th NOAA Annual Climate Diagnostics and Prediction Workshop
Raleigh, NC, 4-7 October 2010

Assessment of Intraseasonal to Interannual Climate Prediction and Predictability

Joseph Casola

Board on Atmospheric Sciences and Climate
National Research Council/National Academy of Sciences, Washington DC

The following is a summary of the recently released report from the National Research Council entitled, "Assessment of Intraseasonal to Interannual Climate Prediction and Predictability". The full report is available online at http://www.nap.edu.

More accurate forecasts of climate conditions over time periods of weeks to a few years could help people plan agricultural activities, mitigate drought, and manage energy resources, amongst other activities; however, current forecast systems have limited ability on these timescales. Models for such climate forecasts must take into account complex interactions among the ocean, atmosphere, and land surface. Such processes can be difficult to represent realistically. To improve the quality of forecasts, this report makes recommendations about the development of the tools used in forecasting and about specific research goals for improving understanding of sources of predictability. To improve the accessibility of these forecasts to decision-makers and researchers, this report also suggests best practices to improve how forecasts are made and disseminated.

1. Best Practices

Operational forecasting centers produce regular forecasts of climate for periods of weeks to years, called intraseasonal to interannual timescales. These centers provide information on drought conditions in the coming seasons or forecasts of the effects of El Niño. This type of information can be useful to both public and private decision-makers, such as farmers, insurance firms, or water resource managers. This report suggests best practices for the procedures and protocols associated with making forecasts, with the goals of increasing transparency and improving forecast quality.

Increase collaboration between operational centers and the research community to encourage the exchange of ideas between the two cultures. For example, operational centers could hold workshops focused on forecast development and grant short-term appointments to visiting researchers.

Enhance transparency by establishing public archives of forecasts, comparisons of past forecasts to actual climate conditions, the measurements used to produce forecasts, and the details of forecasting models. Archives of the inputs, outputs, and tools used in forecasts can help quantify and identify sources of forecast error, assist users as they interpret forecasts to their own needs, and document how forecasts are made using a variety of climate prediction tools.

Broaden the metrics used to assess forecast quality. No perfect metric exists to convey all the information about a forecast; therefore multiple metrics should be used.

2. Improving the Building Blocks of Forecast Systems

Intraseasonal to interannual forecast systems are composed of several "building blocks," including observational systems, models, and data assimilation schemes, systems that expand the types of data that can be used for a forecast. The committee recommended improvements to the building blocks that would enhance forecast quality.

Use statistical techniques to complement predictions from models. Statistical techniques, especially non-linear methods, can be used to identify errors in dynamical models, sets of equations that describe the

Correspondence to: Joseph Casola, Board on Atmospheric Sciences and Climate, National Research Council/National Academy of Sciences, Washington, DC; E-mail: joecasola@gmail.com.

motions of the atmosphere and ocean. Statistical techniques can also be used to translate forecasts to more local scales, which can benefit decision-makers.

Investigate and correct errors in the representation of physical processes in dynamical models. For example, models often fail to represent important processes associated with clouds, which can impact climate on regional and global scales. Sustained observations of complex climate processes are needed to better diagnose and correct these errors.

Continue exploration of multi-model ensembles, tools that combine predictions from different climate models when making a forecast. Work is needed to develop standards and metrics that could help determine the optimal selection and weighting of ensemble members.

State-of-the-art data assimilation systems should be used by forecast centers, and the types of data used to make forecasts should be expanded.

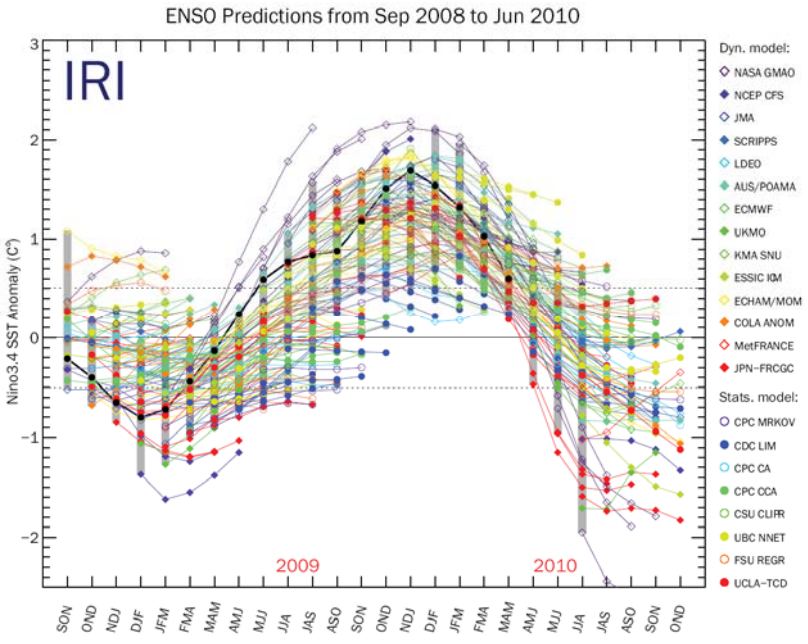

Figure 1. This chart shows predictions of tropical sea surface temperature associated with El Niño and La Niña events over a period of about two years, generated by various statistical (colored circles) and dynamical (colored diamonds) models, along with observations of actual sea surface temperatures (black circles). Many of the models predicted the evolution of sea surface temperature relatively accurately, but the spread among the different models is large.

Source: International Research Institute for Climate and Society.

3. Research Goals for Sources of Predictability

Climate forecasts are based on "sources of predictability," variables or processes in the atmosphere, ocean, or land surface that can influence climate in predictable ways on intraseasonal to interannual timescales. **To better understand key processes that are likely to contribute to improved forecasts, research is needed in several areas,** represented by the questions listed below.

- How could the Madden-Julian Oscillation, a recurrent pattern of tropical rainfall and atmospheric circulation, be used to predict climate on intraseasonal to interannual timescales? How does the Madden-Julian Oscillation interact with other recurrent climate processes, such as El Niño and the Indian monsoon?
- How do interactions between the stratosphere and lower layers of the atmosphere impact climate on intraseasonal to interannual timescales?
- How do interactions between the ocean and the atmosphere, for example the exchange of heat and moisture between the ocean's surface and the atmosphere, impact climate processes? Similarly, how do conditions on the land surface, such as those associated with soil moisture, influence atmospheric conditions, and vice versa?
- How do forecasts represent unexpected events such as volcanic eruptions or nuclear explosions? These events can alter the composition of the atmosphere with consequences for climate in the weeks, months, and years that follow.
- How should forecast systems incorporate information on long-term changes in the climate system, such as increases in greenhouse gas concentrations or alterations in the types of land cover?

Science and Technology Infusion Climate Bulletin
NOAA's National Weather Service
35th NOAA Annual Climate Diagnostics and Prediction Workshop
Raleigh, NC, 4-7 October 2010

Representation of MJO Variability in the NCEP Climate Forecast System

Scott Weaver, Wanqiu Wang, Mingyue Chen and Arun Kumar
Climate Prediction Center, NOAA/NWS/NCEP, Camp Springs, MD 20746

1. Introduction

The Madden Julian Oscillation (MJO) is an eastward propagating intraseasonal (*i.e.*, ~ 30-90 days) oscillation in tropical winds and convection, which is strongest during the boreal cold season months of November through April (Madden and Julian 1994). MJO influences are many and include impacts on global tropical cyclogenesis (Maloney and Hartmann 2000; Vitart 2009), North American and Asian monsoon systems (Zhang and Dong 2004), midlatitude stormtrack variations (Lin and Brunet 2009), and the evolution of El Niño-Southern Oscillation (ENSO) variability (Pohl and Matthews 2007). As such the MJO offers enhanced prospects for improving intraseasonal to interannual climate prediction.

In this study, we conduct an assessment of MJO variability in different National Centers for Environmental Prediction (NCEP) reanalysis and simulations from the coupled atmosphere-ocean Climate Forecast System (CFS). We use seasonal and 45-day retrospective forecasts from two systems: CFS version 1 (CFSv1, Saha *et al.* 2006) and an updated version of the CFS (CFSexp) which is under consideration to become the next generation CFS version 2. Recently, NCEP has also completed a state of the art coupled reanalysis, the Climate Forecast System Reanalysis (CFSR) (Saha *et al.* 2010). The evaluation of an updated CFS and a new long-term reanalysis and reforecast dataset is an added benefit to this analysis, effectively documenting MJO characteristics in an analysis system, *i.e.*, the CFSR, and MJO simulation and prediction in the counterpart coupled climate model.

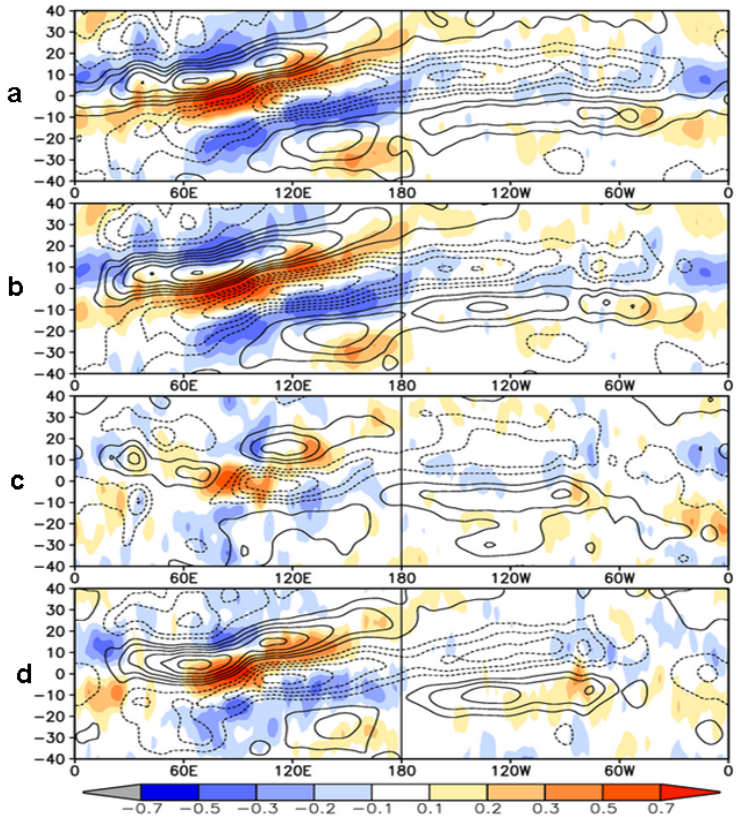

Fig. 1 Lag correlations of 20-100 day filtered 10ºS-10ºN averaged precipitation (shaded) and 850 hPa zonal winds (contoured) with respect to the Indian Ocean precipitation index. (a) R2 850 hPa zonal winds and GPCP precipitation, (b) CFSR 850 hPa zonal winds and GPCP precipitation, (c) R2 850 hPa zonal winds and R2 precipitation, and (d) CFSR 850 hPa zonal winds and CFSR precipitation. Warm (cold) colors indicate positive (negative) correlations for precipitation, while solid (dashed) lines indicate positive (negative) correlations for 850 hPa zonal winds and are contoured at 0.1 intervals.

2. Data and methodology

To assess the observed features of MJO variability we use the NCEP/DOE Reanalysis-2 (R2) (Kanamitsu *et al.* 2002) and the NCEP CFSR (Saha *et al.* 2010). In addition to the various improvements in the model

Correspondence to: Scott Weaver, Climate Prediction Center, NOAA/NWS/NCEP, Camp Springs, MD 20746;
E-mail: Scott.Weaver@noaa.gov.

physics, the CFSR is produced based on a coupled atmosphere-ocean-land guess forecast with a much higher atmospheric horizontal resolution (T382) and includes direct assimilation radiance data (Saha *et al.* 2010). The reliance on two NCEP reanalysis systems is twofold: To assess potential differences in MJO features between the R2 and CFSR, and to provide the proper benchmark data for the CFSv1 and the updated CFSexp simulation and predictionss, as these reforecasts are initialized by the R2 and CFSR respectively. We also employ the use of observed outgoing longwave radiation (OLR) data from the NOAA AVHRR (Liebmann and Smith 1996) and GPCP precipitation data (Xie *et al.* 2003). The assessment of MJO simulations and predictions is based on 4-member ensemble reforecast datasets from the NCEP coupled climate models, CFSv1 and CFSexp. For the simulation analysis the initialization is in early October and the target dates are November 1 – April 30 effectively eliminating the influence of the initial conditions, however, retaining the potential influence of realistic ENSO variability throughout the simulation.

3. MJO variability

Quasi-observed[1] MJO variability is examined in Figure 1 via lagged correlations of the reanalysis and observed 20-100 day bandpass filtered daily anomalies (*i.e.*, MJO timescale) of precipitation and 850 hPa zonal winds against an Indian Ocean precipitation index, representing the area averaged daily precipitation anomalies over the domain 70º-100ºE and 10ºS-10ºN (Waliser *et al.* 2009). The analysis is carried out over the years 1982-2006 for the months of November – April. Figures 1a and 1b display the lag correlations using the observed GPCP precipitation with reanalysis 850 hPa zonal winds from the R2 and CFSR respectively. The 850 hPa zonal wind propagation from R2 and CFSR compare quite nicely when used in conjunction with the same observed precipitation, and similarly capture known features of the MJO evolution, for example robust precipitation propagation to the dateline and faster 850 hPa zonal wind propagation in the western hemisphere.

Significant differences emerge when the lag correlations are computed using internally consistent reanalysis fields, *i.e.*, reanalysis derived winds and precipitation. Figures 1c and 1d highlight this feature as

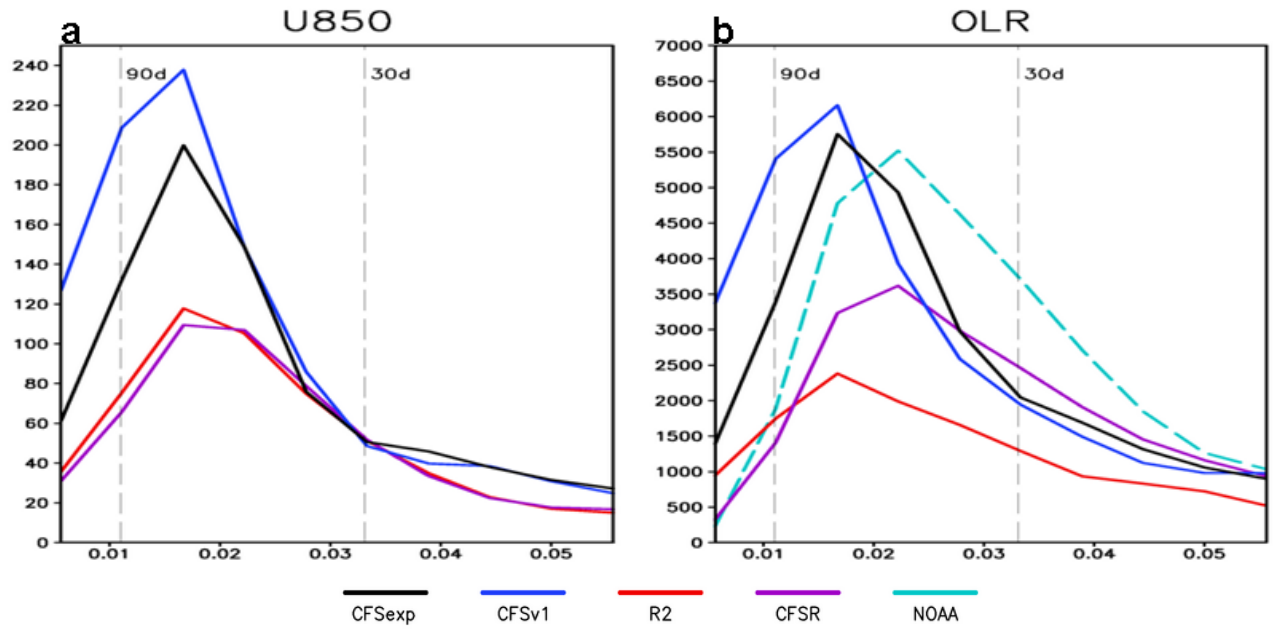

Fig. 2 Power spectra of 850 hPa zonal winds and OLR for the Indian Ocean in the CFSexp (black), CFSv1 (blue) NCEP R2 (red), and NCEP CFSR (purple), and NOAA AVHRR (cyan dashed). The units for 850 hPa zonal winds are $m^2\ s^{-2}$ day while for OLR is $w^2\ m^{-4}$ day. 850 hPa zonal winds are area averaged over the domain of 15ºS-Eq and 70ºE-100ºE in panel a, while OLR is area averaged 10ºS-5ºN and 70ºE-100ºE in panel b.

[1] The reference to "Quasi-observed" reflects the uncertainty in reanalysis based fields over sparsely observed areas (*i.e.*, Indian Ocean) as they are highly model dependent there.

evidenced by the weak propagation of both precipitation and 850 hPa zonal winds in the R2-only representation (Fig. 1c) as compared to the more robust propagating features depicted in the CFSR-only representation (Fig 1d). Particularly noteworthy in the R2-only depiction is the lack of any coherent eastward propagation of an 850 hPa zonal wind anomaly at any lead time prior to t minus 10 days. The eastward propagation of precipitation to the dateline (albeit weaker) and stronger 850 hPa zonal wind propagation into the western hemisphere in the CFSR-only analysis demonstrates the improvement in the depiction of tropical intraseasonal variability in this new reanalysis system. Since the R2 and CFSR 850 hPa zonal winds show similar lag correlations with the GPCP rainfall (Figs 1a and 1b), the improved CFSR-only correlations indicate a better rainfall simulation. Due to the mutual interaction between convection and large-scale circulation, the improved rainfall in the CFSR implies an enhancement of model physics or rainfall-related dynamical processes such as the low-level moisture convergence, or both.

Another useful diagnostic to assess the MJO is to compare the power spectra of selected fields from observations, reanalyses, and climate simulations. Figure 2 a and b shows the power spectra of unfiltered daily anomalies of 850 hPa zonal winds and OLR in the various observed and simulated datasets for the November – April period of 1982-2006 over the Indian Ocean. The extended winter daily anomalies exhibit a maximum in spectral power in the 30-90 day band, representative of the MJO timescale. Both the CFSv1 and CFSexp simulate a similar peak in the power spectra of 850 hPa zonal winds when compared to reanalysis data, however their amplitude is much stronger, although the CFSexp shows some amplitude improvement over its predecessor. The observed power spectra from the NOAA satellite data exhibit a broadened spectrum with a double peak in the 30-90 day band. While both reanalysis products show less power in the intraseasonal band, the structure of the CFSR representation follows that from the observations more closely, *i.e.*, the broadened spectrum and double peak. The NCEP R2, CFSv1 and CFSexp all produce sharp intraseasonal peaks at lower frequencies as compared to observations and the simulations have greater

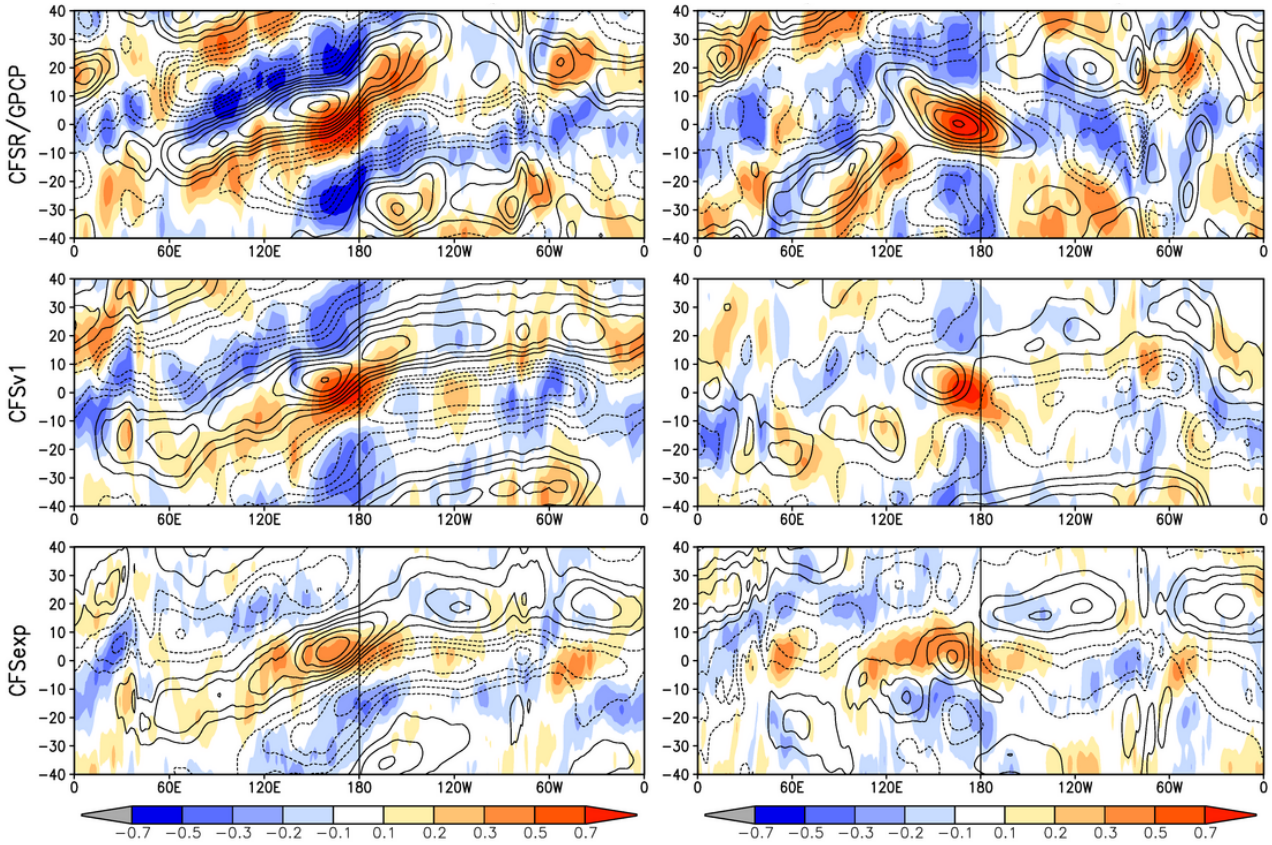

Fig. 3 Same as Figure 1 except for the lag correlations with respect to the Western Pacific precipitation index and for El Niño (left column) and La Niña (right column) years.

amplitude.

4. ENSO/MJO interaction

MJO variability has the potential to be significantly modulated by interannual variations of the climate system, and in particular by ENSO, given the co-location of the MJO and ENSO climate variability modes over the tropical Indian and Pacific oceans. To separate the impacts of ENSO on the structure of MJO variations we first stratify the daily anomaly fields by positive and negative ENSO phases. The classification is gleaned from the Climate Prediction Center (CPC) historical Niño 3.4 indices from 1982-2006.

Figure 3 shows the observed representation (top), and the CFSv1 (middle) and CFSexp (lower) during El Niño (left) and La Niña (right) years respectively. Given our focus on ENSO modulation the lag correlations are performed against a western Pacific precipitation index, calculated as the area averaged precipitation in the 160ºE-185ºE 10ºS-10ºN domain. Striking differences in the propagation features are noted between El Niño and La Niña years. During El Niño the intraseasonal anomalies of precipitation and 850 hPa zonal winds propagate coherently through the Indian Ocean, across the Maritime Continent, and into the western Pacific, separating as they enter the eastern Pacific domain. During La Niña years the propagation of the precipitation and 850 hPa zonal wind anomalies appears to be thwarted as they enter the western Pacific, perhaps a consequence of the negative feedback via coupling of the atmosphere to a cold ENSO SST anomaly.

The model responses are mixed. Both versions of the CFS capture the propagation features over the Eastern Hemisphere during El Niño, however tend to speed up the propagation of 850 hPa zonal wind anomalies upon crossing the dateline. The situation during La Niña is not as clear. Neither version of the CFS seems to coherently propagate the 850 hPa zonal wind and precipitation anomalies over the Indian Ocean as in the observed depiction. This indicates that the simulated intraseasonal activities in the western Pacific are less connected to the variability in the Indian Ocean than that in the observed, a manifestation of the model's failure to propagate across the Maritime Continent. The simulated features east of the Dateline do exhibit some degree of fidelity, mostly in the wind field. The interruption to the eastward propagating intraseasonal anomalies near the Dateline is captured to some degree, more so in the CFSexp.

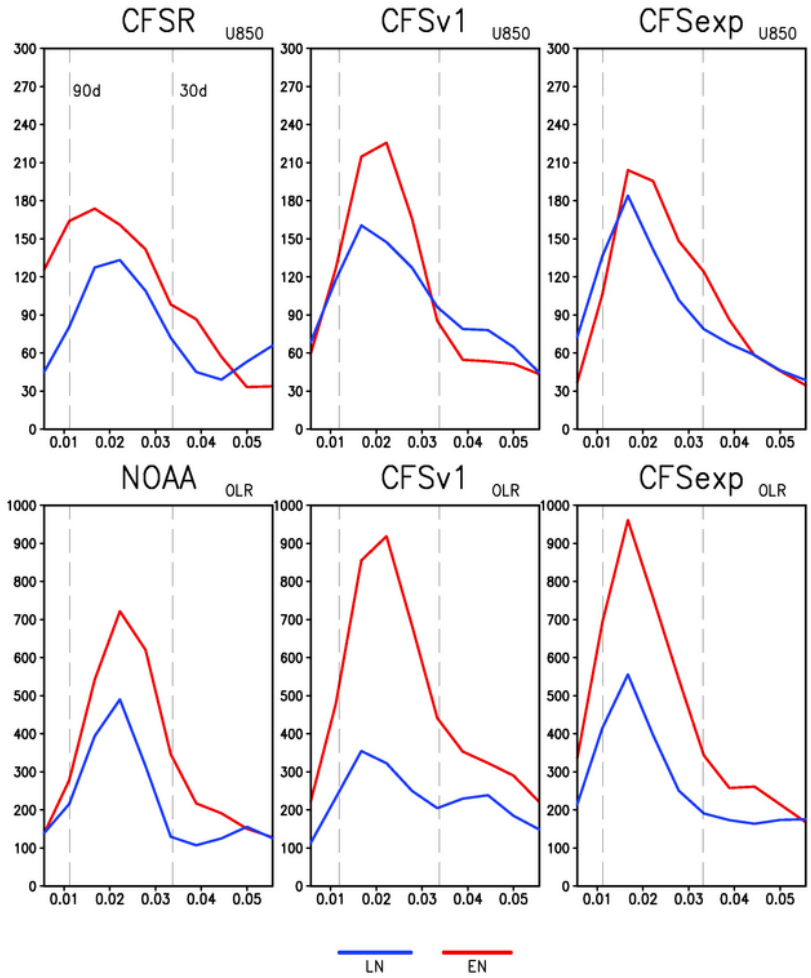

Fig. 4 Western Pacific power spectra as a function of ENSO phase over the domain of 15ºS-Eq and 160ºE-185ºE for 850 hPa zonal winds, and 20ºS-5ºS and 160ºE-185ºE for OLR. The unit is w^2 m^{-4} day for OLR and m^2 s^{-2} day for 850 hPa zonal winds.

The observed power spectra of 850 hPa zonal winds (15°S-Eq; 165°E-190°E) and OLR (20°S-5°S; 160°E-185°E) over the western

Pacific in Figure 4 shows much more significant variability as a function of ENSO phase, with El Niño winters exhibiting stronger spectral density, and in the case of 850 hPa zonal winds a peak at slightly lower frequency than that of La Niña phases. Furthermore, during El Niño the OLR and 850 hPa zonal winds do not have the same spectral peak, with 850 hPa zonal winds maximizing at a lower frequency than that of OLR. This characteristic is absent during La Niña. The relative amplitude of the power spectra as a function of ENSO phase is captured by both versions of the CFS for both OLR and 850 hPa zonal winds.

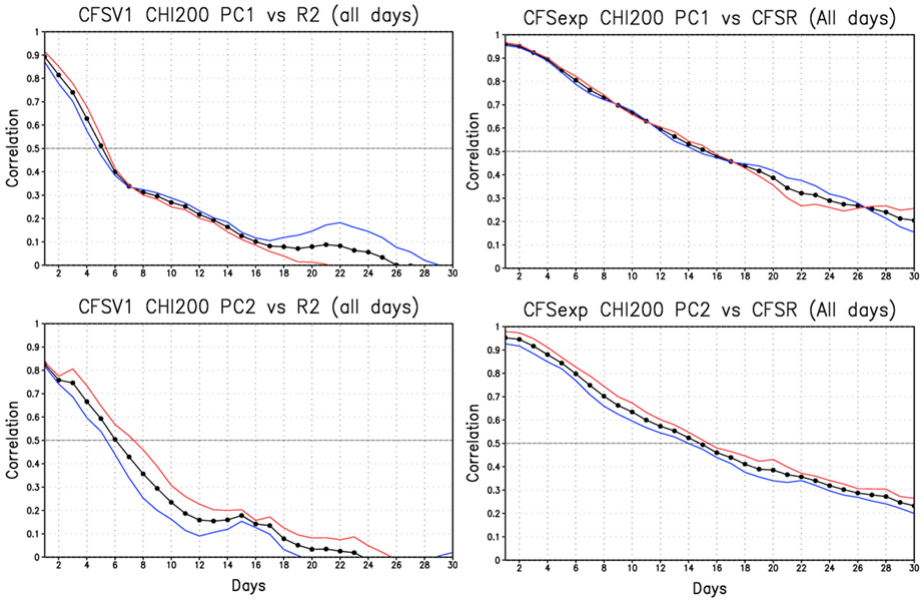

Fig. 5 Forecast skill of PC1 (upper) and PC2 (lower) of velocity potential in the CFSv1 (left) and CFSexp (right).

5. MJO prediction

While we cannot claim significant improvements in MJO simulation from CFSv1 to CFSexp the notable gains in representing the MJO in the new NCEP/CFSR reanalysis system offer the prospect for enhancement in near term (*i.e.* ~ 1-3 weeks) prediction of the MJO in the CFSexp, given the noticeable improvement in MJO related propagation characteristics in the CFSR-only depiction (Fig. 1). The forecast skill is calculated from several experimental 45-day runs for the CFSexp initialized daily between November 9-December 13 and February 9-March 13 for the years 1982-2006. For the CFSv1 it is only possible to calculate the skill for the common days of the period (~40 for each year) as daily initialized runs are not available. Figure 5 shows the forecast skill of the first two principal components of 20-100 day bandpass filtered 200 hPa velocity potential in the CFSv1 (left panels) and CFSexp (right panels). These structures typically represent the likely pattern of MJO variability (not shown). The red and blue curves denote the November-December runs and February-March runs respectively (to assess any potential seasonality), while the black curve is the average skill over all runs. There is a significant increase in useable skill of the CFSexp version in predicting the MJO (~ 16 days) as compared to the CFSv1 (~ 6 days). The skill was not affected by the increased number of forecasts in the CFSexp (*i.e.*, 62 *vs.* 40) as it remained similar when only comparing the common days between the two versions of the model (not shown). Another improvement is seen at the initial timestep where the CFSexp has a higher correlation, apparently a reflection of the improved initial conditions when compared to R2, and minimization of initialization shock due to the use of a similar model for the initializing CFSR and the predicting CFSexp, a situation that doesn't occur for the CFSv1, as the generation of R2 used a significantly different model than that of the CFSv1. A more in depth investigation of the MJO forecast skill in the CFS is currently underway and will be reported on in a forthcoming paper.

References

Kanamitsu, Masao, Wesley Ebisuzaki, Jack Woollen, Shi-Keng Yang, J. J. Hnilo, M. Fiorino, G. L. Potter, 2002: NCEP–DOE AMIP-II Reanalysis (R-2). *Bull. Amer. Meteor. Soc.*, **83**, 1631-1643.

Liebmann, B., and C. A. Smith, 1996: Description of a complete (interpolated) outgoing longwave radiation dataset. *Bull. Amer. Meteor. Soc.*, **77**, 1275-1277.

Lin, H., and G. Brunet, 2009: The influence of the Madden Julian Oscillation on Canadian wintertime surface air temperature. *Mon. Wea. Rev.,* **137**, 2250-2262.

Madden, R. A., and P. R. Julian, 1994: Observations of the 40-50 day tropical oscillation-A review. *Mon. Wea. Rev.,* **122**, 814-837.

Maloney, E. D., and D. L. Hartmann, 2000: Modulation of Eastern north Pacific hurricanes by the Madden-Julian Oscillation, *J. Climate,* **13**, 1451-1460.

Pohl, B., and A. J. Mathews, 2007: Observed changes in the lifetime and amplitude of the Madden-Julian Oscillation associated with interannual ENSO sea surface temperature anomalies. *J. Climate.,* **20**, 2659-2674.

Saha, S., and coauthors, 2006: The NCEP Climate Forecast System. *J. Climate, **19***, 3483-3517.

Saha, S., and coauthors, 2010: The NCEP Climate Forecast System Reanalysis. *Bull. Amer Met Soc,* in press.

Vitart, F, 2009: Impact of the Madden Julian Oscillation on tropical storms and risk of landfall in the ECMWF forecast system. *Geophys. Res. Lett.,* **36**, L15802.

Waliser, D., and coauthors, 2009, MJO simulation diagnostics, *J. Climate,* **22**, 3006-3030.

Xie, P., and Coauthors, 2003: GPCP pentad precipitation analyses: An experimental dataset based on gauge observations and satellite estimates. *J. Climate,* **16**, 2197-2214.

Zhang, C. and M. Dong, 2004: Seasonality in the Madden Julian Oscillation. *J. Climate,* **17**, 3169-3180.

Science and Technology Infusion Climate Bulletin
NOAA's National Weather Service
35th NOAA Annual Climate Diagnostics and Prediction Workshop
Raleigh, NC, 4-7 October 2010

A Synoptic-Climatology of Episodic, Sub-Seasonal Retractions of the Pacific Jet

Sharon C. Jaffe, Jonathan E. Martin, Daniel J. Vimont, and David J. Lorenz

Department of Atmospheric and Oceanic Sciences, University of Wisconsin-Madison, Madison, WI

1. Introduction

There are many sensible weather consequences of fluctuations in the zonal extent of the Pacific jet including a modulation of extreme precipitation events along the west coast of the United States (Higgins *et al.* 2000) as well as precipitation extremes in Hawaii, where a Pacific jet of limited zonal extent has been linked to active kona storm genesis periods in the central subtropical Pacific (Otkin and Martin 2004).

The Pacific jet undergoes rapid, sub-seasonal fluctuations in its zonal extent with the jet exit region potentially located anywhere from the western Pacific near 160°E to 120°W, off the west coast of the North American continent. In this study the evolution of the large-scale environment within which rapid jet retraction events occur will be described by means of a composite analysis of such events.

2. Data and methodology

The present study employs daily values of the horizontal wind (u,v), geopotential height (z), and sea-level pressure (SLP) (NDJFM from 1979-1980 to 2006-2007) taken from the NCEP/NCAR Reanalysis Dataset (Kalnay et al. 1996), daily values of outgoing longwave radiation (OLR) provided by NOAA/OAR/ESRL (Liebmann and Smith 1996), and a storm track dataset (K. Weickmann, personal communication) that provides pertinent records related to the lifecycle of cyclones in the Northern Hemisphere. In addition to daily data smoothed using a five-day running mean, anomaly data sets were also created in which a daily climatology was removed from the smoothed daily data (five-day running mean) in order to reveal the perturbation from mean conditions.

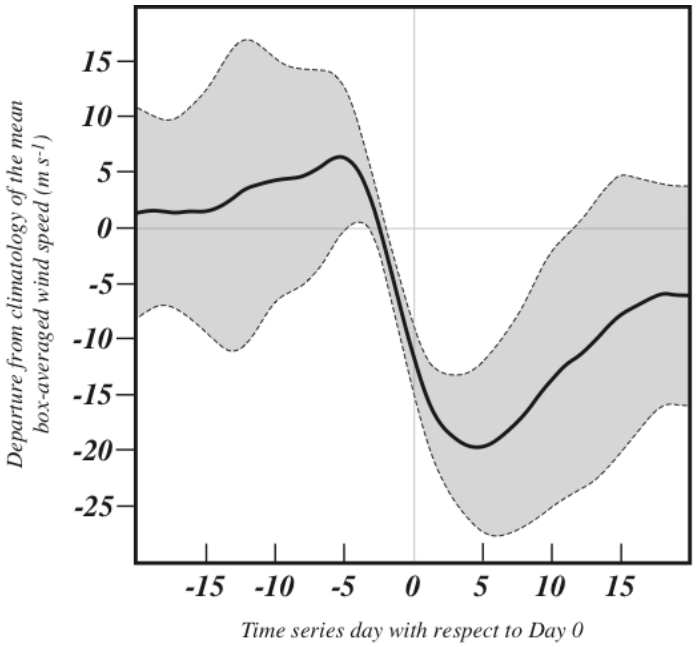

Fig. 1 Time series of the behavior of the composite zonal wind at 300 hPa. Solid line is the departure from climatology of the mean box-averaged 300 hPa zonal wind (m s^{-1}) over the 41 days comprising the analysis period for the 19 jet retraction events. Surrounding shaded area bounds the one standard deviation of the same variable for each of the 41 days comprising the analysis period for each of the 19 events.

Two methods were used to identify jet retraction events. The first, visual inspection, identified a jet retraction event whenever the 40 m s^{-1} isotach of the 300 hPa zonal wind retreated west of 180° for five or more consecutive days. The first day in such a series of days was regarded as the beginning of a retraction event and was designated Day 0 for that event. The second method used to identify jet retractions, the "box-average" method, identified retraction events based upon the area-averaged zonal wind speed in a box defined over the central Pacific Ocean (25°-40°N, 180°-160°W). Using the box-average method, a jet retraction event was identified when the average

Correspondence to: Jonathan Martin, Department of Atmospheric and Oceanic Sciences, University of Wisconsin-Madison, 1225 W. Dayton St., Madison, WI 53706; Email: jemarti1@wisc.edu

zonal wind speed in the box was 10 m s^{-1} slower than the climatological wind speed for at least five consecutive days *and* dropped below climatology by at least 18 m s^{-1} at some point during the period. The nineteen events that were identified in both the visual and box-average methods were used for subsequent analysis. The significance of jet retraction events is further supported by EOF/PC analysis, applied to the 300 hPa zonal wind field, where the dominant mode of variability of the upper-level zonal wind is found to be a strengthening/weakening of the zonal wind in the jet exit region.

Figure 1 shows a time series of the departure from climatology of the mean box-averaged zonal wind speed for all 19 retraction events bounded by one standard deviation from the mean for each day with respect to Day 0. The rapidity of the jet retraction is unmistakable: the zonal wind speed is at or above its climatological value before the retraction, suddenly decreases by ~20 m s^{-1} at the retraction, and then increases toward climatological values after the retraction. Such a time series testifies to an initial jet of climatological zonal extent, which rapidly retracts and then slowly recovers back toward climatology. Also, a correlation analysis (not shown) demonstrates that the predominant weakening of the zonal wind speed is concentrated near the jet exit region and does not reflect a uniform weakening of the entire jet structure.

3. Results of the composite analysis

The composite analysis was performed such that the 19 jet retractions were averaged together with respect to Day 0, forming the composite mean jet retraction event. The significance of the structures identified in the composites was assessed using a two-tailed student's t-test and only structures that are statistically significant at the 95% confidence level are discussed.

a. 500 hPa geopotential height and sea-level pressure

Figure 2 shows the composite structure of the associated 500 hPa geopotential height anomalies. The height field is initially characterized by an expansive negative height anomaly of -75 m that stretches over the entire mid-latitude north Pacific basin at Day –10 (Fig. 2a). The negative height anomaly is replaced by a growing positive height anomaly (Fig. 2c), which grows rapidly between

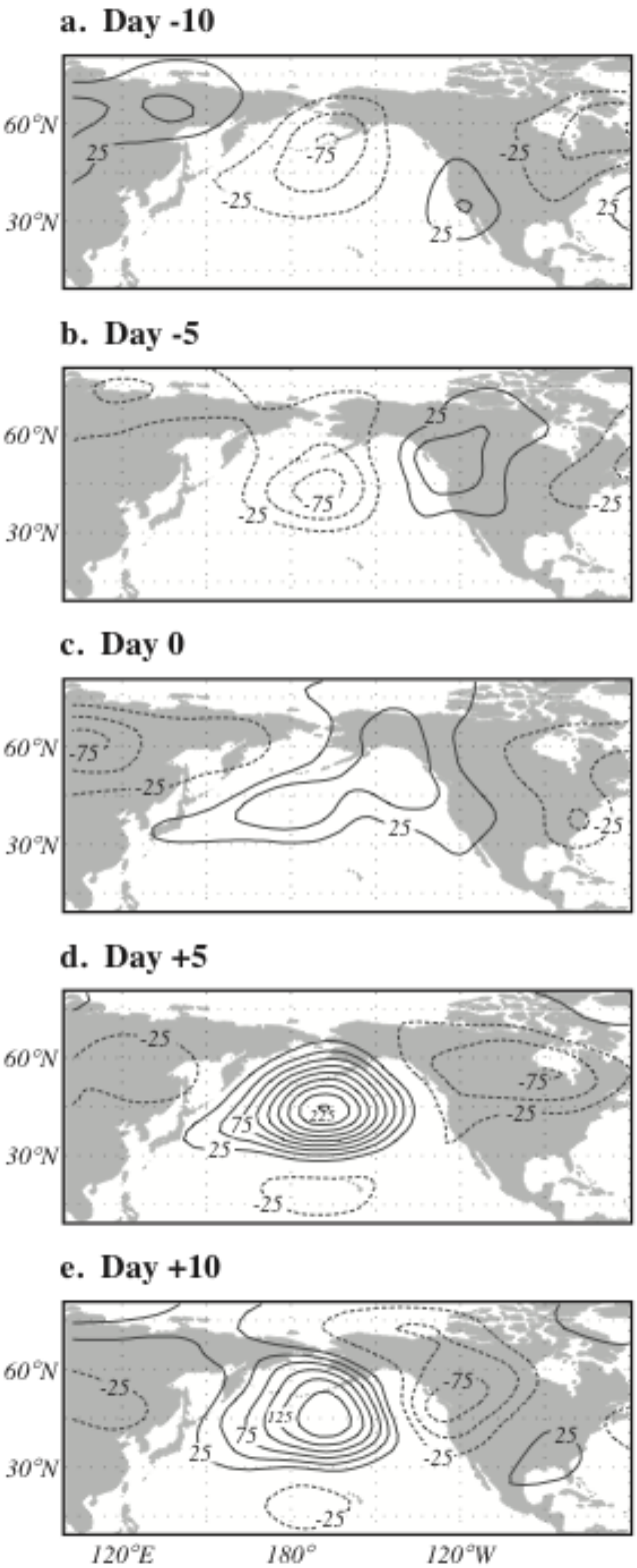

Fig. 2 Composite structure of 500 hPa geopotential height anomalies (m) associated with a jet retraction event at Day (a) -10 (b) -5 (c) 0 (d) +5 (e) +10. Solid (dashed) lines indicate positive (negative) height anomalies, contoured every 25 m with the zero line removed.

Day 0 and Day +5 into a 225 m positive height anomaly south of the Aleutian Islands (Fig. 2d). A transformation broadly similar to that observed at 500 hPa occurs in the SLP composite as well (not shown), with a nearly 20 hPa positive SLP anomaly centered at 35°N, 160°W at Day +5, dominating the central north Pacific basin.

b. Ertel potential vorticity (PV)

The first feature of interest in this composite of the 200-250 hPa Ertel potential vorticity (PV) anomaly, shown in Figure 3, is a negative PV anomaly that appears over the southern Rocky Mountains at Day -10 (Fig. 3a) and moves to the northwest, weakening slightly by Day -5 (Fig. 3b). Meanwhile a negative PV anomaly originating over Mongolia (Fig. 3a) moves eastward along the jet (Fig. 3b) and intensifies as it is stretched along the jet axis. Between Day -5 and Day 0 these two negative PV anomalies merge, with the Rocky Mountain anomaly retrogressing westward and the Mongolian anomaly moving into the jet exit region (Fig. 3b-c). As these negative PV anomalies merge they also amplify, forming a zonally elongated negative PV anomaly in the northern jet exit region by Day 0 (Fig. 3c).

A simultaneous progression occurs involving two positive PV anomalies located to the south of the jet core, forming a large-scale, north-south PV anomaly couplet in the central Pacific basin at Day +5 (Fig. 3d). Both the negative and positive PV anomalies become more isotropic between Day 0 and Day +5 (Fig. 3c-d). The development of this couplet implies anomalous easterly flow in the central Pacific consistent with a retraction of the Pacific jet. It is likely that interactions between the PV anomalies and the circulations associated with the jet exit region are fundamental to initiating jet retraction events.

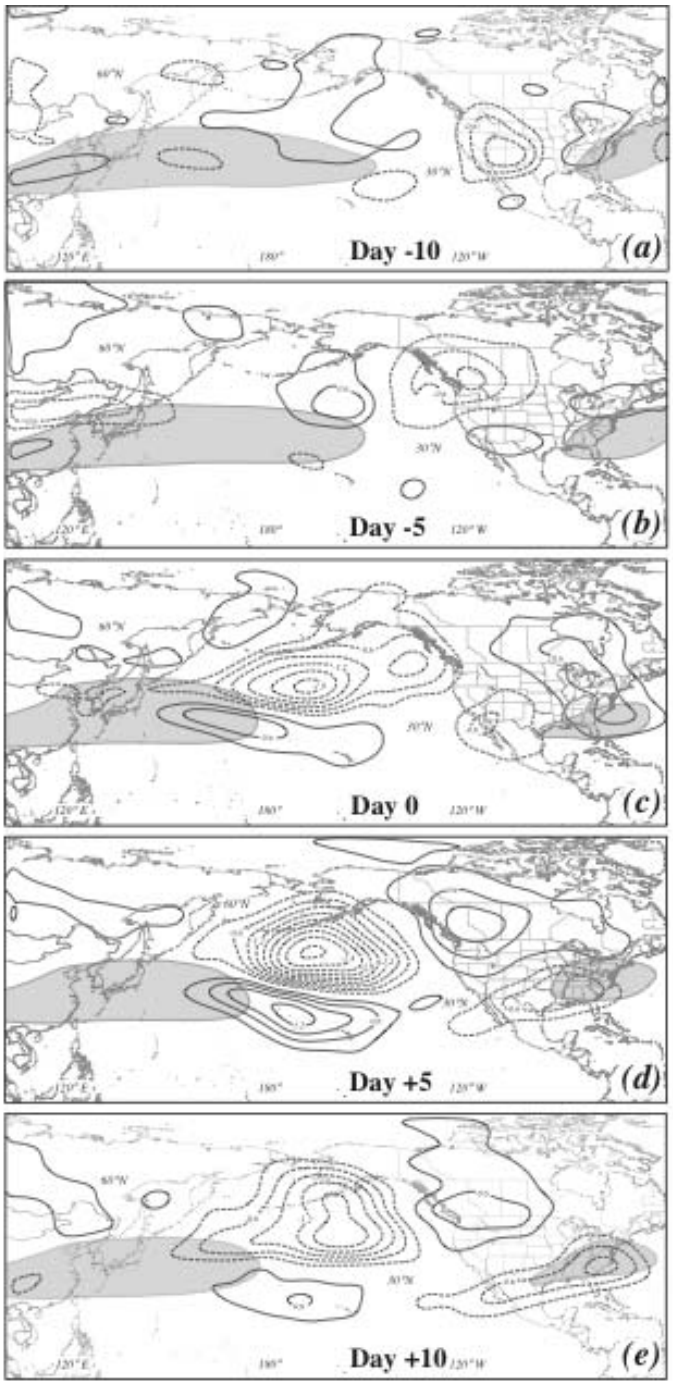

Fig. 3 Isertels of the composite perturbation 200 – 250 hPa Ertel potential vorticity associated with a jet retraction event at Day (a) -10 (b) -5 (c) 0 (d) 5 (e) 10. Solid (dashed) lines indicated positive (negative) perturbation PV, contoured every 0.3 PVU (1 PVU = 10^{-6} m^2 K kg^{-1} s^{-1}) with the zero line removed. Gray shading represents the 40 m s^{-1} isotach of the composite 250 hPa zonal wind.

c. Storm tracks

Using the storm track dataset cyclones were identified as local sea level pressure minima of 1010 hPa or less. A storm track density was then calculated, where the number of storms crossing each grid box was computed for periods encompassing 20 days before and after a jet retraction event. The difference in storm track density between those two periods is shown in Fig. 4, where dark (light) gray circles indicate that more

storms passed through a given point before (after) the jet was retracted. In general, Fig. 4 illustrates a shift in storm activity from the eastern Pacific (prior to the jet retraction) to the central Pacific (after the retraction). After the jet is retracted, there is a notable reduction in storm track density downstream and poleward of the location of the original jet, to the south of the Aleutian Islands. Another region of distinct change in the storm track density is located in the central subtropical Pacific (near 30°N, 180°E) where there is an increase in storm track density after the jet retraction occurs (Fig. 4), corroborating the relationship between the zonal extent of the jet and subtropical cyclone activity presented in Otkin and Martin (2004).

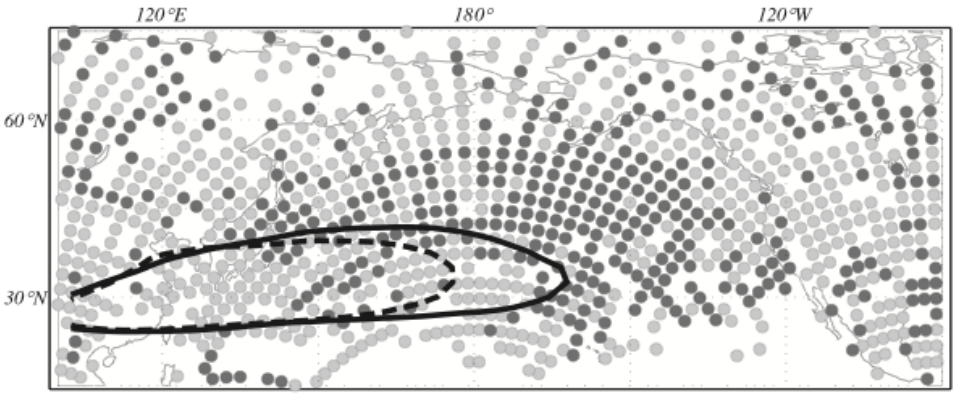

Fig. 4 Difference in storm track density associated with the composite jet retraction event (after – before) and the mean 40 m s^{-1} contour of the zonal wind before and after the event. Dark (light) gray signifies that more storms occur before (after) a jet retraction event at a particular grid point. The solid (dashed) black lines show the 40 m s^{-1} isotach of the composite 300 hPa zonal wind before (after) a jet retraction as in Fig.6.

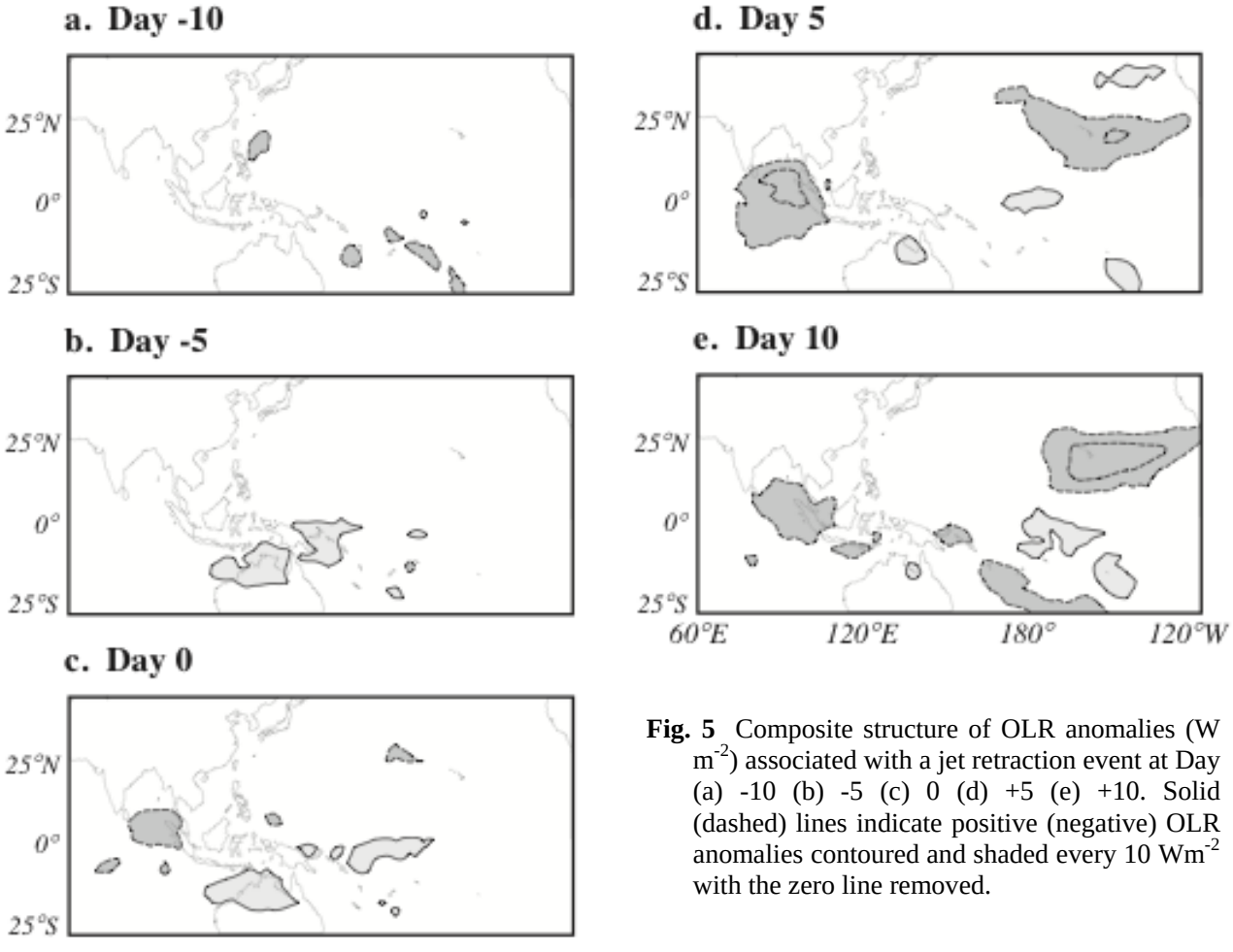

Fig. 5 Composite structure of OLR anomalies (W m^{-2}) associated with a jet retraction event at Day (a) -10 (b) -5 (c) 0 (d) +5 (e) +10. Solid (dashed) lines indicate positive (negative) OLR anomalies contoured and shaded every 10 Wm^{-2} with the zero line removed.

d. Outgoing longwave radiation (OLR)

Figure 5 shows the composite OLR anomalies associated with jet retraction events. The quasi-stationary negative OLR anomaly over Indonesia is first observed at Day 0 (Fig. 5c) and indicates anomalous convection in that region. Since it is relatively stationary, it is most likely not related to the MJO, which has a characteristic wave speed of 5 m s^{-1} (Zhang 2005).

The large negative OLR anomaly located over the central/eastern Pacific after the jet retraction, strongly visible at Day +5 and Day +10 (Fig. 5d-c), is most likely an effect of altered storm track activity related to the retraction of the jet (Fig. 4).

A large positive OLR anomaly, which is first apparent over northern Australia at Day -5 (Fig. 5b) is the third feature in the OLR composite and is not easily explained. The positive anomaly moves gradually eastward through the jet retraction period (Fig. 5b-e) and is located in the tropical central Pacific at Day +10 (Fig. 5e). A positive OLR anomaly in that location is consistent with a localized decrease in the strength of the Hadley cell compared to climatology that could contribute to a decrease in the intensity of the Pacific jet.

4. Summary and conclusions

Composite analysis of jet retraction events shows that the centers of extratropical circulation in the North Pacific basin rapidly undergo a complete reversal within a two-week period in association with jet retractions as a dominant negative anomaly becomes a dominant positive anomaly across the North Pacific in both the 500 hPa geopotential height and SLP fields. The results are consistent with the composite 200 – 250 hPa Ertel PV anomaly field, in which a jet retraction event is characterized by the formation of a zonally elongated, meridionally oriented PV anomaly couplet in the central North Pacific that becomes increasingly isotropic in the jet exit region as the jet retracts.

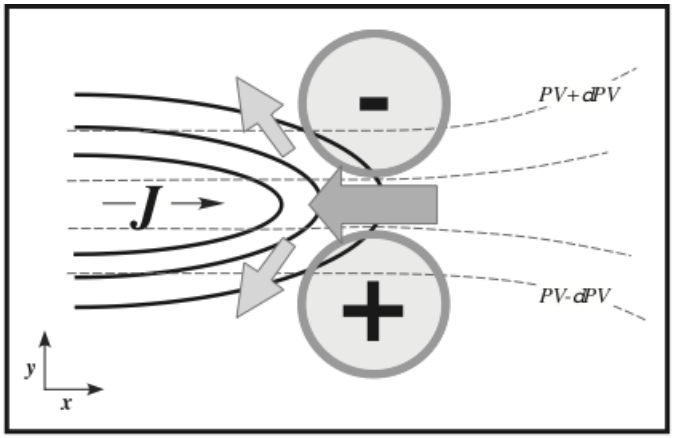

Fig. 6 Conceptual model of the effect of a meridional dipole of perturbation PV on the structure and circulation of the jet exit region during jet retraction events. Dashed lines are isertels of tropopause-level PV. Thick black lines represent schematic isotachs of the jet. Circular regions labeled "+" and "-" are perturbation PV features associated with jet retraction events (i.e. the PV dipole). The dark gray arrow is the perturbation easterly flow at the jet exit region arising from the meridional juxtaposition of the perturbation PV anomalies. The light gray arrows show the perturbation deformation associated with the PV dipole that weakens the PV gradient at and west of the jet exit region.

Variability in the Pacific storm track is found to accompany jet retraction events. When the jet is retracted, a substantial reduction in storm track density occurs poleward and downstream of the climatological jet exit region and subtropical cyclone activity in the central subtropical Pacific increases. Examination of composite OLR anomalies during jet retraction events reflects the changes in storm track activity observed in the region.

Two other features seen on the OLR composite are a quasi-stationary negative OLR anomaly located over the Indian Ocean, with a maximum amplitude at Day +5 and a positive OLR anomaly over Australia, maximized at Day 0. Only the positive OLR anomaly over Australia significantly precedes the jet retraction events. The physical connection between the Indonesian and Australian OLR anomalies and jet retraction events is not yet clear.

Though characterizing the structure and evolution of jet retraction events has been the focus of the present study, there are connections to elements of the large-scale circulation that suggest physical mechanisms, operating in the jet exit region, that may underlie these rapid retractions. Proposed mechanisms include barotropic instability (Hoskins et al. 1983; Otkin and Martin 2004) and the relaxation of the mean PV gradient

in the jet exit region (shown conceptually in Fig. 6). Future research will explore these mechanisms and their possible connection with jet retraction events.

References

Higgins, R.W., J.K.E. Schemm, W. Shi, and A. Leetmaa, 2000: Extreme precipitation events in the western United States related to tropical forcing. *J. Clim.*, **13**, 793-820.

Hoskins, B.J., I.N. James, and G.H. White, 1983: The shape, propagation, and mean-flow interaction of large-scale weather systems. *J. Atmos. Sci.*, **40**, 1595-1612.

Kalnay, E., M. Kanamitsu, R. Kistler, W. Collins, D. Deaven, L. Gandin, M. Iredell, S. Saha, G. White, J. Woollen, Y. Zhu, M. Chelliah, W. Ebisuzaki, W. Higgins, J. Janowiak, K.C. Mo, C. Ropelewski, J. Wang, a. Leetmaa, R. Reynolds, R. Jenne, and D. Joseph, 1996: The NCEP/NCAR 40-year reanalysis project. *Bull. Am. Meteorol. Soc.*, **77**, 437-471.

Liebmann, B., and C.A. Smith, 1996: Description of a Complete (Interpolated) Outgoing longwave radiation dataset. *Bull. Amer. Meteor. Soc.*, **77**, 1275-1277.

Otkin, J.A., and J.E. Martin, 2004: The large-scale modulation of subtropical cyclogenesis in the central and eastern Pacific Ocean. *Mon. Weather Rev.*, **132**, 1813-1828.

Zhang, C., 2005: Madden-Julian Oscillation. *Rev. Geophysics*, **43**, RG2003, doi:10.1029/2004RG000158.

Science and Technology Infusion Climate Bulletin
NOAA's National Weather Service
35th NOAA Annual Climate Diagnostics and Prediction Workshop
Raleigh, NC, 4-7 October 2010

Surface Water and Energy Budgets for the Mississippi River Basin in Three NCEP Reanalyses

Rongqian Yang, Michael Ek, Jesse Meng, and Kenneth Mitchell
Environmental Modeling Center, NOAA/NWS/NCEP, Camp Springs, MD

1. Introduction

An accurate description of model physics, more quality observational data, and the efficiency of the assimilation techniques are essential to the data assimilation system success. For these reasons, advances in the model physics, developments on the analysis scheme, and more available observations almost always prompt a necessity that data from the recent past are being reanalyzed using the state-of-the-art "frozen" model to develop a climate record and understand climate variations.

Over the past decades, the reanalyses developed at the National Centers for Environmental Prediction evolve from the National Centers for Environmental Prediction and the National Center for Atmospheric Research (NCEP-NCAR) Global Reanalysis I (GR1; see Kalnay *et al.*, 1996), then the National Centers for Environmental Prediction and the Department of Energy (NCEP-DOE) Global Reanalysis II (it is an error-fixed GR1; hereinafter referred to as GR2; see Kanamitsu *et al.*, 2002), and the North America Regional Reanalysis (hereinafter referred to as NARR; see Mesinger *et al.*, 2006), to the most recent global Climate Forecast System Reanalysis (hereinafter referred to as CFSR; see Saha *et al.*, 2010). The evolution represents decadal efforts on developing advanced model physics, improving the data assimilation technique, and utilizing more observational datasets to help understand the water and energy climate and its variations.

In this study, these efforts are combined and the large-scale average surface water and energy budgets are compared explicitly with each other and with the available observations to assess the ability of forecast models to estimate the energy and hydrometeorological balances for the large Mississippi basin, which has been a key objective and a focused region of the past Global Energy and Water Experiments (GEWEX) Global Continental-Scale International Project (GCIP), the subsequent GEWEX Americas Prediction Project (GAPP), and presently the Climate Prediction Program for the Americas (CPPA). Of particular social and economic importance, understanding the water and energy budgets is helpful to the water use management and in the preparation of emergency (drought and flood) response. With recent release of the most advanced CFSR dataset with a continuous coverage of 31 years (1979-2009), it is desirable to examine how the coupled high-resolution global reanalysis performs in developing regional budgets. Comparisons among the analyses and with measurements can yield new insights. Since surface water and energy processes are physically coupled. The differences in land model physics (section 2) and approach used to assimilate the observations (section 3) lead to notable differences in the surface water (section 4) and energy (section 5) budgets.

2. Land surface models

There are two land surface models used in the three reanalyses. One is the Oregon State University land surface model (OSU LSM, Pan and Mahrt, 1987), which is used in the GR2. The other is the Noah LSM. It originated from the OSU LSM with many physical improvements and updates added by many researchers. The Noah LSM has the same soil depth of 200 cm as in the OSU LSM, but is configured with four vertical soil layers (at depths of 10, 30, 60, and 100cm). More details are described in Chen *et al.* (1996), Koren *et al.* (1999), and Ek *et al.* (2003). The Noah LSM is used in both CFSR and NARR. The only difference is that the version used in CFSR is a problem-fixed (fluxes over patchy snow) version of that was used in NARR.

3. Assimilation of Observed Precipitation and Snow

Basically, there are three broad approaches to assimilate observed precipitation. The first is being the coupled land/atmosphere 4DDA approach where observed Sea Surface Temperature (SST) is used with

Correspondence to: Rongqian.Yang@noaa.gov, Environmental Modeling Center, NCEP/NWS/NOAA, 5200 Auth Road, Camp Springs, MD 20746; E-mail: Rongqian.Yang@noaa.gov

interactive land and the atmosphere (AMIP style). This method was adopted by the GR2 wherein the precipitation forcing at land surface is from its parent atmospheric model. To prevent long-term climate drift of soil moisture, the GR2 first computes 5-day mean precipitation. The average is then compared with the corresponding observed "pentad" dataset of the Climate Prediction Center (CPC)'s Merged Analysis of Precipitation (CMAP, Xie and Arkin 1997) that merges satellite and gauge measurements on a 2.5° x 2.5° latitude-longitude grid. The difference is used to adjust ("nudge") the first-layer soil moisture during the following pentad. Water equivalent snow depth is handled on a weekly basis as only a weekly Northern Hemisphere analysis of snow cover (without snow depth) was available for ingest. In the GR2, the model snow depth was used (including model predicted snow accumulation) where it was consistent with the input snow cover analysis. When model snow cover disagrees with observation, the model snow depth was adjusted to the snow cover analysis by either removing or adding the model snow without affecting the soil moisture. The GR2 is run on T62 Gaussian grid (approximately 200-km grid) with 28 levels, and retrospectively from 1979 to the present.

The second approach is a hybrid coupled land/atmosphere 4DDA approach (also AMIP style) that was used in the NARR. Unlike the direct use of observed precipitation in the GR2, the NARR assimilates precipitation for driving the land surface, where observed hourly observed precipitation is first converted to latent heat, and then the latent heat is used to adjust the Eta model's low-level moisture and cloud water fields (Lin *et al.* 2005). The hourly precipitation is mainly developed from the real-time 4-km U.S. precipitation analysis (Baldwin and Mitchell, 1997), hourly precipitation estimates from the WSR-88D radar network, and the hourly reports from the approximately 2,500 automated rain gauges via the GOES Data Collection Platform. The NARR uses the operational NCEP Eta model as the background model to better resolve orographic features, and runs on the Eta grid at horizontal space of 32 km with 45 vertical levels. Except the precipitation, most observed data in the GR2 were also used in the NARR (see Mesinger *et al.* 2006 for details on the observational data used in the NARR). The U.S Air Force Weather Agency's 47-km snow analysis was used to replace the model snow depth daily at 00z.

The third method is the uncoupled Land 4DDA (land model only) used in the CFSR. This approach is well-illustrated in the Global Soil Wetness Project (GSWP) of the late 1990's (Dirmeyer *et al.*, 1999). Such approach has become known as Land Data Assimilation Systems (LDAS) that do not actually assimilate observations to directly update the land states, but rather let the LSM-simulated land states physically evolve freely in response to the external analyses of near-surface atmospheric forcing, especially the precipitation analysis.

Two sets of global precipitation analyses are used in the CFSR land surface analysis. One is the CMAP dataset used in the GR2. The other data set used is the CPC unified global daily gauge analysis, constructed on a 0.5° x 0.5° latitude/longitude over the global land. The model precipitation (and snow) is also used in combination with the two precipitation analyses to produce daily global observed precipitation using a blending technique (with different weights given to each product depending on the quality of the analysis, see Saha *et al.* 2010 for details). The optimal interpolation (OI) algorithm of Xie *et al.* (2007) is employed to partially account for the orographic enhancements in precipitation. The resulting precipitation product is used to drive the offline Noah model to provide "observed" soil moisture that updates the CFSR soil moisture every day at 00z. The near-surface atmospheric forcing data for the Global LDAS (GLDAS) are from the NCEP's Global Data Assimilation System (GDAS). An external snow analysis (see Saha *et al.*, 2010 for a description of the analysis) is also used to update the snow depth in such a way that if model guess snow depth was greater than twice (or less than half) the analyzed value, then the model snow depth was set to twice (half) the analyzed value, otherwise, the model snow depth was not affected. In contrast to the direct replacement of model snow depth, this treatment tends to let the model have a relatively smooth evolution of the snowpack and reduce the artificial addition of snow water into the system if the land model has a quick snow meltdown problem. The CFSR is run on T382 Gaussian grid with 64 levels, and respectively from 1979 to the present. The high horizontal resolution (about 35 km) makes possible the direct comparison with the NARR (32 km). Note that as the all the water and energy budget terms are basically a function of the model parameterizations, the direct use of soil moisture from the uncoupled land data assimilation system in a

coupled system requires that the off-line Noah LSM be identical to the version used in the background model to avoid undesirable discrepancies.

	CFSR	NARR	GR2	Obs	CFS vs. NARR	CFSR vs. GR2	NARR vs. GR2	CFSR vs. Obs	NARR vs. Obs	GR2 vs. Obs
SW (W m^{-2})	149.57	158.13	162.83		0.87	0.84	0.84			
LW (W m^{-2})	-68.53	-77.08	-79.12		0.91	0.89	0.89			
-SH (W m^{-2})	-32.49	-34.66	-9.13		0.77	0.61	0.60			
-LH (W m^{-2})	-49.29	-55.34	-68.92		0.73	0.60	0.52			
G (W m^{-2})	2.28	-0.39	-0.38		0.25	0.43	0.34			
-SNOHF (W m^{-2})	-1.26	-1.08	-2.51		0.82	0.47	0.39			
Ts (K)	283.46	284.38	283.14		0.98	0.97	0.96			
UE (W m^{-2})	0.28	-10.42	2.77		-0.03	0.08	0.23			
P (W m^{-2})	2.24	1.92	2.32	2.07	0.81	0.76	0.71	0.64	0.69	0.53
R (mm day^{-1})	0.19	0.22	0.42	0.43	0.84	0.54	0.40	0.41	0.34	0.27
E (mm day^{-1})	1.68	1.91	2.38	1.64	0.70	0.61	0.48			
W (mm)	484.82	484.89	434.50		0.84	0.75	0.67			
-Δ*W*/Δ*t* (mm day^{-1})	0.37	0.01	0.04		0.96	0.84	0.83			
UW (mm day^{-1})	0.0	-0.22	-0.44		0.94	0.81	0.79			

Table 1 CFSR, NARR, and GR2 reanalyses and Obs annual means (1979-2009) for the Mississippi basin, and correlations among the three (CFSR vs. NARR; NARR vs. GR2; and NARR vs. GR2) and observation (CFSR vs. Obs; NARR vs. Obs; and GR2 vs. Obs). Correlations are calculated from time series that have the climatological mean removed, the runoff correlation is based on the period from Oct 1979 to Sep 1999). Shortwave radiation is SW, longwave radiation is LW, sensible heat is SH, latent heat is LH, ground heat is G, snow melting energy is SNOHF, surface temperature is Ts, and unbalanced energy forcing is UE. Precipitation is P, runoff is R, evaporation is E, total surface water W is composed of soil moisture and snow equivalent water, surface water tendency is $\Delta W/\Delta t$, and the unbalanced surface water is UW.

4. Surface water

a) Model formulation

The universal equation for computing surface water budget is

$$0 = -\Delta W/\Delta t + P + \text{Residual} - E - R \qquad (1)$$

The temporal change in surface water $\Delta W/\Delta t$ is equal to precipitation plus Residual (discussed below) minus evaporation P and runoff R (including surface and subsurface flow). The surface water includes total soil moisture in various soil layers (two in OSU and four in Noah), lakes and rivers which is relatively small compared to the total soil moisture and snow water equivalent. The evaporation includes direct evaporation from bare soil, evapotranspiration from vegetation (using the Jarvis-Stewart canopy resistance approach), direct evaporation from canopy surface (very small on a monthly basis; not considered in the present study), and snow sublimation (which is absent in the OSU LSM). The residual term has two sources. One is from the explicit or implicit insertion of the observations (*i.e.*, precipitation and snow analysis). The insertions include, the direct use of observed "pentad" data over a 5-day period and weekly snow update in the GR2, the daily snowpack update in the NARR (the modification of low-level moisture profile is needed to be accounted for in the atmospheric water budget), and the daily replacement of model soil moisture and snow update in the CFSR. The other part of the residual comes from model errors (*e.g.*, unrealistic parameterizations) and post-processing errors (such as interpolation of variable from one grid to another).

Comparisons of the monthly mean surface hydrologic components for the 31 years (1979-2009) are shown below. Monthly anomalies are calculated with the monthly mean climatology for each individual month subtracted. Table 1 provides the annual means for the same variables and the correlations of monthly time series among the three analyses, and those between the precipitation and stream flow observations and each analysis. Table 1 also shows that the evaporation in the CFSR (1.68 mm/day) is in closer agreement with the estimate (1.64 mm/day; found by taking the difference of the observed precipitation and stream flow) than the other two analyses (1.91 mm/day in the NARR and 2.38 mm/day in the GR2, respectively).

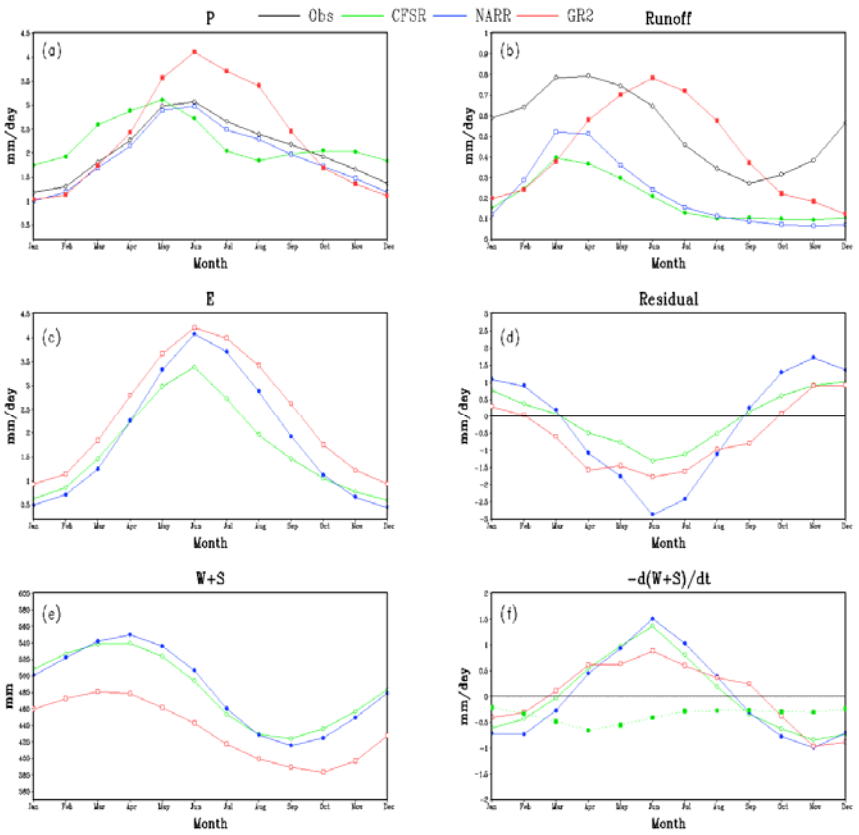

Fig. 1 Seasonal surface water budget terms of CFSR (green), NARR(blue), and GR2(red) Reanalysis for the Mississippi basin: (a) precipitation (P); (b) Runoff; (c) evaporation (E); (d) residual; (e) total soil water plus snow (W+S); and (f) surface water tendency $\Delta W/\Delta t$ (-d (W+S)/dt). In (a) and (b) precipitation and stream flow observations are shown as black lines where the observed runoff climatology is based on the stream flow at Vicksburg, Mississippi covering a period from Oct 1979 to Sep1999.

b) Comparison of reanalysis

Figure 1 shows the mean annual cycle of the terms in Eq. (1) in the surface water budget of the three analyses. The observed precipitation is the precipitation used for driving the off-line Noah LSM (1979-2009) in the CFSR, and the observed runoff is based on the observed daily stream flow at the gauge at Vicksburg, Mississippi covering a 21-yr period from 1979 to 1999.

The mean seasonal cycle of precipitation is accurately described in the NARR, which is the outcome of frequent adjustments to the low-level atmospheric moisture profile and cloud fields using the hourly observed precipitation; has slightly low bias in warm season and high bias in cold season in the CFSR, which are probably related to the atmospheric responses to soil moisture changes in summer and the stable boundary formulations in winter; and has high bias in warm season in the GR2, which is a known problem (*e.g.* Betts *et al.*, 1996), could be attributed to the convection and planetary boundary parameterizations. There also are indeed large differences in the total runoff. The CFSR and NARR runoffs are persistently lower and has smaller annual cycle compared to the observed stream flow, despite both analyses have relatively realistic precipitations, suggesting that the total runoff is mainly from the subsurface where soil moisture has smaller seasonality. Given the Noah LSM has four soil layers, it may also indicate that too much precipitation goes to the storage and the surface runoff may be underestimated. As a result, even with the large snowmelt in early spring (March), the total runoff in both NARR and CFSR is still low. Further study is necessary to confirm this. By contrast, the GR2 has an amplified annual cycle. It is too high during the summer and low during the winter and correlates well with the precipitation bias. Unlike in the CFSR and NARR where total runoff peaks in March to April, the total runoff in GR2 peaks in June. It may have multiple causes including high bias in summer precipitation, the 5-day delay in the nudging scheme, and possibly low bias in the predicted snow

water, among others. Consistent with the precipitation cycle, total evaporation in the CFSR and NARR is lower than in the GR2, even the total surface water is considerably higher, is probably related to more controls over canopy transpiration in the Noah LSM. The higher (lower) evaporation in winter (summer) in CFSR than in NARR is also consistent with the precipitation biases. It is not surprising to see that there are very good agreements in surface water amount and variation between the CFSR and NARR as the success of NARR in assimilating precipitation (Messinger *et al.* 2006) is equivalent to using the observed hourly precipitation to drive the off-line Noah LSM except the time interval is daily in the CFSR. Given the OSU and the Noah LSM have the same soil depth (2m), the considerably low in total surface water and the smaller seasonal cycle in the GR2 may be due to the larger evaporation (less control on surface evaporation) and higher runoff in the OSU LSM. In spite of the differences in assimilating observed precipitation, surface water in the three analyses has a more or less exaggerated seasonal cycle, because of the "nudging" of soil moisture towards an imposed seasonal cycle, which removes water in summer and adds surface water in winter when the model runoff has a low bias. Even in the CFSR where winter precipitation shows a high bias, the excessive precipitation (mainly liquid over the large basin) goes to the deeper soil layers and adds to the seasonal variability and summer precipitation has a low bias, but with the much lower bias in runoff, the soil is still too wet. This cycle acts to damp the seasonal changes in water storage. Note that for the residual in CFSR has the artificial updates removed (the dotted line with solid green dots in the storage change panel). As discussed earlier, it mainly comes from the model errors. During the summer months, the residual is more associated runoff with heavy rain (no routing scheme in this version of Noah LSM), whereas in the cold season, it is possibly more related to the snowpack physics. The post-processing process may contribute a small portion as well. On average, as shown in Table 1, the water budget in CFSR is closed on an annual basis. In the NARR, in addition to the artificial forcing (snow updates), the interpolation from the Eta grid to other user-friendly grids (the output is not on the native Eta grid) may have large errors, especially over steep and high mountains, so it is not surprising to see the highest residual in the summer. The reason of relatively low residual in the GR2 may be partially due to its coarse resolution.

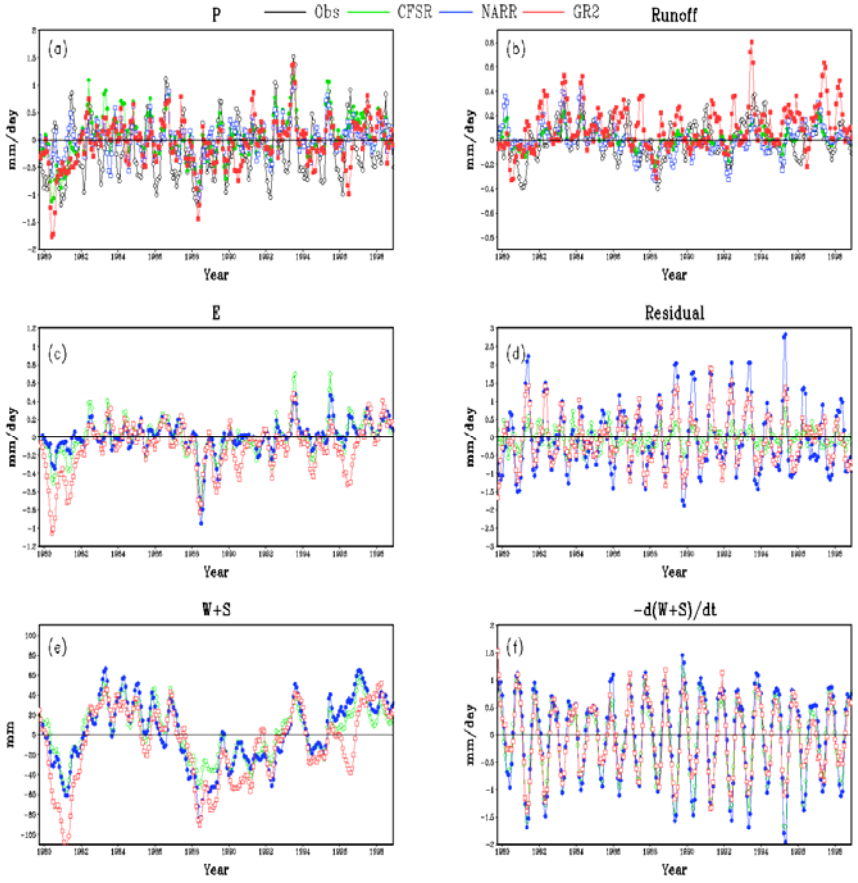

Fig. 2 As in Fig. 1 for monthly anomalies of surface water budget terms from Oct. 1979 to Sep.1999 (three-month running means for the presentation only) for CFSR, NARR, GR2, and observations [(a) and (b) only].

Figure 2 shows the variations of the monthly anomalies in the surface hydrological cycle. Despite the disparities in the seasonal means, the anomaly fields show greater similarity in amplitude and variation than do the corresponding means, which provides some renewed confidence in the value of the reanalyses. In particular, the precipitation in both NARR and CFSR has similar interannual variability and is closer to the

observation (Table 1). In comparison, the GR2 precipitation has more extreme years and larger interannual variation and thus has a lower overall correlation with respect to the observation (Table 1). Similar to precipitation, the GR2 runoff has an amplified interannual variation than do the other two analyses, particularly in the summer months. In spite of the low bias of mean runoff in both NARR and CFSR, the anomaly correlates well with the observation (Table 1). The evaporation in the three analyses seems to agree well over the most years, e.g., the US Drought of 1988 (April to June 1988 from the Midwest to the Great Plains) and the Great Flood of 1993 (April to October 1993 along the Mississippi and Missouri rivers and their tributaries). The disagreements between GR2 and the other two analyses from late summer of 1996 to early spring of 1997 are associated with the negative precipitation anomaly in GR2, which are also reflected in the surface water. An examination of the observed precipitation data during this period is needed to find the causes. Despite the lower total surface amount in GR2, the interannual variation has similar amplitude to what is shown in the CFSR and NARR. Note that the unrealistic interannual variation of soil moisture at the beginning of GR2 might have two causes. One is the spin down of soil moisture from the GR1 that was used to initialize GR2 on December 1, 1978. The other could be the pentad precipitation analysis in which missing rain gauge observations were mistakenly reported to zero. Thus, the use of GR2 soil moisture in the earlier period is cautioned (Kanamitsu *et al.* 2002).

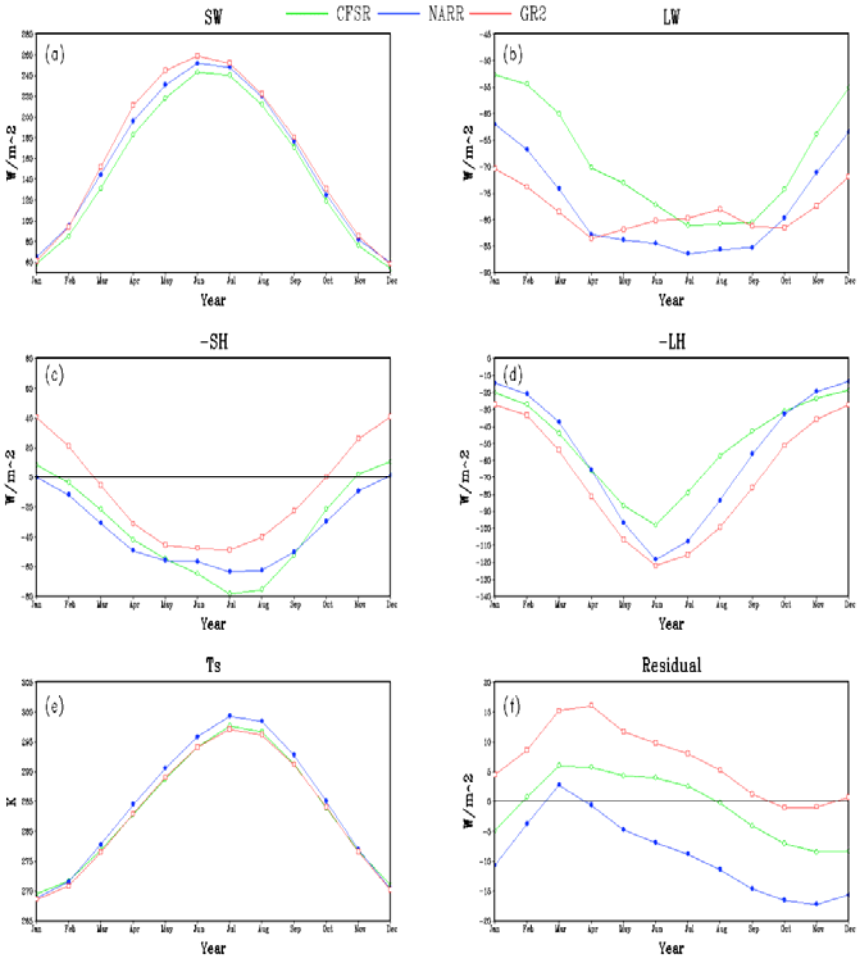

Fig. 3 Seasonal surface energy budget terms of CFSR (green), NARR (blue), and GR2 (red) Reanalysis for the Mississippi basin: (a) Net surface solar radiation (SW); (b) net surface longwave radiation (LW); (c) sensible heat (SH); (d) latent heat (LH); (e) surface temperature (T_s); and (f) residual.

The change in surface water is comparable among the three analyses. Consistent with their mean seasonal cycles, the interannual variability in both CFSR and NARR is slightly higher than that in GR2. The water residual in CFSR has the smallest interannual variability. Unfortunately, the artificial forcings in both NARR and GR2 can't be removed from the calculations, which make it hard to discern the causes that both NARR and GR2 have larger tendency terms.

5. Surface energy

The corresponding surface energy budget can be written as:

$$0 = SW + LW - SH - LH - G - SNOHF \qquad (2)$$

The net shortwave heating SW is balanced by net longwave cooling LW, the sensible heat SH, the latent heat LH, the ground heat G, and the snowmelt heat SNOHF. The analyses compute surface skin temperature diagnostically from the surface energy balance. On the monthly timescales, the variation in surface temperature Ts is closely tied to the changes in surface skin temperature.

As shown in Fig. 3, there is almost a complete seasonal energy balance, where solar radiation provides large positive input; this input is slightly smaller in CFSR and larger in GR2 compared to NARR. This solar flux is balanced by net longwave radiation, sensible heat, latent heat (including snow sublimation), ground heat (see Table 1), and snow melting energy (see Table 1). All act to cool the surface, especially during the summer. Sensible heat and ground heat also help to warm the surface during the winter. The higher SW in GR2 is consistent with higher LH, lower SH, Ts, and LW. Also the lower SW leads to lower LH and LW, and higher Ts in the CFSR. The higher longwave cooling in GR2 during the cold months may be due to high sensible heat exchange that could be related to the stable boundary transfer coefficients. Compared to the NARR, there are stronger (weaker) sensible heating of the atmosphere during the summer (winter) and less (more) latent heat during summer (winter) in the CFSR, although the Ts in CFSR is generally lower. This is probably due to the adjustment to the atmospheric low-level moisture profile, which will impact boundary clouds and the partitioning of the net radiation flux. Note that the seasonal variation of surface temperature is similar in the three reanalyses with slightly larger in the NARR. The residual in GR2 is large during the early months. It is probably due to the lower thermal boundary condition and the absence of snow sublimation physics in the OSU LSM. The NARR has the largest residual in the relatively cold months. It is related to an error involved in flux calculations over patch snow. Unfortunately it was found too late to catch the NARR production phase. The modification of lower boundary moisture profile while assimilating the observed precipitation, especially during the summer, may also contribute to the error as well. The CFSR residual seems to have a seasonal cycle, which is positive during warm months and negative in cold months. It is probably more related to the ground heat flux. As shown in Table 1, the CFSR don't have a near-zero annual ground flux compared to the other two reanalyses. As might be expected, with the coupled nature of the CFSR and the equipment of advanced physics in the Noah LSM, the CFSR has the smallest annual residual heating of 0.28 Wm^{-2}, which is also consistent with its zero residual in the annual water budget. Considering other possible post-processing errors, it is assumed that the energy budget is closed on an annual basis in the CFSR.

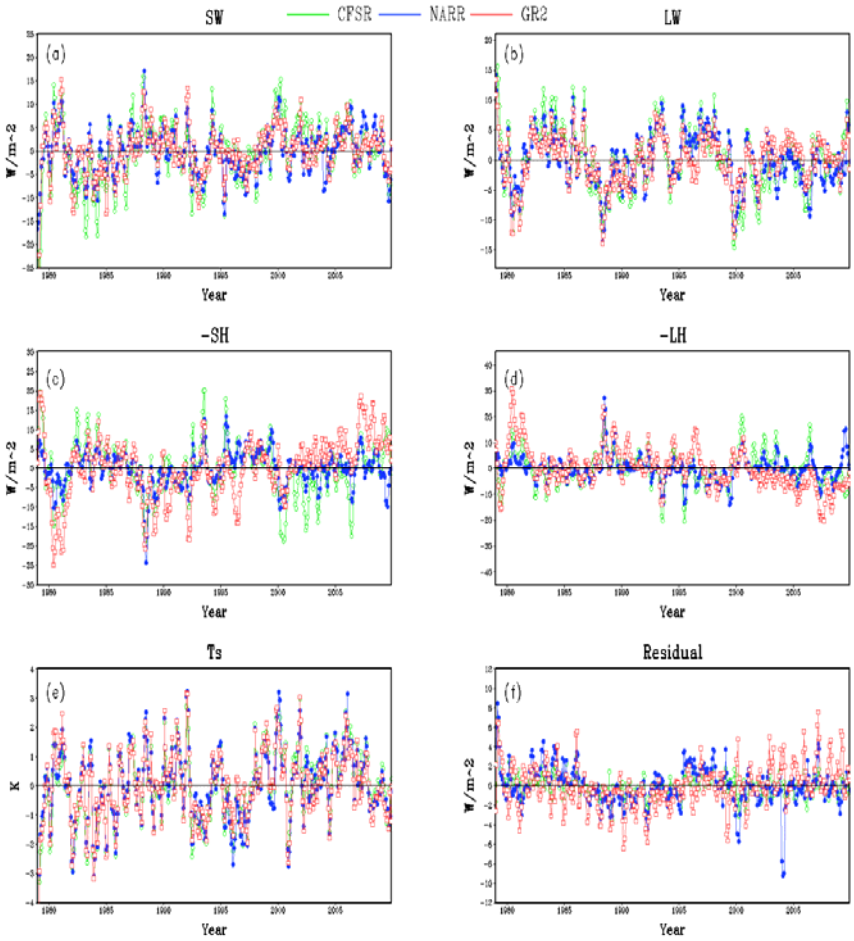

Fig. 4 As in Fig.3 for monthly anomalies of surface energy budget terms (three-month running means for presentation only).

Figure 4 shows the variation of the anomalies in the energy

terms, which again have remarkable consistency among the three analyses. The anomalies in the energy budget have clear phase relationships which are in consistence with their climatologies. Note that shortwave and longwave components have almost opposite variations with each other. So do the sensible heat and latent heat, which probably means that they mirror variations in cloudiness, since less could cover gives more incoming shortwave and more outgoing longwave radiation. Actually, the radiation variations are somewhat similar to the surface water variation, which also suggests that increased surface water produces increased cloudiness. This conclusion also needs further study. The variation in residual heating is comparable with slightly larger in GR2. Table 1 shows the CFSR radiation fluxes are more like the NARR in the correlation of energy terms.

6. Summary and discussion

In this paper, the three analyses developed at the NCEP are compared with each other and with available observations for the Mississippi basin for the period 1979-2009. There are a number of noticeable differences and similarities. The GR2 precipitation, runoff, and possible evaporation are too high compared to the observations, whereas the CFSR and NARR runoff are too small even the precipitations are closer to the observations. The discrepancies are caused by physical parameterizations used in the land models and the approaches in which the observations are ingested in the data assimilation systems. There are large differences in the water budget, the disagreements on water budget terms between GR2 and the other two analyses are mainly caused by the OSU LSM physics, especially surface evaporation control and runoff parameterizations. The nudging scheme used in GR2 is not efficient and the imposed water climate might be quite different from the model's climate, which will adversely impact surface evaporation and subsequent precipitation. These problems have been corrected by using the advanced Noah LSM and an alternative assimilation technique. The success of NARR in assimilating the highly quality observed precipitation through highly controlling the lower boundary moisture profile is a good example. The direct insertion of observed snow depth may also contribute to a slightly better water climate. In contrast, the CFSR assimilates precipitation via changing soil moisture obtained from the uncoupled land data analysis, it imposes less restriction on daily precipitation. However, because soil moisture has long memory and the correlation between soil moisture and precipitation could be very different over different climate regimes, thus this method is also susceptive to background model biases. So is the use of model snow depth within specified range, particularly in the cold months.

Focusing on the large Mississippi basin, this study shows that the CFSR and NARR depict better water climate than the previous GR2. Despite the seasonal differences in water budget among the three reanslyses, the energy terms are comparable and highly correlated with each other (Table 1). Unfortunately, the reanalyses, more or less, carry errors, even in the CFSR where the water and energy budgets can only be balanced on an annual basis. Further study is needed to better represent land surface physics in future reanalyses. Nevertheless, the comparison shows that the CFSR achieves a large improvement over the previous GR2, and compares well with the NARR, and thus can be used in the global climate studies.

Acknowledgements. We thank the EMC CFSR team members for their hard work in completing the CFSR project. This study was supported by the NCEP Core Project component of the NOAA Climate Program Office/Climate Prediction Program for the Americas (CPPA).

References

Baldwin, M. E., and K.E. Mitchell, 1997: The NCEP hourly multi-sensor U.S. precipitation analysis for operations and GCIP research. *Preprints, 13th AMS Conference on Hydrology,* Long Beach, CA, 54-55.

Betts, A., S-Y. Hong, and H-L. Pan, 1996: Comparison of NCEP-NCAR reanalysis with 1987 FIFE data. *Mon. Wea. Rev.*, **124**, 1480-1498.

Chen, F., and Coauthors, 1996: Modeling of land surface evaporation by four schemes and comparison with FIFE observations. *J. Geophys. Res.,* **101**, 7251–7268.

Dirmeyer, P. A., A. J. Dolman, and N. Sato, 1999: The Global Soil Wetness Project: A pilot project for global land surface modeling and validation. *Bull. Amer. Meteor. Soc.*, **80**, 851-878.

Ek, M. B., K. E. Mitchell, Y. Lin, E. Rogers, P. Grunmann, V. Koren, G. Gayno, and J. D. Tarpley, 2003: Implementation of Noah land surface model advances in the National Centers for Environmental Protection operational mesoscale Eta model. *J. Geophys. Res*., **108**, 8851, doi:10.1029/2002JD003296.

Lin, Y., K. E. Mitchell, E. Rogers, and G. J. DiMego, 2005: Using hourly and daily precipitation analyses to improve model water budget. *Preprints, AMS 9th Symp. on Integrated Observing and Assimilation Systems for the Atmosphere, Oceans, and Land Surface,* San Diego, CA. [Available online at http://ams.confex.com/ams/pdfpapers/84484.pdf.]

Kalnay, E., and Coathours,1996: The NCEP/NCAR 40-Year Reanalysis Project. *Bull. Amer. Meteor. Soc.*, **77**, 437-471.

Kanamitsu M., and Coauthors, 2002: NCEP-DOE AMIP-II Reanalysis (R-2). *Bull. Amer. Meteor. Soc*., **83**, 1631-1643.

Koren, V., J. Schaake, K. Mitchell, Q.-Y. Duan, F. Chen, and J. M. Baker, 1999: A parameterization of snowpack and frozen ground intended for NCEP weather and climate models. *J. Geophys. Res.,* **104,** 19 569–19 585.

Mesinger, F., and Coauthors, 2006: North American Regional Reanalysis. *Bull. Amer. Meteor. Soc.*, **87**, 343–360.

Pan, H.-L., and L. Mahrt, 1987: Interaction between soil hydrology and boundary-layer development. *Bound.-Layer Meteor*., **38**, 185–202.

Saha S., and Coauthors. 2010: The NCEP climate forecast system reanalysis. *Bull. Amer. Meteor. Soc.*, **91**, 1015-1057.

Xie, P., and P. A. Arkin, 1997: Global precipitation: A 17-year monthly analysis based on gauge observations, satellite estimates, and numerical model outputs. *Bull. Amer. Meteor. Soc*., **78**, 2539–2558.

Xie, P., M. Chen, A. Yatagai, T. Hayasaka, Y. Fukushima, and S. Yang, 2007: A gauge based analysis of daily precipitation over East Asia. *J. Hydrometeor*., **8**, 607 -626.

Science and Technology Infusion Climate Bulletin
NOAA's National Weather Service
35th NOAA Annual Climate Diagnostics and Prediction Workshop
Raleigh, NC, 4-7 October 2010

Effects of River Routing Processes on a Simulated Climatology in the Air-Sea Coupled Model

Suryun Ham, Song-You Hong, Yign Noh, Soon-Il An
Department of Atmospheric Sciences and Global Environment Laboratory, Yonsei University, Seoul, South Korea

Young-Hwa Byun, Hyun-Suk Kang, Johan Lee and Won-Tae Kwon
Climate Research Laboratory, National Institute of Meteorological Research, Korea Meteorological Administration, Seoul, South Korea

1. Introduction

Understanding the transport of water over the surface of land is an ongoing subject of research. Freshwater flux has a direct effect on salinity in the ocean, which affects climate and water cycles. It modifies the density of water, mixed layer depth, and mixing and entrainment, all of which can affect sea surface temperature (SST) (Zhang and Busalacchi 2009). Moreover, freshwater flux is an important component forcing source driving thermohaline circulation (Yang *et al.* 1999). Studies have been done to determine the quantity of flow along rivers at various points in time and space. Most of them have focused on small watersheds or regional models (*e.g.*, Liston *et al.* 1994; Oki *et al.* 1999; Lucas-Picher *et al.* 2003). For example, Liston *et al.* (1994) presented a runoff routing model that produced discharge hydrographs from regional gridded runoff data. Oki *et al.* (1999) calculated the mean runoff estimated by the Land Surface Models (LSMs) for drainage areas upstream of 250 operational global gauging stations.

Recently, the climate modeling community has found the importance of freshwater forcing from precipitation or river to track the flow of water to the ocean on a global scale (*e.g.*, Yang *et al.* 1999; Zhang and Busalacchi 2009). Yang *et al.* (1999) showed that the inclusion of freshwater input from precipitation could lead to increases in SST by as much as 0.5 K in the tropical ocean in an oceanic general circulation model (OGCM). They also suggested that the effects of salinity should not be neglected for realistic forecasts of tropical oceans. There are only a few modeling studies considering freshwater forcing and its salinity-related effects on climate variability. Zhang and Busalacchi (2009) found that the impact of freshwater flux forcing leads to enhanced interannual variability and ENSO cycles. However, this was investigated using a hybrid coupled model constructed from the OGCM and the simplified atmospheric model. Using the fully coupled ocean-atmosphere GCM, the mechanisms response to the western tropical Pacific freshwater flux forcing were investigated by Wu *et al.* (2010). However, they imposed an idealized forcing over the limited region in the coupled model.

The purpose of this study is to investigate the effects of river routing processes on simulated climatology in the Hadley Centre Global Environmental Model version 2 (HadGEM2) (Collins *et al.* 2008) in conjunction with a river routing scheme using the Total Runoff Integrating Pathways (TRIP) (Oki and Sud 1998).

2. Experimental design

Two experiments are designed to investigate the effects of river flow on a climate system. The run (RIV) with river routing scheme and the experiment (nRIV) without TRIP were performed. The simulations were initialized and spun up from an ocean state, corresponding to climatological fields of September mean potential temperature and salinity (Levitus *et al.* 1998). The atmospheric initial data was from analysis field by Met Office. The atmospheric initial data is largely irrelevant in climate simulations, certainly after the first few months. A more detailed description of the initial data is available in the study of Johns *et al.* (2006). The model integrations were run for an 11-year period from 1 September 1978, with an approximate 4-month lead time. The results for 10-year are analyzed because the key feature in 1979 (1-year) is similar to those during

Correspondence to: Song-You Hong, Department of Atmospheric Sciences, Yonsei University, Seoul 120-749, South Korea; E-mail: shong@yonsei.ac.kr.

1979-1988 (10-year) although it tends to be smoothed. It means the thermodynamic response between ocean and atmosphere is more dominant than ocean dynamics feedback in this study.

3. Results and discussion

The river routing processes in the RIV experiment affect salinity through the discharge of freshwater. Vertical distributions of salinity and temperature from the RIV and nRIV experiments over the tropical eastern Pacific (15°S ~ 15°N, 70°W ~ 110°W) are shown in Fig. 1. The salinity from the RIV simulation is significantly decreased near the sea surface to around 0.6 (PSU*1000), and slightly increased below 55 m compared to that from the nRIV simulation (Fig. 1a). In the RIV run, the temperature profile shows a warming about 1°K near sea surface and a cooling about 1~2°K between 20 m and 150 m compared to that from the nRIV run (Fig. 1b). It is clear that the RIV experiment results in a shallower ocean mixed layer depth (roughly 20 m) than the nRIV experiment (roughly 55 m). The reduced salinity from the RIV run causes an increase in SST due to shallower mixed layer depth. This leads to a weakening of trade winds, and consequently reduction of upwelling, which may further raise the SST by reducing the inflow of cold subsurface water into the mixed layer.

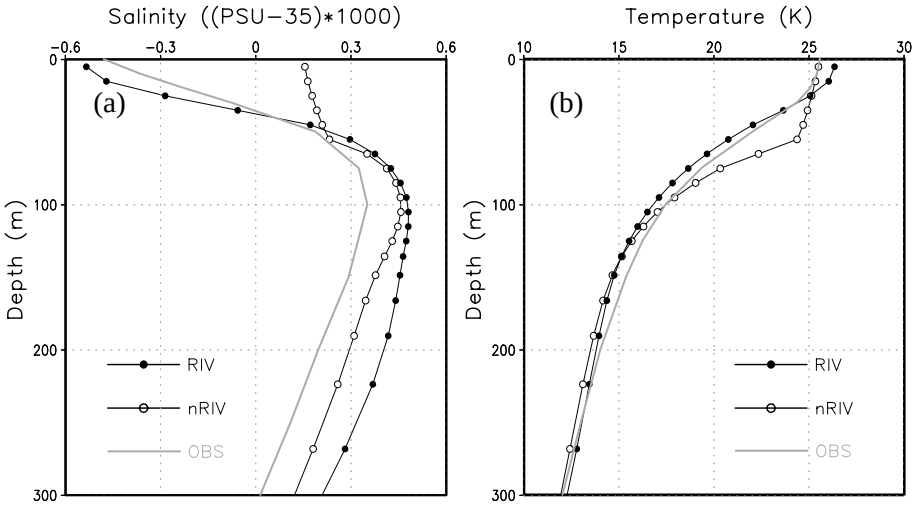

Fig. 1 Vertical distributions of (a) salinity ((PSU-35) × 1000) and (b) temperature (K) averaged for the latitudinal band (15°S ~ 15°N) and the zonal band (70°W ~ 110°W) from the RIV and nRIV experiments. Solid line with open circles for the nRIV run, solid line with closed circles for the RIV run, and gray solid line for the Levitus (1994) observation data, respectively.

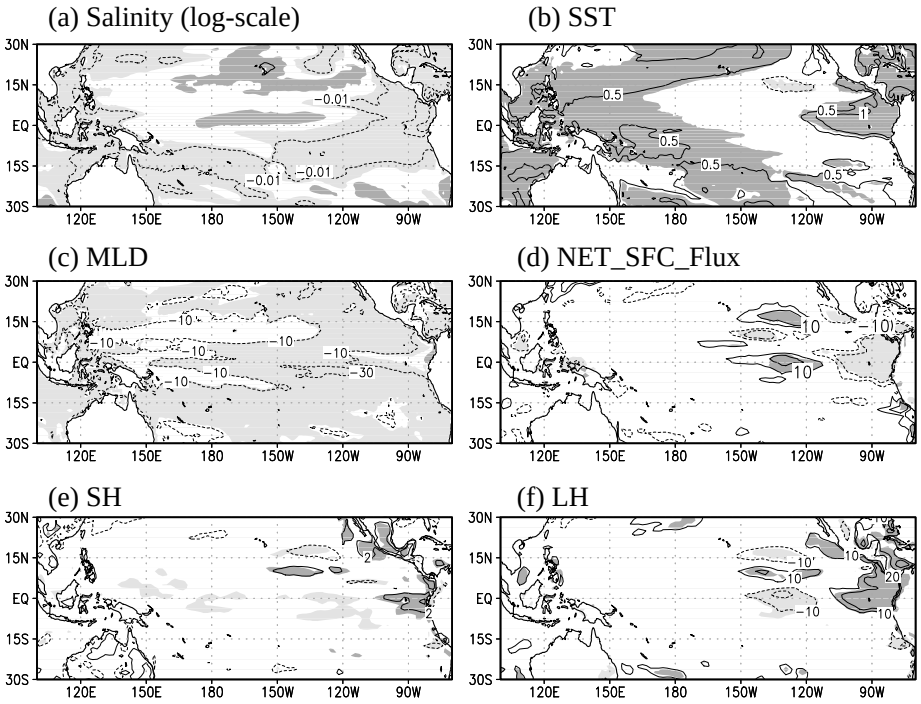

Fig. 2 The distribution of difference in the (a) salinity (PSU), (b) sea surface potential temperature (K), (c) mixed layer depth (m), (d) net surface heat flux (W m^{-2}), (e) sensible heat flux (W m^{-2}), and (f) latent heat flux (W m^{-2}) between the RIV and nRIV experiments. Shading region shows the 95% significance level.

Figure 2 shows the horizontal distributions of differences in salinity, temperature, mixed layer depth, and fluxes for the 10-year period between the RIV and nRIV runs. To estimate 'noise', it shows the 95% significance thresholds as shading area. The significant reduction of salinity is observed in the eastern and western Pacific coastal regions, especially western Ecuador (Fig. 2a). It is due to the fact that the runoff is increased over the Papua New Guinea in the western Pacific region and the Gulf of Guayaquil west of the Ecuadorian coast in the eastern Pacific region. There is a positive feedback between the freshwater runoff and precipitation since the result from the land surface algorithm affects runoff from the TRIP. The runoff over these regions shows a noticeable distinction due to heavy rainfall (not shown). Reduced salinity over the coastal regions in the RIV run leads to an increase in SST over the eastern equatorial Pacific (120°W ~ 80°W), that is, an upwelling region (Fig. 2b).

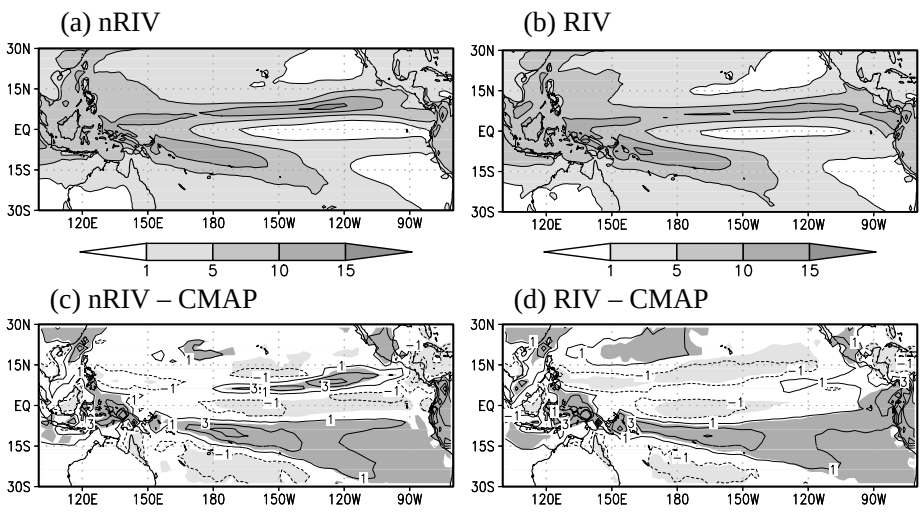

Fig. 3 Precipitation distribution (mm day^{-1}) averaged for the 10 yr (1979-1988) period for (a) nRIV experiment, (b) RIV experiment, (c) the difference between the observation and nRIV experiment, and (d) the difference between the observation and RIV experiment. Contour line indicates difference fields and shading region shows the 95% significance level in (c) and (d).

This is related to a decrease in the upwelling of cold seawater due to a reduction of trade winds. The resultant shallow mixed layer depth can cause the anomalous warming. It is consistent with the finding of previous studies. Yang *et al.* (1999) found that increased freshwater input from ocean precipitation produces a decrease in salinity and an increase in temperature in the upper ocean. Wu *et al.* (2010) indicate that a negative freshwater flux can lead to a tropical cooling. Meanwhile, an increase in SST over the mid-latitude central Pacific region is noticeable although changes in salinity are not significant. It is due to the shallower mixed layer depth over the mid-latitude (Fig. 2c) or to the change in the atmospheric teleconnection associated with the anomalous equatorial eastern Pacific warming. The reduced mixed layer itself also leads the warming of SST as long as no change in net heat fluxes (Yu *et al.* 2006). Although net surface heat fluxes are reduced over the eastern Pacific region (Fig. 2d), a reduction of mixed layer depth leads to an increase in SST.

The RIV run reveals larger sensible and latent heat fluxes over the eastern equatorial Pacific regions (80°W ~ 120°W) than those from the nRIV run (Figs. 2e and f). A dipole pattern of heat fluxes difference appear over the central Pacific (120°W ~ 150°W). The ocean surface warming over the eastern Pacific induces the increase of latent and sensible heat fluxes, forming unstable conditions near lower atmosphere, as compared to the nRIV experiment. Meanwhile the differences in heat fluxes over the western Pacific are not significant.

Simulated precipitation from the nRIV and RIV experiments for the 10-year period and Climate Prediction Center (CPC) Merged Analysis Monthly Precipitation (CMAP) data (Xie and Arkin 1997) are compared (Fig. 3). The nRIV simulation satisfactorily reproduces the distribution of precipitation (Fig. 3a). Two precipitation peaks appear in the tropics, indicating a double inter-tropical convergence zone (ITCZ), which is a typical defect observed in many GCMs (*e.g.*, Dai 2006). Results from the nRIV experiment exhibit exaggerated precipitation over the central tropical ocean, western South America, and central Indian Ocean, whereas precipitation over the eastern equatorial Pacific and Atlantic Ocean is underestimated (Fig. 3c). Results from the RIV experiment show a better agreement with the observed than those from the nRIV

experiment, due to a decrease in precipitation over the north of the equator in the central Pacific (Figs. 3b and d). However, the amount is exaggerated over the eastern equatorial Pacific region. It can be due to that precipitation activity leads to an increase in the runoff, which in turn raises the SST due to shallow mixed layer depth, and consequently enhances precipitation activity again. Meanwhile the distribution of precipitation in the middle latitudes is not altered distinctly by the introduction of freshwater runoff.

4. Concluding remarks

Our results suggest that the inclusion of freshwater routing from the continents to oceans is not negligible in climate simulation since it alters the SST, which is the external boundary condition for the atmospheric model. Resulting changes in the large-scale structure and precipitation are promising. However, there are a few issues to be cleared. First, the structure of thermohaline needs to be verified over an available observation. Further, modulation of surface evaporation due to the runoff over land needs to be considered. Despite these uncertainties, our study demonstrates that the freshwater runoff and its interaction with atmosphere should be considered in climate simulation.

Acknowledgments. This research was supported by the "Advanced Research on Meteorological Sciences (NIMR-2010-C-1)" project of the National Institute of Meteorological Research/Korea Meteorological Administration. We thank the Met Office for providing the Met Office Unified Model ™ (UK).

References

Collins, W. J., and Coauthors, 2008: Evaluation of the HadGEM2 model. *Met Office Hadley Centre Tech. Note No. 74.*

Dai, A., 2006: Precipitation characteristics in eighteen coupled climate models. *J. Climate*, **19**, 4605-4630.

Johns, T.C., and Coauthors (2006), The new Hadley Centre Climate Model (HadGEM1): Evaluation of coupled simulations, *J. Climate*, **19**, 1327-1353.

Levitus, S., and Coauthors, 1998: World Ocean Database 1998. Vol. 1, *NOAA Atlas NESDIS 18*, 346 pp.

Liston, G. E., Y. C. Sud, and E. F. Wood, 1994: Evaluating GCM land surface hydrology parameterizations by computing river discharges using a runoff routing model: Application to the Mississippi basin. *J. Appl. Meteor.*, **33**, 394-405.

Lucas-Picher, P., V. K. Arora, D. Caya, and R. Laprise, 2003: Implementation of a large-scale variable velocity river flow routing algorithm in the Canadian Regional Climate Model. *ATMOSPHERE-OCEAN*, **41**, 139-153.

Oki, T., and Y. C. Sud, 1998: Design of Total Runoff Integrating Pathways (TRIP) – A global river channel network Earth Interactions 2. (available at http://EarthInteractions.org)

Oki, T., T. Nishimura, and P. Dirmeyer, 1999: Assessment of annual runoff from land surface models using Total Runoff Integrating Pathways (TRIP). *J. Meteorol. Soc. Jpn.*, **77**, 235-255.

Wu, L., Y. Sun, J. Zhang, L. Zhang, and S. Minobe, 2010: Coupled ocean-atmosphere response to idealized freshwater forcing over the western tropical Pacific. *J. Climate*, **23**, 1945-1954.

Xie, P., and P. A. Arkin, 1997: Global precipitation: A 17-year monthly analysis based on gauge observations, satellite estimates, and numerical model prediction. *Bull. Amer. Meteor. Soc.*, **78**, 2539–2558.

Yang, S., K.-M. Lau, and P. S. Schopf, 1999: Sensitivity of the tropical Pacific ocean to precipitation-induced freshwater flux. *Climate Dyn.*, **15**, 737-750.

Yu, L., X. Jin, and R. A. Weller, 2006: Role of net surface heat flux in seasonal variations of sea surface temperature in the tropical Atlantic Ocean. *J. Climate*, **19**, 6153-6169.

Zhang, R.-H, and A. J. Busalacchi, 2009: Freshwater Flux (FWF)-induced oceanic feedback in a Hybrid Coupled Model of the tropical Pacific. *J. Climate*, **22**, 853-879.

Science and Technology Infusion Climate Bulletin
NOAA's National Weather Service
35th NOAA Annual Climate Diagnostics and Prediction Workshop
Raleigh, NC, 4-7 October 2010

Characterizing the Variability of the Indian Monsoon: Changes in Evaporative Sources for Summertime Rainfall Events

Peter Pantina and Vasubandhu Misra

Center for Ocean-Atmospheric Prediction Studies (COAPS)
Florida State University, Tallahassee, FL

1. Introduction

The Indian monsoon is a summertime (June – September) phenomenon that features an annual reversal of the winds over India along with the occurrence of 75% to 90% of the country's annual precipitation (Mooley and Parthasarthy 1984). Because of its enormous contribution to total rainfall, the monsoon has widespread impacts on the Indian economy as well as on the robustness of a given year's agricultural yield (Krishnamurthy and Shukla 2000). Variability of the monsoon on interannual and intraseasonal time scales is a well-documented and common occurrence (Krishnamurthy and Shukla 2000) and has large implications for the population of India. Interannual variability of the monsoon is characterized by flood or drought years, when all-India receives above- or below-average rainfall. Intraseasonal variability is characterized by active and break periods. During an active period, central India (northern and southern India) receive 10 – 30 days of above- (below-) average rainfall; break periods feature the opposite phenomenon. Intraseasonal oscillations have been correlated with the presence or absence of tropical cyclones (TCs) (Goswami and Mohan 2001). There is also significant debate regarding the existence of interannual variability in the intraseasonal oscillations (Goswami and Mohan 2001; Jones *et al.* 2004). Thus, variability studies are necessary for understanding and prediction of the seasonal and intraseasonal changes in the monsoon's character.

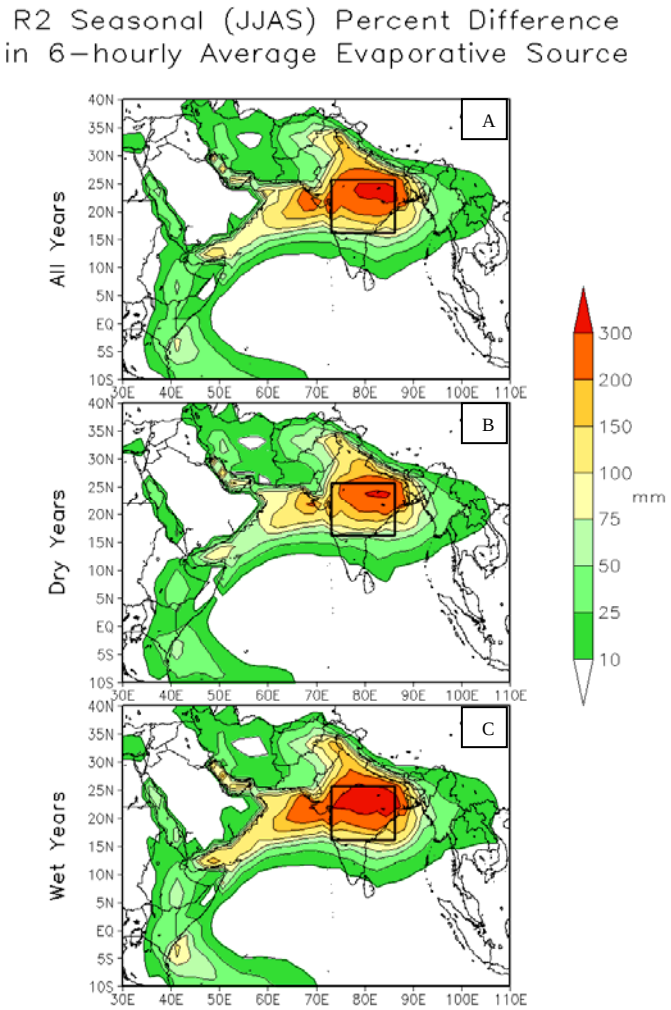

Fig. 1 Seasonal (JJAS) total evaporative source as estimated by R2 in all years (a), dry years (b), and wet years (c). The square box outlines the region from which we released parcels.

To improve the understanding of Indian monsoon variability, we set out to quantify the changes in evaporative sources for the summertime precipitation events over central India. Evaporative sources are the sum total of water molecules for precipitation events over a given region and are both local and remote in origin. Dirmeyer and Brubaker (1999) stated that since evaporation contributes to overall rainfall and soil moisture controls evaporation, rainfall is a direct function of soil moisture. They also claimed

Correspondence to: Peter Pantina, Center for Ocean-Atmospheric Prediction Studies (COAPS), Florida State University, Tallahassee, FL; E-mail: ppantina@fsu.edu

that soil moisture acts as a source of water for precipitation and can change the thermodynamics as well as the atmospheric circulation of a given state. We assume that isolating moisture sources by using back trajectories will help us infer changes in source regions and explain which mechanisms of monsoon variability are responsible for the variation in rainfall that we observe.

2. Data and Methodology

This study incorporates the Indian Meteorological Department (IMD) high-resolution daily gridded rainfall dataset over the Indian region. The dataset was originally created by Rajeevan *et al.* (2006) for their analysis of active and break spells during the Indian monsoon. It is an IMD rain-gauge-based dataset that has been interpolated to a 1^{o} latitude x 1^{o} longitude grid over India and spans each day from 1951 – 2003.

This study also uses three different reanalysis products to provide input parameters for use in the back-trajectory program described below. These include the National Centers for Environmental Prediction/Department (NCEP/DOE) Reanalysis-2 (R2), the NCEP Climate Forecast System Reanalysis (CFSR), and the Modern Era Retrospect-analysis for Research and Applications (MERRA) datasets. From these datasets, we work with surface latent heat flux, surface precipitation rate, surface pressure, specific humidity, temperature, and the u- and v- components of the wind. CFSR and MERRA are considered improvements over R2, and we incorporate them into this study to check consistency of the results between datasets. We regrid each dataset to the T62 grid for intercomparison and also convert the data from pressure-level to sigma-level for use in our program.

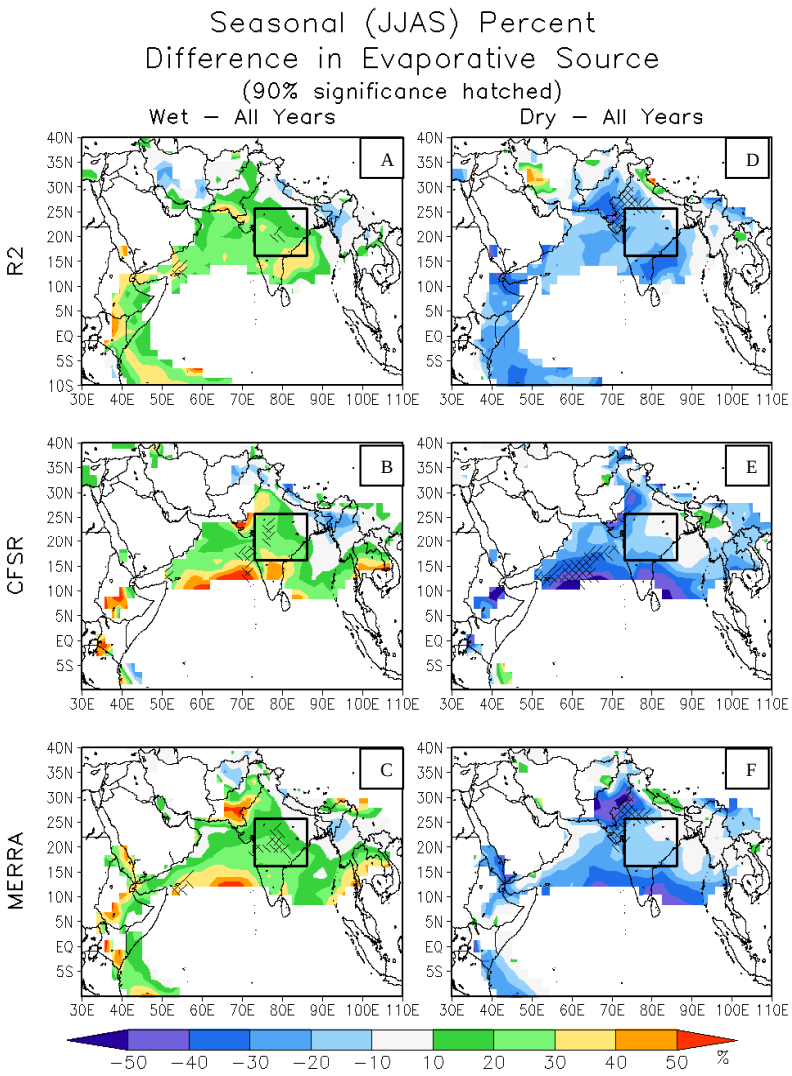

Fig. 2 Percentage difference in evaporative source between wet years and all years for R2 (a), CFSR (b), and MERRA (c), and between dry years and all years for R2 (d), CFSR (e), and MERRA (f). Areas of 90% significance are hatched. We used a mask to remove small values of evaporative source to eliminate artificially high percentage differences.

Rainfall data from the IMD gridded dataset were area-averaged over all-India from 1 June to 30 September for each year from 1951 to 2003. The five wettest, driest, and most-neutral years after 1979 were selected and labeled as wet, dry, and neutral years, respectively. Rainfall anomaly data from the IMD were area-averaged over central India for each day (15 May to 15 October) for each year of interest. We then extracted the low-frequency, 20-60-day mode from the time series using a simple recursive first-order butterworth filter to isolate nonperiodic oscillations of that length (Krishnamurti *et al.* 1995). Next, we recorded an active (break) period if a continuous string of 10–30 days was above (below) a zero mm day^{-1} anomaly.

We used a quasi-isentropic back trajectory (QIBT) program to locate the evaporative sources of precipitation events over central India. Dirmeyer and Brubaker (1999) developed this method for a similar study of evaporative source variability over the central United States. The program releases saturated parcels wherever and whenever rain falls over central India and traces them backward isentropically using reanalysis winds. Moisture is removed from the parcels at a rate proportional to local evaporation at the current grid point to precipitable water at the current grid point, and the parcels advect backward until they lose 90% of their moisture or until 15 days have passed.

3. Results

Plots of evaporative source are shown only for R2 (Figure 1). Most evaporative source is concentrated locally over central India and extends westward and southward toward western Africa as well as eastward toward southeastern Asia. Evaporative source is higher (lower) in wet (dry) years compared to all years (Figure 1). Evaporative source plots for CFSR and MERRA (not shown) are similar to those of R2 but feature more remote and less local moisture sources.

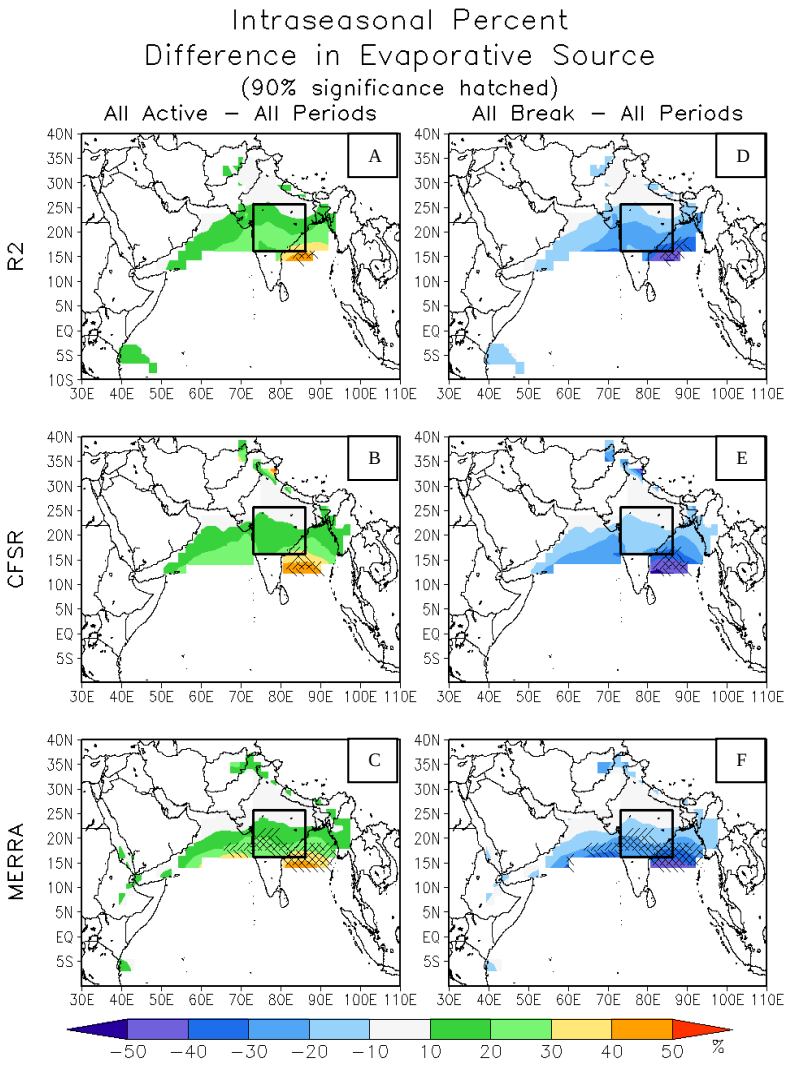

Fig. 3 Same as Figure 2, but for active and break evaporative sources.

Next, we isolate differences in the magnitude and location of the evaporative source in dry years and in wet years. Here, we see patterns that are relatively consistent in each of the datasets. First, we compare wet years to all years in R2 (Figure 2a). We observe a general increase in the evaporative source along the low-level cross-equatorial flow region extending from central India southward and westward toward the coast of Africa. The results are similar for CFSR, but the enhancement of evaporative source does not extend as far to the south and instead extends farther to the east (Figure 2b). For MERRA, we see a pattern similar to that observed for R2 (Figure 2c). None of these results is statistically significant outside central India or the Arabian Sea. We make the claim that wet years feature an overall enhancement of monsoon flow. All regions supply increased moisture in this case, but the largest increase originates from the previously mentioned regions. For dry years, we observe an overall decrease in the magnitude of the evaporative source compared to all years. For R2 and MERRA (Figure 2d, f), the evaporative source is significantly reduced over northwestern India, and for CFSR, the source is significantly reduced over the Arabian Sea (Figure 2e). We conclude that all regions feature reduced moisture contribution in dry years and that the greatest reduction occurs over the cross-equatorial flow region.

Furthermore, we observe the differences in location and strength of the evaporative source for active and break rainfall events. For both R2 (Figure 3a) and CFSR (Figure 3b), we see that active periods feature a significant increase in evaporative source over the western-central Bay of Bengal, which extends westward

over the Arabian Sea. This result is seen in MERRA as well (Figure 3c), but the difference is more significant than in the other datasets. We see the opposite result for all break periods (Figure 3d–f). In this case, there is a decrease in evaporative source and most significance lies over the western-central Bay of Bengal. At this time scale, we assume that TC activity over the Bay of Bengal acts as the dominant moisture source.

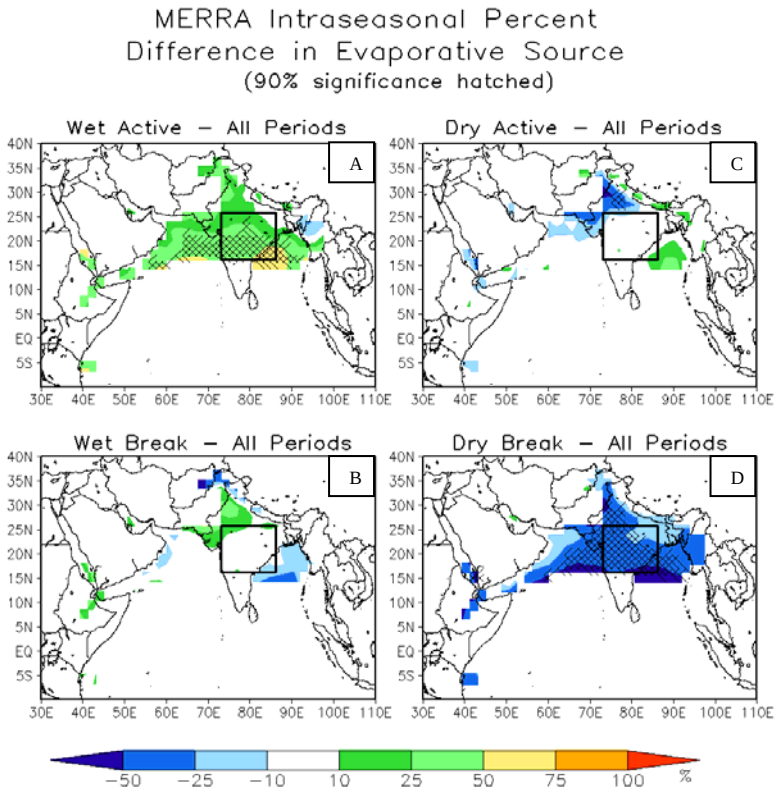

Fig. 4 Same as Figure 2, but for active periods from wet years and all periods (a), break periods from wet years and all periods (b), active periods from dry years and all periods (c), and break periods from dry years (d) for R2. For MERRA only.

Finally, we compare the intraseasonal oscillations on an interannual time scale and focus on the MERRA dataset for this paper. We see a distinct interannual signal in the intraseasonal oscillations. First we compare all active periods from wet years (Figure 4a) to all periods. There is a significant increase in the evaporative source remotely over the northwestern Bay of Bengal and a general increase over all of central India extending into the Arabian Sea. When we look at all active periods from dry years, however, we see a different picture (Figure 4c). There is a slight reduction in evaporative source remotely over the northern Arabian Sea and northern India. In these cases, we see contributions of both the interannual and intraseasonal signals in our evaporative sources, and we therefore conclude that there is interannual variability in the evaporative sources of the active periods of the monsoon. The patterns are similar, but reversed, for the break periods (Figure 4b, d) with cross-correspondence of dry and wet years. These results are consistent among our three datasets (not shown).

4. Summary and Conclusions

In this study, we isolated interannual and intraseasonal changes in the location and magnitude of evaporative sources for rainfall events during the summertime Indian monsoon, and we intended to improve our understanding of the variability of the monsoon.

The *location and strength of the evaporative source for interannual rainfall events changes most significantly over central India and parts of the Arabian Sea in all three datasets*, which suggests changes in the character of the overall monsoon circulation and the cross-equatorial flow. We saw an enhancement in evaporative source for wet years and a reduction in evaporative source in dry years. *The location and strength of the evaporative source for intraseasonal rainfall events changes most significantly over the western-central Bay of Bengal in all three* datasets, which suggests the influence of landfalling TCs in providing moisture during the active periods. We saw an enhancement of the evaporative source for all active periods and a reduction in evaporative source for all break periods. There is convincing evidence suggesting *interannual variability of the evaporative sources for intraseasonal events.*

We observed that the dominant changes in the location of the evaporative sources on interannual and intraseasonal time scales are not collocated. This result has implications for climate predictability over the Indian monsoon region. Models require improved prediction of interannual and intraseasonal variations,

especially over the Bay of Bengal and the Arabian Sea, to improve overall predictability and moisture analyses of the monsoon.

References

Dirmeyer, P. A., and K. L. Brubaker, 1999: Contrasting evaporative moisture sources during the drought of 1988 and the flood of 1993. *J. Geophys. Res.*, **104,** 19383-19397.

Goswami, B. N., and R. S. A. Mohan, 2001: Intraseasonal oscillations and interannual variability of the Indian monsoon. *J. Climate*, **14**, 1180-1198.

Jones, C., L. M. V. Carvalho, R. W. Higgins, D. E. Waliser, and J-K. E. Schemm, 2004: Climatology of tropical intraseasonal convective anomalies: 1979-2002. *J. Climate*, **17**, 523-539.

Krishnamurti, T.N., S.O. Han, and V. Misra, 1995: Predictions of dry and wet spell of the Australian monsoon. *Int. J. Climatol.*, **15**, 753-771.

Krishnamurthy, V., and J. Shukla, 2000: Intraseasonal and interannual variability of rainfall over India. *J. Climate*, **13**, 4366-4377.

Mooley, D. A., and B. Parthasarathy, 1984: Fluctuations in all-India summer monsoon rainfall during 1871-1978. *Clim. Change*, **6**, 287-301.

Rajeevan M., J. Bhate, J.D. Kale, and B. Lal, 2006: High resolution daily gridded rainfall data for the Indian region: Analysis of break and active monsoon spells. *Current Science*, **91**, 296-306.

Science and Technology Infusion Climate Bulletin
NOAA's National Weather Service
35th NOAA Annual Climate Diagnostics and Prediction Workshop
Raleigh, NC, 4-7 October 2010

How Much Colder Would It Have Been If the Circulation of Winter 2009/10 Had Happened 35 Years Ago?

Huug van den Dool
Climate Prediction Center, NCEP/NWS/NOAA, Camp Springs, MD

1. Introduction

Many years ago we noticed in CPC practice that the specified temperatures (as per Bill Klein's equations) started to come out cooler than observed temperatures (Van den Dool, O'Lenic and Klein 1993). Temperatures were specified from 500mb heights (this is a long tradition). The Klein equations were obviously based on years past, representing the climate of 1948-1980, so the impression we got is that climate change may become evident in the relationship between upper level flow patterns and surface air temperature.

We re-address this question, as the 2001-2010 decade comes to a close, and almost 20 more years are available. Specifically, to drive the point home, we ask how much colder winter 2009/10 would have been if that extreme and unusual circulation pattern had happened 35 years earlier. The question may sound curious, because winter 09/10 was already quite cold in parts of the US and Europe. But if global warming is an issue we should not only ask these questions when LA breaks an all time high temperature, but in fact during all circumstances, including a cold winter. We can take the earth's atmosphere's temperature continuously. The exact same question, for Europe only, has been addressed by Cattiaux et al. (2010).

The circulation of 09/10 has never happened before. At least not if we consider the domain 20N-pole which contains many degrees of freedom, i.e. much more than an extreme (N)AO alone. Instead of seeking a natural analogue during years past (which is a mission improbable) we 'construct' an analogue (CA) making a linear combination from years past (Van den Dool 1994) to reproduce winter 09/10. This CA procedure replaces the Klein equations. Moreover, CA is applied to Ψ-500, the 500mb streamfunction, which we think is better for this purpose than Z500, because if the climate is warming, 500 mb heights go up, so the Klein equations will show warmer temperatures automatically. However, Ψ-500 has zero global mean by definition, no matter how much climate change happens.

Equation (1a) expresses the idea of a constructed analogue. It states that Ψ_{CA} can be written as a linear combination of streamfunction anomaly fields that have occurred in the past.

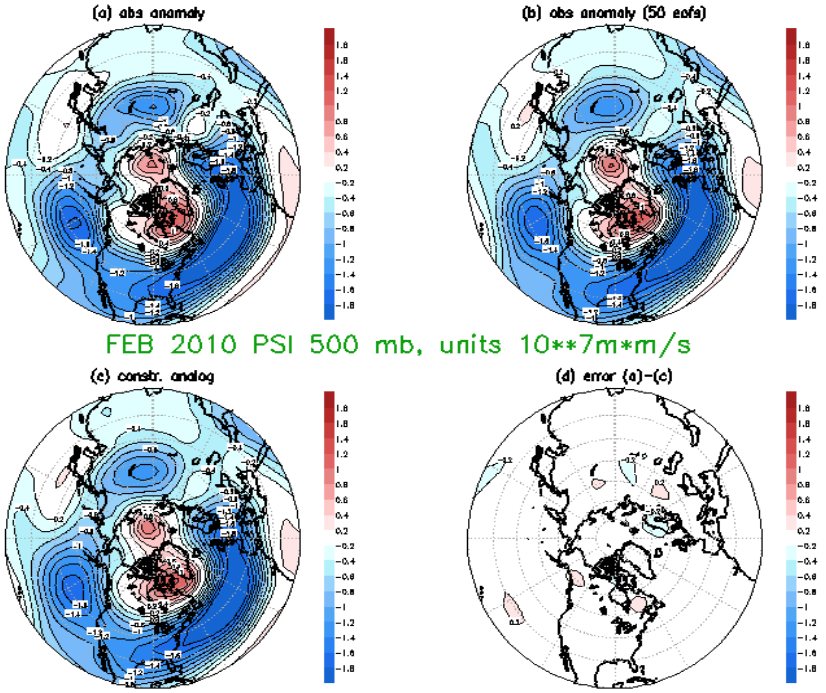

Fig.1 The observed streamfunction anomaly in February 2010 ((a) upper left), the same truncated to 50 EOFs ((b), upper right)), the constructed analogue ((c), lower left) and the difference of (a) and (c) in the lower right (d).

Correspondence to: Huug van den Dool, Climate Prediction Center, NOAA/NWS/NCEP, Camp Springs, MD 20746;
E-mail: Huug.Vandendool@noaa.gov

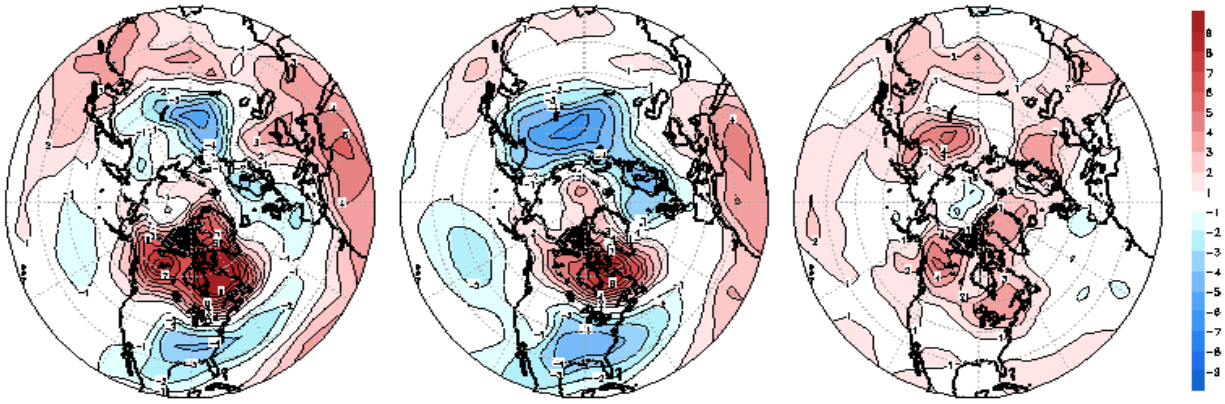

Fig.2 The observed temperature anomaly at 850mb for February 2010 (left), the specified temperature anomaly (using the weights in Table 1, middle), and the difference (right).

$$\Psi_{CA} = \Sigma\, \alpha_i \psi_i, \quad i = 1, 90 \qquad (1a)$$

The coefficients α_i are calculated so as to minimize the distance between Ψ_{CA} and the state for which we seek an analogue. (We skip the many details of this process, but see Van den Dool 2007, chapter 7). We use 30 years in the past, 1961-1990, but make it into a sample of 90 by including the month before and after ("pooling"). Given the α_i (based on streamfunction only), the temperature is simply specified by:

$$T_{CA} = \Sigma \alpha_i T_i, \qquad i = 1,90 \qquad (1b)$$

Our working definitions are that the CA temperatures, specified from Ψ-500 during 1961-1990 and inflated for the estimated damping inherent in specification, are the temperatures nature would have produced if the 09/10 circulation had happened in the 1961-1990 era. The difference between observed and specified is then our estimate of climate change, although we recognize that other factors, not already expressed in Ψ-500, may have an impact on near surface temperature (soil moisture in summer, snow cover and sea-ice, solar variations etc). In addition to winter 09/10 we do CA for all years since 1990 (but will show maps only for 09/10). All years are used to judge the inflation required and give a better statistical basis to the climate change estimate.

JAN		**JAN**		**JAN**		**FEB**		**FEB**		**FEB**		**MAR**		**MAR**		**MAR**			
1961	*-0.05*	**1971**	*0.02*	**1981**	*0.02*	**1961**	*0*	**1971**	*-0.01*	**1981**	*0.06*	**1961**	*-0.14*	**1971**	*-0.01*	**1981**	*0.01*	0	**sum α**
1962	*0.02*	**1972**	*-0.02*	**1982**	*-0.11*	**1962**	*-0.1*	**1972**	*0.06*	**1982**	*-0.06*	**1962**	*-0.09*	**1972**	*-0.05*	**1982**	*-0.04*	0.47	**sum α**2**
1963	*0.01*	**1973**	*-0.11*	**1983**	*-0.03*	**1963**	*-0.04*	**1973**	*0.07*	**1983**	*0.04*	**1963**	*0.09*	**1973**	*0.04*	**1983**	*0.1*	5.58	**sum |α|**
1964	*0.12*	**1974**	*-0.03*	**1984**	*-0.04*	**1964**	*-0.02*	**1974**	*0.07*	**1984**	*-0.04*	**1964**	*0.06*	**1974**	*-0.08*	**1984**	*0.09*		
1965	*0.02*	**1975**	*0.04*	**1985**	*-0.06*	**1965**	*-0.02*	**1975**	*-0.09*	**1985**	*0.07*	**1965**	*-0.11*	**1975**	*-0.03*	**1985**	*0.03*		
1966	*0.11*	**1976**	*0.07*	**1986**	*0.03*	**1966**	*0.11*	**1976**	*-0.09*	**1986**	*-0.02*	**1966**	*0.05*	**1976**	*-0.05*	**1986**	*0.02*		
1967	*-0.07*	**1977**	*0.03*	**1987**	*-0.04*	**1967**	*0.01*	**1977**	*-0.08*	**1987**	*0.16*	**1967**	*-0.11*	**1977**	*0.12*	**1987**	*0.06*		
1968	*0.15*	**1978**	*-0.04*	**1988**	*0.06*	**1968**	*0.08*	**1978**	*-0.12*	**1988**	*0.11*	**1968**	*0.12*	**1978**	*-0.05*	**1988**	*-0.08*		
1969	*-0.01*	**1979**	*0.04*	**1989**	*-0.04*	**1969**	*-0.05*	**1979**	*-0.02*	**1989**	*-0.07*	**1969**	*0.1*	**1979**	*0.09*	**1989**	*-0.03*		
1970	*-0.05*	**1980**	*-0.03*	**1990**	*-0.02*	**1970**	*-0.04*	**1980**	*0.12*	**1990**	*-0.06*	**1970**	*-0.11*	**1980**	*0.09*	**1990**	*-0.12*		
	0.25		-0.03		-0.22		-0.07		-0.1		0.18		-0.13		0.07		0.06		

Table 1 Weights assigned to 90 Januaries, Februaries and Marches to reproduce the February 2010 streamfunction anomaly over the NH.

Note that any warming in the specified temps (which we do find! in all months!) has to come from preferentially warm circulation types, circulation types that did also occur during 1961-1990, but not as frequently as during 1991-2010. This we do not consider climate change, admittedly a debatable point of view.

2. Example of specification

Table 1 shows the weights α_i required to reproduce the February 2010 500mb streamfunction anomaly over 20N to the pole. The calculation refers to the maps shown in Fig.1 which has the observed streamfunction anomaly in panel (a). Clearly this is a case with highly negative (N)AO, as reported extensively by others in this workshop (Wolter 2010). The construction is done in a space truncated to 50 EOFs, so the answer is very accurate; the difference of the CA and the untruncated observed anomaly (Fig.1 panel (d)) is almost blank. We use the 2 surrounding months (after the appropriate monthly climatology has been removed) so Table 1 shows 90 weights, all small (<=0.15). If a natural analogue existed we would find a +1.0 for that case, and zeros for all other 89 cases. The Table has some marginal totals at the bottom, and three pieces of information on the right about the sum of the weights, sum of squared weights, and sum of absolute weights. The latter three parameters signal any problems there might be in solving an ill-posed matrix problem which was treated by ridging the matrix (Van den Dool 2007).

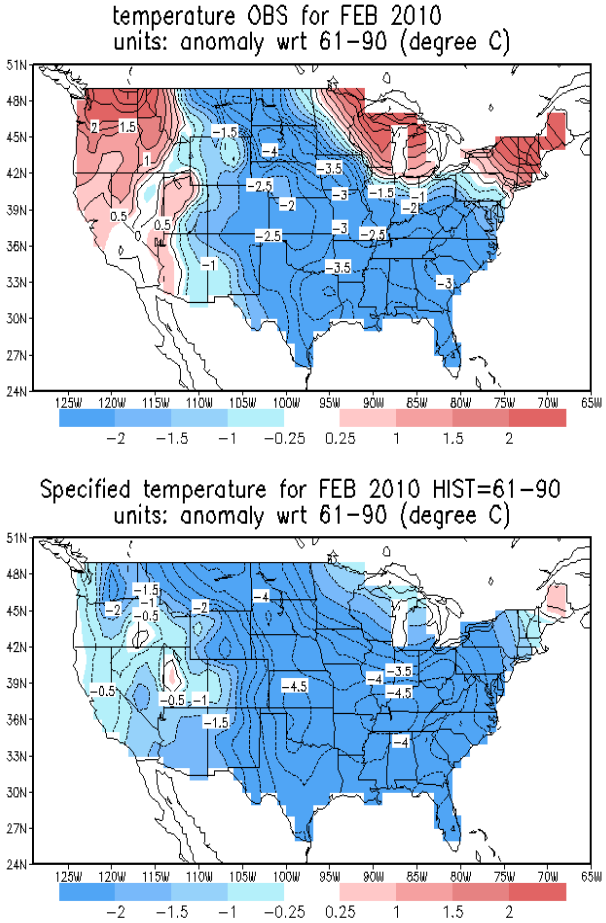

Fig. 3 The observed (top) and specified (bottom) surface air temperature over the US for February 2010.

Figure 2 shows the observed and specified temperature anomaly for February, and their difference in the lower right. The specification entails the multiplication of 90 temperature anomaly field (in Jan-Feb-Mar 1961-1990) by the 90 coefficients in Table 1 (which are based on simultaneously occurring streamfunction only), as per Eq 1b. Clearly the observed temperatures are generally warmer than specified nearly everywhere in the NH. Instead of surface air temperature we actually show T850 because R1 (the data we use throughout) has known technical problems at the surface. Fig.3 show specified and observed surface air T-anomaly over the US only, using the NCDC monthly Climate Division data. This shows the same as Fig.2 for T-850, i.e. observed temperatures were generally warmer than it would have been had this circulation happened 35 years ago (in the center of 1961-1990 period). Note that neither Fig.2 nor Fig.3 specified temperatures have been inflated.

3. How much warming?

Figure 2 and 3 is only one example. But we find typically that observed is warmer than specified. Using CA for all Februaries in the period 1991-2010 we analyze the results as follows. For February we find that T-specified is 0.09, i.e. the circulation alone made 1991-2010 0.09K warmer than 1961-1990 averaged over the area 20N-pole. T-observed, however, was 0.61K above the 1961-1990 normal.

We assume that

$$\text{T-observed} = \text{T-specified} * 1/d + \text{delta} \qquad (2)$$

which means that we assume that the specified anomalies are damped. Multiplication by 1/d will undo the damping. The offset delta is the mean temperature

	T-specified	T-observed	damping	Delta
January	0.06K	0.62K	0.64	0.52K
February	0.09K	0.61K	0.67	0.48K

Table 2 Specified and observed temperature anomaly (K) from 1961-1990 mean, the degree of damping and climate offset (delta in K) derived for the entire extratropical NH 1991-2010.

change unexplained by circulation considerations. 1/d and offset are determined from a regression using all 20 years, and all gridpoints between 20N and the pole, a lot of material. At this point we consider d and delta to be constant in time and space (this can be finessed later).

We find the damping in February to be 0.67, and after inflation we find the offset to be 0.48K. Our estimate (mean over all years and whole extratropical NH) is thus that temperature has gone up by 0.48K and this has to be caused by something other than the circulation. Table 2 also shows the same calculation for January, and the result is essentially the same. We appear to be about 0.5K warmer in winter than can be expected on the basis of the circulation anomalies alone.

References

Cattiaux, J., R. Vautard, C. Cassou, P. Yiou, V. Masson-Delmotte, and F. Codron (2010), Winter 2010 in Europe: A cold extreme in a warming climate, *Geophys. Res. Lett.*, **37**, L20704, doi: 10.1029/2010GL044613.

H. M. van den Dool, E. A. O'Lenic and W. H. Klein, 1993: Consistency check for trends in surface temperature and upper level circulation: 1950-1992. *J. Climate*, **6**, 2288-2297.

H. M. van den Dool, 1994: Searching for analogues, how long must one wait? *Tellus*, **46A**, 314-324.

Huug van den Dool, 2007: Empirical methods in short-term climate prediction. Oxford University Press: 215 pp. ISBN-10: 0-19-920278-8 and ISBN-13: 978-0-19-920278-2

Klaus Wolter, 2010: 2009-10 snow siege: Role of El Niño, NAO, & 'Global Change'. 35th NOAA Annual Climate Diagnostics and Prediction Workshop presentation, (http://www.cicsnc.org/media/CDPW/Monday%20Morning/Wolter.Raleigh.Oct10.ppt)

Science and Technology Infusion Climate Bulletin
NOAA's National Weather Service
35th NOAA Annual Climate Diagnostics and Prediction Workshop
Raleigh, NC, 4-7 October 2010

Atlantic Tropical Cyclones in the 20th Century: Natural Variability and Secular Change in Cyclone Count

Sumant Nigam[1] and Bin Guan[2]

[1]*Department of Atmospheric and Oceanic Science, University of Maryland, College Park, MD*
[2]*Jet Propulsion Laboratory, MS 300-233, California Institute of Technology, Pasadena,CA*

1. Background

The recent increase in Atlantic hurricane activity has generated intense scientific debate as to its origin. Following a relatively quiescent phase in the 1970s/80s, the number of Atlantic tropical cyclones (TCs) has steeply increased in the recent 1–2 decades (e.g., Mann and Emanuel 2006). Annual TC numbers averaged ~7 during 1986–95 and ~11 during 1996–2005, *i.e.*, a 50% increase in one decade. The intensity of TCs measured by the number and/or proportion of the most intense ones has also increased during recent decades (Goldenberg *et al.* 2001, Webster *et al.* 2005, Kossin et al. 2007, Elsner et al. 2008). An increase in hurricane destructiveness has also been noted (Emanuel 2005).

The cause of the recent increase in Atlantic TC activity is intensely debated in context of climate change. Some studies (*e.g.*, Goldenberg *et al.* 2001, Zhang and Delworth 2006) suggest that increased TC activity is related to the natural variability of Atlantic sea surface temperatures (SSTs), especially the Atlantic Multidecadal Oscillation (AMO; Enfield *et al.* 2001, Delworth and Mann 2000, Guan and Nigam 2009), while others attribute the increase in activity to anthropogenic climate change (Webster *et al.* 2005, Trenberth and Shea 2006, Mann and Emanuel 2006, Holland and Webster 2007). It has also been argued that annual TC counts do not presently exhibit any low-frequency variability beyond the range expected from a random Poisson process (Elsner 2008). The attribution of heightened TC activity to natural variations and/or secular change of climate thus remains challenging, especially in view of the short length of the observational record and its uneven quality (Landsea 2007, Mann et al. 2007, Chang and Guo 2007, Veechi and Knutson 2008, Landsea *et al.* 2010), and the modest simulation skill of current climate models; leaving much to debate.

The TC activity in the Atlantic is closely related to SST variations in the main development region (MDR; Mann and Emanuel 2006; 6°-18°N, 20°-60°W; marked in Figs. 1 and 3) where ocean waters above 26.5°C are generally required for TC formation (Gray 1979). More than half of the decadal time-scale variance in the annual Atlantic TC count can be explained by SST variations in the main development region (MDR, Mann and Emanuel 2006). The nonlocal SSTs, *i.e.*, the ones outside MDR are also influential as indicated by analyses that show the MDR SST variations relative to the global tropical average to be more pertinent (Emanuel 2005, Swanson 2008, Vecchi *et al.* 2008, Vecchi and Soden 2007), and studies that document the impact of Pacific SST on tropospheric circulation (vertical shear and stability) over the tropical-subtropical Atlantic (*e.g.*, Elsner *et al.* 2001, Aiyyer and Thorncroft 2006, Camargo *et al.* 2007). Swanson specifically cautions against a singular focus on MDR SSTs by showing improved accounting of the TC power dissipation index using the 'relative' MDR SST variations. The following features of current analyses of Atlantic TC count variability motivate the present study:

- Natural variability is generally estimated, statistically, as a residual from detrending the observational record. The residual approach can be problematic as there is no assurance that natural variability is not aliased into the detrending index/marker or the linear trend. If such aliasing did occur, it would preclude the possibility of obtaining decadal-to-multidecadal trends from natural variability alone. For robust attribution, especially to secular change, the analysis scheme must allow for this possibility; flexibility not found in current analyses.
- The focus is almost exclusively on the recent increase in TC activity whereas causes of a similar (percentage wise) increase in the 1930s when the annual TC count increased from ~7 in the 1910s/20s

Correspondence to: Sumant Nigam, Department of Atmospheric and Oceanic Science, University of Maryland, College Park, MD 20742; E-mail: nigam@atmos.umd.edu

to ~10 in the 1930s (*cf.* Fig. 2a) has generally not been addressed. Although TC counts in this period are somewhat uncertain, the jump is too large to be ignored (Goldenberg *et al.* 2001).

- Inter-basin interaction is ignored when investigating the origin of the recent warming of SSTs in the main hurricane development region (in the northern tropical Atlantic)[1] – this despite evidence for the Pacific's influence on the Atlantic at both interannual (*e.g.*, Lanzante 1996, Enfield and Mayer 1997, Ruiz-Barradas *et al.* 2000, Kossin et al. 2010) and decadal time scales (Latif 2001, Guan and Nigam 2008, 2009).

Interestingly, the authors recently concluded an analysis of natural variability and secular trend in the Pacific and Atlantic SSTs (Guan and Nigam 2008, 2009) – one where both components are simultaneously characterized, *i.e.*, contextually, as opposed to residual estimation of the former. By focusing on spatial *and* temporal recurrence but without imposition of any periodicity constraints, their analysis discriminates between biennial, ENSO, and decadal variabilities in the Pacific, leading to refined evolutionary descriptions and, equally importantly, separation of natural variability and the secular trend; all without any advance filtering (and potential aliasing) of the seasonally resolved SST record.[2] The implicit accommodation of natural variability leads to a nonstationary SST secular trend, one that includes mid-century cooling. The physicality of decadal variability modes – of key interest here – was evaluated using analog counts and fish recruitment records (Guan and Nigam 2008, hereafter GN2008).

The Atlantic SSTs were subjected to a similar spatiotemporal analysis but after removal of the Pacific basin's influence; footprints of the seven Pacific variability modes (including SST-trend) on Atlantic SST were linearly removed. The leading mode – a multidecadal oscillation focused in the extratropical basin with a period of ~70 years, and referred as the AMO-*Atl* – differs from this mode's conventional description (*e.g.*, Enfield *et al.* 2001, Enfield and Cid-Serrano 2010) in the near-quiescence of the tropical-subtropical basin (which includes the MDR). The different signal strengths in this region in current and previous analyses indicate, implicitly, the significant influence of the Pacific basin on this region. The related principal components and modal structures are shown in Guan and Nigam (2009, hereafter GN2009) where robustness of the analysis, including the impact of pre-filtering the Pacific influence, is also assessed.[3]

The Pacific basin influences Atlantic TC activity through its impact on Atlantic SSTs as well as the overlying atmospheric circulation. The impact on SST during ENSO episodes is well documented in the aforementioned studies. For instance, ENSO accounts for ~20% of the record-high warming of the tropical North Atlantic in 2005 in the multivariate regression analysis of Trenberth and Shea (2006), surpassing the AMO contribution. The Pacific's influence on the Atlantic atmosphere is also pronounced during ENSO when it impacts the 200–850-hPa zonal-wind shear (e.g., Aiyyer and Thorncroft 2006) and tropospheric temperatures (Tang and Neelin 2004) over the tropical Atlantic, and consequently TC activity in the basin. The Pacific's influence on decadal time scales is of more interest in context of the low-frequency fluctuations and trends in Atlantic TC activity, but such influences have not been extensively studied. Latif (2001) made a case for inter-basin links using a low-pass filtered ENSO index. More recently, the authors have presented

[1] Mann and Emanuel's (2006) diagnosis, for instance, seeks evidence for AMO's role in the spectrum of the residual obtained after fitting SST variation in the main hurricane development region with a large-scale warming index (the global SST trend) and an anthropogenic aerosol index (a hemispheric cooling mechanism), but not one representing the influence of Pacific decadal variability.

[2] Canonical ENSO variability is captured as two modes, the growth (ENSO−) and decay (ENSO+) modes. Departure from canonical development, especially in the 1976/77-onward period, is identified as a distinct mode, referred as ENSO Non-Canonical (ENSO-NC), hereafter. Pacific decadal variability is resolved into two modes, Pan-Pacific and North Pacific. The former exhibits connections to the tropical-subtropical Atlantic resembling the AMO. The latter, capturing the 1976/77 climate shift, is close to Pacific Decadal Oscillation in structure, but with interesting links to the North Atlantic as well as the western tropical Pacific and Indian Ocean SSTs. The nonstationary secular trend consists of wide-spread but non-uniform warming of all basins along with a sliver of cooling in the central equatorial Pacific. See Guan and Nigam (2008) for additional details.

[3] The second and third mode capture the growth and decay of interannual variations in the eastern tropical Atlantic, the Atlantic Niño, while the fourth describes lower-frequency variability whose mature phase resembles the SST footprint of the North Atlantic Oscillation. The fourth mode is referred as the low-frequency NAO (LF-NAO).

observational evidence for a significant link between Pacific decadal SST variability and the Atlantic SSTs via the Pan-Pacific mode (see Fig. 11 in GN2008).

The present study seeks to clarify the relationship of Atlantic TC activity (annual count) with global SST variations in the 20th century using improved characterization of natural variability in the Pacific and Atlantic basins, and a simultaneously obtained, and thus, more consistent estimate of the nonstationary SST secular trend. The goal of the study is to obtain a refined estimate of the secular change in Atlantic TC activity as well as resolve its natural variability into components linked with the well-known modes of SST variability in both basins. The present study thus moves away from the traditional focus on MDR SST which, interestingly, is also a reconstruction target but after the Atlantic TC count.

2. Data sets and analysis method

The North Atlantic TC count data set developed by Landsea, Veechi, Bengtsson, and Knutson (2010, hereafter LVBK2010) is analyzed in this study. It is based on the National Hurricane Center's best track data set (HURDAT; Jarvinen *et al.* 1984) which is the longest available and relatively reliable measure of Atlantic TCs, dating back to late 1800s. The earlier part of this record has however been questioned, particularly with respect to the upward trend in annual TC count. Veechi and Knutson (2008) used statistical methods to account for the potentially missing TCs in the pre-satellite period of the record. Meanwhile, LVBK2010 showed the increasing TC count to result, in part, from the growing number of short-lived storms (duration ≤ 2 days) in the recent period; arguably, from improvements in observational platforms and techniques. Based on these adjustments, a new TC count data set was developed – the LVBK2010 record. It factors for TC-subsampling in the earlier period and seeks to track the count of moderate-to-long lived TCs. The 1900-2008 record of LVBK counts is analyzed here.

The SST data come from the U.K. Met Office's (UKMO) Hadley Centre Sea Ice and Sea Surface Temperature dataset (HadISST) 1.1 (Rayner *et al.* 2003). In two recent papers (GN2008; GN2009), the authors characterized the 20th century SST variability in the Pacific and Atlantic basins from spatiotemporal analysis of the seasonal anomalies, using the extended EOF technique (Weare and Nasstrom 1982). A total of 11 principal components (PCs) constitute the analysis backbone. Of these, 7 (including the nonstationary SST Trend mode) are from the Pacific analysis while the remaining 4 come from the analysis of residual (i.e., Pacific basin uninfluenced) SST variability in the Atlantic basin. The intra-basin PCs are temporally orthogonal (assured by the analysis method) while the inter-basin ones are nearly so (ensured by filtering of Pacific's influence from Atlantic SSTs prior to latter's analysis); the largest inter-basin PC correlation is 0.11.

The present analysis is for the fall season (September-November), and not the preferred peak hurricane season (August-October; *e.g.*, Mann and Emanuel 2006), as the underlying SST analysis was based on the conventionally defined seasonal anomalies. Simple linear regressions of the fall season SST PCs (unsmoothed) on the annual Atlantic TC count and concurrent SST anomalies in the full record (1901-2005) constitute the building blocks in reconstruction of the TC count and MDR SST variations, respectively. The reconstruction proceeds, simply, from the multiplication of each SST PC (fall value) with its above-obtained 'fixed' regression pattern (number, in case of TC count), followed by the summing of the 11 (or any subset thereof) elemental contributions.

3. Atlantic TC count: Secular trend and natural variability

The annual Atlantic TC count in the LVBK record is shown in Fig. 1a (TC-Tot Observed, solid black), after 10 applications of the 1-2-1 smoother. Raw counts are also plotted, as departure from the full-record average (~8), using lightly shaded vertical bars and the right scale. An abrupt increase in count is seen in the 1990s. Before that, counts are relatively stable but suppressed over a ~30-yr period beginning in the mid-1950s, albeit with decadal modulation. A strong abrupt increase occurred also in the early 1930s. Both this and the recent count increase will need attribution using a common framework to advance understanding of count variability.

The annual TC count is reconstructed from SST variability in the Pacific and Atlantic basins using fall season regressions of the secular trend and natural variability modes, as discussed in section 2d. The full reconstruction (dashed black) accounts for as much as 60% of the decadal variance in view of the 0.78

correlation between the reconstructed and observed TC-Tot. Increased counts during 1930s-50s and the decline since then are broadly captured in the reconstruction; suppressed counts in the 1950s-60s are however

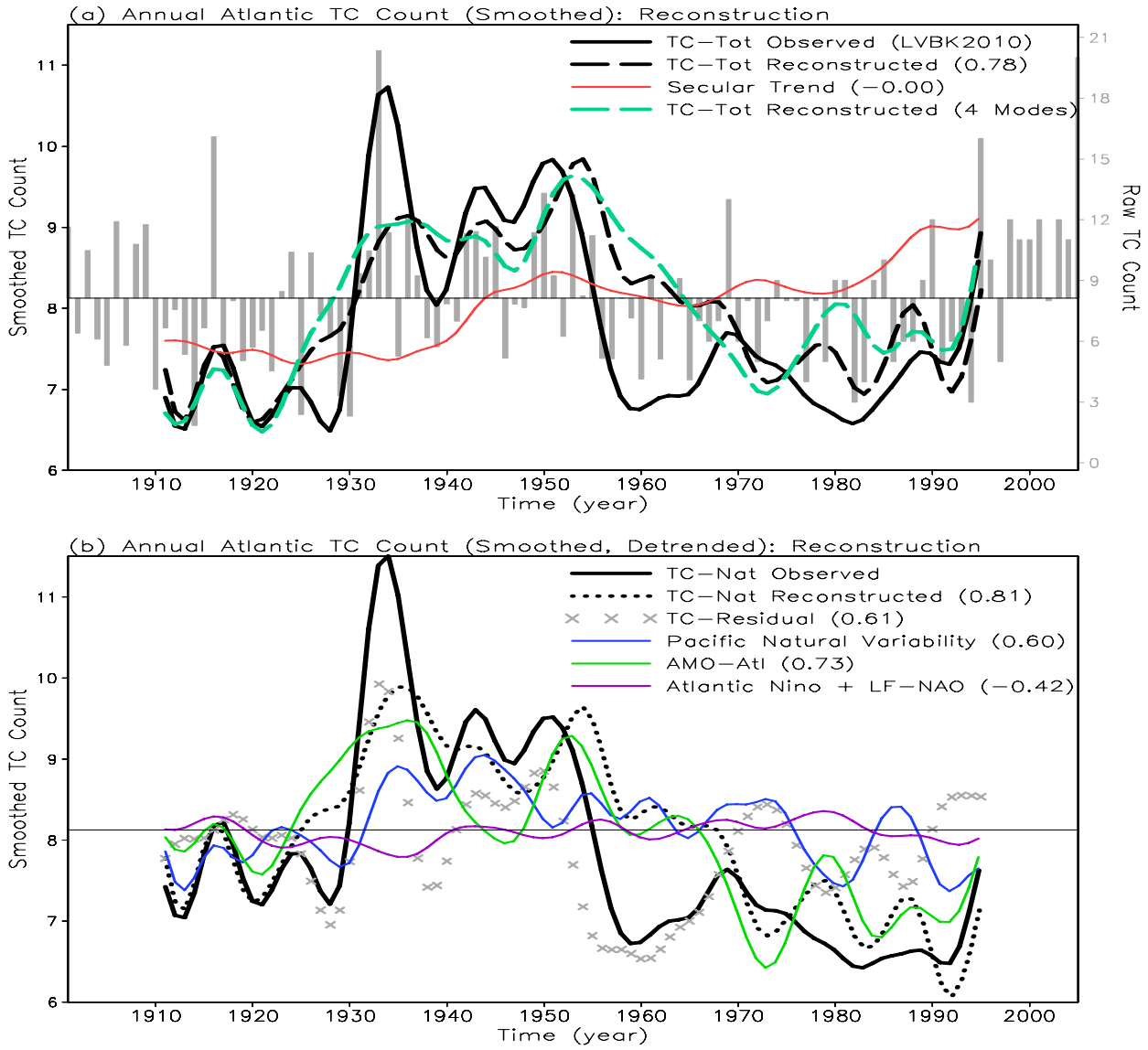

Fig. 1 Reconstruction of the annual Atlantic TC count (Landsea *et al.* 2010, referred as LVBK2010) from Pacific and Atlantic SST variability: a) Observed (solid black) and reconstructed (dashed black) *total* counts are shown after smoothing, using the left scale. Partial reconstruction from the SST secular trend (solid red), and from four decadal time-scale SST principal components (SST Trend, AMO-*Atl*, ENSO Non-Canonical, and Pan-Pacific decadal; dashed green) is also shown; the dashed black and green curve are correlated at 0.93. Lightly shaded vertical bars in the background depict the *raw* (*i.e.*, unsmoothed) TC counts using the right scale, with the horizontal line marking the long-term count-average (8.2) in both; b) Observed (solid black) and reconstructed (dotted black) *natural* count variations. Subtraction of the SST secular trend related counts (red curve in the above panel) from TC-Tot Observed yields the former, while the latter is based on SST natural variability in the Pacific and Atlantic basins. The SST-unrelated count variability (TC-Residual, 'x' marked) is obtained by subtracting the dotted black curve from the solid one in this panel. Contribution of Pacific SST natural variability (blue), AMO-*Atl* (green), and the Atlantic Niño plus Low-Frequency NAO (purple) to TC-Nat Reconstructed are also shown. Time series in both panels are smoothed by 10 applications of the 1-2-1 smoother, which leads to record truncation at both ends. Correlations of the smoothed reconstructed and observed records are indicated next to line labels in each panel.

a notable exception. The SST Trend mode (red) contributes negligibly to this reconstruction given its near-zero correlation (−0.002); all curves are smoothed as TC-Tot Observed, the target. The steep increase in TC count in the 1930s is partially reconstructed. Smoothing related record truncation, unfortunately, precludes assessment of the reconstruction of the 1990s count increase.

The natural variability in TC count (TC-Nat) is the focus of Fig. 1b, which shows both the observed (solid black) and reconstructed (dotted black) counts sans the SST Trend mode contribution. Their 0.81 correlation indicates that ~65% of the natural decadal variance in TC count is related to the basin-scale natural variability of SST, in particular, the 6 Pacific and 4 Atlantic modes of recurrent variability mentioned above. The Pacific contribution to count variance (~35%) is not too far behind the AMO-*Atl* one (~53%). The SST-unrelated variability in TC count (TC- Residual, marked by 'x's), obtained from subtraction of the dotted from solid black curves, must arise from other factors, including SST-unrelated meteorological phenomena (*e.g.*, quasi-biennial oscillation in the lower stratosphere) and, potentially, aerosol's influence on clouds/convection.

The components in reconstruction of TC-Nat are also shown in Fig. 1b, using color. The AMO-*Atl* contribution to TC activity (green) shows both its long time scales and considerable influence, including suppression of TC count in the late-1960s onward period and its enhancement in the 1930s. The other Atlantic modes, Niño and the low-frequency NAO, contribute quite weakly (purple curve), in comparison. Pacific natural variability (blue) is more influential, contributing to increased counts during 1935-45 and diminished activity around 1980 and 1990. Further decomposition (not shown) indicates the Pan-Pacific decadal mode and the ENSO Non-Canonical mode of variability to be largely responsible for the Pacific contribution.

The reconstruction of annual TC counts is formally based on individual regressions of all 11 SST PCs (7 Pacific plus 4 Atlantic, all unsmoothed) but decadal count variations are, in fact, shaped by the contributions of only a select few: SST-Trend, AMO-*Atl*, ENSO Non-Canonical, and perhaps, the Pan-Pacific mode, i.e., just 4 of the 11 modes. A partial reconstruction of TC counts based on these 4 modes (dashed green line in Fig. 1a) closely tracks the full reconstruction at decadal time scales (correlation 0.93), supporting our assertion of the importance of a select few modes of SST variability for annual TC counts in the Atlantic.

a. The 1930s count increase

The SST-based reconstruction can partially account for the steep count-increase in the early 1930s and the precipitous decline in the late 1930s (a signal in the natural variability realm given its short duration?). About one-half of the signal can be linked to SST natural variability which can, evidently, generate the rapid build-up but not the steep decline in counts in the latter part of that decade; the former from in-phase contributions of the Pan-Pacific and AMO-*Atl* modes. Interestingly, Veechi and Knutson (2008) have argued that some of the steep decline in counts is an artifact of undercounting during/preceding World War II.

b. The 1950s-60s count decrease

The large variance in observed and reconstructed counts during the 1950s-60s – largest in the century-long record (see TC-Residual in Fig. 1b) – remain puzzling, not because fields other than SST cannot be influential, but because it is difficult to conceive of factors that can be so singularly influential; in just one sub-period of the 20th century? The 1950s and 1960s are, of course, well known as the period when "average global temperatures leveled off, as increases in aerosols from fossil fuels and other sources cooled the planet." (IPCC 2007, WG1). The cooling is manifest in SST – see the SST secular trend in Fig. 1a – but aerosol's influence on TC counts need not be transmitted only through its SST impact; aerosol induced changes in cloud condensation nuclei distribution can directly impact the strength of deep convection (Cotton *et al.* 2007).

c. The early 1990s count increase

The TC count increased from the early 1990s, in part, from the abatement of count-suppression maintained by SST natural variability in the preceding decades (Fig. 1b, black curves). Were it not for this suppression, TC counts would have risen steeply since the 1970s itself, tracking the secular trend contribution (Fig. 1a, red). The abatement of count suppression in early-1990s is captured in the reconstruction and results mostly from SST natural variability (Fig. 1b). Both basins contribute but the AMO-*Atl* contribution dominates, tracking the combined basin impact (TC-Nat Reconstructed).

d. Count increase during 1996-2005

Smoothing related truncation of TC counts precludes analysis of increased TC activity during 1996-2005, a recent period of considerable interest. A perspective on the relative influence of SST natural variability and secular trend on this period's TC counts can nonetheless be obtained by focusing on the *average value* of the unsmoothed reconstruction components in this 10-year period; all values are relative to the 1901-2005 long-term mean (~8). The analysis indicates that high TC activity during 1996–2005 (a 3.1 count increase over the mean) is as much linked with the SST secular trend (1.5 counts, or ~50% of the observed increase) as with SST natural variability and other effects (which together contribute 1.6 counts, or the remaining 50% increase). As SST-based reconstruction accounts for only 2.1 of the observed 3.1 count increase in this period, the SST secular trend contribution (1.5) dominates the SST natural variability one (0.6). Interestingly, AMO-*Atl* contributes to a 0.9 increase but this is offset by Pacific SST effects, a −0.4 count contribution.

4. Summary and concluding remarks

Consistent estimates of natural variability and secular trend in Tropical Cyclone (TC) count in the Landsea et al. (2010) data set are obtained using modes of observed decadal-multidecadal SST variability in the Pacific and Atlantic basins. The analysis scheme permits development of multidecadal trends from natural variability alone -- a flexibility needed in attribution studies. We show that

- TC counts can be more closely reconstructed from Pacific and Atlantic SSTs than SST of the main development region (MDR); the former account for ~60% of the decadal count variance vis-a-vi ~30% from MDR SST. An expansive influential SST region is indicated, extending well beyond the MDR.
- Atlantic Multidecadal Oscillation (AMO) dominates count-reconstruction, accounting for ~55% of the natural decadal variance; it is followed by the non-canonical ENSO and PDV contributions. These together with the non-stationary SST Secular Trend account for almost all of the reconstructed counts.
- Some count features are reasonably reconstructed. These include the late-60s to mid-80s count suppression (principally from AMO's cold-phase) and the early-90s increase (from the abatement of AMO-related count-suppression and the increasing secular change contribution since late-80s). [A notable feature that could not be reconstructed was the pronounced count-decrease in 1950s-60s, which we deductively attribute to increased aerosols of the period.]
- Our analysis suggests that when counts get augmented in the flip-phase of SST natural variability (*e.g.*, the AMO warm-phase since the late-1990s) -- some evidence for which exists -- decadal TC counts could rapidly increase unless offset by SST-unrelated effects; SSTs account for only ~60% of the decadal count variance.

References

Nigam, S., and B. Guan, 2010: Atlantic tropical cyclones in the 20th century: Natural variability and secular change in cyclone count. *Climate Dynamics*, DOI 10.1007/s00382-010-0908-x.

Guan, B., and S. Nigam, 2008: Pacific sea surface temperatures in the twentieth century: An evolution-centric analysis of variability and trend. *J. Climate*, **21**, 2790-2809.

Guan, B., and S. Nigam, 2009: Analysis of Atlantic SST variability factoring inter-basin links and the secular trend: Clarified structure of the Atlantic Multidecadal Oscillation. *J. Climate*, **22**, 4228-4240

All cited references are noted in Nigam and Guan 2010 (*i.e.*, the first of the above 3 papers)

Science and Technology Infusion Climate Bulletin
NOAA's National Weather Service
35th NOAA Annual Climate Diagnostics and Prediction Workshop
Raleigh, NC, 4-7 October 2010

Sea Breeze Variations in Florida

Lauren Moeller and Vasubandhu Misra
Center for Ocean-Atmospheric Prediction Studies
Department of Earth, Ocean, and Atmospheric Science
Florida State University, Tallahassee, FL

1. Introduction

Sea breezes play an integral part for convection in the summer, especially for Florida. They form due to land-sea temperature contrasts, which for the case of a summer afternoon, creates a pressure gradient with low pressure over the relatively warmer land. In the Florida peninsula, two sea breeze fronts can form due to two gradients on either side of the peninsula (Blanchard and Lopez 1984). Recent anecdotal observations compare the convection based on sea breezes from year-to-year, suggesting interannual variability. While sea breezes exist every year regardless, they are affected by the background conditions, or synoptic scale motions, as mentioned in Blanchard and Lopez (1984). Another study by Nicholls (1991) observes that sea breezes are affected by the prevailing winds.

Using this knowledge, a hypothesis is made that the interannual variations of the Atlantic Warm Pool (AWP) could affect the sea breeze characteristics. The AWP is defined as the area in the Gulf of Mexico, Caribbean Sea, and tropical North Atlantic in which the sea surface temperature (SST) is at least 28.5^{0}C. The years in which the AWP is large have weaker background trade winds (Wang and Enfield 2001). The warmer waters also hint that the temperature contrast may also be smaller. This study will look at the diurnal variations of winds and precipitation plus composites of large and small AWP years to verify the AWP variability impacts.

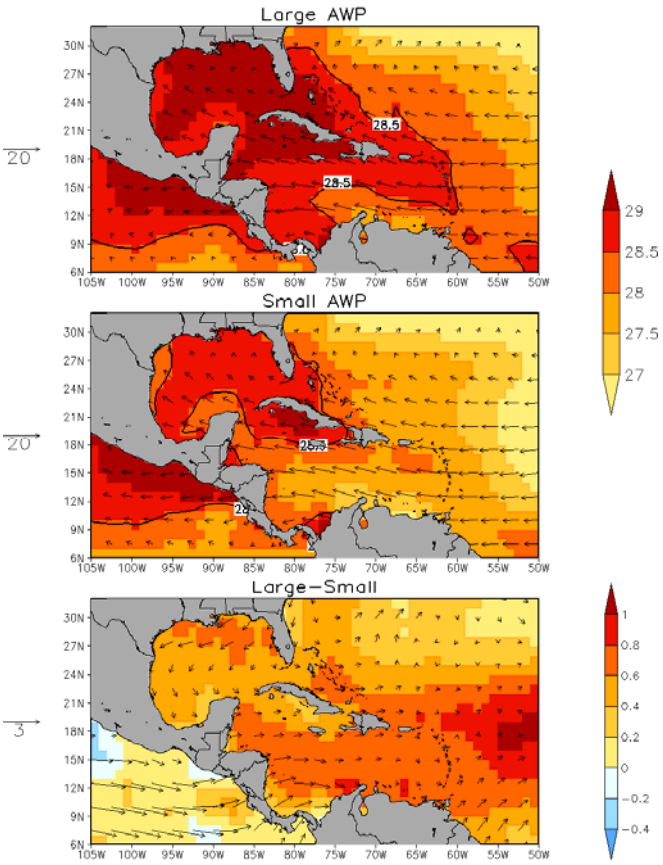

Fig. 1 Average SST from ERSSTV3 and 850hPa winds from NCEP-DOE reanalysis for 5 large AWP years (1981, 1987, 1995, 1998, 1999) (top), 5 small AWP years (1984, 1986, 1989, 1993, 1994) (middle) and the difference between the two (bottom).

2. Data and methodology

The model used is the NCEP Scripps Regional Spectral Model (RSM; Kanamitsu *et al.* 2005) forced with NCEP-DOE Reanalysis II (R2; Kanamitsu *et al.* 2002). The R2 reanalysis is dynamically downscaled to 10 km. The spatial domain of the RSM-R2 model consists of the southeastern United States and the majority of the Gulf of Mexico, and the temporal domain is 23 years (1979-2001). While the data was available year-round, the focus of the study was the summer months of June, July, and August (JJA). SSTs were available from the National Oceanic and Atmospheric Administration (NOAA) Extended Reconstruction Sea Surface

Correspondence to: Lauren Moeller, Center for Ocean-Atmospheric Prediction Studies, Department of Earth, Ocean and Atmospheric Sciences, The Florida State University, Tallahassee, FL; E-mail: lrnemllr@gmail.com

Temperature analysis version 3 (ERSSTV3; Smith *et al.* 2008). For verification the precipitation used is from the Climate Prediction Center (CPC) and the NCEP/EMC US gridded radar estimates (Lin and Mitchell 2005).

To examine the data and the sea breeze variability, two groups of figures were made. The first set includes 3-hour climatology to examine the diurnal variability of the convection and sea breeze-related phenomenon. Two different cross-section latitudes were chosen: one along 26^0N to represent the Florida peninsula, and the other along 30.5^0N for the Florida panhandle. The second group of figures consists of large and small AWP composites. These were chosen by grouping the years with average SSTs of more (less) than one standard deviation away from the mean to be classified as a large (small) AWP year. Typical conditions for each composite are shown in Figure 1. The large AWP years typically have the warmer SSTs dipping into the tropical North Atlantic, while the small AWP years have 28.5^0C SSTs confined to mainly the Gulf of Mexico and parts of the Caribbean. The main defining features are the weaker winds and warmer Gulf temperatures for large AWP years. In Figure 2, the CPC rainfall observations show a decrease in convection for large AWP years, especially along the Florida panhandle, which suggests weaker sea breeze events.

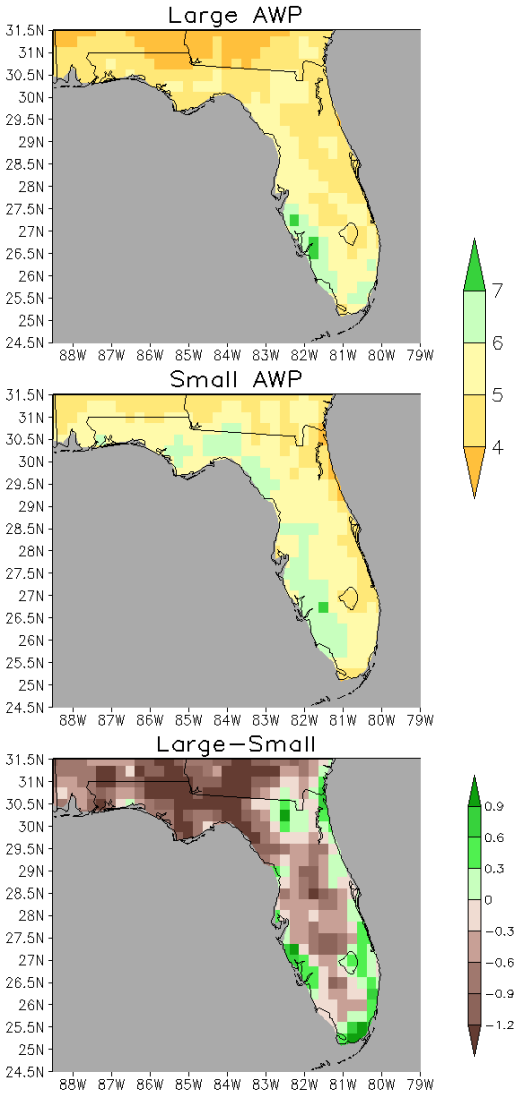

Fig. 2 Average rainfall from CPC rain gauge-based rainfall (Higgins *et al.* 2000) for 5 large AWP years (top), 5 small AWP years (middle), and difference between the two (bottom). The units are in mm day^{-1}.

3. Results

The first objective was to validate the model choice by comparing it with an observational data set. This is accomplished in Figures 3, which compare the 3-hourly climatology of rainfall for JJA in Florida. The RSM-R2 model, though it does not display correct magnitudes, captures the diurnal variability of the precipitation shown in the observations. Both show a peak in rainfall at 4 pm, with a decline in precipitation afterwards. These diurnal patterns are also found in Figure 4, in which the vertical motion associated with the circulations peaks at 4pm for the Florida peninsula. While the panhandle cross-section is not shown, the vertical motion peaks at the same time. The diurnal change in the sea breeze is also consistent between the two locations, in which the circulations increase throughout the day, and decrease rapidly by 7 pm. The planetary boundary layer (PBL) also behaves as expected given the previous results: it expands during the day with diurnal heating and increased vertical motion, and peaks around 1pm. As stronger mixing occurs due to convection, the PBL decreases in height starting at 4 pm, and continues to do so over land as the solar heating decreases.

A composite JJA plot for precipitation rates for large and small AWP years was made using the RSM-R2 model to compare with the CPC results in Figure 2. The RSM-R2 model composite (not shown) does fairly well in modeling the difference in precipitation between the composites, capturing the decrease in precipitation for large AWP years over the panhandle. However, this model shows an increase in precipitation over most of the peninsula for large AWP years in comparison to small, which does not reflect the patterns found in the CPC composite.

One of the reasons why the model is capturing the lower amounts of convection for large AWP years is hinted at with Figure 5. The land temperature plots show that on average, large AWP years have cooler

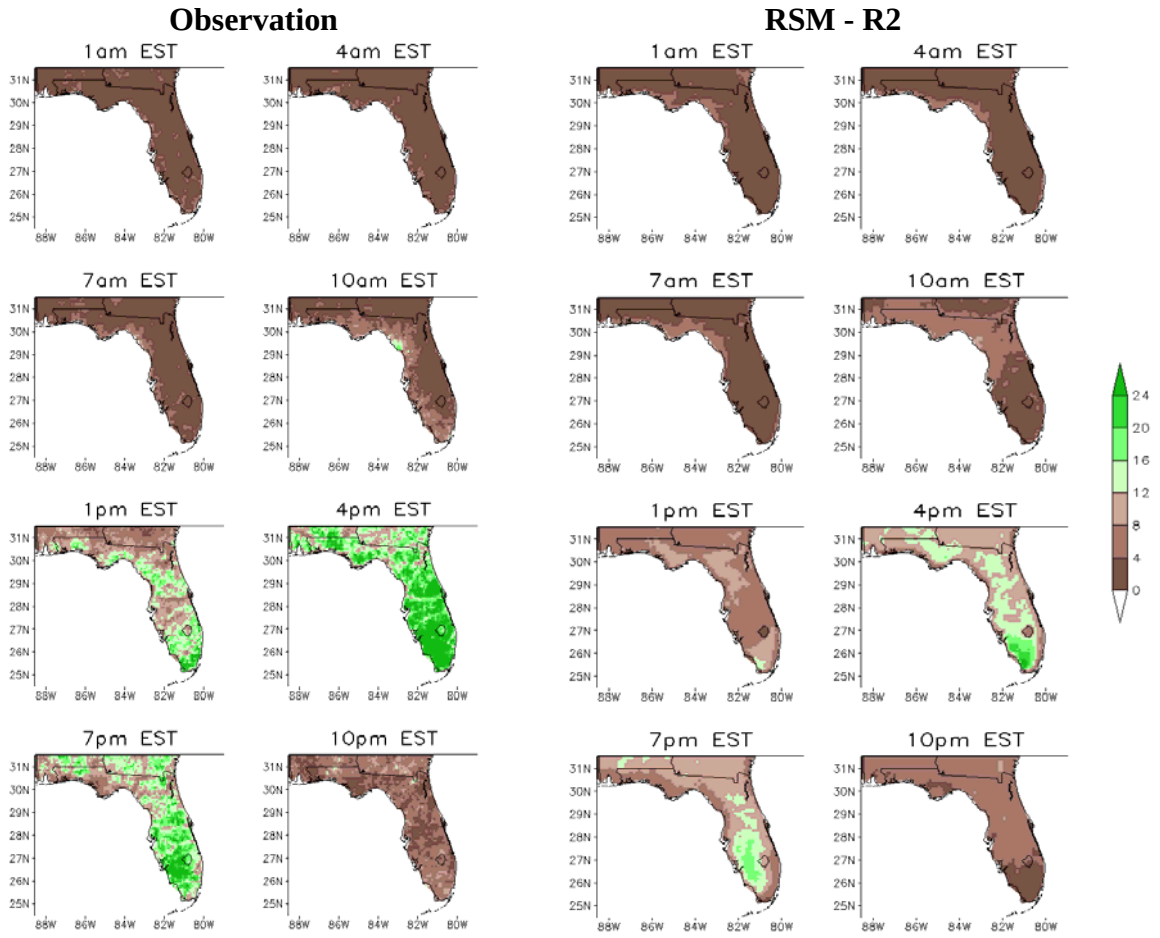

Fig. 3 The observed and RSM-R2 model simulated climatology of summer season (June-July-August) rainfall at 3-hour interval. The former was computed for the available period of 2002-2008 and the latter was from 1979-2001. The units are in mm day^{-1}.

temperatures on land than the small AWP years. As mentioned previously, the land-sea temperature gradients cause the sea breezes and that land temperatures are much higher than ocean temperatures during a summer afternoon. However, the Gulf of Mexico is warmer for large AWP years, and the land temperatures are cooler over the panhandle. This hints that, on average, the land-sea temperature gradient is smaller in magnitude for large AWP years, leading to a weaker pressure gradient and sea breeze circulation. This would, in turn, yield to less convection. More plots are necessary for confirmation, however, to show that the weaker gradient does occur during the afternoon hours.

Another plot that highlights this decrease in precipitation and convection for large AWP years is shown in Figure 6. The time of 4pm was chosen because other diagrams have shown that the highest difference in precipitation between the two composites was at 4pm. The most noticeable feature in Figure 6 is that there is a positive difference in PBL height between large and small, indicated by two bottom panels. This is occurring because there is weaker convection occurring over land for large AWP years, and thus less mixing is taking place to shrink the PBL depth. This would indicate that the sea breeze circulation is weaker for large AWP years than for small, for both the peninsula and panhandle of Florida.

4. Conclusions

This study examined the interannual variations of convection over peninsular and panhandle regions of Florida, with the understanding that in the summer months the main driver for daily convection is the sea breeze. The NCEP-Scripps RSM forced with downscaled NCEP-DOE R2 data proved to portray the diurnal

variations of precipitation quite well when compared to the NCEP/EMC US gridded observations. The model also showed that for large AWP years, there is less convective precipitation over Florida, especially over the panhandle. Possible contributions to this lack of rainfall are the weaker winds exhibited in large AWP years, plus a weaker sea-breeze temperature gradient, both of which lead to a weaker sea breeze circulation. Also, these differences are most pronounced at 4 pm, the time of day with the highest rainfall amounts. The results of this study demonstrate the importance of interannual variations of sea breeze convection to rainfall totals in the summer over Florida.

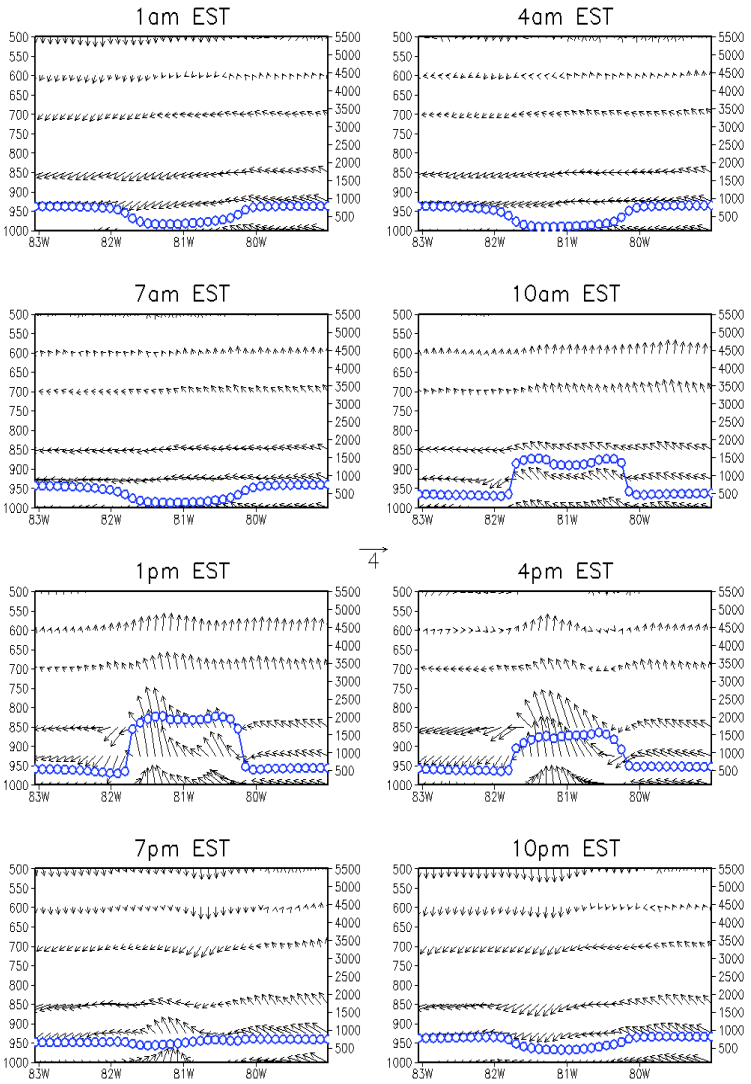

Fig. 4 Vertical cross-section of the climatological June-July-August wind (vertical velocity and zonal wind in ms^{-1}) at 26^0N latitude, across south Florida at 3 hourly interval. The PBL height is shown by solid line with open circles. The vertical velocity is scaled by a factor of 100.

References

Blanchard, D. O. and R. E. Lopez, 1984: *Spatial patterns of convection in South Florida*. Mon. Wea. Rev., 113, 1282- 1299.

Higgins, R. W., W. Shi, E. Yarosh, and R. Joyce, 2000*: Improved United States Precipitation Quality Control System and Analysis*. NCEP/Climate Prediction Center Atlas 7, NOAA, 40pp.

Kanamitsu, M., W. Ebisuzaki, J. Woollen, S. Yang, J. J. Hnilo, M. Fiorino, and G. L. Potter, 2002: *NCEP-DOE AMIP-II reanalysis (R-2)*. Bull. Amer. Soc., 83, 1631-1643.

Kanamitsu, M., H. Kanamaru, Y. Cui and H. Juang, 2005: Parallel Implementation of the Regional Spectral Atmospheric Model. CEC-500-2005-014. Available from http://www.energy.ca.gov/publications/displayOneReport.php?pubNum=CEC-500-2005-014

Lin, Y., and K. E. Mitchell, 2005: *The NCEP stage II/IV hourly precipitation analyses: development and applications.* Preprints, 19th Conf. on Hydrology, American Meteorological Society, San Diego, CA, 9-13 January, Paper 1.2.

Nicholls, M. E., R. A. Pielke, and W. R. Cotton, 1991: *A two-dimensional numerical investigation of the interaction between sea breezes and deep convection over the Florida peninsula*. Mon. Wea. Rev., 119, 298-323.

Wang, C. and D. B. Enfield, 2001: *The tropical western hemisphere warm pool*. Geophys. Res. Lett., 28, 1635-1638.

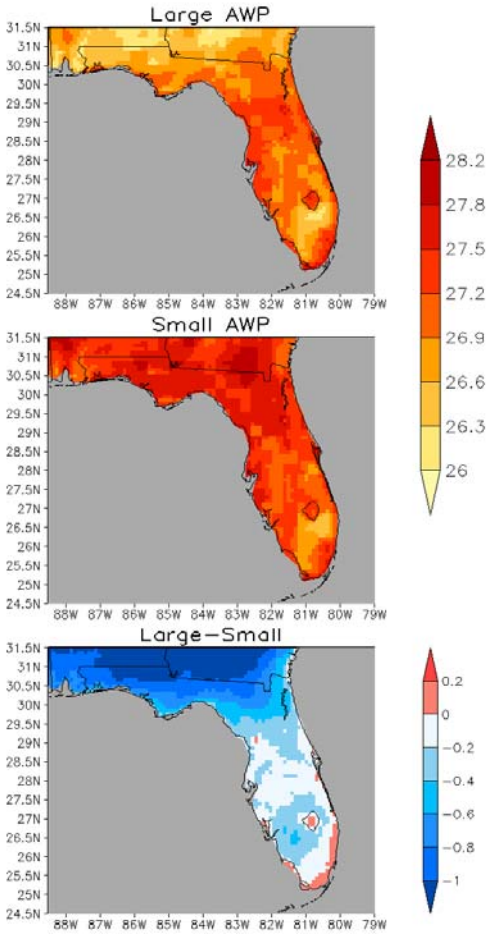

Fig. 5 Same as Fig. 2 but for land surface temperature and from RSM-R2 simulation. The units are in ^{0}C.

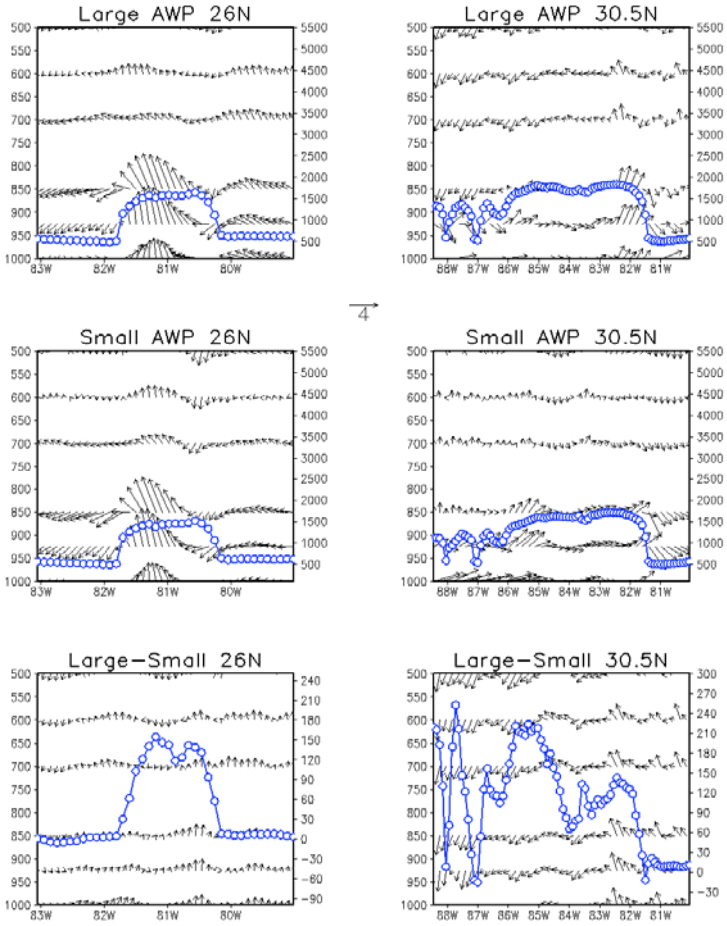

Fig. 6 Composite means of variables as in Figure 4 at 4 pm for the 5 large AWP years (top), the 5 small AWP years (middle), and the difference (bottom) from the RSM-R2 simulation at 26ºN (left column) and 30.5ºN (right column), respectively.

Science and Technology Infusion Climate Bulletin
NOAA's National Weather Service
35th NOAA Annual Climate Diagnostics and Prediction Workshop
Raleigh, NC, 4-7 October 2010

Impact of Low Clouds on Tropical Climate in the NCEP CFS

Zeng-Zhen Hu[1,2], Bohua Huang[2,3], Yu-Tai Hou[4], Wanqiu Wang[1]
FanglinYang[4], Cristiana Stan[2], and Edwin K. Schneider[2,3]

[1]*Climate Prediction Center, NCEP/NWS/NOAA, Camp Springs, MD*
[2] *Center for Ocean-Land-Atmosphere Studies, Calverton, MD*
[3]*Department of Atmospheric, Oceanic, and Earth Sciences, George Mason University, Fairfax, VA*
[4]*Environmental Modeling Center, NCEP/NWS/NOAA, Camp Springs, MD*

1. Introduction

Stratocumulus cloud decks in the southeastern Pacific and Atlantic Oceans have been documented by Klein and Hartmann (1993), Norris (1998), and Xie (2005). Climatologically, the daytime frequency of the existence of stratocumulus clouds reaches 30-70% in the southeastern tropical Pacific and Atlantic (Klein and Hartmann 1993; Norris 1998). The existence of these stratocumulus clouds substantially reduces the shortwave radiation reaching the sea surface and cools the ocean, which reinforces the inversion stratification (Siebesma *et al.* 2004; Huang and Hu 2007). Underestimation of the amount of stratocumulus clouds over the tropical oceans is a common defect of contemporary coupled climate models (Huang *et al.* 2007; Hu et al. 2008a), which seems to be tied to pronounced warm biases in the tropical eastern oceans (*e.g.*, Neelin et al. 1992; Mechoso *et al.* 1995; Davey *et al.* 2002; Collins *et al.* 2006; Deser *et al.* 2006; Huang et al. 2007; Hu *et al.* 2008a). For example, warm biases can reach 4-5ºC in the southeastern tropical Pacific and Atlantic in versions 2 and 3 of the Community Climate System Model (Collins *et al.* 2006). Furthermore, Hu and Huang (2007) and Hu *et al.* (2008a) found that these biases can reduce climate prediction skill and may alter the southern subtropical variability mode in the tropical Atlantic. Thus, it is necessary to examine the impact of the stratocumulus clouds on model systematic errors.

In this work, using the CFS, we examine the sensitivity of the tropical mean climate and seasonal cycle not only to the change of low cloud cover, but also to the change of cloud liquid water path (CLWP). Through these experiments, a scheme of model bias correction is proposed and its efficiency is tested.

2. Observation-based data, model, and experimental design

Observation-based monthly cloud coverage data used in this work were produced by the International Satellite Cloud Climatology Project (ISCCP) (Rossow and Dueñas 2004). The CLWP data, termed the University of Wisconsin climatology (O'Dell et al., 2008), are adopted. Also, the simulations are compared with observation based data, such as the NCEP/NCAR re-analysis (Kalnay *et al*. 1996), ER-v2 SST (Smith and Reynolds 2003), and analyzed precipitation (Xie and Arkin 1997).

The ocean-atmosphere coupled general circulation model used in this work is the NCEP CFS (Wang *et al.* 2005; Saha *et al.* 2006). For the atmospheric component, the horizontal resolution is T62 and there are total 64 vertical sigma levels with about 20 sigma levels below 650 hPa. The oceanic component is configured from the MOM3 of GFDL. There are 40 levels vertically, with 27 in the upper 400 meters for the ocean model. The domain of the ocean model is from 74ºS to 64ºN with a horizontal grid of 1ºx1º poleward of 30ºS and 30º N, and with gradually increased meridional resolution to 1/3º between 10ºS and 10ºN. The atmospheric and oceanic components are coupled by exchanging surface fluxes on a daily interval without flux adjustment.

To investigate the impact of prescribed low-level cloud cover and CLWP on tropical climate in the CFS, a set of coupled integrations were conducted (see Table 1). **CONTROL** is a 101 year integration using the same version of the CFS as Wang *et al.* (2005) and Saha *et al.* (2006). In cloud cover modification experiments, CFS simulated low clouds are replaced by global climatological low cloud amount of ISCCP in

Correspondence to: Zeng-Zhen Hu, Climate Prediction Center, NCEP/NWS/NOAA, 5200 Auth Road, Camp Springs, MD 20746; E-mail: Zeng-Zhen.Hu@noaa.gov.

LCA1, and by observed global monthly low clouds of ISCCP in January 1984-December 2004 in **LCA2**. The vertical distribution of cloud amount in the layers between surface and 650 hPa is prescribed by the following equation: $CFS_{cloud}(z)=\alpha*ISCCP_{low\ cloud}*\cos(\beta)$, where, $\beta = \frac{\pi}{2} * \frac{Pm-Pz}{Pm-Pt}$. P_z is the pressure in layer "z" in hPa. P_t and P_m are the pressures of the top and middle layers with cloud prescribed, respectively. According to diagnostic results, we use following parameter values: P_t=650 hPa, P_m=850 hPa, and α=1.0 here.

Experiment Name	Experiment Description	Length of the integration and Initial Condition
CONTROL	no modification for clouds	101 years, Jan. 1985
LCA1	model global low clouds replaced by ISCCP climatological low clouds	5 years, Jan. 1985
LCA2	similar to LCA1, but replaced by ISCCP monthly low clouds	21 years, Jan. 1984
CLWP1	model low cloud portion of CLWP over global oceans is modified by adding observed monthly low cloud CLWP	20 years, Jan. 1988
CLWP2	similar to CLWP1, but modified only in the southeastern Atlantic	20 years, Jan. 1988
CORRECTION	similar to CLWP2, but modified by using observed annual mean climatology of CLWP in the southeastern Atlantic	50 years, Jan. 1988

Table 1 Experiments

To examine the impact of CLWP, we conduct two CLWP experiments (**CLWP1**, **CLWP2**). In CLWP1 and CLWP2, similar to LCA2, the low cloud portion of observed monthly CLWP over the oceans is used to build vertical profiles of cloud using the above equation with α=0.0824 in order to keep the accumulation of the vertically interpolated CLWP between the surface and 650 hPa equal to the low cloud portion of the observed CLWP. Model low cloud portion of CLWP is modified by adding observed monthly low cloud CLWP for global oceans in CLWP1, and just for the southeastern Atlantic Ocean in CLWP2. Then, we propose a scheme to eliminate the model biases by prescribing climatological CLWP in the model and test it in experiment: **CORRECTION**. It is similar to CLWP2 (only the CLWP in the southeastern Atlantic is prescribed), but uses annual mean climatology of observed CLWP. More details about the experiment design, refer to Table 1 or Hu *et al.* (2010).

3. Impact of low cloud on tropical mean climate

3.1 Impact of low cloud cover

Figure 1 shows the mean low cloud amount, as well as mean and difference of net shortwave radiation at the surface in observations, CONTROL, and LCA2. As indicated by Hu *et al.* (2008a, 2008b), although the seasonal variations of the low clouds are reasonably well simulated in the southeastern Atlantic Ocean, CFS underestimates the mean low clouds by about 25%, which is connected to the warm biases there. On the other hand, the mean low cloud amount in the whole tropical Atlantic Ocean and the interannual variation in the southeastern Atlantic Ocean are almost perfectly presented in LCA2, as well as in LCA1 for the mean low cloud amount (not shown), which is a significant improvement compared with CONTROL. This demonstrates that a realistic 3-dimensional low cloud distribution is successfully prescribed in the CFS.

Nevertheless, the improved low cloud cover only has a minor influence on the amount of net shortwave radiation reaching the surface (Figs. 1d-1f) in the southeastern Atlantic. This result suggests that low cloud cover plays a secondary role in blocking and absorbing the radiation in the radiation parameterization of the CFS. The absorption and reflection of shortwave radiation by clouds mainly depend on optical depth which is largely determined by cloud liquid water content (Hou *et al.* 2002), that is confirmed by the results in next subsection.

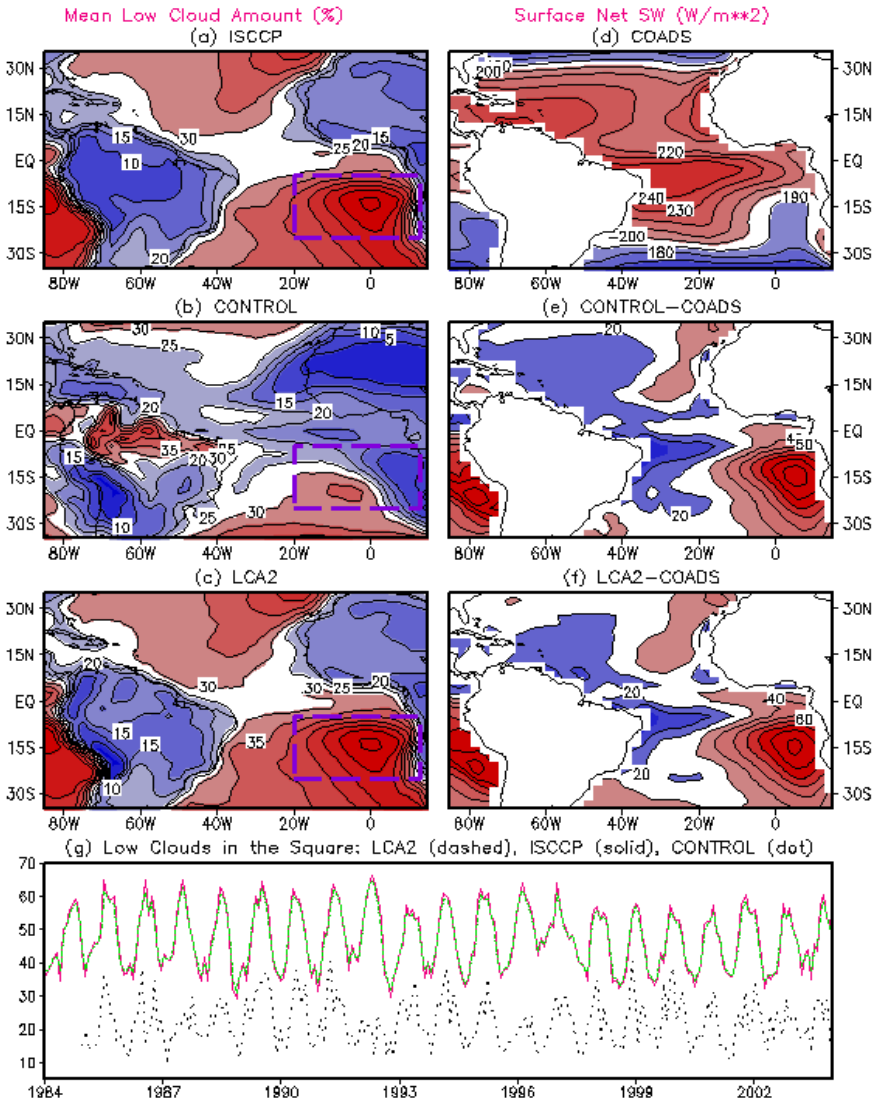

Fig. 1 Left column: Mean cloud amount in observations (ISCCP) (a), CONTROL (b), and LCA2 (c). Right column: Net shortwave radiation at the surface for observation (COADS) (d), the differences of CONTROL-COADS (d) and LCA2-CONTROL (e). Bottom: regional averaged monthly low cloud amount in ISCCP (solid), LCA2 (dashed), and CONTROL (dot). The averaged region is the square in (a-c). Contour interval is 5% in (a-c), 10 W/m^2 in (d-f).

3.2 Impact of CLWP

Compared with CONTROL, modifying CLWP can improve the simulation of low clouds, because the low cloud in the CFS is diagnosed from cloud condensation. The improvement of low clouds and CLWP consistently reduces the biases of net shortwave radiation at the ocean surface. The radiation change causes cooling in the troposphere. Meanwhile, the cold tongue becomes much stronger and warm biases are reduced significantly in the eastern tropical oceans, and the easterly surface wind stress is enhanced along the equator compared with CONTROL (Figs. 2c, 2f, 2g, 2j). However, when CLWP is prescribed only in the tropical Atlantic, improvement of SST and intensification of easterly surface wind stress are found only in the tropical Atlantic and changes in other regions are relatively small (Figs. 2d, 2e, 2f, 2h, 2i).

Also, the simulation of the inter-tropical convergence zone (ITCZ) in the tropical Atlantic is improved in CLWP1, CLWP2, and CORRECTION compared with CONTROL (Fig. 3). For example, there are double ITCZs in March-June in CONTROL, and the unrealistic southern branch of the ITCZ in 5ºS-10ºS (Fig. 3b) is largely eliminated in CLWP1, CLWP2, and CORRECTION (Fig. 3c-3e). The northward movement of the ITCZ is steady in the observations (Fig. 3a), but is more abrupt in CONTROL due to a sudden enhancement of the southerly wind in June (see the thick line in Fig. 3b). In the CLWP prescribed experiments (CLWP1, CLWP2, CORRECTION), the northward movement of the ITCZ is in between that of the observations and

CONTROL (Figs. 3c-3e). The improvement of the ITCZ is mainly associated with the enhancement of the southerly wind in the early part of the year.

4. Concluding remarks

In this work, we examined the impact of low clouds and CLWP changes on tropical mean climate and

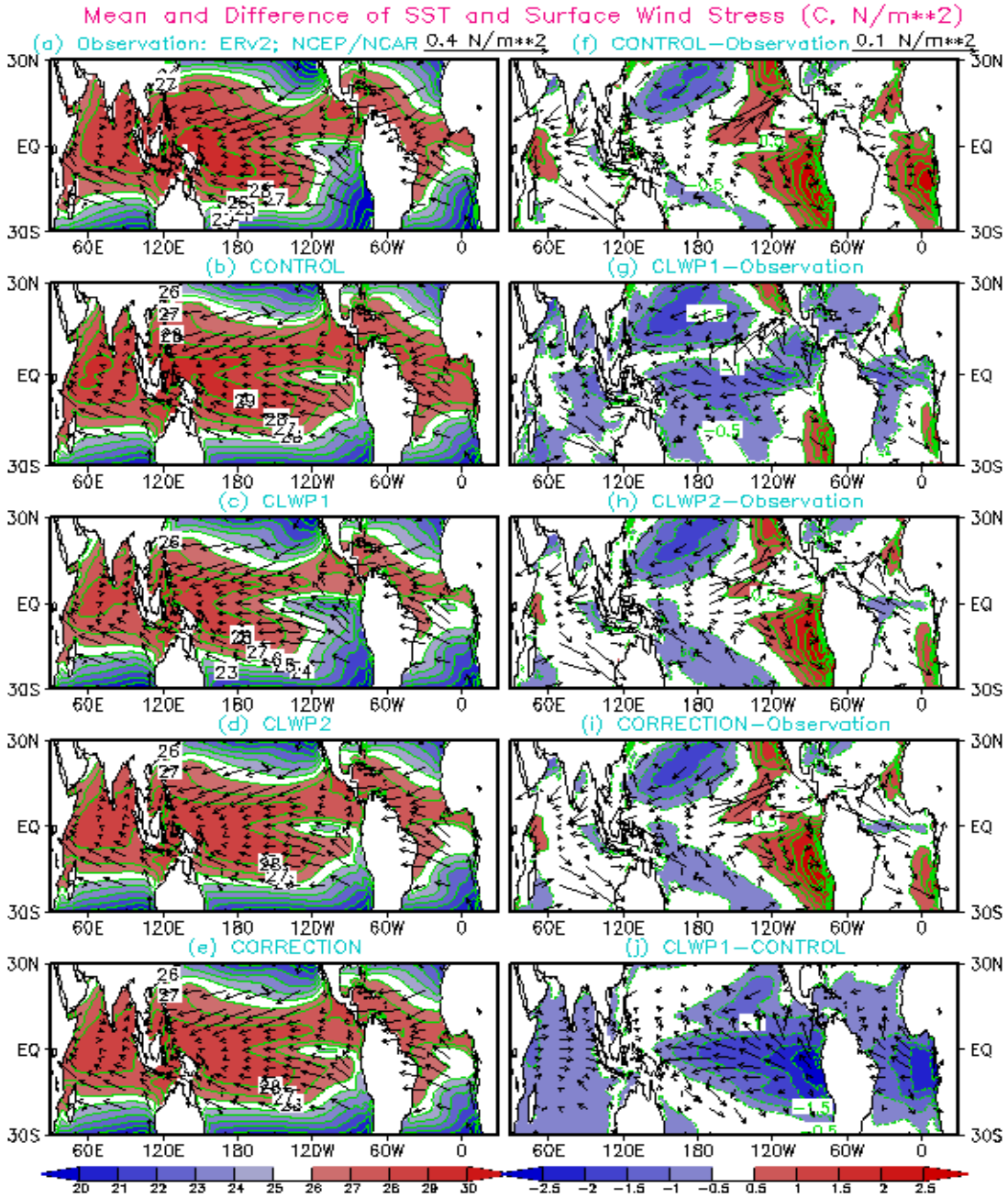

Fig. 2 Left column: Mean of SST (shading and contour) and surface wind stress (vector) in observations (NCEP/NCAR reanalysis and ERv2) (a), CONTROL (b), CLWP1 (c), CLWP2 (d), and CORRECTION (e). Right column: Difference of SST and surface wind stress between CONTROL and observations (f), between CLWP1 and observations (g), between CLWP2 and observations (h), between CORRECTION and observations (i), and between CLWP1 and CONTROL (j). Contour intervals of SST are 1^{O}C in (a-e) and 0.5^{O}C in (f-j). The scales of the vectors are shown at the top of each column.

seasonal cycle by prescribing them in the NCEP CFS. It is found that the change of low cloud cover alone has a minor influence on the amount of net shortwave radiation reaching the surface and on the warm biases in the southeastern Atlantic. Further experiments show that shortwave radiation absorption by CLWP is mainly responsible for reducing the excessive surface net shortwave radiation over the southern oceans in the CFS. By prescribing CLWP in the CFS, the cold tongue and associated surface wind stress in the eastern oceans become stronger and more realistic. The seasonal cycle in the tropical Atlantic is also improved. It seems that prescribing CLWP in the CFS is an effective interim technique to reduce model biases and to improve the simulation of seasonal cycle in the tropics. This could then serve as a model bias correction approach.

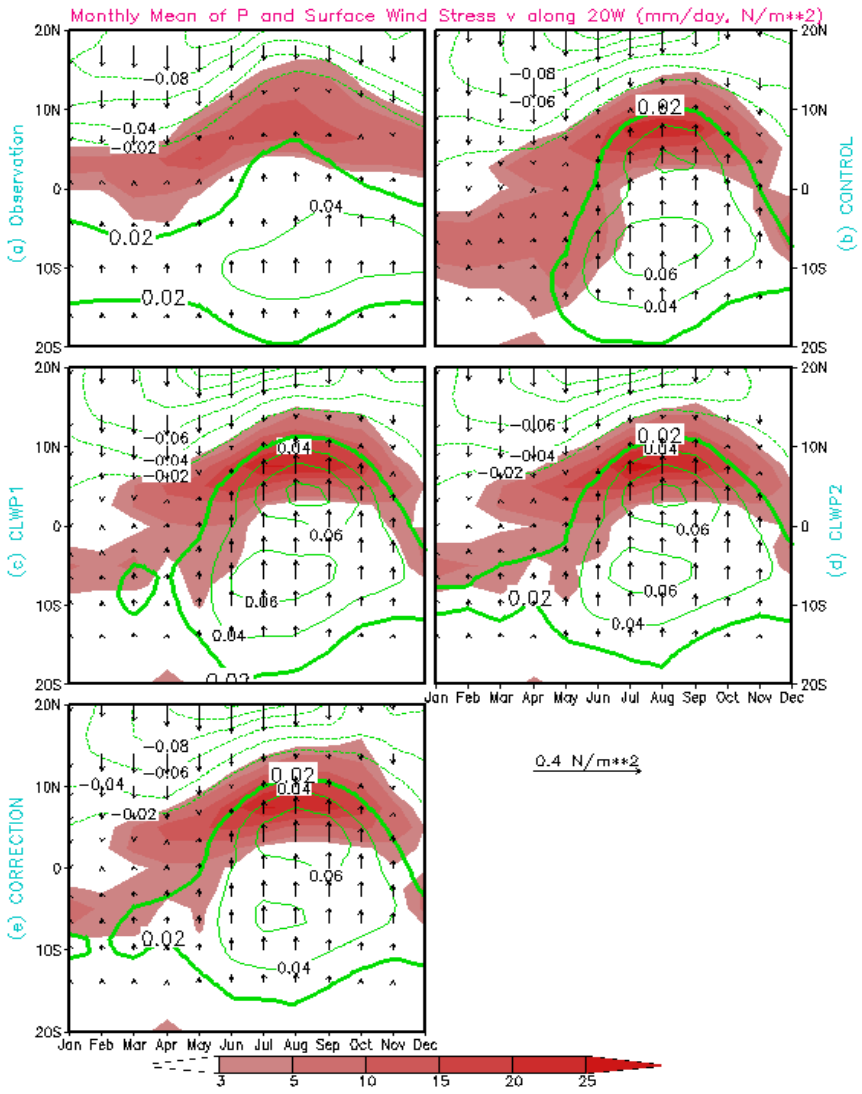

Fig. 3 Climatology of monthly mean of precipitation (shading) and v component of surface wind stress (vectors and contours) between 20°S and 20°N along 20°W in observation (NCEP/NCAR reanalysis and CAMP) (a), CONTROL (b), CLWP1 (c), CLWP2 (d), and CORRECTION (e). Zero contour line is omitted, thick line represents the contour of 0.02 N/m^2, and contour interval is 0.02 N/m^2. The scale of the vector is shown at the bottom of the right column.

References

Collins, W and co-authors, 2006: The Community Climate System Model: CCSM3. *J. Climate*, **19**, 2122-2143.

Davey, M.K. and co-authors, 2002: STOIC: A study of coupled model climatology and variability in tropical ocean regions. *Clim. Dyn.*, **18**, 403-420, doi: 10.1007/s00382-001-0188-6.

Deser, C, A. Capotondi, R. Sravanan, and A.S. Phillips, 2006: Tropical Pacific and Atlantic climate variability in CCSM3. *J. Climate*, **19**, 2451-2481.

Hou, Y-T, S. Moorthi, and K. Campana, 2002: Parameterization of solar radiation transfer in the NCEP models. NCEP Office Note, Vol 441, pp 1-46 (available at http://www.emc.ncep.noaa.gov/officenotes/newernotes/on441.pdf).

Hu, Z.-Z., B. Huang, Y.-T. Hou, W. Wang, F. Yang, C. Stan, and E. K. Schneider, 2010: Sensitivity of tropical climate to low-level clouds in the NCEP Climate Forecast System. *Clim. Dyn.*, doi: 10.1007/s00382-010-0797-z.

Hu, Z-Z, B. Huang, and K. Pegion, 2008a: Low cloud errors over the southeastern Atlantic in the NCEP CFS and their association with lower-tropospheric stability and air-sea interaction. *J. Geophys Res (Atmosphere),* **113**: D12114, doi:10.1029/2007JD009514.

Hu, Z-Z, B. Huang, and K. Pegion, 2008b: Leading patterns of the tropical Atlantic variability in a coupled GCM. *Clim. Dyn.*, **30** (7/8), 703-726, doi:10.1007/s00382-007-0318-x.

Hu, Z-Z and B. Huang, 2007: The predictive skill and the most predictable pattern in the tropical Atlantic: The effect of ENSO. *Mon. Wea. Rev.*, **135** (5), 1786-1806

Huang, B, Z-Z Hu, and B Jha, 2007: Evolution of model systematic errors in the tropical Atlantic basin from the NCEP coupled hindcasts. *Clim. Dyn.*, **28** (7/8), 661-682, doi:10.1007/s00382-006-0223-8

Huang, B. and Hu Z-Z, 2007: Cloud-SST feedback in southeastern tropical Atlantic anomalous events. *J Geophys Res (Ocean)*, **112**, C03015, doi: 10.1029/2006JC003626.

Kalnay, E. and co-authors, 1996: The NCEP/NCAR 40-year reanalysis project. *Bull. Am. Meteorol. Soc.*, **77,** 437-471.

Klein, S.A. and D.L. Hartmann, 1993: The seasonal cycle of low stratiform clouds. *J. Climate*, **6**, 1587-1606.

Mechoso, C.R. and co-authors, 1995: The seasonal cycle over the tropical Pacific in general circulation models. *Mon. Wea. Rev.*, **123**, 2825-2838.

Neelin, J.D. and co-authors, 1992: Tropical air-sea interaction in general circulation models. *Clim. Dyn.*, **7**, 73-104.

Norris, J.R., 1998: Low cloud type over the ocean from surface observations. Part II: geographical and seasonal variations. *J. Climate*, **11**, 383-403.

O'Dell, C.W., F.J. Wentz, and R. Bennartz, 2008: Cloud liquid water path from satellite based passive microwave observations: A new climatology over the global oceans. *J. Climate*, **21**, 1721-1739.

Rossow, W.B. and E.N. Dueñas, 2004: The International Satellite Cloud Climatology Project (ISCCP) web site: An online resource for research. *Bull. Am. Meteorol. Soc.*, **85**, 167-172.

Saha, S. and co-authors, 2006: The NCEP climate forecast system. *J. Climate*, **19**: 3483-3517.

Siebesma, A.P. and co-authors, 2004: Cloud representation in general-circulation models over the northern Pacific Ocean: A EUROCS intercomparison study. *Q. J. R. Meteorol. Soc.*, **130**, 3245-3267.

Smith, T.M. and R.W. Reynolds, 2003: Extended reconstruction of global sea surface temperatures based on COADS data (1854-1997). *J. Climate*, **16**: 1495-1510.

Wang, W. and co-authors, 2005: Simulation of ENSO in the new NCEP coupled forecast system model. *Mon. Wea. Rev.*, **133**, 1574-1593.

Xie, P. and P.A. Arkin, 1997: Global precipitation: A 17-year monthly analysis based on gauge observations, satellite estimates and numerical model outputs. *Bull. Am. Meteorol. Soc.*, **78**, 2539-2558.

Xie, S.-P., 2005: Chapter 4: The Shape of Continents, Air-Sea Interaction, and the Rising Branch of the Hadley Circulation. *In The Hadley Circulation: Present, Past and Future*, Eds: Diaz, H. F. and R. S. Bradley. Kluwer Academic Publishers, the Netherlands, 121-152.

Science and Technology Infusion Climate Bulletin
NOAA's National Weather Service
35th NOAA Annual Climate Diagnostics and Prediction Workshop
Raleigh, NC, 4-7 October 2010

CFS Prediction of Winter Persistent Inversions in the Intermountain West

Robert Gillies[1, 2], Shih-Yu Wang[1, 2], Marty Booth[1], Jin-Ho Yoon[3*], and Scott Weaver[3]

[1]*Utah Climate Center, Utah State University, Logan, UT*
[2]*Department of Plants, Soils, and Climate, Utah State University, Logan, UT*
[3] *NOAA Climate Prediction Center, Camp Springs, MD*

1. Introduction

During the winter season, heavy rainfall events in the western United States are known to be associated with the intraseasonal oscillation (ISO) (Mo and Nogues-Paegle 2005). In the Intermountain West, a different weather event is gaining increasing attention, *i.e.* persistent inversions. Deep inversions often develop in valleys and mountain basins and frequently lead to poor air quality. In 2007, in order to forecast winter inversions along with expected air quality, the National Weather Service (NWS) at Salt Lake City began periodic special weather briefings before the onset of and during inversion situation[1]: In the briefings, it has been regularly mentioned that estimating inversion duration and pollution intensity is frequently difficult to specify in definitive terms. Recently, a close linkage between the occurrence of wintertime persistent inversions and the 20-40 day ISO was identified (Gillies *et al.* 2010; hereafter GWB). The 20-40 day ISO is a pronounced mode in the midlatitude circulations (Horel and Mechoso 1988; Lau and Nath 1999) but more so, its intraseasonal timescale implies that forecasting persistent inversions in the Intermountain West is beyond the ~10 day horizon of weather forecast models.

A number of studies (*e.g.*, Weickmann *et al.* 1985; Mo 1999) suggest that the ISO in North America is an atmospheric response to diabatic heating anomalies associated with the Madden-Julian Oscillation (MJO; Madden and Julian 2005). Empirical and dynamical forecasts of the MJO exhibit skill at lead times beyond two weeks, including the operational Climate Forecast System (CFS; Saha *et al.* 2006) of the National Centers for Environmental Prediction (NCEP) which has demonstrated credible skill in predicting the MJO circulations as far out as one month (Seo *et al.* 2007, 2009). Additionally, the CFS shows similar skill in forecasting west coast winter rainfall events (Jones *et al.* 2009). Such circumstances, together with the inversion-ISO relationship observed in GWB, imply that the CFS may exhibit potential in predicting the inversion development with a lead time beyond that of ~10 days. These circumstances lead us to undertake an investigation of the CFS's performance skill in predicting persistent inversions for Salt Lake City, Utah.

2. Data sources and the inversion-ISO relationship

For each predicted period, the CFS hindcast is initialized from three ensemble means (denoted by μ_1, μ_2, and μ_3) of five consecutive days computed from days 10–14, 20–24 of a particular month, and from days 1-4 of the following month. Observed atmospheric variables were obtained from the NCEP–DOE Global Reanalysis 2 (GR2; Kanamitsu *et al.* 2002). Upper-air soundings at Salt Lake City International Airport (KSLC) were utilized to analyze inversion conditions over the period from December 1980 to February 2008, as identified in GWB. Criteria for deep stable layers were utilized by GWB to classify *surface inversion* with a neutral or increasing temperature profile extending from the ground level up to a certain height (Wolyn and McKee 1989). The dates and classification of inversions are summarized in GWB. Air quality measurements in Salt Lake City were adopted from daily observations of particulate matter of 2.5 micrometers in diameter or smaller (PM2.5) from a Utah Division of Air Quality station (site ID 4-035-3006).

GWB established an index via bandpass filtered KSLC geopotential height at 300 mb (20-40 days; hereafter Z_{30d}), and used the index to conduct a composite analysis for the inversion frequency and PM2.5 concentrations. The composite was made of eight phases that evenly divide the Z_{30d} "index cycle". The

Correspondence to: Robert Gillies, Utah Climate Center, Utah State University, Logan, UT;
E-mail: Robert.Gillies@usu.edu

* Current affiliation: Pacific Northwest National Laboratory, Richland, WA

selection of this 20-40 day spectrum is due to the fact that the North American circulation responds only to the higher-frequency end (~30 days) of the MJO (Mo and Nogues-Paegle 2005). The results of GWB are summarized in Fig. 1 and show that the occurrence of surface inversions and the PM2.5 concentrations in Salt Lake City are profoundly modulated by the ISO which are coherent with the Z_{30d} index. The surface inversion probability (SIP) in Fig. 1 was obtained from the relative frequency of surface inversions at each phase within a full cycle of the Z_{30d} index, through all identified cycles over the 1981-2008 period.

Following GWB, we used the 200-mb Z_{30d} index at KSLC (since the CFS hindcasts do not have data at 300 mb) and derived a second-order polynomial regression to estimate the SIP,

$$SIP = 0.00001\,(Z_{30d})^2 + 0.003\,(Z_{30d}) + 0.237. \quad (1)$$

The SIP regression was derived from the composite mean Z_{30d} at 200mb for each phase from all significantly strong cycles, defined by the one standard deviation criterion in GWB. The obtained SIP was then regressed to estimate the PM2.5 concentration as,

$$PM2.5 = 52.16\,(SIP)^2 + 24.82\,(SIP) + 10.54. \quad (2)$$

Regression models (1) and (2) have the largest R^2 (the proportion of variance explained) values over linear and higher-order models. As an example, the estimated SIP and PM2.5 concentrations during the 2003-04 winter are shown in Fig. 2. A persistent surface inversion event occurred in mid-January 2004

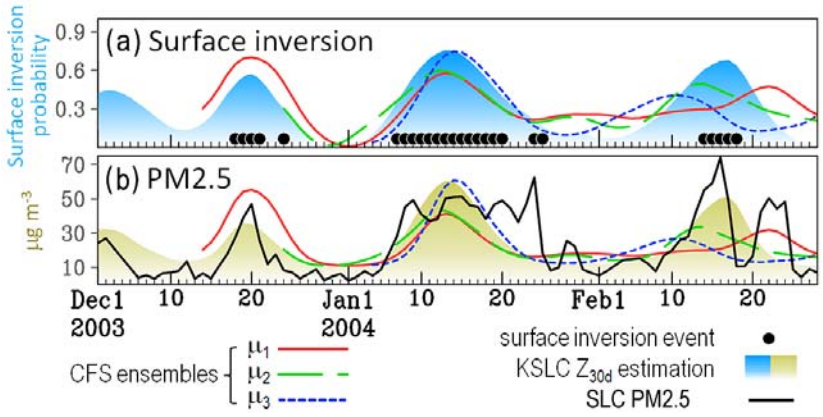

Fig. 2 (a) Estimated surface inversion probability (SIP) from Eq.(1) using the KSLC Z_{30d} at 200 mb (blue shaded curve) overlaid with surface inversion days (dots) during December 2003-February 2004. (b) Estimated PM2.5 concentrations for Salt Lake City from Eq.(2) (green shaded curve) superimposed with the observed PM2.5 concentrations (black line). Three CFS ensembles (μ_1, μ_2, μ_3) are plotted as color lines.

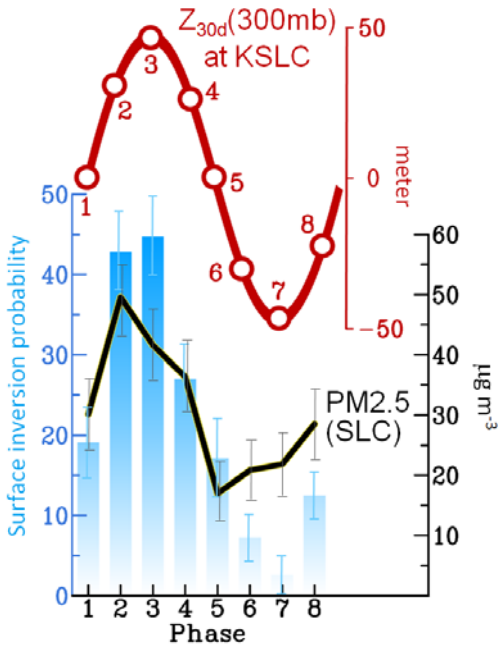

Fig. 1 Composite 300-mb Z_{30d} index at KSLC and the evenly divided 8 phases (red line), probability of surface inversion days (blue bars), and PM2.5 concentrations at the Salt Lake City site (black line). Error bars are added to the probability and PM2.5 fields. Modified from Gillies *et al.* (2010).

that lasted for 14 days (denoted by a sequence of black dots). Two shorter events also occurred around 20 December 2003 and 16 February 2004. The estimated SIP from the KSLC Z_{30d} (blue shaded area) corresponds well with all three persistent surface inversion events, with a higher probability centered around the 14-day event. Moreover, the estimated PM2.5 concentrations (Fig. 2b; yellow shaded area) are in good agreement with observed PM2.5 (black line) and both strongly coincide with the observed persistent surface inversion events. Since Eqs.(1) and (2) use the filtered geopotential height, short-term variations in the inversion and PM2.5 estimates are inevitably smoothed out.

[1] http://www.wrh.noaa.gov/slc/projects/AQ_Briefing/AQ_Briefing.htm

Nevertheless, short inversion events, such as observed on 24-25 January, are coupled with synoptic modes which are not as crucial as the 30-day cycle.

3. CFS prediction skill

To predict the SIP, we constructed the Z_{30d} index using the CFS's 200-mb geopotential height at the grid point nearest to KSLC (112.5°W, 40°N). For each CFS member, two months of the observed (GR2) data prior to the initial day were added to the CFS output before filtering in order to avoid "ends of data" problems associated with the bandpass filter. The predicted SIP from all three CFS ensembles for January 2004 (Fig. 2a) captures the mid-January persistent surface inversion event, but the CFS nearly misses the mid-February event. The predicted PM2.5 concentrations (Fig. 2b) are similar to the estimated ones, indicating that the CFS exhibits reasonable skill in predicting the ISO for up to one month. Thus, forecast skill for the synoptic circulation pattern was assessed by calculating the spatial correlation between the CFS and the verifying values of the GR2. For the domain defined as 150°-80°W and 20°-65°N (over western North America), correlations computed between the CFS hindcast and the GR2 for December, January, and February from 1981 to 2008 are shown in Fig. 3a: The CFS correlation skills are positive beyond seven weeks of lead time. Using a threshold of 0.5 for the correlation skill, as was used in Seo et al. (2009), the CFS appears to predict the synoptic pattern that pertains to persistent inversion events for up to about four weeks.

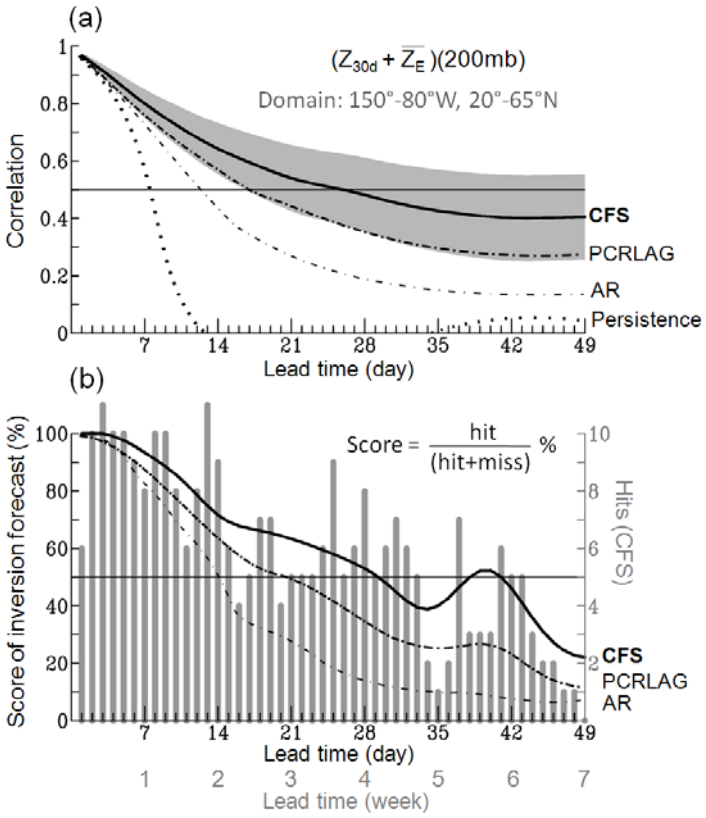

Fig. 3 (a) Spatial correlation of the 200-mb geopotential height as a function of forecast lead time for the CFS, PCRLAG, AR, and Persistence forecasts. The shaded area outlines one standard deviation of the CFS skill. (b) Scores of persistent surface inversion forecasting (lines) for the CFS, PCRLAB and AR, superimposed with the number of hits of persistent surface inversion events by the CFS (gray bars). The computation was performed for DJF over the 28-yr (1981-2008) period.

The CFS forecast skills were compared with various empirical forecast skills, including a principal component (PC)–lagged regression model (PCRLAG) which uses the first two PCs of the filtered geopotential height at 200 mb, an auto-regression (AR) model with the filtered geopotential height at each grid point, and the Persistence forecast. We used three months of the GR2 data prior to the initial day of each ensemble and applied these to the empirical forecasts. As shown in Fig. 3a, the CFS skill is consistently greater than all other competing forecasts.

Next, we evaluated the CFS's prediction of persistent surface inversion events by averaging the composite SIP during peak ISO phases 2-4 (see Fig. 1), which yields a value of 35%, and subsequently used this 35% as the threshold SIP in the prediction of persistent surface inversion events. Such events were defined as any consecutive four days of surface inversions. On either the second or the third day of a persistent surface inversion event (events identified in GWB), if the predicted SIP is greater than or equal to 35% then this event was defined as a "hit"; otherwise the event was a "miss". For any persistent surface inversion event lasting longer than four days, the hits and misses were computed independently within each 4-day period. For instance, a 7-day persistent surface inversion event would be evaluated as four individual 4-day events. After obtaining such hits and misses we constructed a simple score,

$$\text{Score} = \frac{\text{hit}}{(\text{hit} + \text{miss})}\%, \qquad (3)$$

to evaluate the CFS's forecast skill for predicting persistent surface inversion events via Eq.(1).

Figure 3b shows the number of hits (histogram) and the score (time series) of the CFS prediction with respect to lead time. The CFS's score exhibits a similar downward tendency but remains above 50% until week 4 and rising again to above 50% near week 6. Such prediction skill is consistent with the 2004 case in which the CFS successfully predicted the persistent surface inversion events out to five weeks (*cf.* red line in Fig. 2a), yet barely predicted the mid-February event with a similar lead time (*cf.* blue dashed line in Fig. 2a). Such forecasts echo the 50% skill scores between weeks 5 and 6 in Fig. 3b. Nevertheless, skill scores of the CFS are consistently higher than those obtained from the empirical models, suggesting that the CFS offers a better forecast of persistent surface inversion events with a 4 week lead time. Such a skill greatly surpasses the current inversion prediction procedure that relies on weather forecast models. Moreover, since Eq.(2) is practically a function of Eq.(1), the results also indicate an extended predictability of prolonged, high concentration events of PM2.5 by the CFS.

4. Summary

How does the CFS's skill in capturing the MJO contribute to its skill in predicting the midlatitude circulations over western North America? To investigate, the circulation responses to the MJO were analyzed through a compiled composite of the 200-mb streamfunction and velocity potential, following the eight phases of the Z_{30d} index at KSLC (*cf.* Fig. 1). Each phase covers three days centered on the second day (dates of the composite are identical to those analyzed in GWB). Prior to the composite analysis, the streamfunction and velocity potential were bandpassed

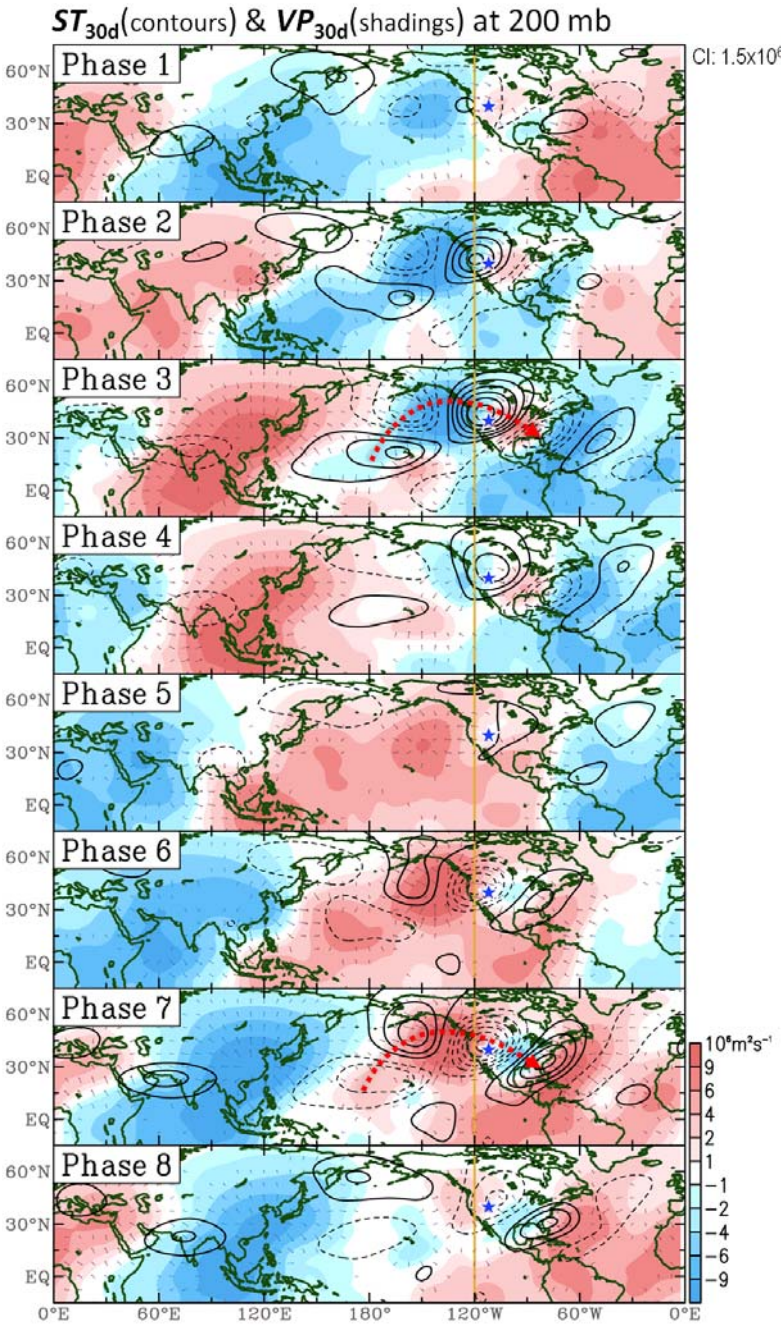

Fig. 4 Composite eight phases of the 200-mb Z_{30d} index at KSLC in terms of the filtered streamfunction (ST_{30d}, contours) and velocity potential (VP_{30d}, shadings) at 200 mb superimposed with the divergent winds (vectors; above the 10% significance level). The calculation was based on the 28-yr GR2 data. The contour interval (CI) of ST_{30d} is 1.5×10^6 m^2 s^{-1} while zero contours are omitted. The golden line at 120°W indicates the approximated position of the winter mean ridge. The ST_{30d} wave train is illustrated by a red dashed arrow at Phases 3 and 7.

with 20-40 days, denoted respectively as ST_{30d} and VP_{30d}. As shown in Fig. 4, the eight phases of the composite depict a clear eastward propagation of VP_{30d} with predominant zonal wavenumber-1 patterns. Embedded in this typical MJO structure is a series of short-wave VP_{30d} cells across the northeast Pacific Ocean and North America. These regional short wave cells are accompanied by similarly definite, yet spatially in-quadrature, wave trains of ST_{30d}. At phases 2-3 when the SIP in Salt Lake City is elevated, the ST_{30d} wave trains appear to follow the classic "great circle" route leading to a prevailing ridge in western North America. An oppositely signed circulation anomaly is also evident at phases 6-7. Despite the pronounced eastward propagation of global VP_{30d}, the regional wave trains of both VP_{30d} and ST_{30d} appear quasi-stationary.

Such a feature underscores the fact that the semi-permanent ridge over western North America fluctuates in response to the tropical–extratropical linkages of the MJO. These results strongly suggest that the occurrence of persistent inversions in the Intermountain West is "phase locked" with the MJO evolution. As a result, the CFS's documented skill in predicting the MJO likely assists in predicting the circulation systems that lead to persistent inversions. In addition, past studies of the MJO prediction have noted that forecast skill of precipitation typically declines faster than atmospheric circulation. This is attributable to precipitation's sensitivity to high-frequency weather disturbances which have little long term predictability. The proposed regression scheme with the CFS output, to predict persistent surface inversion events in the Intermountain West, may bear relatively high skill also because such inversion events are coupled with slow-moving circulation patterns (*i.e.* ridges) in contrast to unstable, highly variable precipitation systems (such as fronts).

References

Gillies, R. R., S.-Y. Wang, and M. R. Booth, 2010: Atmospheric scale interactions on wintertime Intermountain inversions. *Wea. Forecasting*, 25, 1196–1210.

Horel, J. D., and C. R. Mechoso, 1988: Observed and simulated intraseasonal variability of the wintertime planetary circulation. *J. Climate*, **1**, 582–599.

Jones, C., J. Gottschalk, L. Carvalho, and W. Higgins, 2009: Probabilistic forecast skill of extreme weather in weeks 1-4 in the United States during winter. 34th Annual Climate Diagnostics and Prediction Workshop. Monterey, CA, October 26-30, 2009.

Kanamitsu, M., W. Ebisuzaki, J. Woollen, S.-K. Yang, J. J. Hnilo, M. Fiorino, and G. L. Potter, 2002: NCEP/DOE AMIP-II reanalysis (R-2). *Bull. Amer. Meteor. Soc.*, **83**, 1631-1643.

Lau, N. C., and M. J. Nath, 1999: Observed and GCM-simulated westward-propagating, planetary-scale fluctuations with approximately three-week periods. *Mon. Wea. Rev.*, **127**, 2324–2345.

Madden, R. A., and P. R. Julian, 2005: Historical perspective, *Intraseasonal Variability in the Atmosphere-Ocean Climate System*, K.-M. Lau and D. E. Waliser Eds., Springer, pp 1-16.

Mo, K. C., 1999: Alternating wet and dry episodes over California and intraseasonal oscillations. *Mon. Wea. Rev.*, **127**, 2759–2776.

____, and J. Nogues-Paegle, 2005: Pan-America, *Intraseasonal Variability in the Atmosphere-Ocean Climate System*, K.-M. Lau and D. E. Waliser Eds., Springer, pp 95-124.

Saha S., Coauthors, 2006: The NCEP Climate Forecast System. *J. Climate*, **19**, 3483–3517.

Seo, K.-H., J. K. E. Schemm, W. Wang, and A. Kumar, 2007: The boreal summer intraseasonal oscillation simulated in the NCEP Climate Forecast System: The effect of sea surface temperature. *Mon. Wea. Rev.*, **135**, 1807–1827.

____, W. Wang, J. Gottschalck, Q. Zhang, J. K. E. Schemm, W. R. Higgins, and A. Kumar, 2009: Evaluation of MJO forecast skill from several statistical and dynamical forecast models. *J. Climate*, **22**, 2372–2388.

Weickmann, K. M., G.R. Lussky, and J.E. Kutzbach, 1985: Intraseasonal (30–60 Day) fluctuations of outgoing longwave radiation and 250 mb streamfunction during Northern winter. *Mon. Wea. Rev.*, **113**, 941–961.

Wolyn, P.G., and T.B. McKee, 1989: Deep stable layers in the Intermountain Western United States. *Mon. Wea. Rev.*, **117**, 461–472.

Science and Technology Infusion Climate Bulletin
NOAA's National Weather Service
35th NOAA Annual Climate Diagnostics and Prediction Workshop
Raleigh, NC, 4-7 October 2010

Forecast Meteorological Drought Based on the Standardized Precipitation Index

Jin-Ho Yoon[1], and Kingtse Mo[2]

[1]*Pacific Northwest National Laboratory, Richland, WA*
[2] *Climate Prediction Center, NCEP/NWS/NOAA, Camp Springs, MD*

1. Introduction

Drought and persistent wet spells are costly disasters in the United States. Losses are easily in the tens of billions. If drought can be predicted a few months in advance, then the losses can be reduced. In the recent decade, advances have been made in hydrologic prediction of streamflow and soil moisture by using climate forecasts at seasonal lead times (Wood and Lettenmaier 2006; Luo *et al.* 2007). In this present work, we will extend the hydrologic prediction to cover the meteorological drought measured by precipitation (P) deficits based on the CFS forecasts. The meteorological drought is often measured by the standardized precipitation index (SPI) (Hayes *et al.* 1999). The advantage is that it is a function of precipitation alone and can be applied to both station and gridded data.

The impacts of drought are regional. Therefore, drought assessment and prediction need to be at as high as the local County level. Because the atmospheric model for the CFS has the horizontal resolution of T62 which is approximately 250 km, it is too coarse for this purpose. To provide regional drought information, spatial downscaling is needed. In general, there are two categories of downscaling techniques (Wilby and Wigley 1997). One is statistical downscaling based on the historical relationship between global model hindcasts and high-resolution observation, and the other one is dynamic downscaling method using limited area, high-resolution models.

In this study, four statistical downscaling methods were tested. The statistical downscaling methods will be compared with the dynamic downscaling based on the NCEP regional spectral model (RSM) (Juang and Kanamistu 1994, Juang *et al.* 1997) for April-May initial conditions. They are also compared with the CFS T382 model forecasts directly.

2. Data sources and procedure

Monthly mean time series of P are obtained from the CFS hindcast archive (Saha *et al.* 2006). Hindcasts monthly means have 15 members for the period from 1982 to 2008. The NCEP RSM (Juang et al. 1997) is a regional spectral model with similar dynamic core and same physics package to the NCEP GFS. Lateral boundary condition is obtained from the CFS forecasts every 6 hours. The spatial resolution of the NCEP RSM is 50 km and 5 members initialized from 29April to 3 May each year. High-resolution coupled global climate model (CGCM) was the operational version of the 2007 GFS model with T382L64 resolution coupled with the GFDL MOM 3 ocean model. The high resolution hindcasts were initialized from 19-23 April each year from 1981 to 2008. There are 5 members in the ensemble. The ensemble mean is the equally weighted mean of five members. The observed P data set used in this study is the CPC unified P analysis (Xie *et al.* 2010). The spatial resolution is 50-km. It covers the period from 1950 to present. For verification, the monthly mean P anomaly is defined as the departure from the monthly mean climatology from 1981-2008 for that month.

The downscaled P and SPI are cross validated for our analysis period from 1981 to 2008. Hindcasts with initial conditions from October-November, January-February, April-May and July-August were evaluated. The cross validation was done for each lead time and each set of initial conditions separately with both anomaly correlation (AC) and the root mean square error (RMSE). In validation process, we exclude the target year.

Correspondence to: Jin-Ho Yoon, Pacific Northwest National Laboratory, Richland, WA;
E-mail: Jin-Ho.Yoon@pnl.gov

3. Precipitation downscaling and bias correction

a) Bilinear interpolation (BI)

The precipitation anomaly P_a (T_y, τ, M) for month M, target year T_y and lead time τ is defined as the departure from the model climatology averaged over the ensemble means of hindcasts for the same lead time τ from the training period. The hindcasts at year T_y were not included in the climatology. We bilinearly interpolated P_a (T_y, τ, M) to a 50-km grid. It should be verified against the observed P anomaly at month τ - 1+M and year T_y.

Figure 1 shows an example of hindcast anomaly at τ =1 for November 1988. November 1988 was a cold El Nino Southern Oscillation (ENSO) month. The BI downscaling P hindcast captures the ENSO signal well, but the magnitudes of anomalies are too weak to be useful and cannot capture terrain related features over the Pacific Northwest. But this BI method can be used as a building block and reference for other methods. One potential shortcoming of correcting model's climatology is that the corrected total precipitation can be negative when the model climatology is much wetter than the observed climatology.

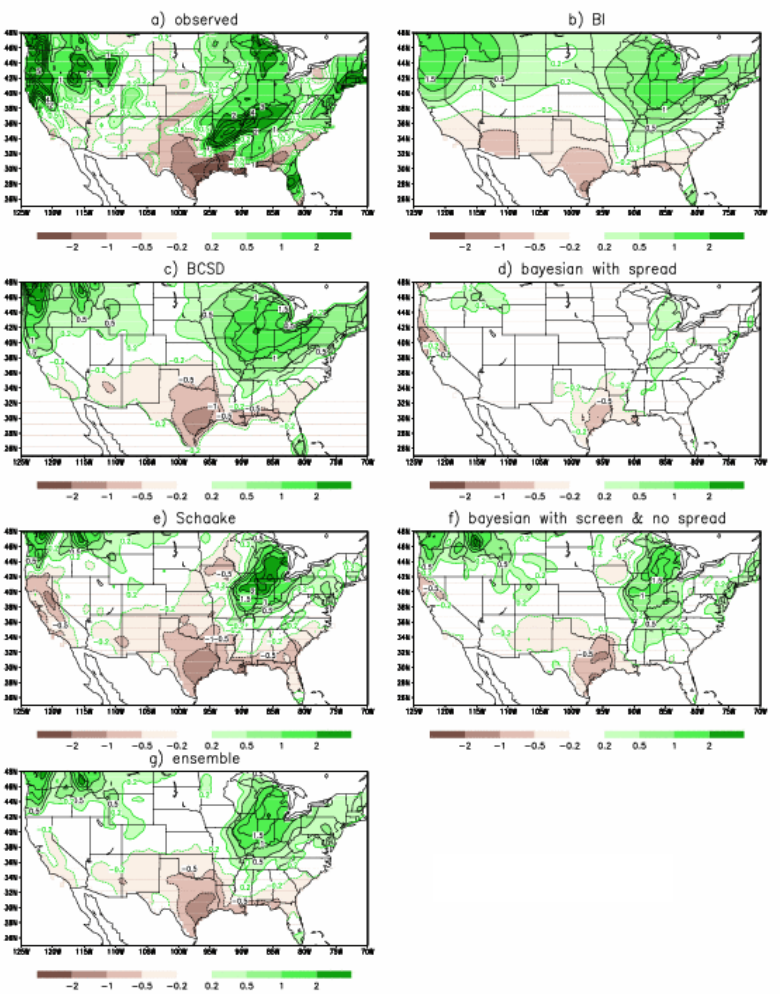

Fig. 1 (a) 1988 November precipitation anomaly from the P analyses. Contour interval is 1 mm day^{-1}. Contours -0.5 -0.2, 0.2 and 0.5 mm day^{-1} are added. November P forecast at 1 month lead produced by downscaling from the T62 CFS forecasts with (b) Bilinear interpolation (BI), (c) BCSD, (d) Bayesian method including spread, (e) Schaake linear regression, (f) Bayesian method without spread and with screening the CFS forecasts, and (g) same as (f), but the multi-method ensemble mean of (c), (e), and (f). Contour interval in (b)-(g) is 0.5 mm day^{-1}. Contours -0.2 and 0.2 mm day^{-1} are added. Zero contours are omitted.

b) Bias correlation and spatial downscaling (BCSD)

Before applying BCSD, all P hindcasts were bilinearly interpolated to the 50-km grid first. For the month M and lead time τ, to modify P (T_y, τ, M) for the target year T_y, the Cumulative Distribution Function (CDF) was computed at each grid point using all ensemble members with the lead time τ based on CFS hindcasts in the training period. At each grid point, the percentile of P (T_y, τ, M) for the target year T_y was determined according to the CDF (hindcast). Given the same percentile, we computed P backward from the CDF (obs). In comparison to BI, the BCSD method corrects both the mean and the standard deviation of the ensemble hindcasts in the normal space. The hindcasts have higher amplitudes and they are terrain adjusted. Because of its simplicity and robustness in correcting terrain related features, this method has been applied in hydrologic forecast application (Wood *et al.* 2002).

c) Schaake linear regression method (Schaake method)

The BCSD method does not take into account of the forecast skill of hindcasts. Both the Schaake method and the Bayesian method do. For the Schaake method, the idea is to use a simple linear regression to calibrate

raw hindcast ensembles in the normal space for hydrologic prediction (Wood and Schaake 2008). The first part of the procedure is the same as the BCSD. Difference is to consider correlation between hindcasts and analyses. For November 1988, anomalies from the Schaake method (Fig.1e) have the similar pattern as anomalies downscaled with BCSD, but there are certain differences. It shows some improvements over the Great Lake area. Negative anomalies over Northern California, which are not verified, illustrate the weakness of this method. The negative anomaly is caused by the negative correlation. In reality, it is unlikely that the forecasts and the corresponding observations are systematically opposite in sign.

d) Bayesian merging

The methodology is described in details in Luo *et al.* (2007). Bayes' theorem updates the probability distribution on P based on the hindcasts in the training period. Computation is similar to the Schaake method. But, it uses Bayes' theorem to update probability distribution of forecast based on the likelihood function, which is determined by least square fit of the ensemble mean hindcasts to the corresponding observation (Coelho *et al.* 2004, Luo *et al.* 2007). For the multi-model ensemble forecasts, the Bayesian merge will adjust the distribution function by weighting the skill of the hindcasts from different models and the spread of forecasts accordingly (Luo *et al.* 2007). For the unskillful forecasts, the distribution function will be close to observed P, just like Schaake method. The spread among members of CFS hindcasts are very large because the CFS hindcasts have low skill especially in midlatitudes over a small domain (Luo and Wood 2006). Another reason is that initial conditions for members in the CFS hindcast ensemble are far apart, up to 30 days. If spread is used, then the P anomalies after the Bayesian merging are very weak. For example, the 1988 November forecast for one month lead (Fig. 1d) shows a similar pattern as BI (Fig.1b), but the magnitudes are very weak. Therefore, the spread is not used in our present study. Instead of using spread, we eliminate members in the ensemble that are very different from the ensemble mean before applying the Bayesian method. For the 1988 November case (Fig. 1f), amplitudes of anomalies are higher than those with spread (Fig. 1d). If we do not screen forecasts, the skill is on average lower. In this work results are given for the Bayesian method without spread but with screen.

e) Multi-method ensemble

All three downscaling methods have advantages and disadvantages. They also show skill in different areas during different seasons. Therefore, we can form a multi-method ensemble as the equally weighted mean of hindcasts treated by BCSD (Fig. 1c), Bayesian (Fig. 1f) and Schaake methods (Fig. 1e). Fig. 1g shows the example of the 1988 November hindcast with one month lead. It is terrain adjusted and has comparable amplitudes as hindcasts downscaled with BCSD.

4. The SPI prediction

a) Method

The computation of the SPI is based on Mckee et al. (1993, 1995). The procedures to forecast SPI from month M and year T_y out to the lead time τ is outlined in Fig. 2. We explain in detail by using the 1988 November case as an example.

1. Obtain the monthly mean observed P climatology for the base period T_y -30 to T_y. For 1988 November forecasts, the base period is from 1957 to 1987. One can easily extend the base period to longer period. The only limitation is the record length of historical observational data.
2. Add the observed monthly mean P climatology from the base period to the downscaled forecast P anomaly from lead month τ (τ =1 - 9). For 1988

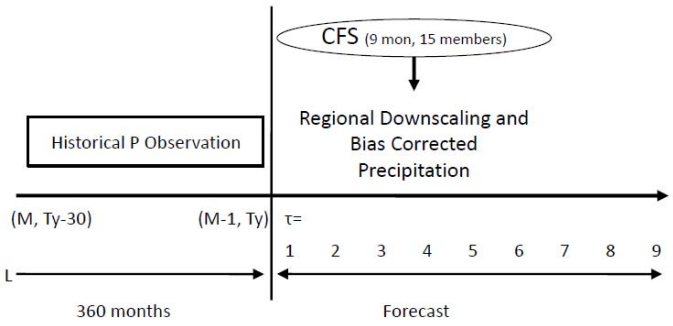

Fig. 2 A schematic diagram of SPI forecast procedure.

November forecasts, the first lead month is November so the November climatology is added to the downscaled P anomaly.

3. The forecast time series then is appended to the observed P time series which covers the period from year T_y -30 month M to year T_y month M-1. For November 1988, the observed time series lasts from 1958 November to 1988 October and followed by forecast time series.
4. Compute SPI from this combined time series.

The important point is that observed P data set after year T_y is not used because the information will not be available in the actual forecast situation. By definition, the one-month lead SPI6 has P which contains 5 months observed P and one month forecast. Therefore, for the first few month lead, the SPI6 forecasts are expected to be skillful, with analogy to influence from initial condition in the land/hydrologic forecast system. Figure 3 shows anomaly correlation (AC) in space and root mean square error (RMSE) of SPI6 hindcasts averaged over the U.S. as a function of the lead time for hindcasts initialized in four different seasons. When SPI6 at a give time is below (above) the threshold -0.8 (0.8), it is classified as extreme dry (wet) event. If we use this criterion, then SPI6 forecasts are on average skillful up to the lead time of 4 months. The winter forecasts are more skillful than summer in general. There is no statistical significant difference in skill for forecasts downscaled with different methods for the first 4 months when forecasts are skillful. After 4 months, the forecasts are unskillful so differences in skill among different downscaling methods do not matter much.

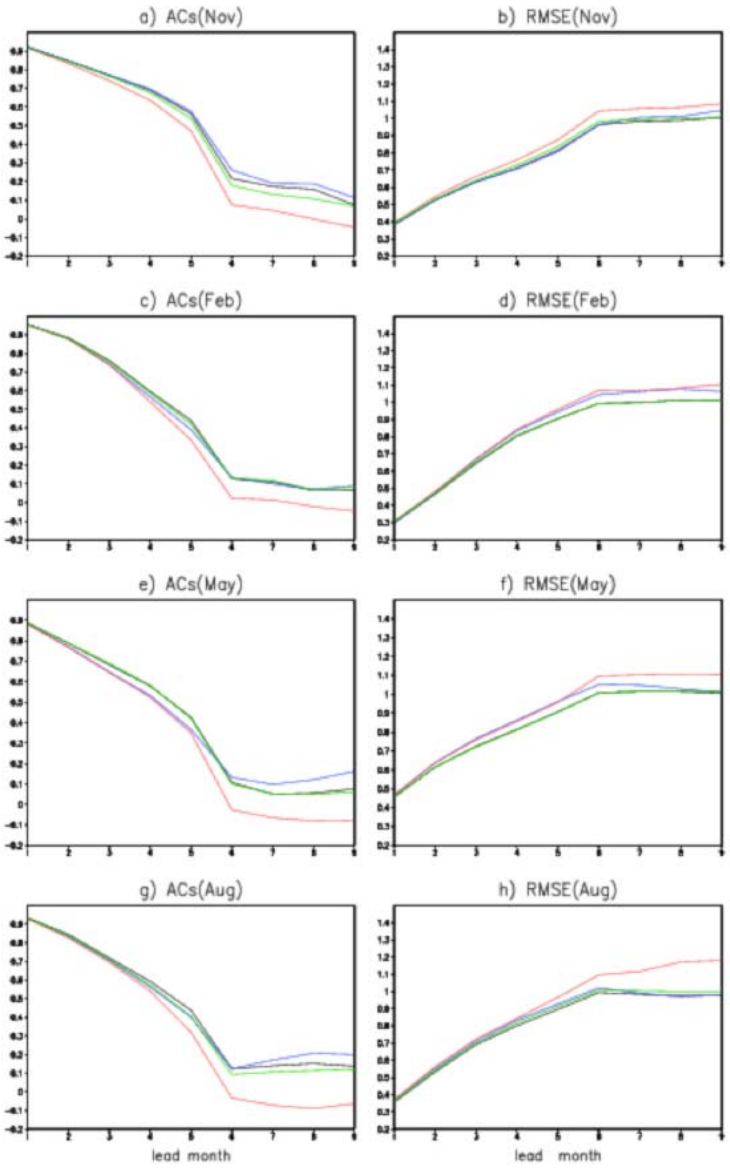

Fig. 3 (a) Anomaly correlation of SPI6 as a function of the lead time for initial conditions in (a) October-November, (c) January-February, (e) April-May, and (g) July-August. SPI6 is derived from P forecasts produced by downscaling with the BCSD (blue), Schaake linear regression (red), Bayesian (green) and multi-method ensemble (black). (b), (d), (f), and (h) are the same as (a), (c), (e), and (g), but for RMSE, respectively.

To show the forecast skill for SPI6 from P downscaled with different methods in regional details, the RMSE for forecasts initialized in April-May is given in Fig. 4. This set of forecasts is chosen because they have the lowest skill in comparison with forecasts initialized in other months (Fig. 3). For the first two lead months, skill is comparable. They all show that forecasts are more skillful over the Southeast. Over the West coast and the Southwest, spring is not their rainy season so low RMSE is expected. For May to June, raining season starts over the Great Plains. The forecast skill decreases along 100°W-115°W. After 3 months, forecasts over the Great Plains become less skillful. Among three different methods, the forecasts downscaled with Bayesian deteriorate slower than the BCSD or the Schaake linear regression method.

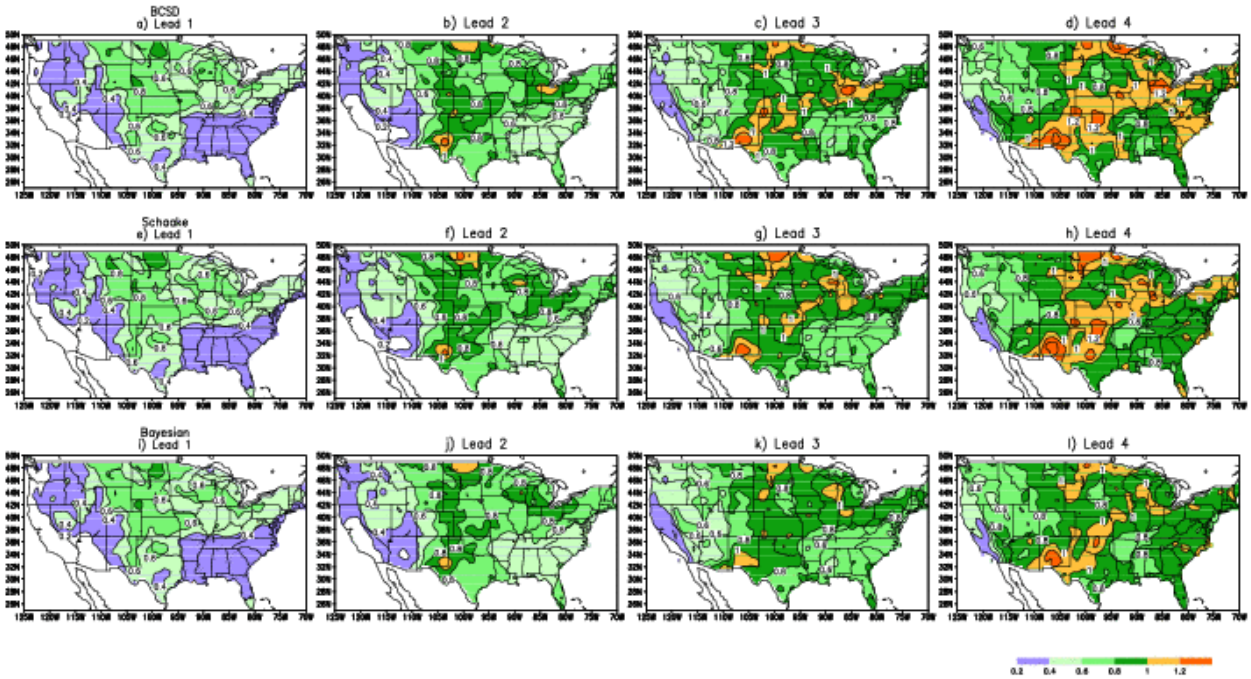

Fig. 4 Spatial pattern of RMSE for SPI6 forecast in function of lead time. Forecast initialized from April-May with three different methods are displayed: BCSD in (a)-(d), Schaake linear regression in (e)-(h), and Bayesian in (i)-(l). First column (a), (e), and (i) shows forecast with the lead time of one month, which is followed by three columns of forcast (from left to right) with the lead time of 2, 3 and 4 months, respectively.

5. Forecasts from the NCEP RSM and the CFS T382 model

In this section, we compare hindcasts from statistical downscaling with dynamic downscaling with the NCEP RSM and hindcasts from a T382 model directly. Only Hindcasts initialized in April-May are available from the high resolution T382experiments.

a) NCEP RSM

The 50-km RSM is nested in the CFS hindcasts to produce downscaled precipitation. The boundary conditions from the CFS were given every 6 hours. The initial conditions were taken from the CFS hindcasts initialized from the period 28 April to 3 May each year in this study. For May P forecasts, the correlation between the P anomalies and the corresponding observations indicates that the RSM downscaled hindcasts (Fig. 5a) are overall more skillful than the 15 member ensemble downscaled with BCSD (Fig. 5c). It is noted that the skill comes from the initial conditions, because the RSM members are the youngest members in the ensemble initialized at the end of April or early May. If the RSM downscaled forecasts are compared with the same 5 youngest members in the ensemble downscaled with BCSD, then skill is more comparable (Fig. 5e). For lead times longer than one month when the influence of initial conditions diminishes, the differences between the dynamic downscaled and the statistical downscaled hindcasts are small. The differences in skill for the SPI6 forecasts are also small (Fig. 5b and 5d). The overall RMSE of SPI6 forecasts shows that the RSM forecasts have comparable skill with the 15 member ensemble downscaled with BCSD and slightly more skillful than the CFS with 5 youngest members after the first month. (Fig. 5f)

b) CFS T382 model

For CFS T382 forecasts, there are five members initialized from April 19-23 each year for the period of 1982-2008. The overall skill is slightly worse than the 15 member ensemble CFS forecasts downscaled with BCSD (Figs. 6a and c). However, it is comparable in skill in comparison with the 5 member ensemble with the same initial conditions (Fig. 6e). This indicates again for the first month, the initial conditions are important. The interesting point is that forecasts from T382 are worse than from the RSM (Fig. 5a). For SPI6,

the T382 forecasts are more skillful than the T62 forecasts with the same initial conditions after downscaled with BCSD. However, they are not as skillful as the 15 member CFS forecasts after statistical downscaling (Fig. 6f).

6. Conclusion

The Standardized Precipitation Index (SPI) has been used routinely to classify the meteorological drought by national and international forecast centers and authorities. Based on the P seasonal forecasts from the NCEP CFS, a method is developed to forecast SPIs to predict the meteorological drought over the United States. Before predicting SPI, the P forecasts from a coarse resolution global model CFS are downscaled and bias-corrected to a regional 50-km grid. Four different methods of statistical downscaling and error correction are tested, which are: (1) bilinear interpolation (BI), (2) a bias correction and spatial downscaling based on the probability distribution functions (BCSD), (3) a linear regression method by Schaake (Schaake) and (4) the Bayesian method used by the Princeton University group and the EMC/NCEP. We tested cases with initial conditions in October-November, January-February, April-May and July-August. Because drought means persistent dry conditions, we are interested in 6-month SPI (SPI6) and short term drought measured by 3-month SPI (SPI3).

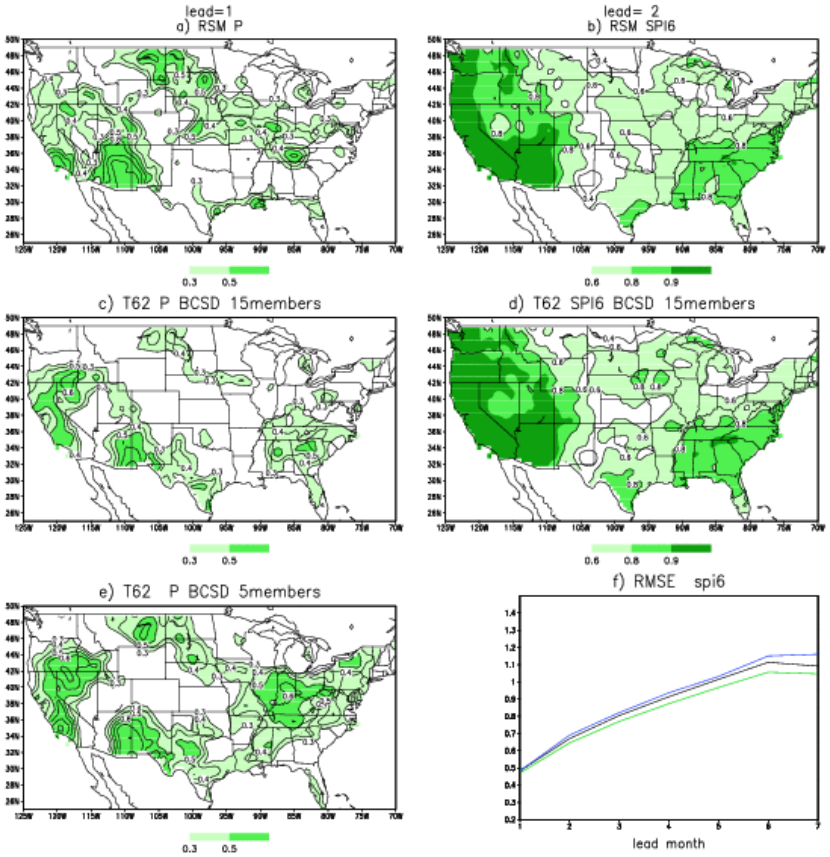

Fig. 5 (a) Correlation between P forecasts from the NCEP RSM five member ensemble and the corresponding P analysis for forecasts initialized in 28 April – 3 May each year. Contour interval is 0.1. Values less than 0.3 are omitted. (b) same as (a), but for 2 month lead SPI6 derived from the RSM forecasts, (c) same as (a), but for the downscaled T62 CFS P forecasts from 15 member ensemble downscaled based on BCSD, (d) same as (b), but for SPI6 forecasts derived from (c) , (e) same as (c), but for 5 members initialized at late April and early May, (f) RMSE for SPI6 forecasts averaged over forecasts from 1982-2007 and averaged over the United States. SPI6 were derived from P from the RSM (black), the 15 member ensemble downscaled T62 CFS forecasts initialized from April-May using the BCSD method (green) and from the 5 member T62 forecasts initialized from late April and early May using the BCSD method (blue).

The skill is regionally and seasonally dependent. Overall, the 6 month SPI is skillful out to 3-4 months. For the first 3 month lead times, there is no statistical significant difference among different methods of downscaling. After 4 months, forecasts downscaled with Schaake method have slightly less skill and forecasts downscaled by Bayesian deteriorate slower than others. Overall, the multi-method ensemble has the best skill. For P downscaling, the simple BCSD method does well. This implies that the systematic errors of the CFS forecasts are in the mean and the standard deviation which are largely caused by the terrain. The Schakke method did well only if the CFS forecasts are skillful. The occasional negative correlation between the hindcasts and the corresponding observations hurts forecast skill because this is not a systematic feature of forecasts. Bayesian method does not stand out in this comparison because the CFS forecasts have low skill and large ensemble spread. Even though the spread is not included here, the method still tends to dump to

climatology. The multi-method ensemble has the best skill because forecasts with different downscaling methods show skill in different locations, so the average has an advantage.

The NCEP RSM and the CFS T382 model have comparable skill with statistical BCSD downscaling. For the first month, the initial conditions dominant, the ensemble with 5 youngest members has the best skill. After the first month, ensemble with 15 members has a slight edge. Large number of ensembles or better initial conditions could reduce potential forecast errors. The importance of initial conditions suggests the needs to have better observational system and better data assimilation schemes.

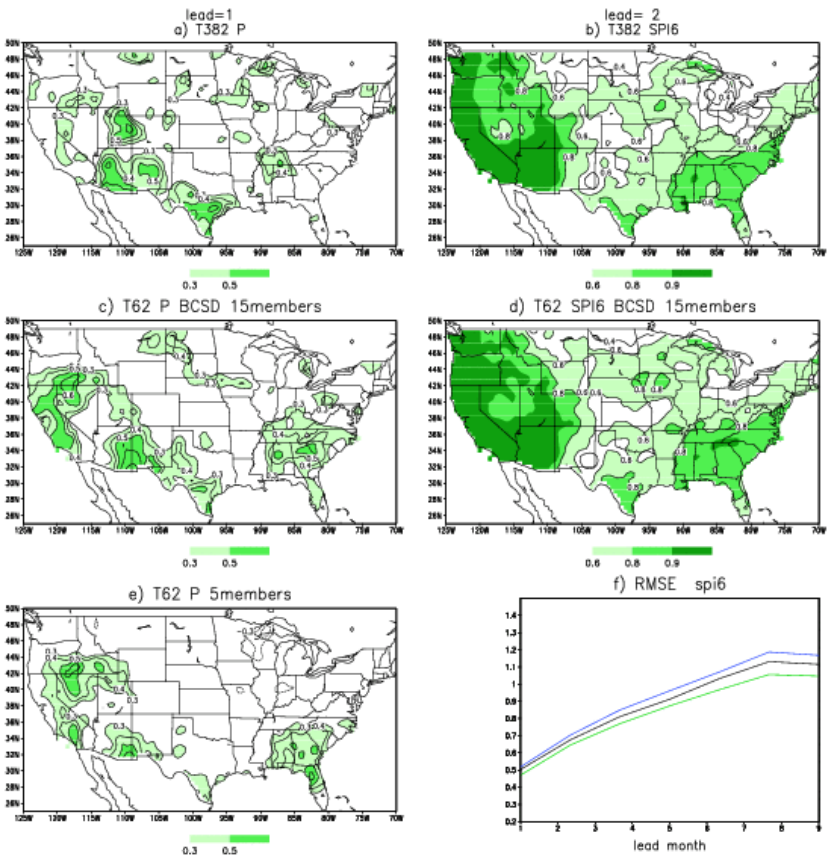

Fig. 6 (a)-(d) same as Fig.5 (a)-(d), but for five member ensemble forecasts from the high resolution CFS T382 model, (e) same as (c), but with 5 members T62 forecasts initialized from 15-20 April each year , (f) RMSE for SPI6 forecasts averaged from 1982-2007 for the United States. SPI6 were derived from the T382 P forecasts (black), the 15 member ensemble T62 forecasts initialized from April-May after BCSD downscaled using the BCSD method (green) and from the 5 member downscaled T62 forecasts initialized in mid-April using the BCSD method (blue).

References

Coelho, C. A. S., S. Pezzulli, M. Balmaseda, E. J. Doblas-Reyes and D. B. Stephenson 2004: Forecast calibration and combination: A simple Bayesian approach for ENSO. *J. Climate*, **17**, 1504-1516.

Hayes, M. J., M. D. Svoboda, D. A. Wilhite and O. V. Vanyarkho, 1999: Monitoring the 1996 drought using the standardized precipitation index. *Bull. Amer. Meteor.Soc.,* **80,** 429-438.

Juang H. M. H., and M. Kanamitsu 1994:The NMC nested regional sprectral model. *Mon. Wea. Rev.,* **122**, 3-26.

—, S. Y. Hong and M. Kanamitsu 1997: The NCEP regional spectral model: an update. *Bull. Amer. Meteor. Soc.,* **78**, 2125-2143.

Luo. L., E. F. Wood, and M. Pan 2007: Bayesian merging of multiple climate model forecasts for seasonal hydrological predictions. *J. Geophys. Reg.*, **112**, D10102, doi:10.1029/2006JH007655.

—, and E. F. Wood 2006: Assessing the idealized predictability of precipitation and temperature in the NCEP Climate Forecast System. *Geophy. Res. Let.*, **33**, doi:10.1029/2005GL02592.

McKee, T. B., N. J. Doesken, and J. Kleist, 1993: The relationship of drought frequency and duration to time scales. Preprints, *English Conf. on Applied Climatology*, Anheim, CA, Amer. Meteor. Soc., 179-184.

—, —, and —, 1995: Drought monitoring with multiple time scale. Preprints, *Ninth Conf. on Applied Climatology*, Dallas, TX, Amer. Meteor. Soc., 233-236.

Saha, S. and co-authors 2006: The NCEP climate forecast system. *J. Climate,* **19**, 3483-3517.

Wilby, R. L., and T. M. L. Wigley, 1997: Downscaling general circulation model output: a review of methods and limitations. *Progress in Physical Geography*, **21(4)**, 530-548.

Wood, A. W.,and D. P. Lettenmaier 2006: A test bed for new seasonal hydrologic forecasting approachs in the western United States. *Bull. Amer. Meteor. Soc.* 87, 1699-1712.

Xie, P. P., M. Chen, and W, Shi , 2010: CPC unified guage based analysis of global daily precipitation. AMS 24th Conf. on hydrology. Jan 18-21, 2010, Atlanta, Ga.

Science and Technology Infusion Climate Bulletin
NOAA's National Weather Service
35th NOAA Annual Climate Diagnostics and Prediction Workshop
Raleigh, NC, 4-7 October 2010

Seasonal Predictability of the Atlantic Warm Pool in the NCEP CFS

Vasubandhu Misra[1, 2] and Steven Chan[2]

[1]*Department of Meteorology, Florida State University, Tallahassee, FL*
[2]*Center for Ocean-Atmospheric Prediction Studies, Florida State University, Tallahassee, FL*

1. Introduction

The Atlantic Warm Pool (AWP) is considered as a potential source of seasonal predictability in the western hemisphere during the boreal summer season (Wang and Enfield 2003; Wang *et al.* 2006). In addition, it is suggested that the interannual variation of the AWP area is independent of El Niño Southern Oscillation (ENSO) variability in the eastern Pacific Ocean (Wang *et al.* 2006). This feature also encourages the exploration of the AWP as a potential alternative source of boreal summer season predictability in the western hemisphere.

This study is aimed at understanding the seasonal predictability of the AWP in the National Centers for Environmental Prediction (NCEP) Climate Forecast System (CFS). NCEP has provided the community with an extensive set of seasonal hindcasts from its CFS (Saha *et al.* 2006), which provides an opportunity to analyze the predictability of the AWP. Furthermore, Misra *et al.* (2009) showed that the NCEP CFS has a reasonable climatology of the AWP. In contrast, many of the Intergovernmental Panel on Climate Change Fourth Assessment Report (IPCC AR4) models showed significant cold bias in the AWP region, which made even defining the AWP difficult (Misra *et al.* 2009).

2. Data

In this study we used 23 years of seasonal hindcast (SH) data (Saha *et al.* 2006) covering the period between 1981-2003. A SH consists of 15 ensemble members (Saha *et al.* 2006), which are initialized from 15 initial conditions that span each month of the year. The length of each SH is 9 months. We specifically examine the SHs that start in the months of January, February, March, April, May, June, and July, because the AWP matures in the July-August-September (JAS) season (Wang and Enfield 2001). These SHs correspond to lead times of 6, 5, 4, 3, 2, 1, and 0 month for the JAS season. We also make use of the long-term NCEP CFS integrations that consist of 4 ensemble members, each integrated to a period of 32 years (Wang *et al.* 2005; hereafter referred as LT). For observations, we use the NOAA Extended Reynolds SST version 3 following Smith *et al.* (2008). When we compare SH with observations, then we match the observation period with the SH. But in comparing with the LT integration we use the modern era of 1958-2008 for observations.

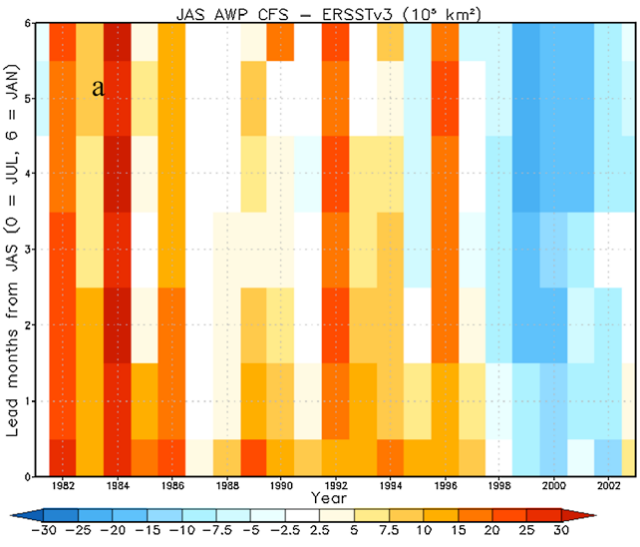

Fig. 1 The JAS seasonal mean errors of the AWP area computed relative to observed SST. (Misra and Chan 2009)

3. Results

a) Seasonal errors

The seasonal AWP error in the SH is shown as a function of lead-time and year in Fig. 1. This figure shows that in many years the seasonal AWP error grows with lead-time. Also, in the period from 1997 to

Correspondence to: Vasubandhu Misra, Department of Meteorology, Florida State University, Tallahassee, FL 32306; E-mail: vmisra@fsu.edu.

2003, the SH displayed an under representation of the AWP area that is largely unprecedented (Fig. 1). This change in sign of the seasonal errors is, we contend, a result of the Atlantic Multi-decadal Oscillation not being properly simulated or initialized in the SH.

The evidence of such a decadal oscillation in the observed SST in the region is clearly evident from Fig. 2. This figure indicates that the linear trend from 1950 to 2003 is relatively small compared to the changing slope of the decadal trends from 1950 to 1981 and 1982 to 2003 in the region, which is also confirmed in other studies (Enfield *et al.* 2001; Kerr 2000). The mean JAS SST climatology for the periods 1982-1996 and 1997-2003 from the observations and the SHs (at 0 lead time for example) are shown in Fig. 3. Clearly, the mean observed SST for the two periods shows significant differences in Figs. 3a and b. In contrast, the SH shows insignificant differences in the seasonal mean climatology between the two periods (Figs. 3c and 3d). The climatological seasonal mean errors of the SH reflect this difference in observations in Figs. 3e and f, which indicates positive SST bias in the 1982-1996 period compared to the negative bias in the 1997-2003 period. This is consistent with Wang *et al.* (2008) who show that the AMO manifestation is also visible in the AWP variations on decadal time scales.

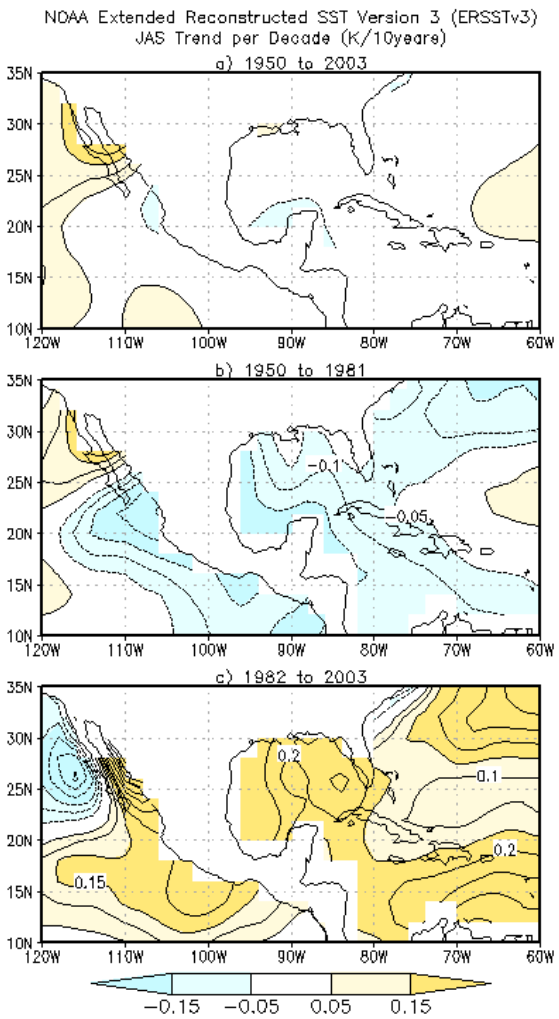

Fig. 2 The observed linear trend (per decade) in the July-August September SST over the period of a) 1950-2003, b) 1950-1981, and c) 1982-2003. (Misra and Chan 2009)

b) Interannual variability

A measure of the deterministic signal to noise ratio is plotted in Fig. 4a as the ratio of the ensemble mean of the AWP area to its ensemble spread (standard deviation about the ensemble mean) as a function of lead time and year of the SH. Here it is seen that for a majority of the years, at short lead times (0 and 1) the ratio is relatively larger than at longer lead times. In 1983, 1987 and 1998, this ratio is relatively large at all lead times, indicating the possible influence of the ENSO variations in the eastern equatorial Pacific Ocean. The ensemble spread (noise) about the ensemble mean in Fig. 4b clearly indicates that it increases with an increase in lead-time. In 1983, 1987 and 1998, the relative increase of this noise with lead-time is less compared to the other years. In Figs. 5a and b, the correlations of the JAS seasonal mean AWP area with the previous DJF global SST correlations are shown for the CFS LT integration and observations. The CFS clearly shows the stronger influence of ENSO variations over the AWP region in Fig. 5a, which is unsubstantiated in the observations (Fig. 5b). Given such an ENSO teleconnection pattern, it is not surprising to observe ENSO's influence on the seasonal predictability of the AWP in the NCEP CFS seasonal hindcasts.

The concept of ensemble integrations for seasonal prediction is not new (Moore and Kleeman 1996). In fact, the indeterminate nature of seasonal predictability warrants that sufficient ensemble integrations are performed so that robust probabilistic forecast measures can be computed (Palmer *et al.* 2000; Kirtman 2003; Misra 2004; Saha *et al.* 2006). Here, the probabilistic skill is evaluated using the area under the Relative Operating Characteristic (ROC) curves (Graham *et al.* 2000; Hanley and McNeil 1982). Owing to decadal variations in the seasonal errors, we compute the ROC curves (Fig. 6) for SH covering the whole period from 1981-2003 and for the period 1981-1996 (when the decadal variations of the observed SST over the AWP area are in one phase). In Fig. 6a, it is apparent that the skill of predicting the AWP area in the SH is rather

disappointing, when considering the whole period of 1981-2003. However when using the truncated period of the SH, Fig. 6b shows that the SH has skill (when area exceeds 0.6 for 90% confidence interval) in predicting the large AWP events (defined in the upper tercile) at all lead times. For small (defined in the lowest tercile) and normal (in between the upper and lower tercile) AWP events, the significant probabilistic skill at 90% confidence level is restricted to lead times of 0 and 1. This yet again shows that the observed robust decadal variation in the AWP area is detrimental to the CFS SH prediction skill of AWP.

4. Conclusions

The NCEP CFS Seasonal Hindcasts (SH) produce a reasonable climatology of the AWP. The SH lack the robust decadal SST variations observed over the AWP region. This points to a possible issue with model error (possibly with the ocean model dynamics) and/or the inadequacy of the ocean initialization procedure to capture the decadal variations in the sub-surface oceans. In majority of the years of the SH, the ensemble spread of the area of the AWP increases with lead time, with a consequent decrease

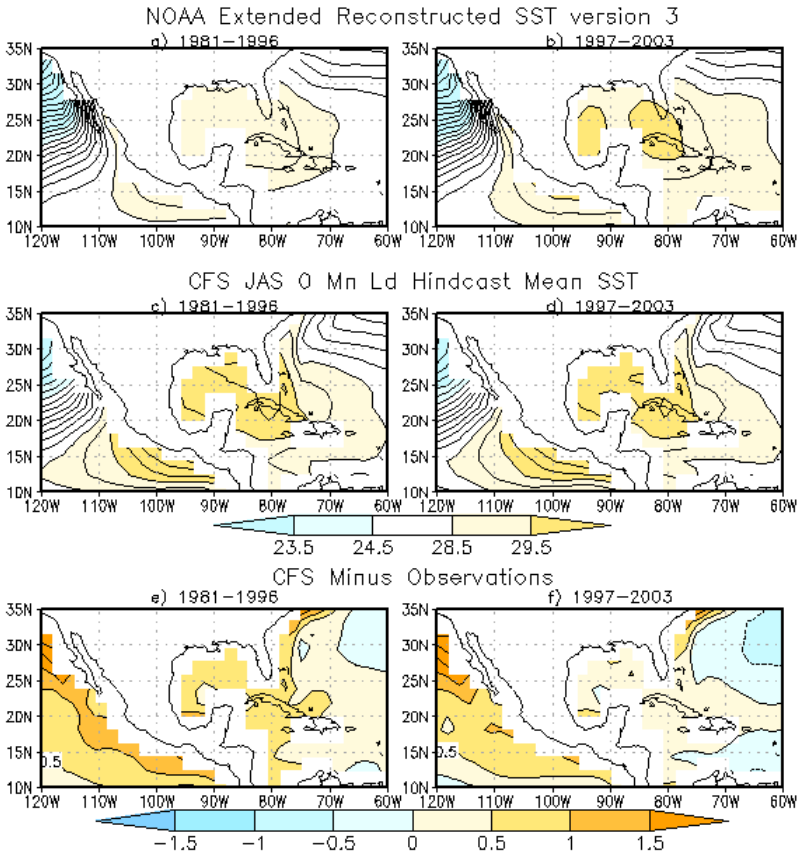

Fig. 3 Climatological July-August-September (JAS) seasonal mean SST from observations computed over the period of a) 1982-1996, and b) 1997-2003. Similarly, climatological JAS seasonal mean SST from the SH at 0 lead time computed over a period of c) 1982-1996, and d) 1997-2003. Climatological JAS seasonal mean SH errors computed over a period of e) 1982-1996, and f) 1997-2003. (Misra and Chan 2009)

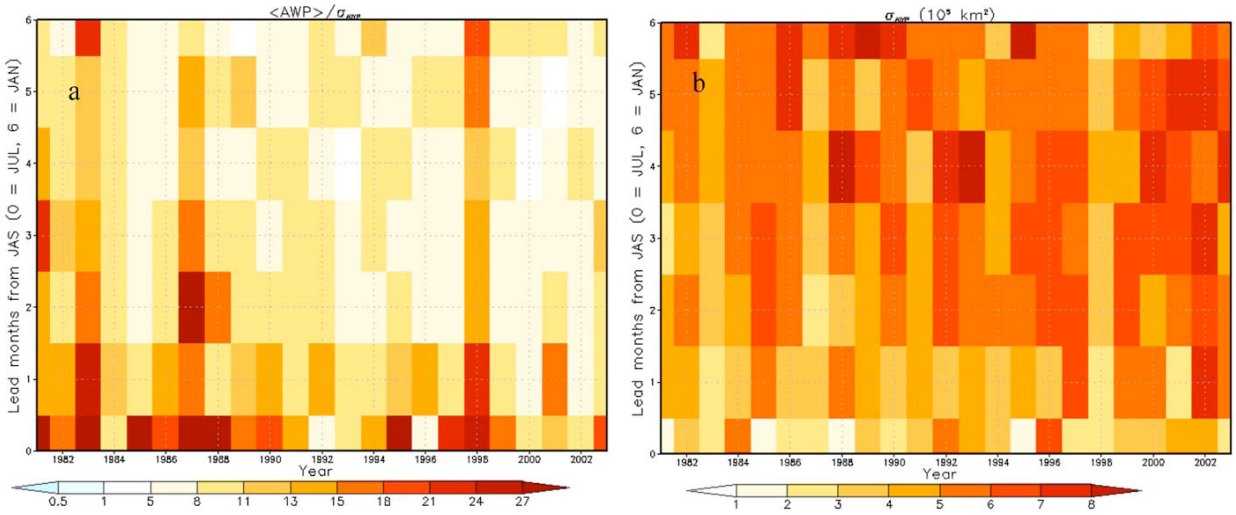

Fig. 4 a) The ratio of the ensemble mean of the AWP area (<AWP>) to its ensemble spread (σ_{AWP}) and b) the ensemble spread of SH as a function of lead time and year. (Misra and Chan 2009)

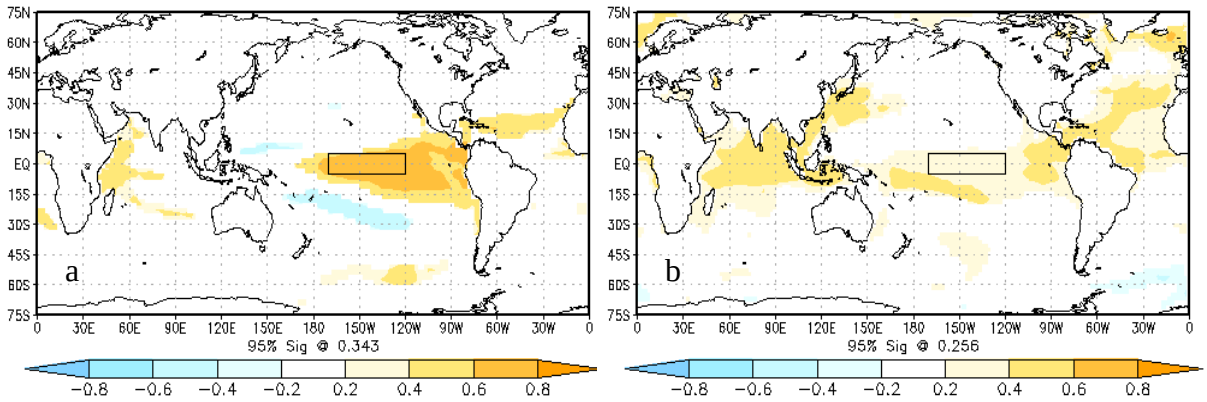

Fig. 5 The lead-lag correlation of the JAS seasonal mean area of the AWP with the previous DJF mean global SST from a) NCEP CFS LT integration, and b) observations (Smith *et al.* 2008). Only significant values at 95% confidence interval according to t-test are plotted. The Niño3.4 region is outlined over central Pacific. (Misra and Chan 2009)

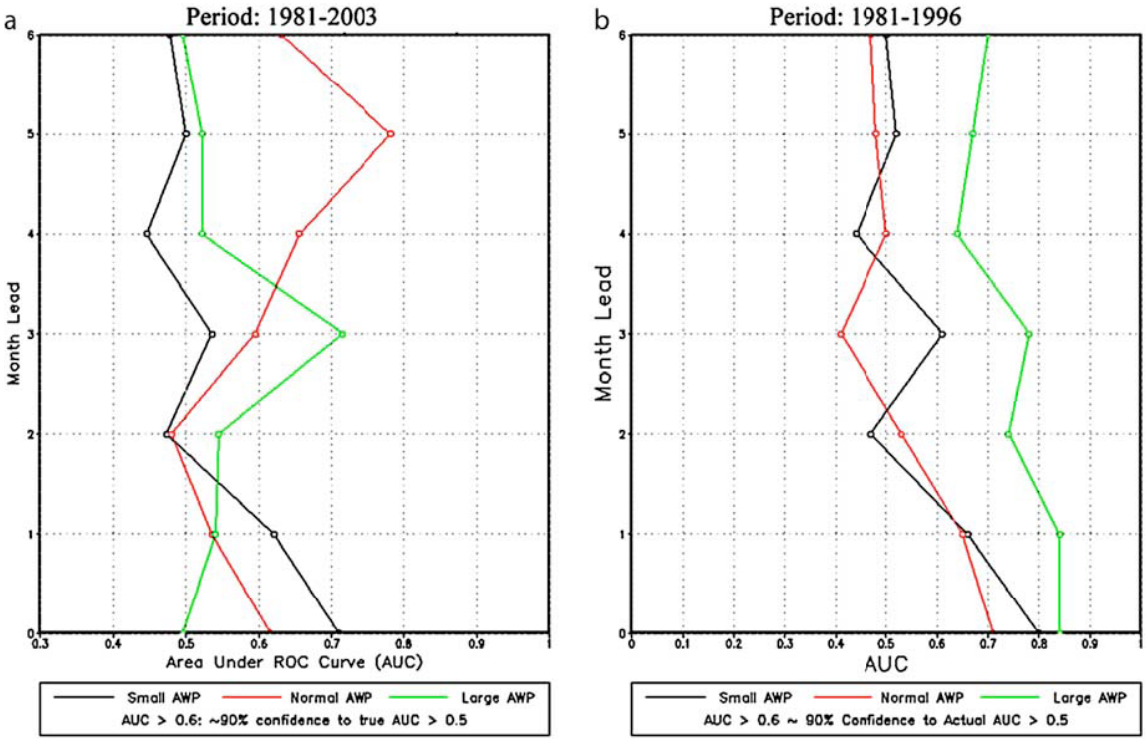

Fig. 6 The Area Under the Relative Operating Curve (AUC) for a) the full hindcast period of 1981-2003, and b) for the period 1981-1996 when the decadal variations of observed SST in the AWP region are in one phase. (Misra and Chan 2009)

in signal to noise ratio with lead time. However such linear relationship of the seasonal errors of the area of AWP with lead time is found lacking in the SH. In contrast, the signal to noise ratio decreases with lead time, which is most likely a result of the noise (ensemble spread) increasing with the lead time. However, in some of the major ENSO years, the SH displays significant increases in signal to noise ratio at all lead times relative to other years. This seems to suggest that large ENSO events, as seen in 1998, 1987, and 1983, may have some influence on the predictability of the AWP events in the NCEP CFS. It is seen that the NCEP CFS displays erroneously stronger influence of ENSO on the interannual variation of the AWP area. The probabilistic skill as measured by the area under the ROC curve clearly indicates the absence of any useful skill in predicting the modulation of the AWP area in the SH. However, it is found that when we examine a

truncated period of the SH (1981-1996 when the observed SST is one phase of the prevalent decadal variation) then some useful skill for the large AWP events (that occur in the upper tercile) at all lead times of the SH is noticed. But in this truncated period of the SH the significant probabilistic skill for the small AWP events (that occur in the lower tercile) and for normal AWP events (that occur in between the lower and upper terciles) is restricted to lead times of 0 and 1month. These results clearly suggest the importance of decadal variations of Atlantic SST and its lack of adequate representation in the NCEP CFS SH that reflects in its prediction skill of the AWP modulation at interannual scales.

References

Enfield, D.B., A. M. M.-Nuñez, and P. J. Trimble, 2001: The Atlantic multidecadal oscillation and its relation to rainfall and river flows in the continental U.S. *Geophys. Res. Lett.*, **28**, 2077-2080.

Graham, R. J., A. D. L. Evans, K. R. Mylne, M. S. J. Harrison, and K. B. Robertson, 2000: An assessment of seasonal predictability using atmospheric general circulation models. *Q. J. R. Meteorol. Soc.*, **126**, 2211-2240.

Hanley, J. A. and B. J. McNeil, 1982: The meaning and use of the area under a receiver operating characteristic curve. *Diagnostic Radiology*, **143**, 29-36.

Kerr, R. A., 2000: A North Atlantic climate pacemaker for the centuries. *Science*, **288**, 1984-1986.

Kirtman, B. P. (2003), The COLA anomaly coupled model: Ensemble ENSO prediction, *Mon. Wea. Rev.*, **131**, 2324–2341.

Misra, V., 2004: An evaluation of the predictability of austral summer season precipitation over South America. *J. Climate*, **17**, 1161-1175.

_____, S. Chan, R. Wu, and E. Chassignet, 2009: Air-sea interaction over the Atlantic Warm Pool in the NCEP CFS. *Geophys. Res. Lett.*, **36**, L15702, doi:10.1029/2009GL038737.

_____ and S. Chan, 2009: Seasonal Predictability of the Atlantic Warm Pool in the NCEP CFS. Geophys. Res. Lett., **36**, L16708, doi:10.1029/2009GL039762.

Moore, A. M., and R. Kleeman, 1996: The dynamics of error growth and predictability in a coupled model of ENSO. *Q. J. R. Meteorol. Soc.*, **122**, 1405-1446.

Palmer, T. N., C. Brankovic, and D. S. Richardson (2000), A probability and decision model analysis of PROVOST seasonal multi-model ensemble integrations, *Q. J. R.. Meteorol. Soc.*, ***126***, 2013–2034.

Saha, S., S. Nadiga, C. Thiaw, J. Wang, W. Wang, Q. Zhang, D. Behringer, W. Ebisuzaki, S. Lord, S. Moorthi, H.L. Pan, P. Peng, D. Stokes, H. M. van den Dool, G. White, and P. Xie, 2006: The climate forecast system at NCEP. *J. Climate*, **19**, 3483-3517.

Smith, T. M., R. W. Reynolds, T. C. Peterson, and J. Lawrimore, 2008: Improvements to NOAA's historical merged land-ocean surface temperature analysis (1880-2006). *J. Climate*, **21**, 2283-2296.

Wang, C., and D. B. Enfield, 2001: The tropical western hemisphere warm pool. *Geophys. Res. Lett.*, **28**, 1635-1638.

_____, and _____, 2003: A further study of the tropical Western Hemisphere Warm Pool. *J. Climate*, **6**, 1476-1493.

____, D. B. Enfield, S. –K. Lee, C. W. Landsea, 2006: Influences of the Atlantic warm pool on western hemisphere summer rainfall and Atlantic hurricanes. *J. Climate*, **19**, 3011-3028.

_____, _____, and_____ 2008: Atlantic warm pool acting as a link between Atlantic multidecadal oscillation and Atlantic tropical cyclone activity. *Geochem. Geophys. Geosys.*, **9**, Q05V03, doi:10.1029/2007GC001809.

Wang, W., S. Saha, H.-L. Pan, S. Nadiga, and G. White, 2005: Simulation of ENSO in the new NCEP Coupled Forecast System Model. *Mon. Wea. Rev.*, **133**, 1574-1593.

Science and Technology Infusion Climate Bulletin
NOAA's National Weather Service
35th NOAA Annual Climate Diagnostics and Prediction Workshop
Raleigh, NC, 4-7 October 2010

The Madden-Julian Oscillation and the Relative Value of Deterministic Forecasts of Extreme Precipitation in the Contiguous United States

Charles Jones[1], Leila M. V. Carvalho[1,2], Jon Gottschalck[3] and Wayne Higgins[3]

[1] *Earth Research Institute, University of California, Santa Barbara, California*
[2] *Department of Geography, University of California, Santa Barbara, California*
[3] *Climate Prediction Center, NOAA / National Centers for Environmental Prediction*

1. Introduction

Extreme (or heavy) precipitation events are frequently accompanied by floods or crippling snowfall, which increase the potential for loss of life and property. The Madden-Julian Oscillation (MJO) is the most prominent form of tropical intraseasonal variability that impacts weather and climate (Carvalho *et al.* 2004; Lau and Waliser 2005; Zhang 2005).

Important linkages have been identified between the MJO and the occurrence of heavy precipitation (Higgins *et al.* 2000; Jones 2000; Carvalho *et al.* 2004; Jones *et al.* 2004a). Since the MJO involves intense tropical convective heating anomalies, tropical-extratropical interactions are significant during its life cycle. Consequently, the MJO modulates the skill of weather forecasts in the medium and extended ranges (Jones and Schemm 2000; Jones *et al.* 2000; Vitart and Molteni 2010) as well as the potential predictability at these time ranges (Jones *et al.* 2004a, 2004b).

Recently, Jones *et al.* (2010) investigated the MJO and the forecast skill of extreme precipitation in the contiguous United States (CONUS) during boreal winter. Forecast skill is usually higher when the MJO is active and has enhanced convection occurring over the western hemisphere, Africa, and/or the western Indian Ocean. Heidke skill scores (HSS) greater than 0.1 extend to lead times of up to two weeks in these situations. Approximately 10-30% of the CONUS has HSS greater than 0.1 at all lead times from 1 to 14 days when the MJO is active. This study applies a simple decision model to examine the relationships between the MJO and the relative value of deterministic forecasts of extreme precipitation in the CONUS.

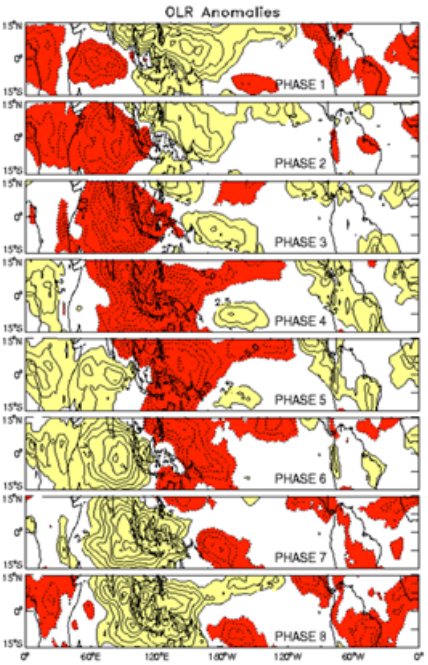

Fig. 1 Phase composites of OLR anomalies. Yellow (red) indicates positive (negative) anomalies. Contour interval is 2.5 Wm^{-2}.

2. Data

The observed occurrence of extreme precipitation events was analyzed with the NCEP Climate Prediction Center (CPC) unified precipitation dataset. Daily precipitation over the CONUS was used for the period 1 November–31 March, 1981-2008. Extreme precipitation was defined when the daily precipitation exceeded the 90th percentile of the gamma frequency distribution. The MJO was studied with daily averages of zonal winds at 850-hPa (U850) and 200-hPa (U200) from the NCEP/NCAR reanalysis. Figure 1 displays composites of outgoing longwave radiation (OLR) anomalies and illustrates the life cycle of the MJO. Forecasts of extreme precipitation were analyzed with reforecasts of the Climate Forecast System model (version 1) (Saha *et al.* 2006).

3. Forecasts of extreme precipitation

For each winter season, the monthly mean model bias was subtracted from the forecasts of precipitation. Next, each forecast was

Correspondence to: Charles Jones, Earth Research Institute, University of California, Santa Barbara, CA 93106; Email: cjones@eri.ucsb.edu

analyzed and a forecast of extreme precipitation was identified when the daily precipitation exceeded an adjusted 90th percentile of the frequency precipitation.

The validation consisted of binary pairs of forecasts and observations (1=occurrence, 0=non-occurrence). Forecasts were validated separately on days in which the MJO was active and inactive. In active cases, the validation was performed on each MJO phase and lead times from 1-14 days, regardless of the state of the MJO in the initial conditions. Statistical significance between forecasts of extreme precipitation during active and inactive MJO days was assessed by a resampling technique. The results suggested that when the MJO is active and in phases 1 or 8 (Fig. 1), CFS forecasts of extreme precipitation are more skillful than in inactive MJO periods. HSS ≥ 0.1 extend to 14 day lead times, which contrasts to the overall skill of 7-8 days during inactive MJO days.

4. The relative value of deterministic forecasts of extreme precipitation

A simple cost/loss ratio decision model was applied to investigate the potential influence of the MJO on the value of forecasts of extreme precipitation. The model envisions a decision maker who is sensitive to hazardous weather and has two possible courses of action. If extreme precipitation occurs and protective action is not taken, a loss L will happen. If protective action is taken, it will cost an amount C in addition to normal expenses. For a given set of [forecasts, observations], four possible combinations exist: 1) action taken-event occurs with cost C, 2) action taken-event does not occur with cost C, 3) action not taken-event occurs with loss L, and 4) action not taken-event does not occur with no cost or loss. The relative value (V) of deterministic forecasts in this simple model is:

$$V = \frac{min(\alpha,\ s) - F(1-s)\alpha + Hs(1-\alpha) - s}{\min(\alpha, s) - s\alpha}$$

where α = C/L is the decision maker's cost/loss ratio, s is the climatological probability of the weather event, H and F are hit rate and false alarm rate in the forecasts, respectively. In addition, maximum value (V_{max}) occurs when $\alpha = s$ and given by: V_{max}= H-F. V_{max} can be interpreted as potential forecast value or forecast quality. The reader is referred to Richardson (2003) for an extensive discussion of the model above.

The relative value (V) of deterministic forecasts of extreme precipitation was evaluated on the samples of active and inactive MJO days. Figure 2 shows V when the MJO was active and in phases 1, 2, 7 or 8. The curves indicate V averaged on 1-3, 5-7, 9-11 and 12-14 day lead times and averaged over the CONUS only on gridpoints where there were statistically significant (5% level) differences in HSS between active and inactive MJO days. While the results are comparable for all four phases, slightly higher values are noticed when the MJO is in phase 8, particularly on 1-3 day leads than in other phases. A decision maker with C/L ratios between 0.1-0.7 would observe value between 0.0-0.4 for

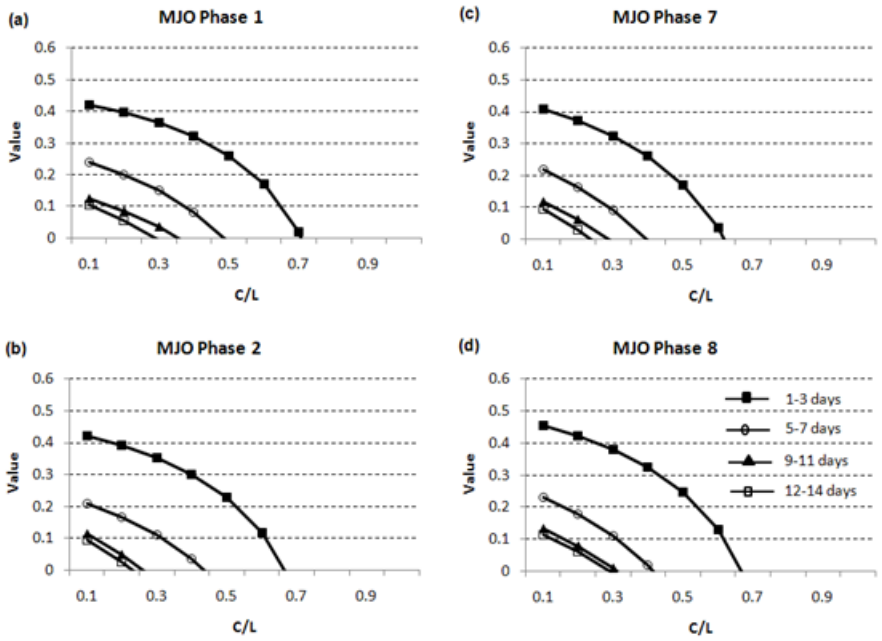

Fig. 2 Relative value of deterministic forecasts of extreme precipitation in the USA. Horizontal and vertical axes denote cost/loss ratio and value, respectively. Panels show value when the MJO is active and in four specific phases. Each curve corresponds to value averaged in four lead times as described in the inset in panel (d).

forecasts on 1-3 days lead when the MJO was active. Although the magnitudes of *V* decrease with increasing lead times, relative value *V* remains positive and extends to Week-2 lead times.

Figure 3 shows *V* during inactive MJO days on 1-3, 5-7, 9-11 and 12-14 days lead times and averaged over the entire CONUS. A decision maker with C/L=0.15, would observe *V*=0.2 at 1-3 days lead during inactive days (Fig. 3), whereas *V*=0.4 when the MJO was active and in phases 1, 2, 7 or 8 (Fig. 2). Also, when the MJO is inactive, *V* nearly decreases to zero for forecasts at 7-days (Fig. 3).

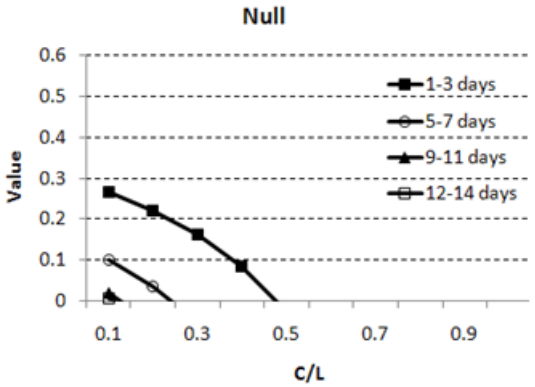

Fig. 3 As in Fig.2, but for value when the MJO is inactive.

To summarize the importance of the MJO on the potential relative value of forecasts of extreme precipitation, Figure 4 shows V_{max} when the MJO was active, in phases 1, 2 , 7 or 8 and lead times from 1 to 14 days. Although there are some small variations among these four MJO phases, V_{max} remains above 0.1 by 14-day lead times. In contrast, during inactive MJO days, V_{max}, which was averaged only over grid points with statistical differences of 5% or higher from inactive MJO, starts from 0.3 at 1-day and decreases to less than 0.1 at 7-day lead time.

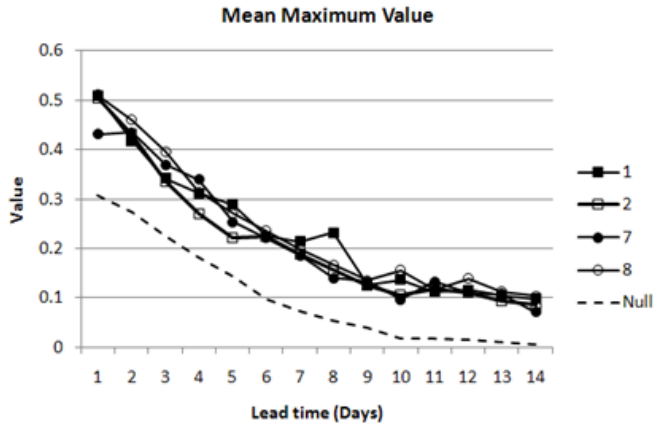

Fig. 4 Maximum relative value of deterministic forecasts of extreme precipitation in the USA. Curves indicate maximum value when the MJO is active and in four specific phases; dashed line shows maximum value when the MJO is inactive.

5. Conclusions

The MJO is the most important mode of tropical intraseasonal variations and plays a significant role in global precipitation variability (e.g., Jones et al. 2004b). This study applied a simple decision model to estimate the relative value of deterministic forecasts of extreme precipitation over the CONUS during winter. The results clearly show the influential nature of the MJO. This influence is particularly important when enhanced convection associated with the MJO is located over the western hemisphere, Africa, and/or the western Indian Ocean. In these situations, relative values in the forecasts are larger and extend to longer leads than when the MJO is inactive.

Acknowledgements. The authors would like to thank the support of NOAA's Climate Program Office and specifically the Climate Test Bed program that supported this work under the grant NA08OAR4310698. NCEP/NCAR Reanalysis and OLR data were provided by the NOAA/OAR/ESRL PSD, Boulder, Colorado, USA and obtained from their web site at www.esrl.noaa.gov.

References

Carvalho, L. M. V., C. Jones, and B. Liebmann, 2004: The South Atlantic convergence zone: Intensity, form, persistence, and relationships with intraseasonal to interannual activity and extreme rainfall. *J. Climate*, **17,** 88-108.

Higgins, R. W., J. K. E. Schemm, W. Shi, and A. Leetmaa, 2000: Extreme precipitation events in the western United States related to tropical forcing. *J. Climate*, **13,** 793-820.

Jones, C., 2000: Occurrence of extreme precipitation events in California and relationships with the Madden-Julian oscillation. *J. Climate*, **13,** 3576-3587.

Jones, C., and J.-K. E. Schemm, 2000: The influence of intraseasonal variations on medium-range weather forecasts over South America. *Mon. Wea. Rev.*, **128,** 486–494.

Jones, C., D. E. Waliser, J. K. E. Schemm, and W. K. M. Lau, 2000: Prediction skill of the Madden and Julian Oscillation in dynamical extended range forecasts. *Climate Dyn.*, **16,** 273-289.

Jones, C., D. E. Waliser, K. M. Lau, and W. Stern, 2004a: Global occurrences of extreme precipitation and the Madden-Julian oscillation: Observations and predictability. *J. Climate*, **17,** 4575-4589.

——, 2004b: The Madden-Julian oscillation and its impact on Northern Hemisphere weather predictability. *Mon. Wea. Rev.*, **132,** 1462-1471.

Jones, C., J. Gottschalck, L. M. V. Carvalho, and W. R. Higgins, 2010: Influence of the Madden-Julian Oscillation on forecasts of extreme precipitation in the contiguous United States. *Mon. Wea. Rev.,* doi: 10.1175/2010MWR3512.1.

Lau, W. K. M., and D. E. Waliser, 2005: *Intraseasonal Variability in the Atmosphere-Ocean Climate System.* Springer, 436 pp.

Richardson, D. V., 2003: Economic value and skill. *Forecast Verification : A Practitioner's Guide in Atmospheric Science*, I. T. Jolliffe and D. B. Stephenson Eds., Wiley, 240 pp.

Saha, S., and Coauthors, 2006: The NCEP Climate Forecast System. *J. Climate*, **19,** 3483-3517.

Vitart, F., and F. Molteni, 2010: Simulation of the Madden- Julian Oscillation and its teleconnections in the ECMWF forecast system. *Quart. J. Roy. Meteor. Soc.*, **136,** 842-855.

Zhang, C. D., 2005: Madden-Julian Oscillation. *Rev. Geophys.*, **43,** 1-36.

Science and Technology Infusion Climate Bulletin
NOAA's National Weather Service
35th NOAA Annual Climate Diagnostics and Prediction Workshop
Raleigh, NC, 4-7 October 2010

Simulation of Dominant Intraseasonal Variability Modes over the Eastern Pacific ITCZ in Climate Models

Xianan Jiang
Joint Institute for Regional Earth System Science & Engineering
University of California, Los Angeles, California

1. Introduction

Intraseasonal variability (ISV) plays a significant role in the tropical atmosphere. While the strongest ISV is found to be associated with the Asian monsoon, vigorous intraseasonal variations in winds and convection have also been widely reported over the eastern Pacific (EPAC) inter-tropical convergence zone (ITCZ) during boreal summer (*e.g.*, Maloney and Esbensen, 2003, 2007; Jiang and Waliser, 2008, 2009; and many others). The ISV over the EPAC exerts significant influences on regional weather/climate, including tropical cyclone activity, the summertime wind jets in the Gulfs of Tehuantepec and Papagayo, the Caribbean Low-Level Jet and precipitation, and the North American monsoon. If the predictability of the EPAC ISV is similar to the Madden-Julian Oscillation (MJO; about 2-4 weeks; *Waliser*, 2006), therefore, a better understanding of the ISV over the EPAC would greatly benefit the improved predictive skill for regional climate.

Our previous observational study identified two dominant ISV modes over the EPAC (Jiang and Waliser, 2008, 2009), *i.e.*, a 40-day mode and a quasi-biweekly mode (QBM). The 40-day ISV mode (see Fig. 1a) is generally considered a local expression of the MJO. In addition to the eastward propagation, it is illustrated that northward propagation of the 40-day mode is also evident (Jiang and Waliser, 2008), exhibiting a strong resemblance to its counterpart over the Asian summer monsoon region (Jiang *et al.*, 2004). The QBM mode bears a relatively smaller spatial scale than the 40-day mode, and is largely characterized by northward propagation (Fig. 1b).

While the study of the capability of general circulation models (GCMs) to represent the MJO

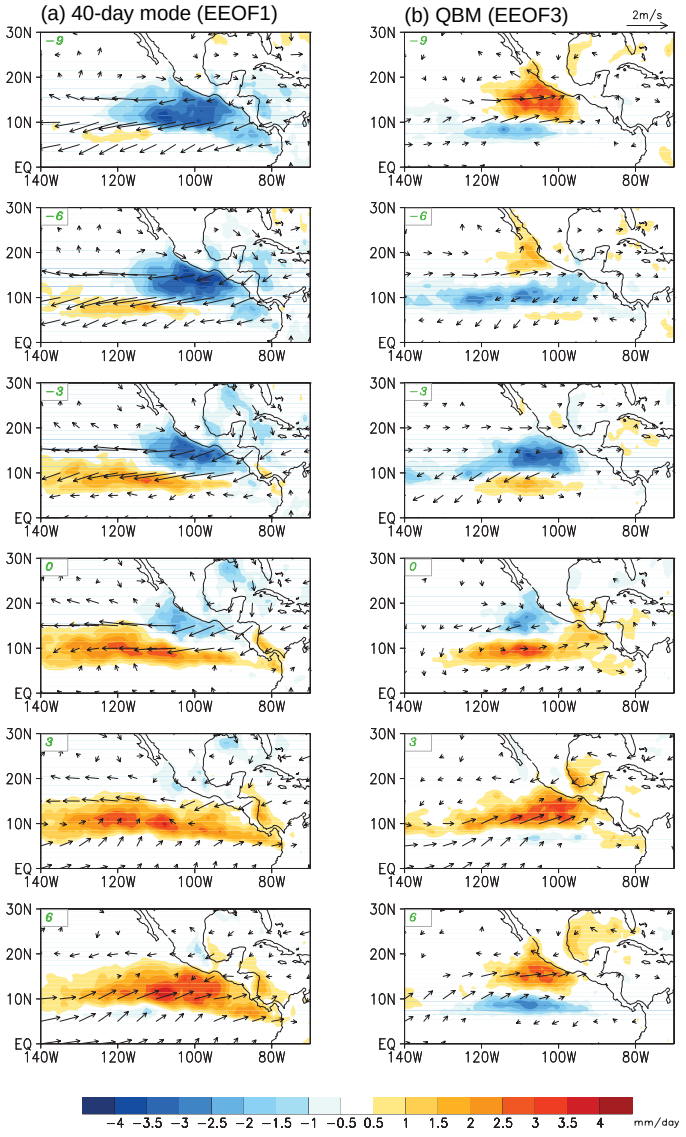

Fig. 1 Evolution of anomalous rainfall (shading) and 850hPa winds (vectors) associated with (a) the 40-day ISV mode and (b) the QBM over the EPAC. The time interval between two neighboring panels is 3 days.

Correspondence to: Xianan Jiang, Jet Propulsion Laboratory, MS 183-501, California Institute of Technology, 4800 Oak Grove Dr., Pasadena, CA 91109; Email: xianan@jifresse.ucla.edu

has been the subject of widespread interest in the climate research community, much less effort has been placed on the assessment of GCM simulations of the ISV over the EPAC. In the present study, we assess capabilities of current GCMs in simulating the dominant ISV modes over the EPAC.

2. Participating models, observational datasets, and methods

A brief description of the six uncoupled (CAM3.5, CAM3z, GEOS5, SNU, SPCAM, HIRAM) GCMs and three coupled (CFS, CM2.1, ECHAM4/OPYC) GCMs analyzed in this study is given in Table 1. Note that while the sub-grid cumulus processes in the parent GCM of SPCAM are explicitly represented based on the embedded 2-D CRMs, they are parameterized based on mass-flux-type schemes in all other eight conventional GCMs. In eight of the nine models except HIRAM analyzed herein, MJO variability was evaluated by the Climate Variability and Predictability (CLIVAR) MJO Working Group (Kim *et al.*, 2009). The ninth model analyzed herein, *i.e.*, HIRAM, is a new high resolution AGCM developed at NOAA's GFDL. We will evaluate how well the observed two leading ISV modes over the EPAC are represented in these models. In addition, model output from a low resolution version of HIRAM (~2.5 degrees; hereafter HIRAM-lores) is also analyzed to explore the sensitivity to horizontal resolution on simulation of the ISV over the EPAC.

Model	Horizontal Resolution	Vertical Levels	Cumulus Scheme	Reference
CAM3.5 (NCAR)	1.9^o lat × 2.5^o lon	26	Mass flux	Neale *et al.* (2008)
CAM3z (SIO)	T42 (2.8°)	26	Mass flux	Zhang and Mu (2005)
CFS (NCEP)	T62 (1.8°)	64	Mass flux	Wang *et al.* (2005)
CM2.1 (GFDL)	2^o lat × 2.5^o lon	24	Mass flux	Delworth *et al.* (2006)
ECHAM4/OPYC (MPI via PCMDI)	T42 (2.8°)	19	Mass flux	Roeckner *et al.* (1996) Sperber *et al.* (2005)
GEOS5 (NASA)	1^o lat × 1.25° lon	72	Mass flux	Rienecker *et al.* (2008)
SNU-AGCM (SNU)	T42 (2.8°)	20	Mass flux	Lee *et al.* (2003)
SPCAM (CSU)	T42 (2.8°)	26	Super-parameterization	Khairoutdinov *et al.* (2005)
HIRAM HIRAM-lores (GFDL)	0.5^o lat × 0.6^o lon 2.0^o lat × 2.5^o lon	32	Mass flux	Zhao *et al.* (2009)

Table 1 Participating models and brief descriptions

Most of the above nine models are integrated for 20 years. Daily output of rainfall over the EPAC from these models are analyzed and compared to observations including the mean state and intraseasonal variances. Rainfall observations are based on Tropical Rainfall Measuring Mission (TRMM, version 3B42; Huffman *et al.*, 1995) during the period from 1998 to 2008.

The approach to identify the leading ISV modes in both observations and each model is based on an EEOF analysis for boreal summer rainfall (May-October) over the EPAC (140^oW-90^oW; EQ-30^oN) following our previous study (Jiang and Waliser, 2009; hereafter JW09). Prior to the EEOF analysis, 3-day mean anomalous rainfall data (non-overlapping) are calculated from the daily 10-90 day band-pass filtered anomalies for both the TRMM observations and GCM simulations. The EEOF is conducted with 9 temporal lags of the 3-day mean anomalous data.

Each leading ISV mode over the EPAC based on observed rainfall is represented by two EEOF modes that are in quadrature to each other, suggesting the propagating nature of these ISV modes. The first (second)

pair of the EEOFs represents the first (second) leading ISV mode. The evolution patterns of anomalous rainfall and 850hPa winds associated with the two observed leading ISV modes are depicted by $EEOF_1$ and $EEOF_3$ in Fig1a, b, respectively.

To identify model counterparts of the two observed leading ISV modes, we calculate pattern correlations between each of the first ten leading EEOF modes from each model simulation and observed $EEOF_1$ / $EEOF_3$. The EEOF mode with largest pattern correlation coefficient against the observed $EEOF_1$ / $EEOF_3$ will then be selected as the corresponding first / second ISV mode in each model. Note that as in the observations, each leading ISV mode in GCM simulations is also usually described by a pair of EEOF modes quadratic to each other. In addition, to consider the possible phase differences between the EEOFs based on each dataset, which is not unexpected, we conduct lead/lag pattern correlations of the model EEOFs against the observed reference. Then, the maximum absolute value of these lead/lag correlation coefficients is selected to represent the pattern correlation between model EEOF mode and the observed $EEOF_1$/$EEOF_3$.

3. Results

Model skill in simulating summer mean rainfall and the ISV variance (10-90 day filtered) patterns over the EPAC is summarized in Fig. 2 by showing pattern correlations of these fields between GCM simulations and observations over the domain of 150°W-60°W, 5°S-30°N. SPCAM, HIRAM, and GEOS5 exhibit relatively better performance in simulating both mean rainfall and the ISV variance patterns than other GCMs. For SNU, although it shows moderate skill in mean rainfall pattern, the distribution of the ISV variance over the EPAC is well simulated in this model.

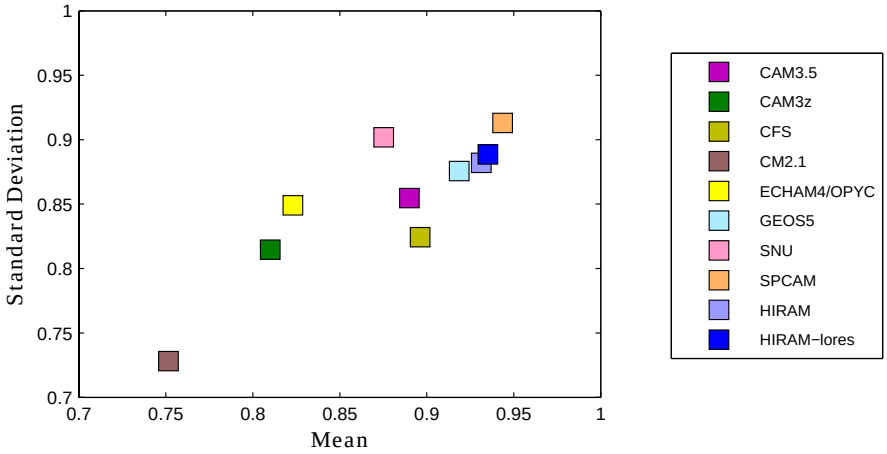

Fig. 2 Pattern correlation coefficients for mean precipitation and precipitation standard deviation during summer (May-Oct) between TRMM observations and model simulations. The region for pattern correlation is 5ºS-30ºN. 150ºW-80ºW.

The pattern correlation coefficients of the first and second ISV modes between model simulations and observations are illustrated in Fig. 3. The results suggest that four GCMs, including CFS, SPCAM, HIRAM, and SNU, show the best skill in capturing the observed evolution pattern of the first ISV mode, *i.e.*, the 40-day mode, with pattern correlations surpassing 0.8. Particularly noteworthy is that both the standard and low-resolution versions of HIRAM exhibit excellent skill in depicting the observed 40-day ISV mode. This result may suggest that model physics rather than the horizontal resolution may play a more essential role in faithfully simulating the 40-day mode over the EPAC. On the other hand, three GCMs, SPCAM, HIRAM, and GEOS5, demonstrate the best skill in simulating the second ISV mode, *i.e.*, the QBM, with pattern correlations greater than 0.6. It is interesting to note that while the QBM is well represented in the standard HIRAM, it is not well captured in

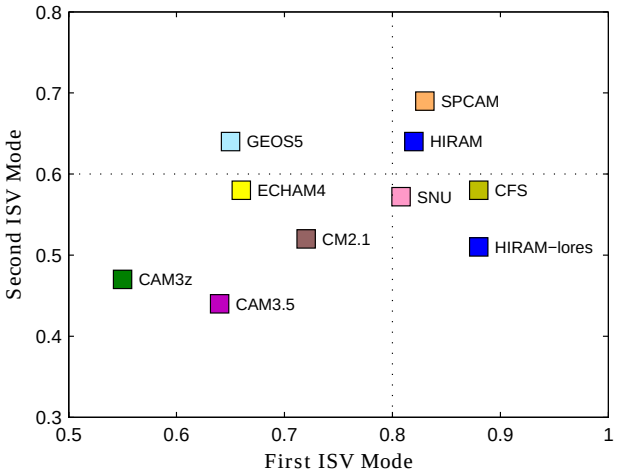

Fig. 3 Pattern correlation coefficients of the first ISV mode (x-axis) / second ISV mode (y-axis) between TRMM observations and simulations.

its lower resolution version. This result may suggest the importance of fine horizontal resolution in simulating the observed QBM over the EPAC, which may be due to the smaller scales of the QBM versus the 40-day ISV mode. The relatively better simulation of the QBM in GEOS5 could also be ascribed to the relatively higher resolution in this model ($1^{o}\times1.25^{o}$). Despite the coarse resolution (T42) of the parent GCM of SPCAM, the QBM is also well simulated by the SPCAM, indicating that an improved simulation of the convective processes by the embedded 2D CRMs could represent another method for improving simulations of the ISV over the EPAC.

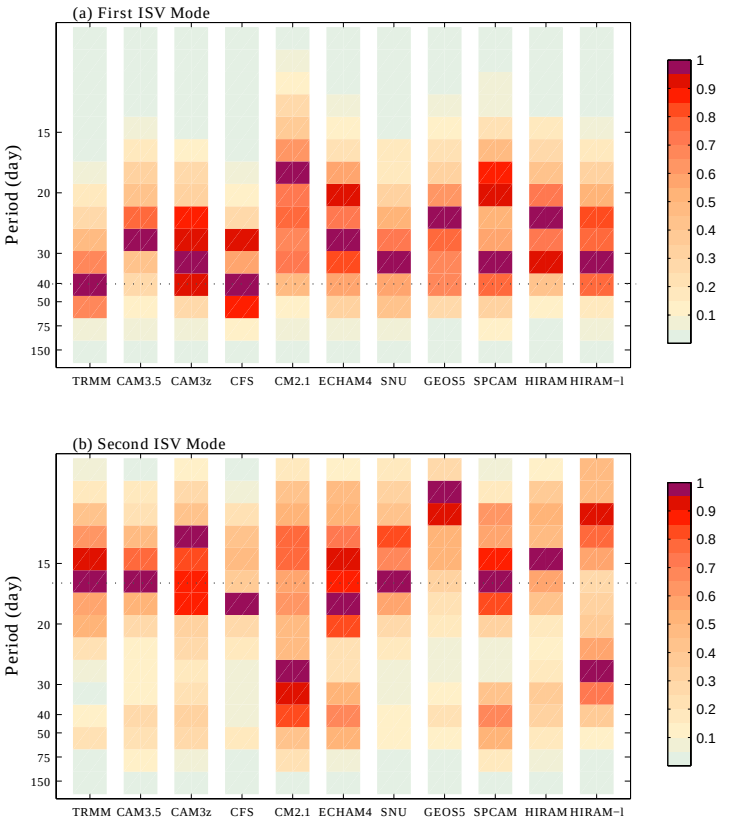

Fig. 4 Normalized spectral density of PC time series corresponding to (a) the first ISV mode and (b) the second ISV mode based on TRMM and model simulated rainfall.

Spectral analyses are further applied to corresponding principal components (PCs) from the EEOF to derive the dominant periodicities of the two leading ISV modes in each dataset. Figure 4 illustrates the spectral density profiles based on both observed and model simulated rainfall, which have been normalized by their corresponding maximum values such that the peak value is unity in each profile. Spectral analysis based on TRMM rainfall (left columns in Fig. 4a, b) are consistent with JW09 and further confirm the dominant periods of about 40 and 16 days associated with the observed first and second leading ISV modes over the EPAC. For the first ISV mode (Fig. 4a), CFS realistically captures the observed 40-day spectral peak, while CAM3z, SNU, SPCAM, and HIRAM_lores simulate dominant periods of about 35 days for the first ISV mode, reasonably comparable to the observations. Note that although a peak spectrum of about 25 days is noticed in the standard HIRAM run, a second peak of about 35 days can also be detected. Meanwhile, a second 25-day peak is also noticed in the HIRAM_lores run, suggesting coexistence of these two prevailing periods in HIRAM and a shifting between each other with the change of the model horizontal resolution.

For the dominant periods of the second ISV mode, most of GCMs, except CM2.1 and HIRAM-lores, reasonably capture a quasi-biweekly period of the second ISV mode (Fig. 4b). In GEOS5, a higher-frequency mode with a period of 12 days is dominant, while a period of about 30 days is found in CM2.1 and HIRAM-lores. It is of particular interest to note again that while a biweekly period of the second ISV mode is realistically simulated in the standard HIRAM run, it is not captured in its lower resolution version. This result further suggests that the increased horizontal resolution could be conducive to a better representation of the QBM over the EPAC.

In Fig. 5, the eastward propagation associated with the first ISV mode is illustrated by displaying time-longitude profiles of rainfall anomalies based on both observations and GCM simulations. The rainfall in each panel is averaged between 8^{o}N-15^{o}N and the slope of the dashed line represents the observed eastward phase speed of 4 deg day^{-1} between 120^{o}W and 140^{o}W (Fig. 5a). To the east of 100^{o}W, the westward propagating signal of the 40-day ISV mode is also observed. It is shown that the four GCMs that exhibit relatively higher pattern correlation coefficients for the 40-day mode, i.e., CFS, SNU, SPCAM, and HIRAM as shown in Fig. 2, generally simulate a more realistic eastward propagation of this mode. Both the HIRAM versions capture well the eastward propagation of the first ISV mode. While the eastward propagation is reasonably well represented in SPCAM, the westward propagation near 100^{o}W tends to be slightly overestimated in this

model. A very fast eastward propagation speed of about 15 deg day^{-1} is found in SNU. The eastward propagation associated with the 40-day ISV mode is not well defined in several other GCMs, including CAM3.5, ECHAM4/OPYC, CAM3z, GEOS5, and CM2.1.

4. Summary and discussion

In this study, the model fidelity in representing the two dominant ISV modes over the EPAC is assessed by analyzing six atmospheric and three coupled GCMs, including one super-parameterized GCM (SPCAM) and one recently developed high-resolution GCM (GFDL HIRAM) with horizontal resolution of about 50km. While it remains challenging for GCMs to faithfully represent these two ISV modes including their amplitude, evolution patterns, and periodicities, very encouraging simulations are also noted.

In general, SPCAM and HIRAM exhibit relatively superior skill in representing the two ISV modes over the EPAC. It is generally considered that the explicit representation of the sub-grid cumulus process by the embedded 2-D CRMs in SPCAM could be largely responsible for its improved performance. Similarly, the improved simulations of the ISV over the EPAC achieved in HIRAM could be largely ascribed to the improved cumulus parameterization schemes, most likely by adopting a strongly entraining plume cumulus scheme following the parameterization of shallow convection by Bretherton *et al.* (2004) instead of the relaxed Arakawa-Schubert convective closure in GFDL CM2.1 (Zhao *et al.*, 2009).

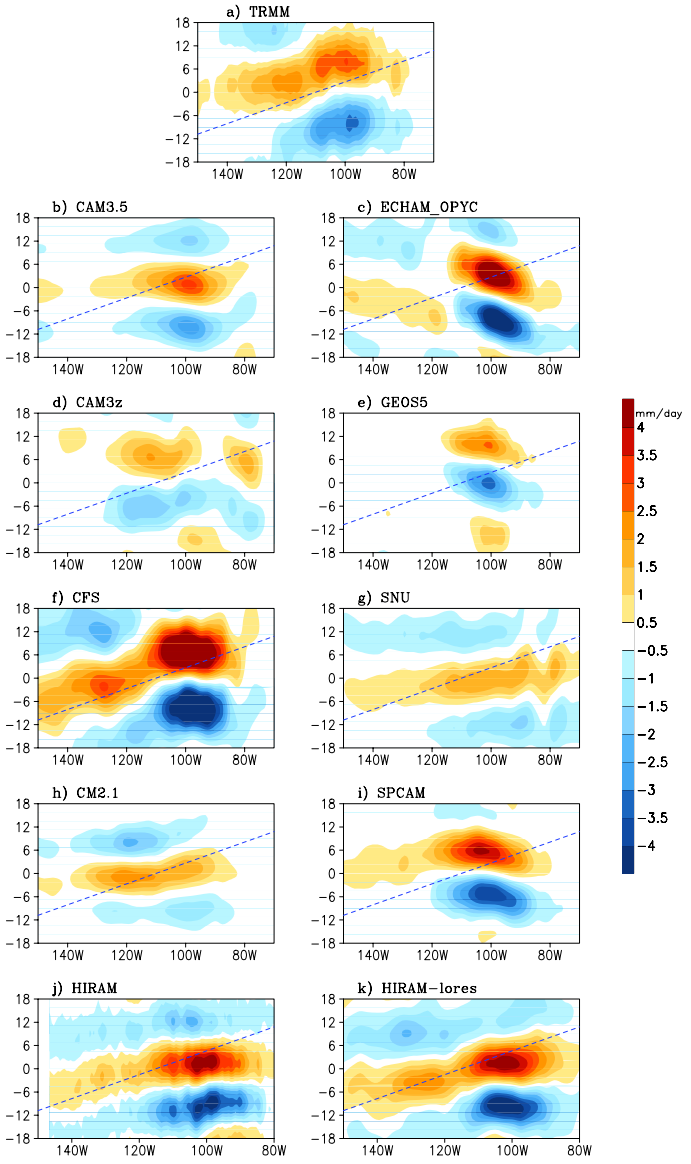

Fig. 5 Longitude (x-axis) - time (y-axis; units: day) evolution of rainfall anomalies over the EPAC (8°N-15°N) associated with the first ISV mode based on observed and GCM simulated rainfall. Dashed lines represent an eastward propagation speed of 4 deg day^{-1}.

By adopting a strongly entraining cumulus scheme in HIRAM, the plume can only provide deep convection when the atmosphere is sufficiently moist; it thus limits the loss of buoyancy due to the entrainment. As a result, deep convection is sufficiently inhibited such that a substantial fraction of the rainfall in the tropics (30-40% in both HIRAM and HIRAM_lores runs) occurs through the large-scale (stratiform) cloud module rather than through the convection module in HIRAM (Zhao *et al.*, 2009), which is largely comparable to the observed stratiform rainfall partitions. In contrast, only 7.5% of the total rainfall is through the large-scale condensation in CM2.1. Moreover, as previously mentioned, an increase of the horizontal resolution appears to further help the simulation of the ISV over the EPAC, particularly for the second ISV mode.

For future study, further investigations are warranted for improved understanding on various aspects of the ISV over the EPAC, including role of the MJO on the ISV over the EPAC, how the two ISV modes

interact to make impacts on regional climate/weather events, and the role of multi-scale interaction associated with the ISV over the EPAC.

References

Bretherton, C. S., J. R. McCaa, and H. Grenier, 2004: A new parameterization for shallow cumulus convection and its application to marine subtropical cloud-topped boundary layers, Part I: Description and 1D results. *Mon. Weather Rev.*, **132**, 864-882.

Delworth, T. L., and Coauthers, 2006: GFDL's CM2 global coupled climate models, Part I: Formulation and simulation characteristics. *J. Climate*, **19**, 643-674.

Huffman, G. J., R. F. Adler, B. Rudolf, U. Schneider, and P. R. Keehn, 1995: Global precipitation estimates based on a technique for combining satellite-based estimates, rain-gauge analysis, and NWP model precipitation information. *J. Climate*, **8**, 1284-1295.

Jiang, X., T. Li, and B. Wang, 2004: Structures and mechanisms of the northward propagating boreal Summer intraseasonal oscillation. *J. Climate*, **17**, 1022-1039.

Jiang, X., and D. E. Waliser, 2008: Northward propagation of the subseasonal variability over the eastern Pacific warm pool. *Geophys. Res. Lett.*, **35**, L09814, doi:10.1029/2008GL033723.

Jiang, X., and D. E. Waliser, 2009: Two dominant subseasonal variability modes of the eastern Pacific ITCZ. *Geophys. Res. Lett.*, **36,** L04704, doi:10.1029/2008GL036820.

Khairoutdinov, M., D. Randall, and C. DeMott, 2005: Simulations of the atmospheric general circulation using a cloud-resolving model as a superparameterization of physical processes. *J. Atmos. Sci.*, **62**, 2136-2154.

Kim, D., K. Sperber, W. Stern, D. Waliser, I. S. Kang, E. Maloney, W. Wang, K. Weickmann, J. Benedict, M. Khairoutdinov, M. I. Lee, R. Neale, M. Suarez, K. Thayer-Calder, and G. Zhang, 2009: Application of MJO simulation diagnostics to climate models. *J. Climate*, **22**, 6413-6436.

Lee, M. I., I. S. Kang, and B. E. Mapes, 2003: Impacts of cumulus convection parameterization on aqua-planet AGCM Simulations of tropical intraseasonal variability. *J. Meteorol. Soc. Japan*, **81**, 963-992.

Maloney, E. D., and S. K. Esbensen, 2003: The amplification of east Pacific Madden-Julian Oscillation convection and wind anomalies during June-November. *J. Climate*, **16**, 3482-3497.

Maloney, E. D., and S. K. Esbensen 2007: Satellite and buoy observations of boreal summer intraseasonal variability in the tropical northeast Pacific. *Mon. Wea. Rev.*, **135**, 3-19.

Neale, R. B., J. H. Richter, and M. Jochum, 2008: The impact of convection on ENSO: From a delayed oscillator to a series of events. *J. Climate*, **21**, 5904-5924.

Rienecker, M. M., M. J. Suarez, R. Todling, J. T. Bacmeister, L. Takacs, H.-C. Liu, W. Gu, M. Sienkiewicz, R. D. Koster, R. Gelaro, I. Stajner, and J. E. Nielsen, 2008: The GEOS-5 data assimilation system-documentation of versions 5.0.1, 5.1.0, and 5.2.0. Goddard Space Flight Center, Greenbelt, Maryland 20771.

Roeckner, E., and Coauthors, 1996: The atmospheric general circulation model ECHAM-4: Model description and simulation of present-day climate. Rep. 218, Max-Planck-Institut fur Meteorologie, 94 pp.

Sperber, K. R., S. Gualdi, S. Legutke, and V. Gayler, 2005: The Madden-Julian oscillation in ECHAM4 coupled and uncoupled general circulation models. *Climate Dyn.*, **25**, 117-140.

Waliser, D. E., 2006: Predictability of tropical intraseasonal variability, in *Predictability of weather and climate*, edited by T. Palmer and R. Hagedorn, Cambridge University Press, 718 pp.

Wang, W. Q., S. Saha, H. L. Pan, S. Nadiga, and G. White, 2005: Simulation of ENSO in the new NCEP coupled forecast system model (CFS03). *Mon. Wea. Rev.*, **133**, 1574-1593.

Zhang, G. J., and M. Mu, 2005: Effects of modifications to the Zhang-McFarlane convection parameterization on the simulation of the tropical precipitation in the National Center for Atmospheric Research Community Climate Model, version 3. *J. Geophys. Res.*, **110**, D09109.

Zhao, M., I. M. Held, S. J. Lin, and G. A. Vecchi, 2009: Simulations of global hurricane climatology, interannual variability, and response to global warming using a 50-km resolution GCM. *J. Climate*, **22**, 6653-6678.

Science and Technology Infusion Climate Bulletin
NOAA's National Weather Service
35th NOAA Annual Climate Diagnostics and Prediction Workshop
Raleigh, NC, 4-7 October 2010

Seasonal Temperature Forecast Skill of OCN and EOCN with Seasonally Dependent and Yearly Updated Parameters

Peitao Peng, Arun Kumar and Huug van den Dool

Climate Prediction Center, NCEP/NWS/NOAA, Camp Springs, Maryland

1. Introduction

Rapid changes of climate in last 30 years has made the WMO recommended climate normal (*i.e.*, 30-year mean and updated every 10 years) no longer appropriate. The average over shorter period may be more representative of current state and a better estimate of the upcoming expected value. Based on this perspective, the optimal climate normal (OCN) method (*i.e.*, taking average over optimal shorter period) has been developed as a tool of seasonal climate forecast (Huang *et al.* 1996). In an effort to take account of multiple time scales in climate variability and avoid the spatial discontinuity of the optimal averaging time in OCN method, Peng and van den Dool (2002) modified the OCN tool by invoking EOF-PC decomposition technique, that is, applying OCN method to principal components (PCs) of temperature field and then combining the forecasted PCs with their associated EOFs to construct a temperature forecast. This EOF based OCN method is called EOCN.

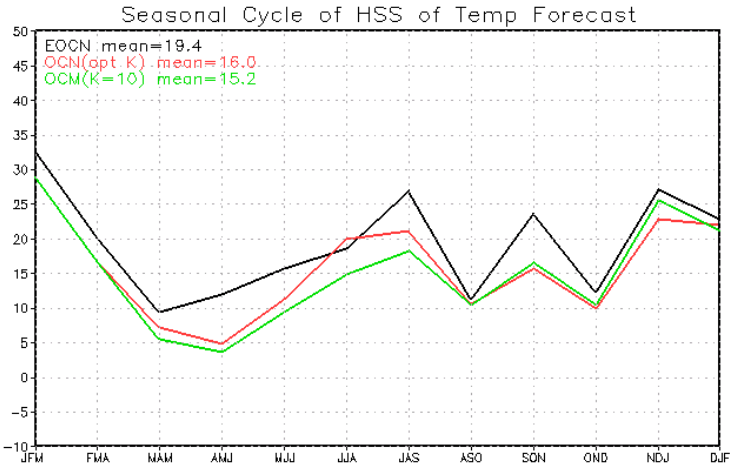

Fig.1 Seasonal cycle of Heidke skill score over the period of 1995-2009 for the temperature forecast with EOCN, OCN with K=10 years and OCN with yearly updated K.

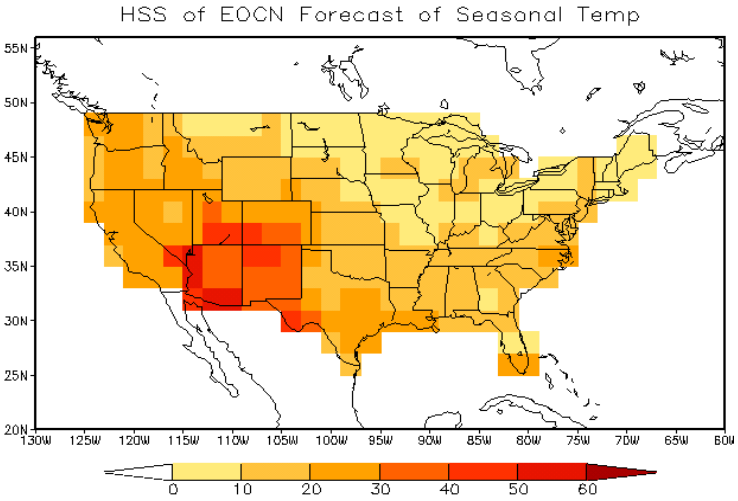

Fig.2 Spatial distribution of HSS for EOCN seasonal temperature forecast.

The length of the optimal averaging time (OAT) used in current operational OCN method (*i.e.*, 10 years) was determined with the data before 1994 and has been kept in use thereafter. Similarly in the EOCN, the EOF dependent OATs were determined with the data before 2003 and also not changed. Considering that the climate record may not be very stationary in terms of its statistics, we expect that having the OATs updated may be helpful to catch some secular changes in the data. Also, because of the limited data length back to the time, the skill of the OCN and EOCN were estimated with the data not quite independent of that used for training the tools, we therefore feel it is time to have a more objective skill assessment for the tools with the data added in recent years.

The purpose of this study is to examine the impact of the yearly updated OAT onto the performance of

Correspondence to: Peitao Peng, Climate Prediction Center, NOAA/NWS/NCEP, Camp Springs, MD 20746;
E-mail: Peitao.Peng@noaa.gov

OCN, assess the forecast skill of both OCN and EOCN in past two decades and then have a comparison with some other seasonal forecast tools used in the Climate Prediction Center (CPC).

2. Data and methodology

The data used in this study are the seasonally averaged daily temperature of 102 United States' climate divisions from JFM of 1931 to DJF of 2009/2010. The skill assessment is performed over the period of JFM 1995- DJF 2010, aligned with the assessment for CPC official seasonal forecast.

In the OCN method, the forecast for a given season is simply the average of the same season data over the most recent K years. The K, or the length of OAT, corresponds to the minimum root-mean-square error of all the retrospective forecast since 1961 and for all the 102 climate divisions. Therefore, it is seasonally dependent and yearly updated.

In the EOCN method, the temperature anomaly of a given season in year n and at climate division i is expressed as

$$T(i,n) = \sum_{m=1}^{M} \alpha_m(n) E_m(i),$$

where E_m and α_m are the m^{th} rotated EOF pattern and its associated PC respectively, M is the number of the kept modes. We take M = 6 because the modes with m>6 are basically noise for temperature. Applying the OCN method to the m^{th} PC, we have the PC forecast as

$$\overline{\alpha}_{m,K}(n) = \frac{1}{K_m(n)} \sum_{j=1}^{K} \alpha_m(n-j),$$

where the $K_m(n)$, depending on both mode and time, corresponds to the minimum root-mean-square error of all the retrospective forecast since 1961. The anomalous temperature forecast thus is given by

$$T^f(i,n) = \sum_{m=1}^{M} \overline{\alpha}_{m,K_m(n)}(n) E_m(i).$$

For the forecast verification, the Heidke skill score (HSS) is used to measure the skill. Denoting n as the number of observation and h as that of hit (correct forecast), the skill score is written as

$$HSS = 100\left(\frac{h - n/3}{n - n/3}\right).$$

Its range is from -50 to 100, with 0 as non-skill and 100 as perfect.

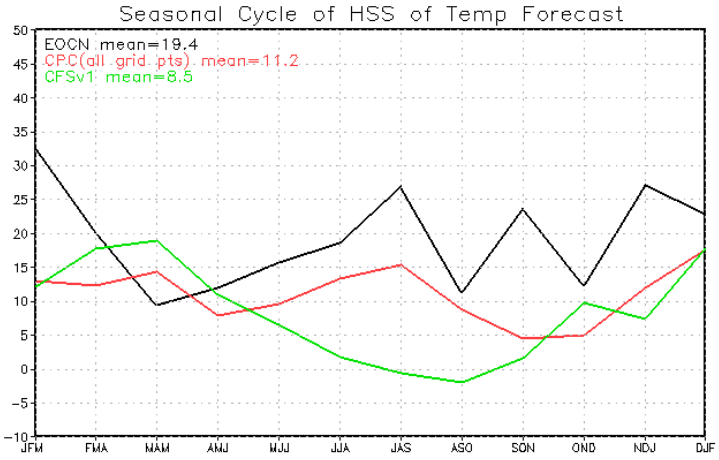

Fig.3 Seasonal cycle of HSS over the period of 1995-2009 for the temperature forecast with EOCN, CPC official and CFSv1.

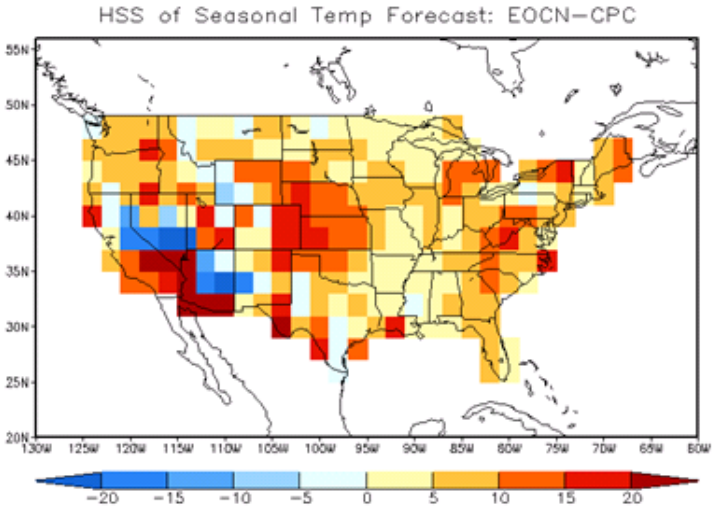

Fig.4 HSS difference between EOCN and CPC official with former minus later.

Season	*JFM*	*AMJ*	*JAS*	*OND*
OAT	*10*	*8-10*	*10 to 8*	*9 to 8*

Table 1 Optimal averaging time (in years) in OCN method for the 1995-2009 period

3. Results

(a) Variations of OAT

For the OCN method, as shown in Table 1, the OAT of JFM season has kept 10 years over the whole verification period (1995-2009); for AMJ season, it fluctuated between 10 and 8 years; while for other two seasons, it gradually got little bit shorter to 8 years. The fluctuation in AMJ may be due to the sampling error, while the tendency towards shorter period in JJA and SON may reflect the non-stationary characteristics of the data.

For the EOCN method, table 2 gives the OAT averaged over the verification period for the 6 modes and the four seasons. Except the season to season change as in the OCN method, the OAT in EOCN also changes from one mode to the other, with a range from 5 to 10. This mode dependence may indicate that the EOCN method is able to catch some variability with multiple time scales.

Season	*JFM*	*AMJ*	*JAS*	*OND*
RPC1	*10*	*10*	*8*	*8*
RPC2	*9*	*8*	*8*	*9*
RPC3	*9*	*7*	*10*	*7*
RPC4	*8*	*9*	*9*	*9*
RPC5	*5*	*9*	*5*	*8*
RPC6	*5*	*5*	*9*	*5*

Table 2 Optimal averaging time (in years) in EOCN method for the 1995-2009 period. The numbers are time averaged. There is 10-20% fluctuation for some modes in some seasons.

(b) Skill comparison for EOCN and OCN

Fig.1 shows the seasonal cycle of HSS over the verification period (1995-2009) for the EOCN, the OCN with 10-year OAT and the OCN with yearly updated OAT. Obviously, EOCN is the best for almost all the seasons, with annually averaged score to be 19.4, about 4 points higher than the OCN with 10-year OAT. On the other hand it is somewhat disappointed that the OCN with yearly updated OAT is only slightly better than that with OAT=10 in summer seasons.

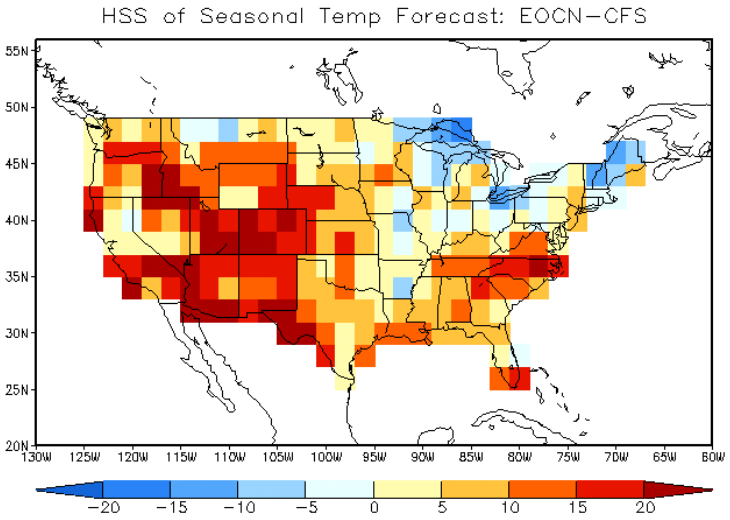

Fig.5 HSS difference between EOCN and CFSv1 with former minus later.

Fig.2 gives the spatial distribution of HSS for the EOCN. It shows the higher skill in southwest and the lower skill in northeast. Both versions of OCN has a similar skill distribution to the EOCN, except the OCN's is significantly lower in middle and south whereas slightly higher in northeast than the EOCN's (not shown).

(c) Comparison of EOCN with CPC official forecast and CFSv1

Fig.3 presents the seasonal cycle of HSS for CPC official forecast, CFSv1 and EOCN. Once again, EOCN performed the best among the all for most seasons. Its skill score averaged over all the seasons is about 8 points higher than the CPC official and 11 points higher than the CFSv1. CFSv1 is superior only for MAM season. CPC official did pretty good job for JJA and JAS seasons, but is still in the shadow of EOCN. The spatial distribution of the HSS differences between EOCN and CPC official is shown in Fig.4, where it can be seen that the EOCN is superior almost everywhere except in a narrow strip in southwest. Fig.5 shows the same type of information but for CFS v1, which lost to EOCN in central, west and south, but won in northeast.

4. Summary

The skill scores averaged over the period of 1995-2009 and the 102 climate divisions for all the forecast tools discussed above are compared in Fig 6. It turns out that the impact of the OAT updating is quite limited. The EOF adjustment is still the major player in the skill improvement for OCN.

It is quite surprising that the skill of CFSv1 is so much lower than the OCN and EOCN methods. The failure of CFSv1 in predicting low frequency climate variability may be partially due to its fixed CO_2 content. Some improvement can be expected from CFSv2, which has been in operational recently. The modest skill of CPC official forecast may reflect the difficulty in the consolidation of different forecast tools. How to optimally combine the forecasts from different tools is still a challenging issue.

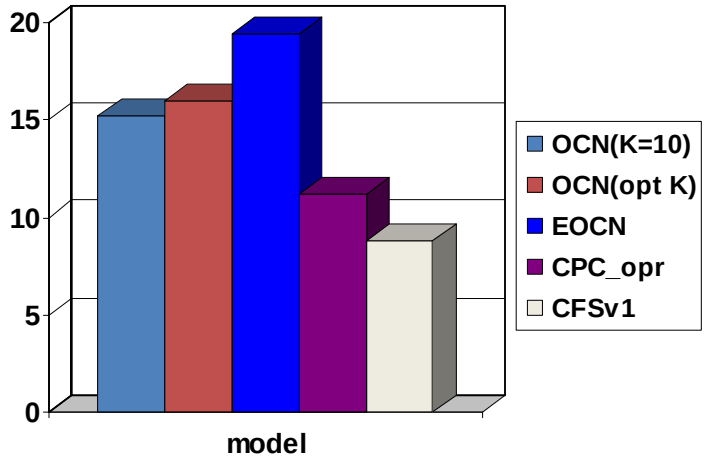

Fig.6 HSS averaged over the period of 1995-2009 and 102 climate divisions for the temperature forecast with OCN (K=10), OCN (changing K), EOCN, CPC official and CFSv1.

References

Huang, Jin, H. M. van den Dool and A. Barnston, 1996: Long-lead seasonal temperature prediction using Optimal Climate Normals. *J. Climate*, **9**, 809-817.

Peng, Peitao and H. M. van den Dool, 2002: Adjusting the OCN prediction methods invoking EOFs. *27th Climate Prediction and Diagnostics Workshop*. George Mason University, October, 21-25, 2002.

Science and Technology Infusion Climate Bulletin
NOAA's National Weather Service
35th NOAA Annual Climate Diagnostics and Prediction Workshop
Raleigh, NC, 4-7 October 2010

What Can We Learn about the Northern Hemisphere Circulation from the 20th Century Reanalysis?

Philip Pegion[1,2], Martin Hoerling[1] and Judith Perlwitz[1,2]

[1]*NOAA Earth System Research Laboratory / Physical Sciences Division*
[2]*CIRES / University of Colorado*

1. Introduction

The Winter of 2009/2010 saw record negative values of the North Atlantic Oscillation (NAO), and associated with these large departures of the NAO, there was record cold temperatures in the Eastern United States and throughout Europe. The recently completed 20th Century Reanalysis allows for an in-depth analysis of the atmosphere's circulation dating back to 1871. The questions we aim to answer is how unusual was the Atmosphere's circulation during the winter of 2009/2010, and are the NAO and the Arctic Oscillation just different terms for the same phenomena?

2. Data

Monthly mean near surface and upper-air fields from the NCEP/NCAR Reanalysis (Kalnay 1995) and 20th Century Reanalysis (Compo et al. 2010) are used to calculate the NAO/AO indices and correlations. Also, the Thompson Wallace AO Index (Thompson and Wallace 2000) is also used for comparison. In addition, daily fields from the 20th Century reanalysis are used to calculate daily indices.

The two indices calculated in the study are the Arctic Oscillation (AO) and the North Atlantic Oscillation (NAO). The spatial pattern of the AO is defined as the leading EOF of monthly surface pressure (or 1000 hPa Height) poleward of 20°N for the years 1979-2000. Monthly and daily values of the AO index are derived by projecting anomalies onto the leading EOF and normalizing by the standard deviation of the AO index over the base period.

The North Atlantic Oscillation has several definitions. Four of them are used in this study, and they are referred as the CPC method (CPC-NAO), sector EOFS of 500 mb Height (z500-EOF) and Surface pressure (PSF-EOF) and box averages (Boxes). The CPC method is a regression of standardized 500 hPa height onto sliding 3 month windows of the first 10 rotated EOFs pole-ward of 20°N. The Sector EOFs are a projection of 500 hPa height or surface pressure anomalies onto the leading EOF of Dec-Jan-Feb means over the Atlantic sector (20°N–90°N;120°W-60°E), and the box averages are defined as the monthly sea-level pressure anomaly difference (35°N-45°N, 10°W-70°W) – (55°N-70°N,10°W-70W).

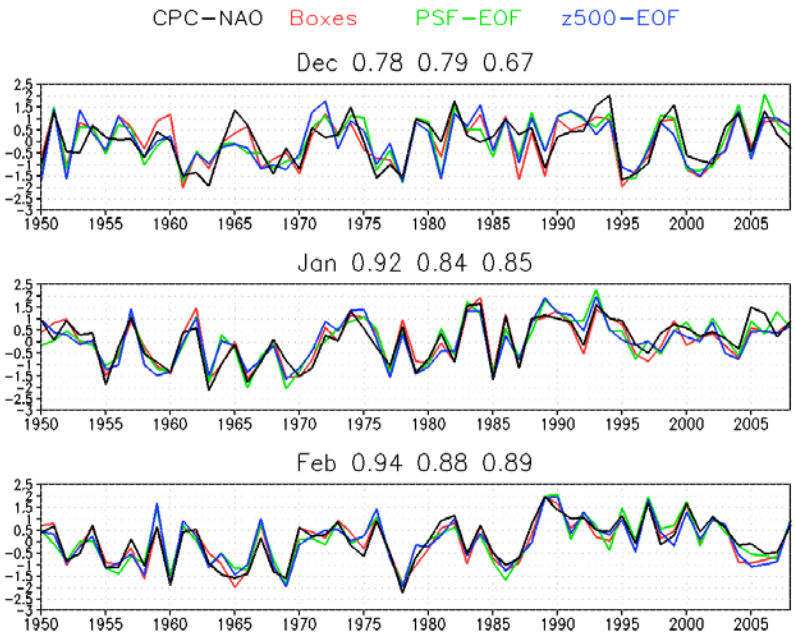

Fig. 1 Monthly values of the NAO index from four different methods. There is disagreement among the indices for December. The values in the title are the correlation of the CPC-NAO index with the others.

Correspondence to: Philip Pegion, Physical Sciences Division, NOAA Earth System Research Laboratory, Boulder, CO; E-mail: Philip.Pegion@noaa.gov

3. Results

Monthly values of the NAO index for the months of December, January and February (Fig. 1) show that the different methods give similar values for January and February, but December has less agreement. The CPC method has been determined to be an outlier and CPC has been contacted out this issue.

The spatial structure of the wintertime (DJF) AO and NAO show very similar correlations across much of the Northern Hemisphere (Fig. 2), with negative correlations over the polar region, and positive correlations in the mid-latitudes. Even the loading pattern of the AO has more explained variance in the Pacific sector. Regressions of the NAO and AO index also show similar patterns, and the difference of the regressions (Fig. 3) show no coherent structure, which provides more evidence that these two indices are capturing the same physical process, but we are unable to say which one does a better job.

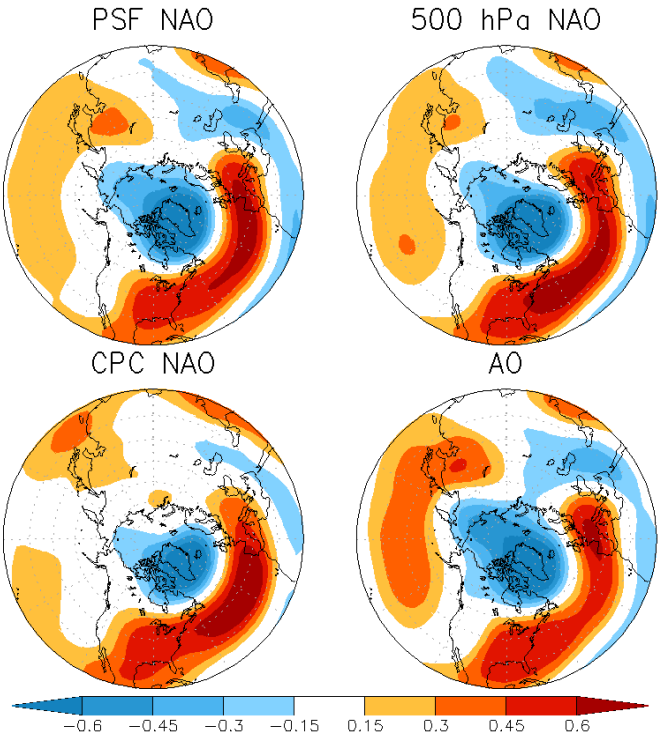

Fig. 2 Spatial correlation averaged for December-January-February for 3 different NAO indices and the AO index for 500 hPa height. All indices show similar spatial correlations.

Since the 20th Century reanalysis is available 4 times a day, a daily AO or NAO index is able to be calculated back to 1871. Several other years that had extremely negative monthly values of the AO are shown (Fig. 4) in order to put the winter of 2009/10 into a historical context. This analysis shows that although the seasonal mean for the winter of 2009/10 is the lowest on record, there have been periods in previous years with much lower daily values. It was the combination of the low values along with the persistence of these values that made 2009/10 the record year.

4. Conclusions

The 20th Century reanalysis allows for daily AO indices to be calculated back to 1871. A look at the daily values shows that this past winter did not have extremely negative daily AO values, but was very persistent compared to other extremely negative winters. Also, the winter (DJF) seasonal mean AO value was -3.4, which is a record for the past 140 years.

The AO and NAO indices calculated from the 20th Century Reanalysis are indistinguishable, and the difference to the CPC NAO index is limited to the Pacific Sector. We have not been able to determine

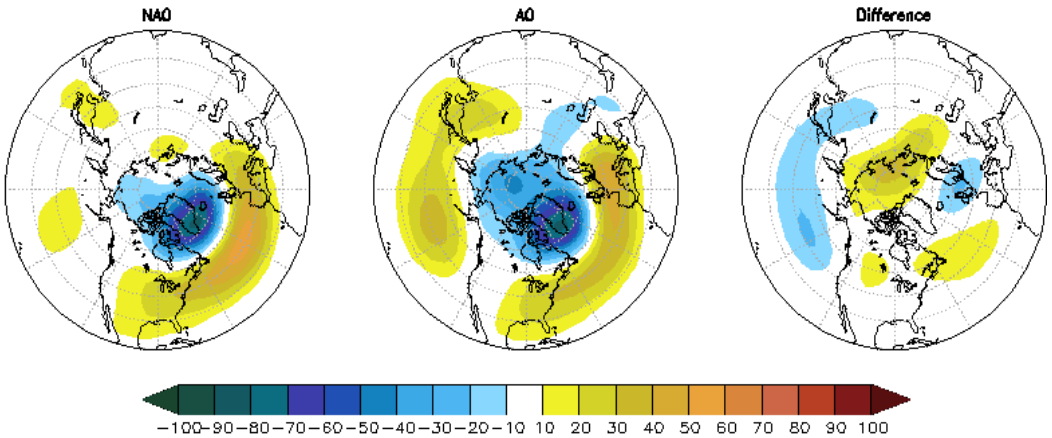

Fig. 3 DJF averages of 500 hPa height regressed onto the monthly CPC NAO (left column), AO (middle column) and difference (right column).

which index captures the physical mode of the atmosphere.

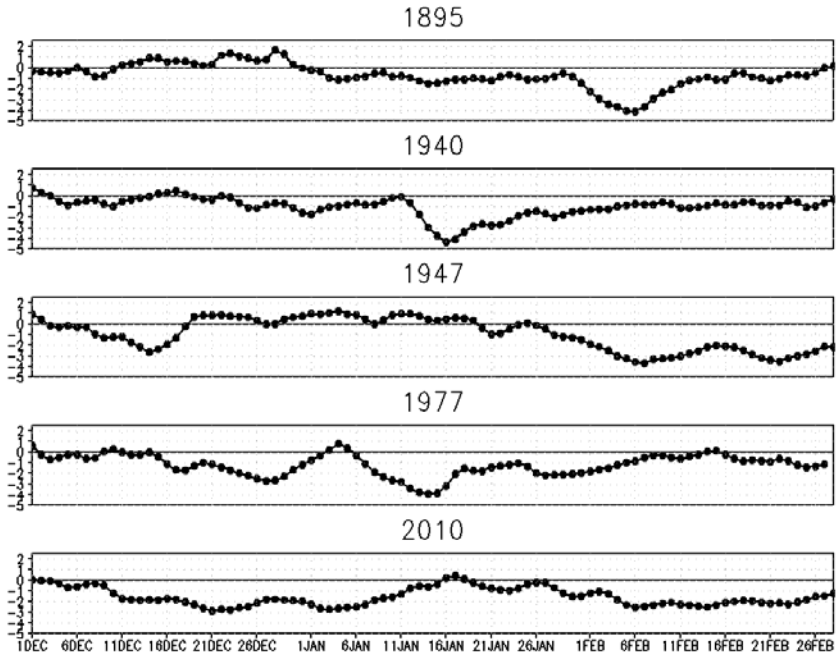

Fig. 4 Daily AO values for select years. Although the winter 2010 had the lowest seasonal AO on record, individual daily values have been lower in other years.

References

Compo, G.P., J.S. Whitaker, P.D. Sardeshmukh, N. Matsui, R.J. Allan, X. Yin,B.E. Gleason, R.S. Vose, G. Rutledge, P. Bessemoulin, S. Brönnimann, M. Brunet, R.I. Crouthamel, A.N. Grant, P.Y. Groisman, P.D. Jones, M.C. Kruk, A.C. Kruger, G.J. Marshall, M. Maugeri, H.Y. Mok, Ø. Nordli, T.F. Ross, R.M. Trigo, X.L. Wang, S.D. Woodruff, S.J. Worley, 2010: “The Twentieth Century Reanalysis Project”. *Quart. J. Roy. Meteor. Soc.*, submitted.

E. Kalnay, M. Kanamitsu, R. Kistler, W. Collins, D. Deaven, L. Gandin, M. Iredell, S. Saha, G. White, J. Woollen, Y. Zhu, M. Chelliah, W. Ebisuzaki, W.Higgins, J. Janowiak, K. C. Mo, C. Ropelewski, J. Wang, A. Leetmaa, R. Reynolds, Roy Jenne, Dennis Joseph 1996: "The NCEP/NCAR 40-Year Reanalysis Project". *Bulletin of the American Meteorological Society* **77** (3): 437–471.

Thompson, David W. J., John M. Wallace, 2000: Annular Modes in the Extratropical Circulation. Part I: Month-to-Month Variability*. *J. Climate*, **13**, 1000–1016.

Science and Technology Infusion Climate Bulletin
NOAA's National Weather Service
35th NOAA Annual Climate Diagnostics and Prediction Workshop
Raleigh, NC, 4-7 October 2010

Predictability of Dry Season Reforecasts over the Tropical South American Region

Adam J. Frumkin and Vasubandhu Misra

Center for Ocean-Atmospheric Prediction Studies,
Department of Earth Ocean and Atmospheric Sciences,
Florida State University, Tallahassee, FL

1. Introduction

The potential predictability of the dry phase of South American monsoon (SAM) has been studied relatively little when compared to the wet phase. In fact it was not until Zhou and Lau (1998) that South America (SA) was recognized as having a monsoon climate. The SAM went unrecognized for such a long period due to the fact that it does not exhibit a distinct seasonal reversal of winds. It is not until the annual mean is removed from the seasonal mean that a wind reversal appears. Although the SAM does not exhibit a seasonal reversal in the wind field, it does exhibit a distinct seasonal cycle in precipitation; a wet phase occurs during Austral summer [December-February (DJF)] and a dry phase occurs during the winter [June-August (JJA)]. A rapid increase in precipitation occurs during the spring [September-November (SON)] and a decrease during March-May (MAM). Additionally, the SAM exhibits large-scale land-sea temperature differences, a large-scale thermally direct circulation with a continental rising branch and an oceanic sinking branch, land-atmosphere interactions associate with elevated terrain and land surface conditions, surface low pressure and an upper level anticyclone, and intense low-level inflow of moisture to the continent (Vera *et al.* 2006).

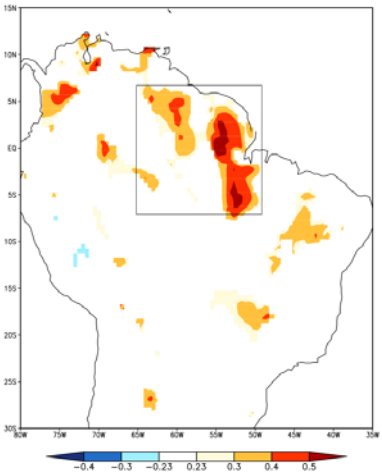

Fig. 1 Correlation of JJA rainfall with the following DJF rainfall. Only statistically significant values are shaded. The box represents the middle-lower reaches of the Amazon River.

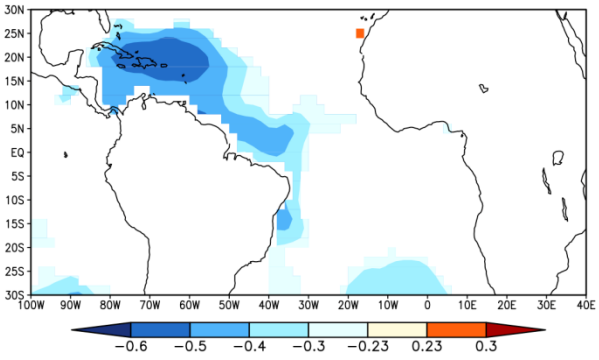

Fig. 2 Correlation of JJA ERSSTv3 with DJF Climate Research Unit (CRU) Rainfall. Only statistically significant values are plotted.

In this study we wish to investigate the predictability of the dry phase of the SAM (JJA) in two climate models and the potential improvement that dynamical downscaling and bias correction processes can have on forecasts. New research suggests that the dry phase of the SAM may be more significant than previously anticipated. Strong positive correlations exist between JJA rainfall and the following DJF rainfall particularly over north east Brazil (Figure 1). Additionally, strong negative correlations exist between DJF rainfall within the box in Figure 1 and JJA SSTs in the region of the Atlantic Warm Pool (AWP; Figure 2). This implies that higher than normal precipitation during JJA is followed by higher than normal precipitation during the following DJF and a cooler than normal AWP during the following JJA.

Prior research has shown that dynamical downscaling can improve model output primarily through improved resolution and model physics (Chan and Misra 2009). Anomaly nesting (i.e. bias correction) should

Correspondence to: Adam J. Frumkin, Center for Ocean-Atmospheric Prediction Studies, Department of Earth Ocean and Atmospheric Sciences, Florida State University, Tallahassee, FL 32306; E-mail: ajf09f@fsu.edu

also improve model output by reducing the bias of the global climate model (GCM) before the downscaling is performed with the regional climate model (RCM) (Misra and Kanimitsu 2004).

2. Data and Methodology

Model reforecasts from eight dry seasons (2000-2007) are analyzed in this study. Reforecasts are performed using the NCEP Climate Forecast System (CFS) and the NCEP Scripps Regional Spectral Model (RSM). A second integration of the RSM (RSM-AN), which uses a bias correction process, is also used for comparison. The bias correction process used in this study is based on the Anomaly Nesting method from Misra and Kanamitsu (2004). This method replaces the GCM climatology with the climatology from reanalysis before the downscaling process is performed. In this study, CFS climatology is replaced with NCEP NCAR Reanalysis I (atmosphere) and ERSSTv2 (ocean). The CFS is run at triangular spectral truncation T62 and the RSM is run at a 60km resolution. Both models use six ensemble members which are generated by perturbing the initial atmospheric conditions. Atmospheric conditions are perturbed by resetting the initial date of the atmospheric restart file after integrating the model for a week. Land and ocean states remain unchanged between ensemble members.

The fidelity of the three models' reforecasts is investigated. Particular attention is paid to the two regions outlined in figure 3 (Amazon River Basin (ARB) and the subtropical region (ST)). Using CFSR (temperature and precipitation) and TRMM 3B-43 (not shown) and CMAP (not shown) regions of significant model bias for the fields of temperature and precipitation are identified. Fields are averaged over JJA, 2000-2007 so as to provide an eight-year seasonal average. The Relative Operator Characteristic (ROC) curves are plotted and the area under the curve (AUC) is calculated as a measure of the model's skill at predicting an event (Mason and Graham, 1999). ROC curves are scatter plots of hit rate to false alarm rate for varying thresholds of accuracy. In this study, events are defined as above normal, normal, and below normal temperature and precipitation. The threshold used to determine whether or not a model will predict a "yes" or "no" occurrence of an event is the number of ensemble members required to have correctly identified an event. For example, if the threshold were "4 ensemble members" and observations identified a particular year to have had above average precipitation, we would require 4 or more members to predict above average precipitation in order to say that the model got a "hit". A model can "perfectly" predict an event for a given threshold if it gets a "hit" for each of the 8 years in our study.

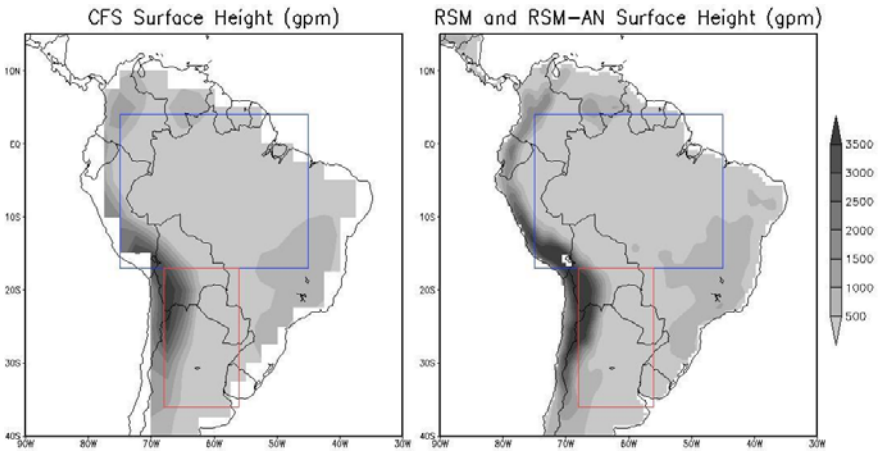

Fig. 3 Topography (gpm) is plotted with the land surface mask applied for the CFS (left) and RSM (right). The blue box represents the Amazon River Basin region and the red box represents the subtropical region.

3. Results

a. Model Bias

Precipitation patterns are realistic in all three models (Figure 4). The ITCZ is well defined around 8ºN. All models also show precipitation minima over a majority of the ARB and the ST regions as well as over the equatorial South Pacific Ocean.

When compared to the CFSR, regions of significant model bias become evident (Figure 5). All three models show a significant positive bias over mountainous terrain and large negative biases over the tropical South Pacific Ocean. The CFS and the RSM-AN have similar patterns of bias. Both have large negative bias

in the northern SA, negative bias in the La Plata Basin, and weak positive bias over southeastern Brazil. The anomaly nesting process in the RSM-AN is potentially responsible for the observed reduction in the magnitude of positive and negative biases in the CFS in southeastern Brazil and points further south. The RSM has large positive bias over most of Brazil, with the exception of extreme northeastern coastal regions. At first glance, it appears that the bias in the models is very large, with many regions having over 100% difference when compared to CFSR. However, it is important to remember that the precipitation rates in many of these regions are very small (*i.e.* <1mm/day) and a large percentage difference is easily achieved.

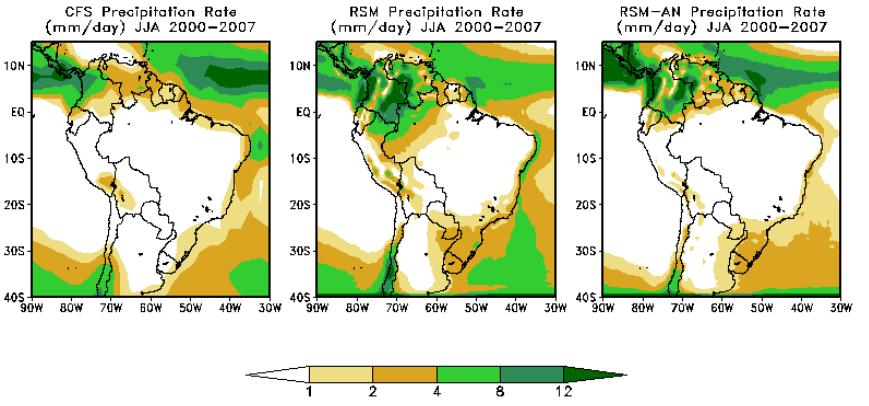

Fig. 4 Precipitation rate (mm/day) averaged over JJA and over all eight years (2000-2007). Values less than 1mm/day are masked. CFS (left), RSM (center) and RSM-AN (right).

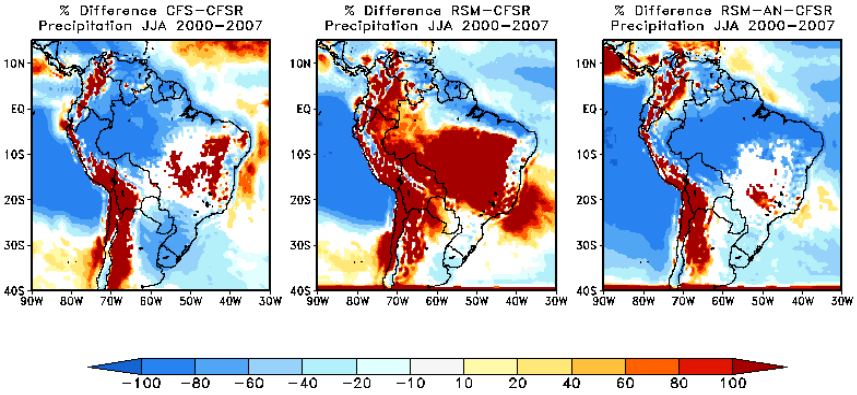

Fig. 5 Shows the percentage difference between the climatologically averaged JJA precipitation rate of the model (CFS[left], RSM[center], RSM-AN[right]) and CFSR averaged over the same period. Only significant values are plotted. Each plot is normalized using the CFSR.

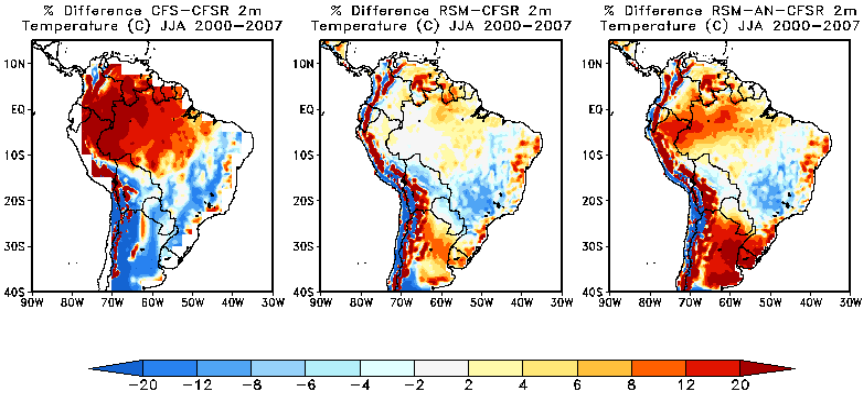

Fig. 6 Same as Figure 5 except for temperature (°C).

Bias maps of temperature are much nosier than precipitation (Fig. 6). One similarity between all three models is positive biases in equatorial regions. Both the RSM and RSM-AN have less bias than the CFS in this region. Interestingly, the RSM reduces the bias more than the RSM-AN. All models also show small negative biases in southern Brazil. In subtropical regions the CFS has primarily negative biases while the RSM and RSM-AN have positive biases.

b. Model Skill

In this study the RCM shows some improvement over the GCM at forecasting temperature but not necessarily when forecasting precipitation. In the ARB the CFS predicts above average temperatures most skillfully (Table 1; AUC=0.667). While the RSM and RSM-AN also forecast above normal temperatures best, they improve upon the CFS with scores of 0.792 and 1 respectively. In the ST region, the CFS has AUCs of 0.5 for all 3 events, which indicates no skill. The RSM and RSM-AN again improve upon the CFS; both have AUCs around 0.9 when predicting below normal temperatures.

AUCs are generally much less when predicting precipitation due to the random nature of this field. This characteristic is replicated in our results. In the ARB the CFS predicts only below normal precipitation with some skill (AUC=0.792). It is interesting to see that the RSM shows very little skill in this region for any event while the RSM-AN improves upon the CFS significantly with an AUC of 0.958 when forecasting above normal precipitation. In the ST, only the RSM achieves an AUC above 0.5, with a score of 0.67 when forecasting above normal precipitation. The fact that no model has high AUCs in the ST is consistent with signal to noise ratio plots (not shown), which show significantly more signal in the ARB than the ST during the dry season.

Area Under The ROC Curve Amazon River Basin	CFSR					
	Temperature			Precipitation		
	A	N	B	A	N	B
8 Years of CFS 6 ensembles	0.667	0.438	0.625	0.458	0.5	0.792
8 years of RSM, 6 Ensembles	0.792	0.75	0.75	0.583	0.22	0.458
8 Years of RSM-AN, 6 Ensembles	1	0.969	0.625	0.958	0.59	0.708

Area Under The ROC Curve Subtropical Region	CFSR					
	Temperature			Precipitation		
	A	N	B	A	N	B
8 Years of CFS 6 ensembles	0.5	0.5	0.5	0.417	0.438	0.5
8 years of RSM, 6 Ensembles	0.5	0.75	0.958	0.67	0.5	0.208
8 Years of RSM-AN, 6 Ensembles	0.542	0.34	0.917	0.167	0.5	0.167

Table 1 Shows the area under the ROC curves for the ARB (top) and ST (bottom). Areas are calculated by comparing models with CFSR. Areas are calculated for three events, above normal (A; orange), normal (N; white), and below normal (B; blue) and are calculated for temperature and precipitation. Values less than or equal to 0.5 indicate that the model has no skill at forecasting the variable for that particular event and the user would be better off using climatology as a forecast. A value of 1 means that the model is close to being perfect.

4. Concluding Remarks

All 3 models produced realistic looking fields of temperature and precipitation. However, bias plots show that all models are strongly biased in particular regions when compared to CFSR. As expected, biases of precipitation were significantly larger than those of temperature. This is most likely due to two factors. Precipitation is a noisy field that is not resolved well, particularly in climate models. Additionally, values of rain rate during the dry season are low; therefore, large percentage differences between data sets are easily achieved.

We have found that for both regions of interest, the downscaling process improves predictability of temperature, but not necessarily precipitation. In both the ARB and ST, AUCs for temperature increased from the CFS, to the RSM and RSM-AN. The anomaly nesting process improved upon the RSM, but only in the ST. It was not as clear whether the downscaling and anomaly nesting processes significantly improve the predictability of precipitation.

References

Chan, S.C., and V. Misra: Dynamic downscaling of the North American Monsoon with the NCEP Scripps Regional Spectral Model from the NCEP CFS global model. *J. Climate*, submitted.

Mason, S. J., and N. E. Graham, 1999: Conditional probabilities, relative operating characteristics and relative operating levels. *Wea. Forecasting*, **14,** 713–725.

Misra, V. and M. Kanamitsu, 2004: Anomaly nesting: a methodology to downscale seasonal 8 climate simulations from AGCMs. *J. Climate*, **17**, 3249-3262.

Vera, C, W. Higgins, J. Amador, T. Ambrizzi, R. Garreaud, D. Gochis, D. Gutzler, D. Lettenmaier, J. Marengo, J. Nogues-Paegle, P.L. Silva Dias, and C. Zhang, 2006: Toward a unified view of the American monsoon systems. *J. Climate*, **19**, 4977–5000.

Zhou, J., and K.-M. Lau, 1998: Does a monsoon climate exist over South America? *J. Climate*, **11**, 1020–1040.

Science and Technology Infusion Climate Bulletin
NOAA's National Weather Service
35th NOAA Annual Climate Diagnostics and Prediction Workshop
Raleigh, NC, 4-7 October 2010

Seasonality of the Pacific Decadal Oscillation

Hui Wang[1,2], Arun Kumar[1], Wanqiu Wang[1], and Yan Xue[1]

[1]*Climate Prediction Center, NCEP/NWS/NOAA, Camp Springs, Maryland*
[2]*Wyle Information Systems, McLean, Virginia*

1. Introduction

The Pacific decadal oscillation (PDO) is the leading EOF of monthly mean SST anomalies in the North Pacific (Mantua *et al.* 1997). With much focus on the low-frequency evolution of the PDO, its seasonal variation has received less attention. A better understanding of the seasonality of the PDO is important for potential improvements in our understanding of its predictability, its interaction with ENSO SST variability, and its global impacts.

This study aims to characterize the seasonality of the PDO and potential mechanisms. Our hypothesis is that the PDO seasonality is dominated by the combined influence of the seasonal variations in atmospheric forcing and oceanic mixed layer depth (MLD). Our emphasis is on the PDO evolution from spring to summer because there are significant changes in the characteristics of the PDO, the strength of the atmospheric forcing, and the MLD between the two seasons.

2. Data and methodology

Our analysis is based on data from observations and a coupled model simulation. The SST includes the NOAA OISST (Reynolds *et al.* 2002), NOAA ERSST (Smith *et al.* 2008), and simulated data from the NCEP Climate Forecast System (CFS; Saha *et al.* 2006). The OISST is over 28 years from 1982 to 2009. The 28-yr period of the satellite observations may be too short to represent PDO. The ERSST, with a longer record is also employed, which covers 100 years from 1910 to 2009. The last 480 years of SST from a 500-yr CFS coupled simulation are used in the analysis. The data from the CFS is divided into 16 segments of 30-yr periods. Each shorter-period segment is comparable with the 28 years of the OISST, and the analysis of PDO seasonality over 16 such realizations provides an estimate of variability in results due to sampling.

Monthly mean oceanic and atmospheric fields from the CFS are utilized to analyze their roles in the PDO seasonal variation. Ocean temperatures (5–300 m) are used to characterize the vertical structure of the PDO and to derive the MLD, which is estimated as the depth at which the temperature change from the ocean surface is

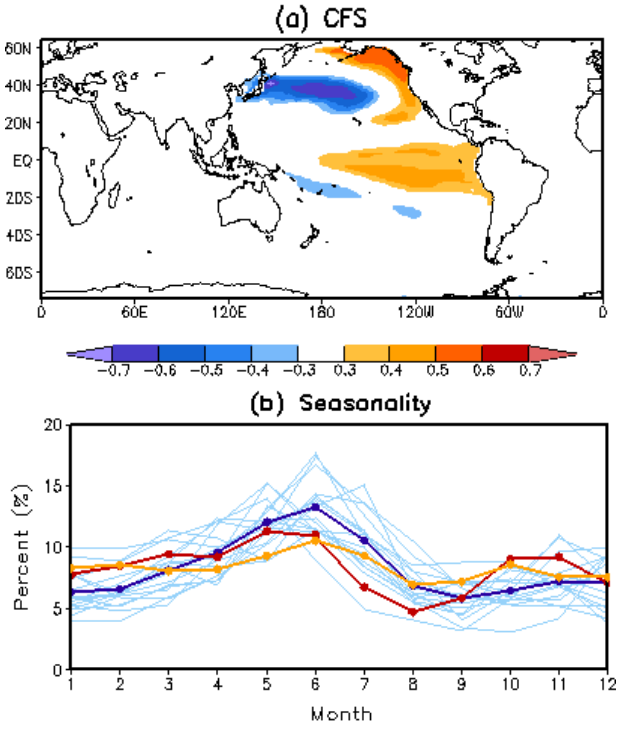

Fig. 1 (a) Spatial pattern of SST associated with the first EOF of monthly mean SST over the North Pacific based on the ensemble average of 16 leading EOFs for individual 30-yr segments from the 480-year CFS coupled run, and (b) seasonal distribution of the percentage variance of PC time series for OISST (red), ERSST (orange), 16 individual 30-yr segments (light blue), and 16-member ensemble (dark blue). The spatial pattern in (a) is displayed in the correlation map in which the monthly mean SST anomalies at each grid point are correlated with the PC time series.

Correspondence to: Hui Wang, Climate Prediction Center, NCEP/NWS/NOAA, Camp Springs, Maryland;
E-mail: Hui.Wang@noaa.gov

0.5 °C (Monterey and Levitus 1997). The atmospheric field from the CFS is inferred from 1000-hPa wind.

The PDO is identified as the first EOF of North Pacific SST between 20°N and 65°N based on the covariance matrix of the SST anomalies. Similar to Zhang *et al.* (1997), global mean SST anomaly is removed prior to the EOF analysis, to suppress the influence of the trend of global mean SST. The spatial structure of the PDO in the CFS is the ensemble mean of the 16 different realizations of the first EOF based on the individual 30-yr long segments.

3. Results

a. Seasonality of the PDO

Figure 1a shows the spatial pattern of SST associated with the PDO. The pattern correlation coefficient between the PDO in the observations and that in the CFS ensemble mean (Fig. 1a) is 0.88 and 0.92 for the OISST and ERSST (not shown), respectively. This mode accounts for 23% of North Pacific SST variance in the OISST, 24% in the ERSST, and 21% in the CFS.

The seasonality of the PDO is quantified by the distribution of the fraction (%) of total SST variance explained by the principal component (PC) time series over 12 calendar months, as shown in Fig. 1b. It is a measure of the seasonal variation of the amplitude of the PDO pattern. The amplitude of the PDO in the OISST and ERSST increases from winter to spring, reaches peak values in May and June, and then declines during summer, with a secondary maximum in fall. The PDO for the CFS ensemble mean displays a similar seasonality with a peak in June, but relatively higher variability in summer and lower variability in winter and fall. Overall, the seasonal distribution of the percentage variance for the observed PDO is well within the spread of 16 CFS ensemble members. Figure 1 suggests that both the spatial pattern and seasonality of the PDO in the CFS resemble those in observations. The following analysis focuses on the ensemble mean of 16 30-yr CFS coupled runs.

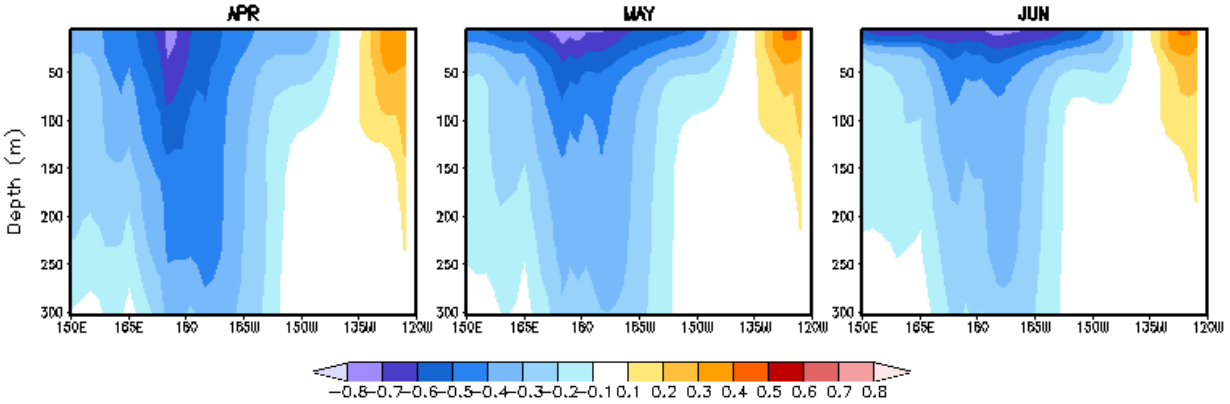

Fig. 2 PDO-related monthly ocean temperature anomaly (°C) at 37°N. The anomalies are associated with one standard deviation in the PC time series for months from April to June.

Figure 2 shows the depth–longitude cross-section of the PDO-related monthly mean ocean temperature anomalies at 37°N from April to June. They are obtained by regressing monthly mean ocean temperature anomalies onto the PC time series of each 30-yr segment for each calendar month and then averaging regression patterns over the 16 such regression patterns. Latitude 37°N is the location at which the PDO SST anomaly has the largest amplitude (Fig. 1a). Colder ocean temperature anomalies greater than 0.4°C penetrate to the depth of 250 m in April. In May, there is an abrupt decrease in the depth of the temperature anomalies colder than 0.4°C. These anomalies become progressively shallower during summer. The seasonal variation of the PDO is coupled with the seasonal changes of ocean temperature underneath.

b. The role of seasonal variations of the MLD and atmospheric forcing

In this section we show that the mean seasonal cycle of the MLD is important in determining the timing of the maximum variability of the PDO. Figure 3 shows the 16-member ensemble of 30-yr climatological

MLD from April to June derived from the CFS. The seasonal variation of the mixed layer is characterized by deep MLD in winter and early spring (not shown) and shallow MLD in May and summer. The MLD experiences a sharp decrease from more than 100 m in April to less than 50 m in May over most of the North Pacific. This sudden change coincides with the seasonal change of the depth of the ocean temperature anomalies associated with the PDO (Fig. 2).

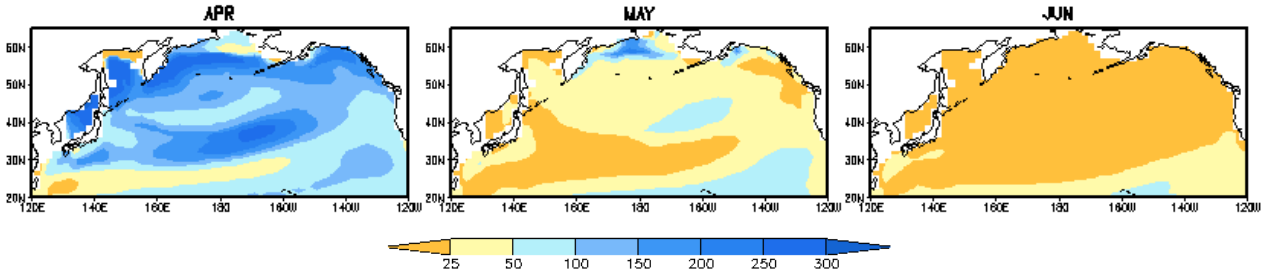

Fig. 3 Monthly climatology of the mixed layer depth (MLD; m) in the North Pacific derived from the CFS coupled run ensemble averaged over 16 30-yr segments for months from April to June.

To explore the contribution of surface wind forcing in generating PDO seasonality, an EOF analysis is performed for 1000-hPa zonal wind over the North Pacific to identify the dominant mode of the atmospheric circulation variability. The leading EOF of the surface wind (not shown) exhibits a basin wide cyclonic circulation over the North Pacific associated with the variability of the Aleutian low. The budget analysis in Chhak *et al.* (2009) suggests that anomalous horizontal advection of mean SST by anomalous Ekman transport contributes primarily to the PDO-related SST pattern. In addition, the distribution of the surface wind also infers partially the wind-driven SST anomalies related to the PDO. Overall, both the warm and cold SST anomalies in the North Pacific are dynamically consistent with the surface wind pattern, indicating the PDO-related SST anomalies are likely driven by the dominant mode of the atmospheric circulation. It is noted also that the surface wind anomalies are strongest in February and March (not shown), whereas the SST anomalies are strongest in May and June.

The cause and effect relationship between the surface wind and SST anomalies is further inferred from lag correlations between the two PC time series of the first EOFs of the 1000-hPa zonal wind and North Pacific SST, as shown in Fig. 4. Significant correlations are found when the zonal wind leads the SST up to three months, but correlations are weak when the zonal wind lags the SST. The strongest correlation occurs for the zonal wind leading the SST by one month. This implies that the time scale for the SST response to atmospheric wind forcing is about one month.

To illustrate the importance of the interaction between the atmospheric forcing and the MLD on the seasonality of the PDO, shown in Figs. 5a and 5b are the seasonal variation of area-averaged monthly 1000-hPa zonal wind variance associated with the first EOF of the 1000-hPa zonal wind and the evolution of the MLD over the North Pacific domain. The surface zonal wind displays strong seasonality with the largest variability in February and March. The atmospheric forcing is thus strong in February and March and weak in summer. The MLD shows a similar seasonality with deepest depth in February and March and shallowest in summer.

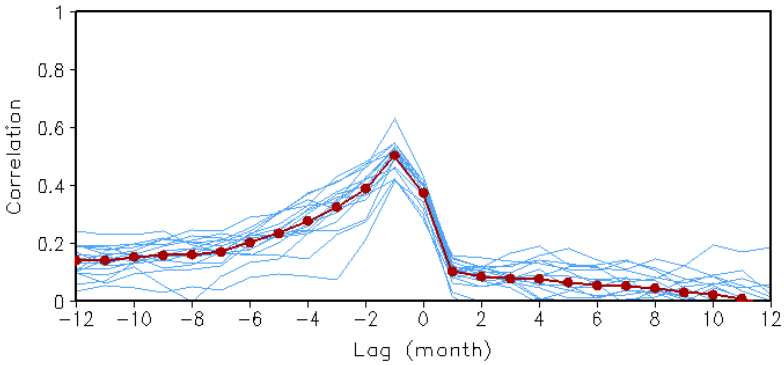

Fig. 4 Lag correlations between the PC time series of the first EOF of monthly 1000-hPa zonal wind and SST over the North Pacific in the CFS coupled run for each 30-yr period (blue) and ensemble average (red) of the 16 correlation coefficients at different lags. Negative (positive) lag means the 1000-hPa zonal wind leading (lagging) the SST.

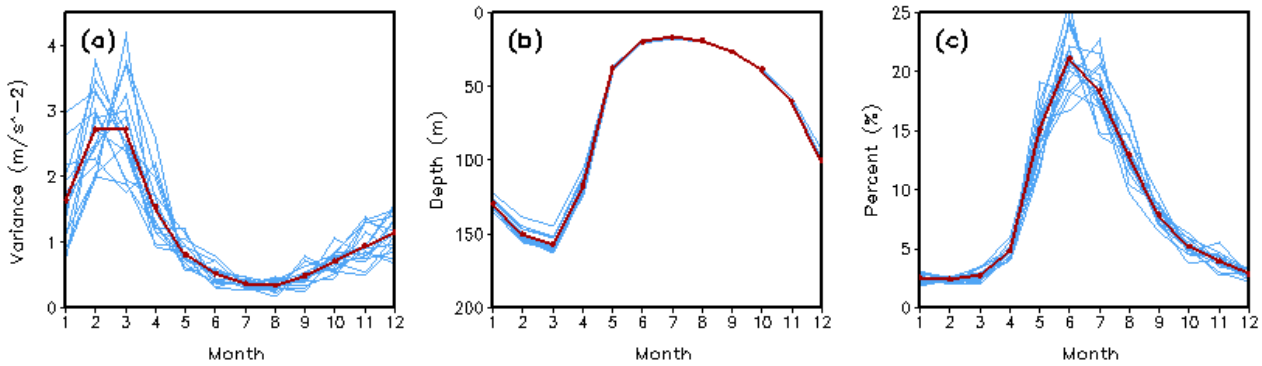

Fig. 5 Seasonal variations of area average over the North Pacific (20°–65°N, 125°E–100°W) for individual 30-yr periods for (a) variance of the 1000-hPa zonal wind anomaly associated with the first EOF, (b) climatological MLD, and (c) square root of the zonal wind variance in month N–1 divided by the MLD in month N. Blue lines are for 16 individual members and red lines for ensemble means.

Variations in the surface wind forcing clearly cannot explain the peak of the PDO variability in May and June. Since it is the mixed layer in the upper ocean that directly responds to the atmospheric forcing, the MLD is also expected to play an important role in determining the effectiveness of SST response to the atmospheric forcing. To illustrate this, Fig. 5c shows the seasonal variation of the square root of the zonal wind variance divided by the MLD. The square root of the zonal wind variance denotes the amplitude of the zonal wind anomaly and thus the amplitude of atmospheric forcing. As divided by the MLD, the value is approximately proportional to the forcing per unit mass for the mixed layer over which the influence of atmospheric forcing gets distributed and affects the SST anomaly. Given that it takes about one month for the SST to respond to the atmospheric forcing, the values plotted in Fig. 5c for month N are obtained by using the MLD in month N and the zonal wind variance in previous month N–1. The rate of the zonal wind variance square root to the MLD in Fig. 5c peaks around June as the PDO variability in Fig. 1b. This implies that the 1-month time scale for the SST to respond to the atmospheric forcing, shallow MLD in summer, and relatively strong atmospheric forcing in spring, are critical to the timing of the maximum variability of the PDO in late spring and early summer.

4. Summary

The PDO, both in observations and in the CFS, shows similar seasonality, with increasing SST variance during spring and a maximum in late spring and early summer. The PDO-related ocean temperature anomaly displays a significant transition from a deep to a shallow structure during late spring. There is a 1-month delay in the PDO-related SST response to the atmospheric wind forcing. The 1-month delay together with the seasonal variation of the mean MLD leads to the maximum variability of the PDO in late spring and early summer.

References

Chhak, K. C., E. D. Lorenzo, N. Schneider, and P. F. Cummins, 2009: Forcing of low-frequency ocean variability in the northeast Pacific. *J. Climate*, **22,** 1255–1276.

Mantua, N. J., S. R. Hare, Y. Zhang, J. M. Wallace, and R. Francis, 1997: A Pacific interdecadal climate oscillation with impacts on salmon production. *Bull. Amer. Meteor. Soc.*, **78,** 1069–1079.

Monterey, G., and S. Levitus, 1997: Seasonal variability of mixed layer depth for the world ocean. *NOAA Atlas NESDIS*, **14,** U.S. Gov. Printing Office, Washington, D.C., 96pp.

Reynolds, R. W., N. A. Rayner, T. M. Smith, D. C. Stokes, and W. Wang, 2002: An improved in situ and satellite SST analysis for climate. *J. Climate*, **15,** 1609–1625.

Saha, S., and Coauthors, 2006: The NCEP Climate Forecast System. *J. Climate*, **19,** 3483–3517.

Smith, T. M., R. W. Reynolds, T. C. Peterson, and J. Lawrimore, 2008: Improvements to NOAA's historical merged land–ocean surface temperature analysis (1880–2006). *J. Climate*, **21,** 2283–2296.

Zhang, Y., J. M. Wallace, and D. S. Battisti, 1997: ENSO-like interdecadal variability. *J. Climate*, **10,** 1004–1020.

Science and Technology Infusion Climate Bulletin
NOAA's National Weather Service
35th NOAA Annual Climate Diagnostics and Prediction Workshop
Raleigh, NC, 4-7 October 2010

Predictability of Near-Surface Climate Extreme Events

Emily J. Becker [1], Huug van den Dool [1], Malaquias Peña [2]

[1] *Climate Prediction Center, NCEP/NWS/NOAA, Camp Springs, MD*
[2] *Environmental Modeling Center, NCEP/NWS/NOAA, Camp Springs, MD*

Climate extremes, for this study defined as a monthly mean value above or below a specific local threshold, have important implications for energy use, agriculture, and flood or drought preparation. In this study, we investigate our current ability to predict climate extremes at lead times of one to eight months over the Americas, with the goal of understanding the strengths and weaknesses of current models. This report focuses on the results of our examination of 2-meter temperature.

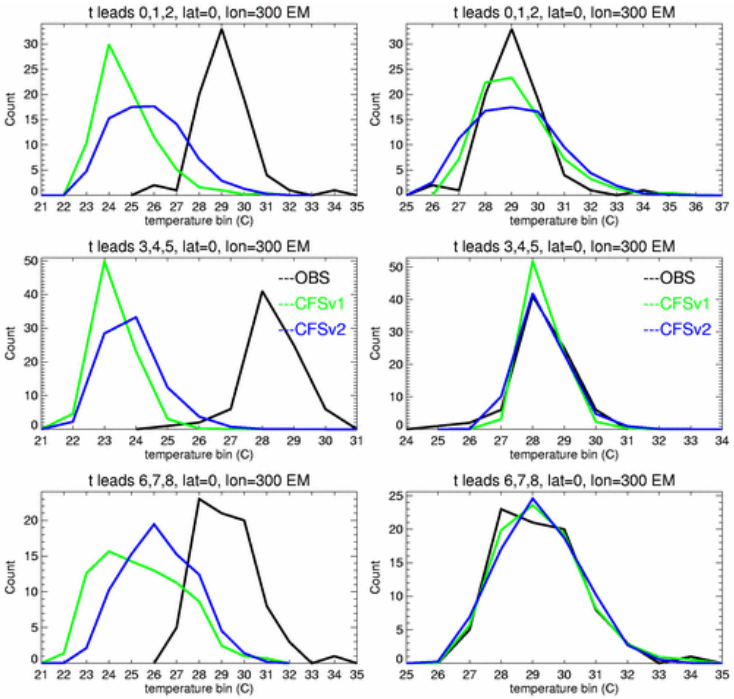

Fig. 1 Example raw (left) and corrected (right) PDFs for the single gridpoint 0°N, 60°W. PDF is corrected by removing the model climatology from the ensemble mean model values and replacing it with the observed climatology. Green lines depict the PDF from the CFSv1 ensemble mean, blue the CFSv2, and black are observed values from the GHCN-CAMS 2-meter temperature.

We have examined the predictability of near-surface climate extremes in the region of the Americas, in the form of monthly anomalies in 2-meter surface temperature, using retrospective forecasts from two versions of the NOAA Climate Forecast System (CFS), a "state of the art" coupled ocean-land-atmosphere model. 9-month forecasts for the 27-year span between 1982 and 2008 were available for both versions, with January – December monthly initial conditions (Saha *et al.* 2006, 2010). Reforecasts for both versions were obtained from the Environmental Modeling Center (EMC, NOAA/NWS/NCEP). Additionally, 17 years (1982-1998) of CCSM3.5 12-month forecasts were available, for January and July initial conditions, obtained from the University of Miami (Kirtman and Min 2009). The observed temperature used in this study is GHCN-CAMS (Fan and van den Dool 2008).

As an initial assessment of the models, the climatologies and PDFs of the model forecasts were compared to those of corresponding observations. To approximate removing the model biases, we removed the model climatology from the forecast and replaced it with the observed climatology, which substantially corrects the PDF (Fig. 1).

For the purposes of this study, we have defined a "climate extreme" as a departure from the monthly mean above/below a specified multiple of the local standard deviation of the variable. Specifically, we considered both +/- 1 std. dev. and +/- 1.645 std. dev., which is approximately the "90th percentile" threshold. The anomaly correlation (AC), which measures the association between the anomalies of gridpoint forecast and observed values, is the primary measure of forecast skill employed. .

Correspondence to: Emily J. Becker, Climate Prediction Center, NCEP/NWS/NOAA, 5200 Auth Road, Camp Springs, MD 20746; E-mail: Emily.Becker@noaa.gov.

Some positive skill scores for forecast climate extremes at leads of 1 – 4 months were found for 2-meter surface temperature (Fig. 2). Prediction skill is higher over South America than North America. Skill, by any measure, increases when the sample is restricted to extreme events.

Anomaly correlations are generally higher when verification of a predicted extreme was assessed (*i.e.* the model predicted an extreme, did one occur?) than when an extreme event occurred in the observed record (*i.e.*, an extreme occurred, was it predicted?) (Fig. 3). Prediction skill of CFSv1 and CCSM3.5 are roughly comparable; anomaly correlations of CFSv2 are somewhat higher. Anomaly correlations of climate extremes using the multi-model ensemble mean does not show a significant increase in skill over CFSv2 individual model results.

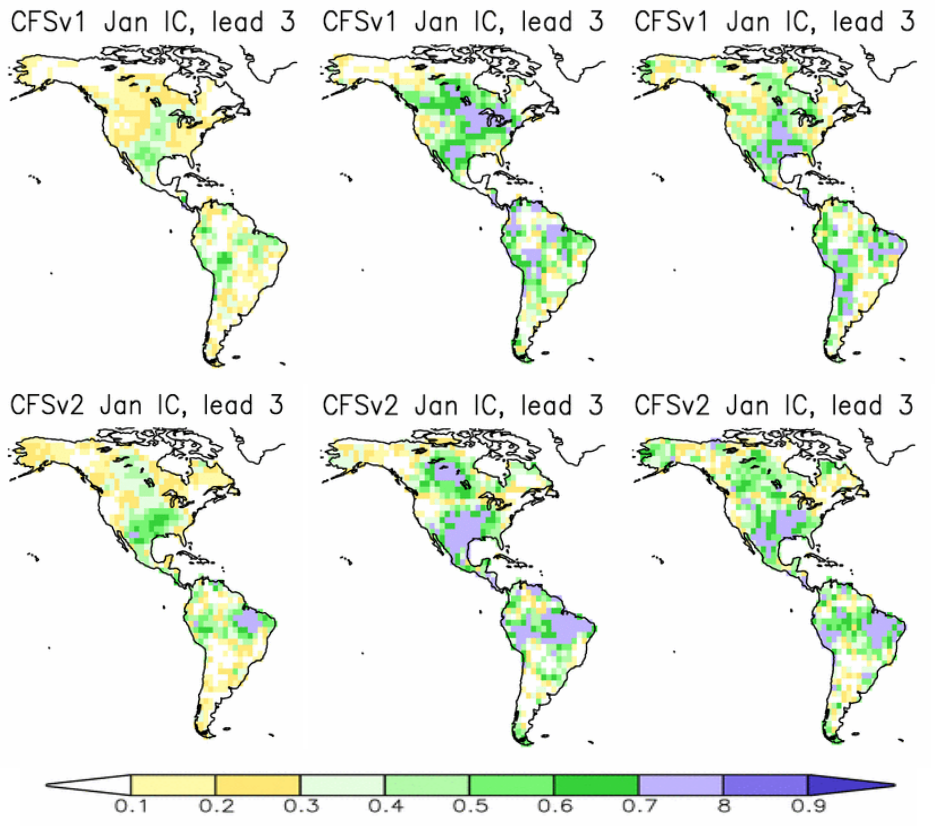

Fig. 2 Anomaly correlations for CFSv1 (upper row) and CFSv2 (lower row). The three columns depict the anomaly correlation over all cases (left), over the sample restricted to when the model predicts an extreme (center) and when the sample is restricted to observed extremes (right). Only January initial conditions, lead 3 (*i.e.* the April forecast) are shown. Extremes defined here as +/- 1 std. dev.

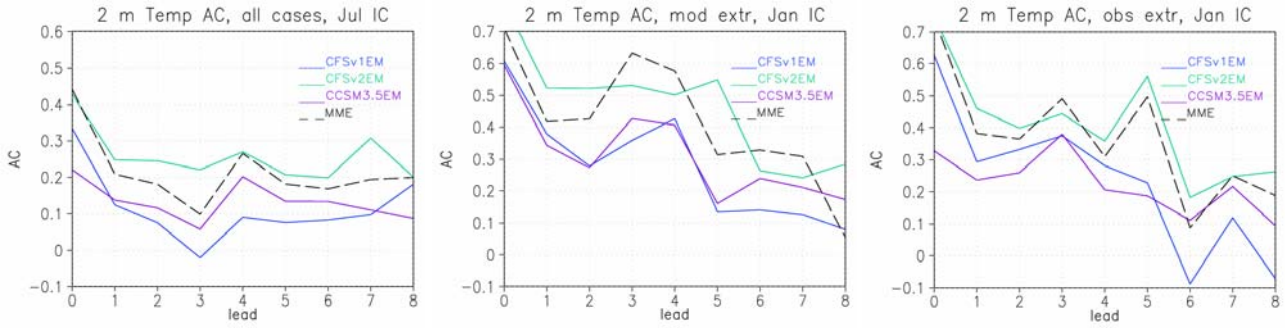

Fig. 3 Area-averaged anomaly correlations for the Americas. Left: all cases, center: sample restricted to model extremes, and right: sample restricted to observed extremes. All lead times for January initial conditions are shown. Extremes are defined as +/- 1.645 std. dev.

This report represents a piece of larger study. We have also examined the prediction of precipitation extremes over the Americas, and sea surface temperature in the waters near to the Americas. We will use these results to assess where and why prediction skill is better, with the goal of improving forecasts in the future.

References

Fan, Y. and H. Van den Dool, 2008: A global monthly land surface air temperature analysis for 1948–present. *J. Geophys. Res.*, **113**:D01103, doi:10.1029/2007JD008470.

Kirtman, B. and D. Min, 2009: Multimodel Ensemble ENSO Prediction with CCSM and CFS. *Mon. Wea. Rev.*, **137**, 2908-2930.

Saha, S., Coauthors, 2006: The climate forecast system at NCEP. *J. Climate*, **19**, 3483– 3517.

Saha, S., Coauthors, 2010: The NCEP Climate Forecast System Reanalysis. *Bull. Amer. Meteor. Soc.*, **91**, 1015-1057.

3. DYNAMO/IASCLIP

Science and Technology Infusion Climate Bulletin
NOAA's National Weather Service
35th NOAA Annual Climate Diagnostics and Prediction Workshop
Raleigh, NC, 4-7 October 2010

Better Initial Conditions Significantly Improve Intraseasonal Prediction

Joshua X. Fu[1], Bin Wang[1], June-Yi Lee[1], Wanqiu Wang[2], and Li Gao[1]

[1]*IPRC, SOEST, University of Hawaii at Manoa, Honolulu, Hawaii*
[2]*CPC, National Centers for Environmental Prediction, Camp Spring, Maryland*

1. Introduction

The recurrent Madden-Julian Oscillation (MJO, Madden and Julian 1972) with a period of 30-60-day offers an opportunity to extend weather forecast beyond two weeks, which will bridge the gap between the conventional weather forecasting and seasonal climate prediction. The MJO manifests as a planetary-scale coupled system between organized multi-scale convection and large-scale circulation. It is generated in the equatorial western Indian Ocean and propagates eastward along the equator in boreal winter. During boreal summer, the dominant propagation is northeastward in addition to the along-equator eastward component (Yasunari 1979). Poleward propagation of the MJO brings active and suppressed spells to the Asian-Australian, American, and African monsoon systems.

On its way eastward and poleward, the active phase of the MJO spawns frequent occurrences of tropical cyclones in the Indian Ocean, western Pacific, eastern north Pacific, Gulf of Mexico and Atlantic Basin (Higgins *et al*. 2000). Through tropical-extratropical teleconnection, the MJO modulates the mid-latitude weather activity over North and South America (Jones and Schemm 2000) including the high-latitude circulation. The MJO in the western Pacific also modulates the evolutions of El Nino. Therefore, improved prediction of the MJO can extend the mid-latitude weather forecasts while also potentially improving ENSO and seasonal forecasts.

However, our capability of forecasting MJO is largely limited by model difficulty in realistically simulating the MJO and the biases of global reanalysis/analysis datasets in representing the MJO. When these global reanalysis/analysis datasets with ill-defined MJO are directly used to initialize the forecasts, the MJO forecasting skills are only about one week (*e.g.*, Lin *et al.* 2008; Fu *et al.* 2009). In this study, a signal-recovery method has been proposed to improve the representation of the MJO in several reanalysis datasets (*e.g.*, NCEP_R1, _R2 and ERA_Interim). The impacts of signal-recovered reanalyses on MJO forecasting skills are assessed.

2. Model and experiment design

The model used in this study is a hybrid atmosphere-ocean coupled model developed at International Pacific Research Center, University of Hawaii (so-called UH_HCM, Fu and Wang 2004; Fu *et al.* 2008). The atmospheric component is a general circulation model (ECHAM-4), developed at Max Planck Institute for Meteorology, Germany. The mass flux scheme of Tiedtke is used to represent the deep, shallow, and midlevel convection. The ocean component is an intermediate tropical upper-ocean model developed at University of Hawaii (Wang *et al.* 1995), which comprises of a mixed-layer, in which the temperature and velocity are vertically uniform, and a thermocline layer in which temperature decreases linearly from the mixed-layer base to the thermocline base. Both layers have variable depth and exchange mass and heat through entrainment and detrainment.

The global atmospheric model has been coupled to the ocean model over the tropical Indian and Pacific Oceans without using heat flux correction. Outside the tropical Indian and Pacific Oceans, sea surface temperature is specified as climatologically monthly-mean SST. In all forecast experiments, a restart file from a long-term coupled run has been used to initialize the nudging integration, which in turn generates initial conditions for all forecast experiments.

Correspondence to: Joshua X. Fu, IPRC, SOEST, University of Hawaii at Manoa, Honolulu, Hawaii;
E-mail: xfu@hawaii.edu

In this study, most forecast experiments have targeted five summer seasons (2004-2008). Each year, sixteen forecasts have been initiated every 10 days from May 1 to September 31. Ten ensembles have been executed for each forecast. The way to generate ensemble initial condition is the same as that used in our previous predictability study (Fu *et al.* 2007). Each forecast is integrated for 60 days. Model forecasted ensemble-mean OLR, zonal winds at 850-hPa and 200-hPa have been used to calculate Wheeler-Hendon index (Wheeler and Hendon 2004). Finally, the MJO prediction skills have been assessed as the way used by Lin *et al.* (2008) and Gottschalck *et al.* (2010).

3. Biases of global reanalysis datasets in describing the MJO

Because of the sparseness of the upper-air sounding sites in the active MJO region over the Indo-Pacific warm-pool and the deficiencies of the operational models in MJO simulations, reanalysis datasets unavoidably have various biases in representing MJO. Shinoda *et al.* (1999) found that the MJO-related convective activities (rainfall and OLR) in the NCEP_R1 (Kalnay *et al.* 1996) are two-to-three factors smaller than that in the corresponding observations (also see Figure 1 in Fu *et al.* 2009). Using updated forecast model and data assimilation system and fixing known problems of the NCEP_R1, Kanamitsu *et al.* (2002) developed an updated NCEP_R2 reanalysis. The MJO-related humidity perturbations, however, in the NCEP_R2 and in ECMWF analysis were still underestimated. The increased volumes of satellite observations and improved models/data assimilation techniques steadily improve the quality of reanalysis datasets in representing weather and climate variability including the MJO. On the other hand, the lack of global wind profiles' observations (particularly over the vast oceans) and an efficient constraint between the mass and flow fields in the tropics as well as the difficulties for current data assimilation systems in handling clouds/precipitation-affected radiance make reanalysis datasets vulnerable to errors, particularly in the representation of tropical weather and climate variability.

Two reanalysis datasets: The NCEP_R2 and ERA_Interim will be used to initialize our forecast experiments in this study. Although similar observational data may have been used as input to generate these reanalysis datasets, the different model physics and data assimilation techniques will result in different reanalysis products. In this section, the biases of these two reanalysis datasets in describing the MJO were briefly described. As for MJO prediction, the quality of near-equatorial MJO in the reanalyses is essential because the MJO has a significant eastward-propagating component along the equator year around. Even in boreal summer, the dominant northward propagation of the MJO starts from the equator. Due to the lack of an efficient constraint between the mass and flow fields (like the quasi-geostrophic balance in middle-latitude) and very limited upper-air soundings, the equatorial region has been a very difficult area for data assimilation. It is imperative to take a close look of the MJO near the equator in these two reanalyses.

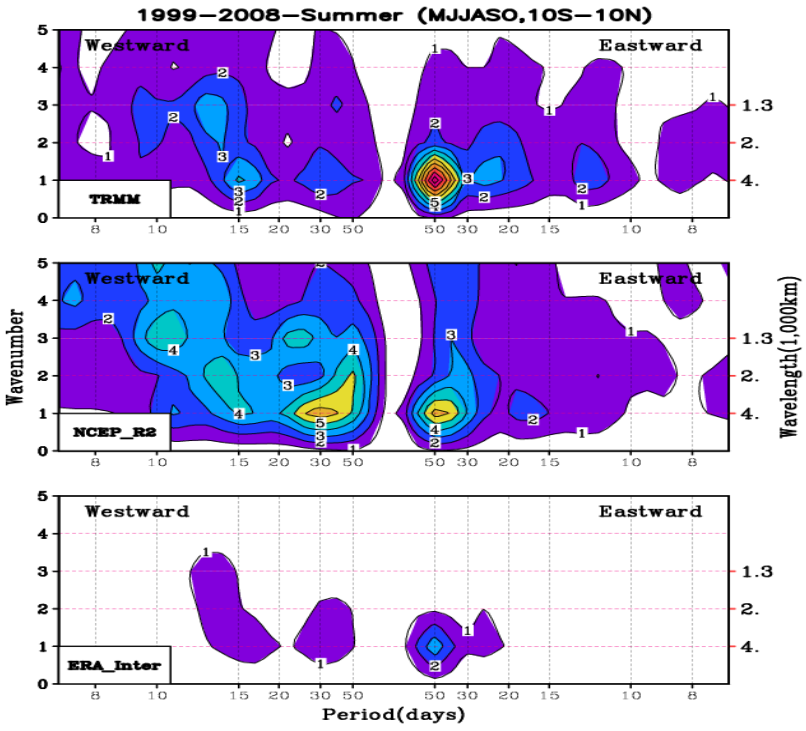

Fig. 1 Wavenumber-frequency spectra of rainfall from TRMM 3B42, NCEP R2, and ERA-Interim (contour interval: 1 (mm day^{-1})^2) averaged between 10^{o}S and 10^{o}N of 1999-2008 summers from TRMM observations (upper panel), NCEP_R2 (middle panel), and ERA_Interim (lower panel).

Figure 1 shows the wavenumber-frequency spectra of rainfall averaged

between 10°S to 10°N from TRMM observations, NCEP_R2, and ERA_Interim. The observations indicate dominant eastward-propagating variance of the MJO. The NCEP_R2 has relatively lower eastward-propagating variance, but much higher westward-propagating variance than the observations. The ERA_Interim has dominant eastward-propagating variance over the westward component, as in the observations. However, the magnitude of the variance in the ERA_Interim is obviously smaller than the observations.

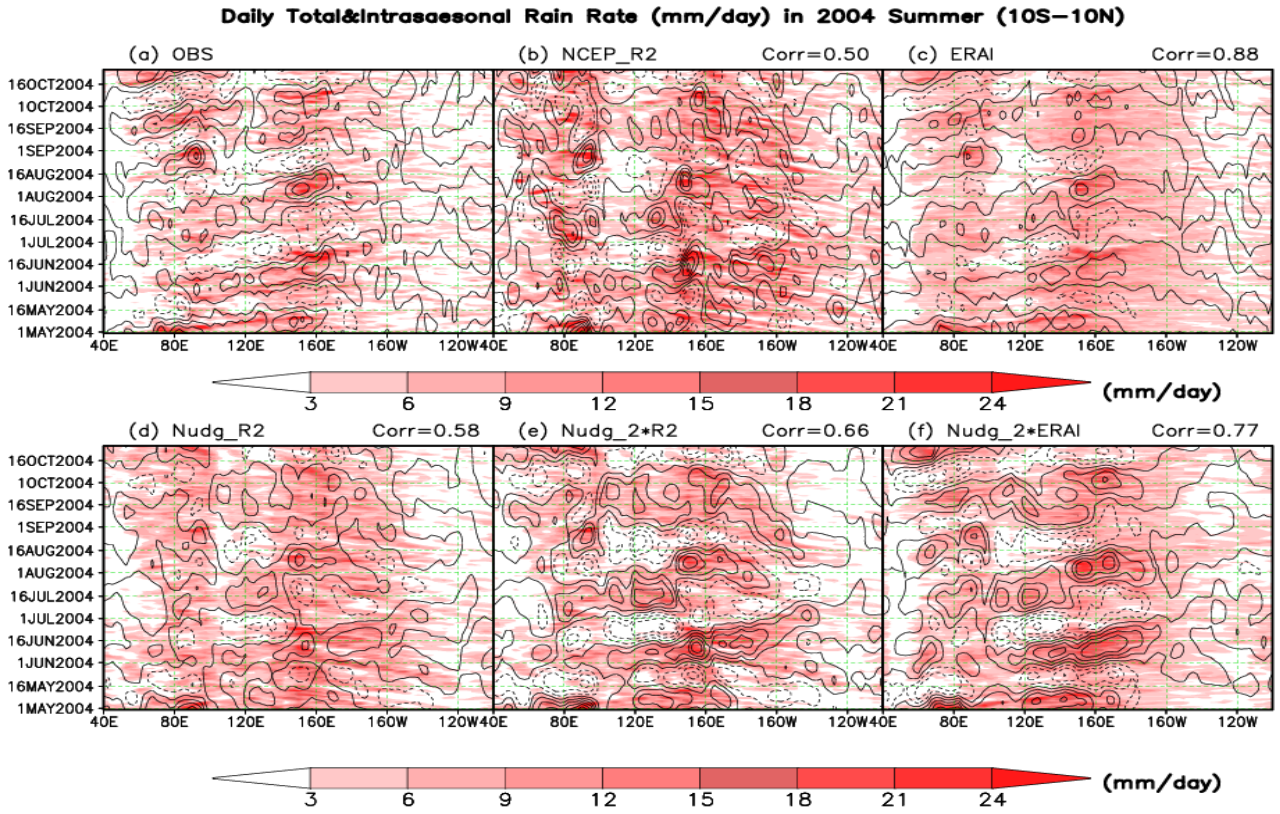

Fig. 2 Longitude-time evolutions of daily total rainfall (shaded) and associated intraseasonal (30-90-day) variability (contour interval: 1 mm day^{-1}) averaged between 10°S and 10°N in 2004 summer from (a) TRMM observations, (b) NCEP_R2, (c) ERA_Interim, (d) Nudged NCEP_R2, (e) signal-recovered NCEP_R2, and (f) signal-recovered ERA_Interim.

For illustration purpose, Figure 2 gives the Hovmoller diagrams of total rainfall and the associated intraseasonal variability along the equator in 2004 summer from TRMM observations, the NCEP_R2 and ERA_Interim along with the nudged[1] R2, signal-recovered NCEP_R2 and signal-recovered ERA_Interim. In the observations (Fig. 2a), four-to-five MJO events develop in the Indian Ocean and propagate eastward into the western Pacific. The NCEP_R2 (Fig. 2b) captures some of the observed features but is not as well organized as the observed events. Too many and too strong high-frequency westward-propagating disturbances exist in the NCEP_R2, particularly in the western Pacific. An obvious fictitious westward-propagating MJO event exists in July over the Indian Ocean. The correlation coefficient, which measures the similarity of the longitude-temporal evolutions between the reanalysis MJO rainfall anomaly and the observations, is about 0.5. The ERA_Interim (Fig. 2c) has very similar spatial-temporal evolutions as the observations but with the amplitude underestimated. The correlation coefficient with the observations reaches 0.88.

After nudging the NCEP_R2 into the UH_HCM (Fig. 2d), the too strong small-scale convection presented in the original R2 has been mitigated. The fictitious westward propagating ISO event in July over

[1] "nudged" denotes the results after nudging reanalysis into the UH_HCM model.

the Indian Ocean disappeared. The correlation coefficient with the observations increases to 0.58. This improvement after nudging is likely due to the better representation of convective processes in the UH_HCM than that in the NCEP model because the associated dynamical fields in both cases are very similar.

4. A signal-recovery method and Its impact on MJO prediction

In realizing that reanalysis/analysis datasets (*e.g.*, NCEP_R1, _R2, and ERA_Interim) bear a variety of biases in representing the observed MJO, we here propose an idea of signal-recovery. The objective of signal-recovery is to recover MJO signal in reanalysis/analysis datasets before using them to initialize MJO forecasts. A prototype signal-recovery method has been used to augment the underestimated MJO signal in the NCEP_R1 (Fu *et al.* 2009). The procedure is as following: first, 30-90-day variability is extracted from one-year raw time series with harmonic analysis; second, the extracted MJO signal is augmented by doubling its magnitude; then, the 30-90-day variability in the original time series is replaced with augmented MJO signal. Finally, the resultant time series is nudged into the UH_HCM to generate a new product: so-called *signal-recovered reanalysis*.

After doubling the intraseasonal signals in both the NCEP_R2 and ERA_Interim and nudging into the UH_HCM, the resultant products own much stronger intraseasonal variability than the original reanalyses (Fig. 2e, f), which are called signal-recovered NCEP_R2 and ERA_Interim. The signal-recovered ERA_Interim, however, has lower correlation with the observations than the original reanalysis. The underlying reasons call for further study.

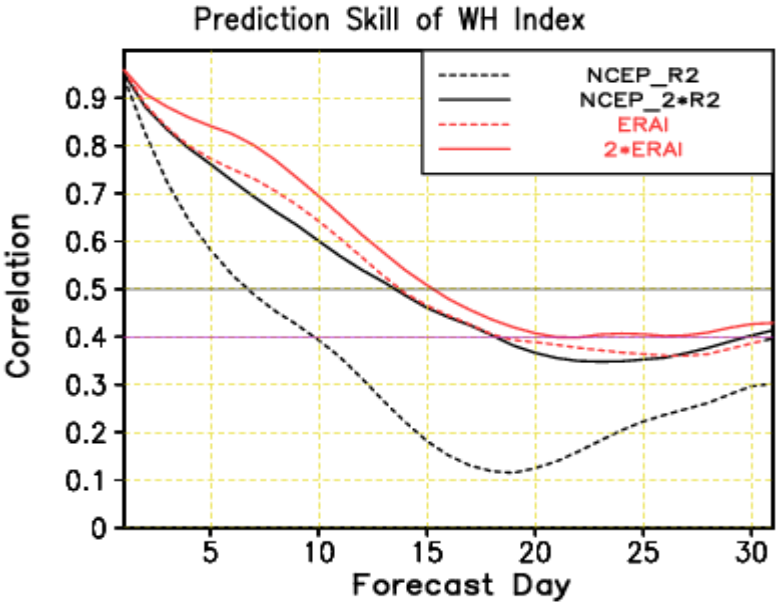

Fig. 3 Anomalous Correlation Coefficients (ACC) of Wheeler-Hendon Index as function of forecast lead time. The forecasts were initiated with the nudged NCEP_R2 (black dash line), signal-recovered NCEP_R2 (black solid line), and the nudged ERA_Interim (red dash line), signal-recovered ERA_Interim (red solid line).

When intraseasonal signal of the NCEP_R1 in 2004 summer was recovered to be comparable to the observations, the resultant MJO prediction skill increased accordingly (Fu *et al.* 2009). A natural question arises: What will happen for other years and with other reanalysis datasets? To answer this question, extended forecast experiments have been conducted for five continuous summers (2004-2008) initialized with signal-recovered NCEP_R2 and ERA_Interim reanalyses. As shown in Figure 2, the quality of the MJO in the signal-recovered NCEP_R2 is much better than that in the original reanalysis; while the signal-recovered ERA_Interim has stronger intraseasonal variability but lower correlations with the observations than the original reanalysis. Will these so-called signal-recovered initial conditions lead to better intraseasonal prediction skills?

Figure 3 shows the Anomalous Correlation Coefficients (ACC) between the forecasts and the observations in terms of Wheeler-Hendon index (Lin *et al.* 2008; Gottschalk *et al.* 2010). The forecast lead day with ACC dropping to 0.5 has been defined as MJO prediction skill. When the NCEP_R2 is directly used as initial condition, the resultant prediction skill is only about a week. The prediction skill is doubled (14 days) after initializing the forecasts with signal-recovered NCEP_R2. When signal-recovered ERA_Interim is used to initialize the forecasts, the MJO prediction skill is also consistently better than that directly initialized with the ERA_Interim, although the improvement is not as dramatic as for the NCEP_R2 case.

5. Concluding remarks

In this study, the biases of three reanalysis datasets (*e.g.*, NCEP_R1, _R2, and ERA_Interim) in describing MJO were revealed and the impacts of these biases as initial conditions on MJO prediction skills were assessed. A prototype signal-recovery method is proposed to improve the representation of the MJO in initial conditions. Although all three reanalyses underestimate the intensity of the equatorial eastward-propagating MJO, the overall quality of the ERA_Interim is much better than the NCEP_R1 and R2. When the NCEP_R1 and_R2 are directly used to initialize the forecasts, MJO prediction skill is only about one week (Fig.3). The MJO prediction skill initialized with the ERA_Inerim, however, reaches two weeks. Using the signal-recovered reanalyses as initial conditions, MJO prediction skills are consistently better than that directly initialized with the original reanalyses (Fig. 3).

It is well-known that the MJO modulates global weather and climate systems from tropical cyclones, mid-latitude extreme weather, wet and dry spells of monsoon systems to ENSO evolutions. Knowing the phase of the MJO 2-4 weeks ahead offers a reliable source for probabilistic assessments on the occurrences of tropical extreme events (*e.g.*, Gottschalk *et al.* 2010). This information has great socio-economic value particularly for those weather sensitive sectors, *e.g.*, water management, agriculture, disaster prevention, and so on (Brunet *et al.* 2010).

This study is a step towards this direction. In order to ensure steady progress in the advancement of MJO prediction, synergetic efforts between weather and climate communities are needed at least in three fronts: (i) To acquire better initial conditions, through deploying new observations (*e.g.*, DYNAMO) and developing new data assimilation techniques, for the atmosphere-ocean-land coupled forecast systems; (ii) To improve the representations of multi-scale convective systems and their interactions with large-scale circulations in atmospheric models, which are key processes of the observed MJO; (iii) To advance the coupling processes among atmosphere, ocean, and land that are crucial to the realistic simulations of the MJO.

Recently, a great effort has been made at NOAA/NCEP to produce a new generation reanalysis (CFSR) (Saha *et al.* 2010). The CFSR developed at NCEP has very high horizontal and vertical resolution (T382L64) of the atmosphere and includes atmosphere-ocean coupling, which reproduces the observed lead-lag phase relationships between precipitation and sea surface temperature (Saha *et al.* 2010). Preliminary results show that the CFSR has better quality than the NCEP_R1 and _R2 in describing the MJO. Future study is needed to comprehensively evaluate the MJO in the CFSR and to assess the MJO prediction skill when the CFSR is used as initial condition.

References

Brunet, G., M. Hoskins, M. Moncrieff, R. Dole, G. N. Kiladis, B. Kirtman, A. Lorenc, B. Mills, R. Morss, S. Polavarapu, and D. Rogers, 2010: Collaboration of the weather and climate communities to advance sub-seasonal to seasonal prediction. *Bull. Amer. Meteor. Soc.*, **91**, 1397-1406.

Fu, X., and B. Wang, 2004: The boreal-summer intraseasonal oscillations simulated in a hybrid coupled atmosphere-ocean model. *Mon. Wea. Rev.*, **132**, 2628-2649.

Fu, X., B. Wang, D. E. Waliser, and L. Tao, 2007: Impact of atmosphere-ocean coupling on the predictability of monsoon intraseasonal oscillations. *J. Atmos. Sci*., **64**, 157-174.

Fu, X., B. Wang, Q. Bao, P. Liu, and B. Yang, 2008: Experimental dynamical forecast of an MJO event observed during TOGA-COARE period. *Atmos. Oceanic Sci. Lett.*, **1,** 24-28.

Fu, X., B. Wang, Q. Bao, P. Liu, and J.-Y. Lee, 2009: Impacts of initial conditions on monsoon intraseasonal forecasting. *Geophys. Res. Lett.*, **36**, L08801, doi:10.1029/ 2009GL 037166.

Gottschalck, J., and Co-authors, 2010: A framework for assessing operational model MJO forecasts: A project of the CLIVAR Madden-Julian Oscillation working group. *Bull. Amer. Meteor. Soc.*, **91,** 1247-1258.

Higgins, R. W., J. K. E. Schemm, W. Shi, and A. Leetmaa, 2000: Extreme precipitation events in the western United States related to tropical forcing. *J. Climate*, **13**, 793-820.

Jones, C., and J.-K. E. Schemm, 2000: The influence of intraseasonal variations on medium-range weather forecasts over South America. *Mon. Wea. Rev.*, **128**, 486-494.

Kalnay, E., and co-authors, 1996: The NCEP/NCAR 40-year reanalysis project. *Bull. Amer. Meteor. Soc.*, **77**, 437-471.

Kanamitsu, M., W. Ebisuzaki, J. Woollen, S-K Yang, J. J. Hnilo, M. Fiorino, and G. L. Potter, 2002: NCEP-DEO AMIP-II Reanalysis (R-2). *Bull. Amer. Meteor. Soc.*, **83**, 1631-1643.

Lin, H., G. Brunet, and J. Derome, 2008: Forecast skill of the Madden-Julian Oscillation in two Canadian atmospheric models. *Mon. Wea. Rev.*, **136**, 4130-4149.

Madden, R. A., and P. R. Julian, 1972: Description of global-scale circulation cells in the tropics with a 40-50 day period. *J. Atmos. Sci.*, **29**, 1109-1123.

Saha, S., and Co-authors, 2010: The NCEP Climate Forecast System Reanalysis. *Bull. Amer. Meteor. Soc.*, **91**, 1015-1057; doi: 10.1175/2010BAMS3001.7.

Shinoda, T., H. H. Hendon, and J. Glick, 1999: Intraseasonal surface fluxes in the tropical western Pacific and Indian Oceans from NCEP Reanalysis. *Mon. Wea. Rev.*, **127**, 678-693.

Wang, B., T. Li, and P. Chang, 1995: An intermediate model of the tropical Pacific Ocean. *J. Phys. Oceanogr.*, **25**, 1599-1616.

Wheeler, M. C., and H. H. Hendon, 2004: An all-season real-time multivariate MJO index: development of an index for monitoring and prediction. *Mon. Wea. Rev.*, **132**, 1917-1932.

Yasunari, T., 1979: Cloudiness fluctuations associated with the Northern Hemisphere summer monsoon. *J. Meteor. Soc. Japan*, **57**, 227-242.

Science and Technology Infusion Climate Bulletin
NOAA's National Weather Service
35th NOAA Annual Climate Diagnostics and Prediction Workshop
Raleigh, NC, 4-7 October 2010

Gauging International Interest in the Intra Americas Study of Climate Processes (IASCLIP)

Michael Douglas

National Severe Storms Laboratory/NOAA, Norman, Oklahoma

1. Introduction

The Intra-Americas Study of Climate Processes (IASCLIP) is a climate research activity that is focused on the region of the Intra-American Seas - that region including the Gulf of Mexico and the Caribbean Sea and the adjacent land areas. The IASCLIP has been endorsed as a specific subprogram of the VAMOS, a WCRP / CLIVAR program focused on the climate of the Americas.

The IASCLIP science topics involve questions on all scales of atmospheric motion. A science and implementation plan that has been developed for the IASCLIP can be found at: http://www.eol.ucar.edu/projects/iasclip/documentation/. This plan notes that the IAS region is a unique location where so many countries (more than 20) are affected by the same set of climate phenomena and that international collaboration is essential to the success of any climate research program.

2. Travel to support development of IASCLIP implementation strategies

When planning international research activities there is often a difference between the scientific focus of US climate scientists and those in developing countries, where there may be a greater focus on local issues and where computer facilities may not allow for extensive modeling activities. Most foreign climate scientists are affiliated with universities, while the bulk of the infrastructure support for either short-duration process studies or long-term monitoring are associated with government institutions that may not have a strong climate research component. In the planning for a field activity that may involve costly resources, it is important also to consider institutions that might not have active researchers in climate-related research, but whose facilities may permit effective field measurements. Thus, early interaction with these institutions is important, even if it is outside the normal sphere of basic research.

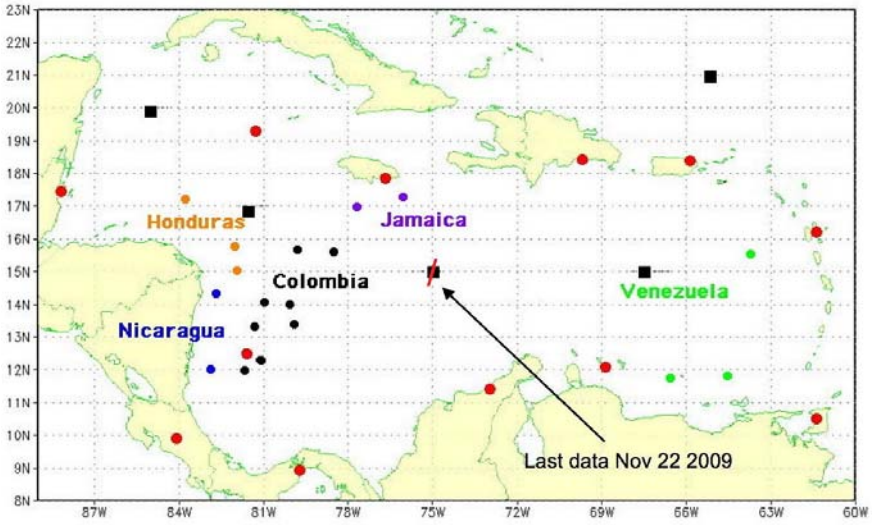

Fig. 1 Possible small-island sites for climate monitoring in Caribbean Sea as part of IASCLIP; sites are color coded by country. NOAA buoys shown as black squares. Radiosonde sites are red dots.

For the above-stated reasons we felt that the most efficient approach to reaching the greatest audience for spinning-up the IASCLIP was to travel to the countries likely to be involved in IASCLIP. During the summer and fall of 2010 a subset (Dave Enfield, Art Douglas, Mike Douglas) of IASCLIP scientific steering committee members traveled to 6 countries that were of some priority to IASCLIP activities (see Fig. 1). This travel was funded by NOAA's Climate Program Office. The first country visited was Colombia, followed by

Correspondence to: Michael Douglas, National Severe Storms Laboratory/NOAA, Norman, Oklahoma;
E-mail: Michael.Douglas@noaa.gov

the Dominican Republic, Costa Rica, Honduras, Nicaragua and El Salvador. There we presented an overview of the IASCLIP research objectives and described some possible strategies for improving climate monitoring and prediction over the region. We also solicited perspectives and opinions on what was most important to each institution. A highly condensed summary of the visits to each county is described below; the travel is not complete and several more countries are likely to be visited by early 2011. More detailed "raw" descriptions of these visits can be found on the IASCLIP website noted above.

3. Discussions in each country

Colombia

The Colombian Government's Environmental Department IDEAM, operates about 2800 surface climatological stations, with 27 providing synoptic reports. All of the surface data has been digitized, but by law, the entire data set cannot be made available for free. However, if the proper requests are made, much of the data may be made available. More extensive quality control of the data will begin soon.

Problems exist with gas generation at the San Andres Island radiosonde site (and other locations), something that is common throughout the region. This is one a major problem in maintaining regular upper-air soundings.

The Colombian Air Force has a small forecast office of 15 individuals, who provide their own forecasts. They also have personnel at different sites around the country, who may be able to help with observations. The Colombian Air Force, together with IDEAM, had recently established a new radiosonde site at Tres Esquinas, east of the Andes near the border with Ecuador.

Personnel of the Colombian Navy are rotated monthly on the small Caribbean cays; these personnel may be trained to help make meteorological measurements. The need for more formal arrangements was stated. There are 8 coastal oceanographic buoys being operated by the Navy. A surface station has recently been installed on Malpelo Island in the Pacific with the aid of IDEAM.

The National University of Colombia has an MS program in Atmospheric Science and were willing to participate in IASCLIP research activities. They are eager to have researchers visit and give short (or long) courses to their staff and students. They also welcome exchange visits.

Faculties from the Medellin branch of the National University are primarily involved in hydrometeorology research but they are interested in possible collaboration with IASCLIP researchers. They have a graduate program and many students that may contribute to possible research projects.

In Cartagena, the CIOH (Center for Oceanographic and Hydrographic Research), a branch of the Colombian Navy, is directly responsible for the islands and coastal areas in the Atlantic. The rotation of personnel could be a problem for maintaining trained personnel on a regular basis. However some solutions were discussed. The CIOH appeared interested in collaboration with IASCLIP researchers. They do some research themselves as well as prepare their own forecasts. A draft was prepared of a letter of intent to obtain permission for a US researcher or two to participate in one of their routine cruises to Malpelo and other islands. This would be done to evaluate the local conditions and possibilities at each site for installation of meteorological equipment.

Dominican Republic

Discussions were held at the offices of ONAMET, the Dominican National Weather Service. During the first day of meetings there were representatives from different groups such as the Red Cross, Climate change panel, Geological Institute and members of the Agrometeorology, Forecasting, and Climatological divisions within ONAMET. One of their main interests is the forecasting of hurricanes and a good part of their effort is aimed at this. Their forecast office is 24/7 (contrasting to the IDEAM in Colombia which is 16/5). The climatology section is the largest branch of the ONAMET with approximately 20 people. The data is being digitized and quality controlled. They have a rain gauge network composed in part of volunteers; there are 70 reliable sites. They have 10 automatic stations, 5 of them at airports. The meteorological radar in Santo Domingo is not working and funds are needed to repair it. A radar in Punta Cana is operated in part with

funds from the tourism consortium. The ONAMET staff is willing to cooperate with any research project and the personnel seem especially interested in activities that would involve more training or education.

Costa Rica

Costa Rica has about 200 surface stations but only 8 reports via satellite. They have 60 automatic weather stations but most require manual downloading of the data. The forecast office has 5 forecasters, all educated at the University of Costa Rica. They run the WRF, but do not verify their forecasts. The radiosonde station at the San Jose airport has not made observations for about one year – the IMN cannot afford the helium gas that the airport authorities now require for inflating balloons. They are hoping to find funds to purchase helium, which is expensive. There are no radars in Costa Rica, but there is a Central America - wide radar project that we did not have time to discuss with the Director of the IMN.

The quality control section has 8 staff and they publish a monthly bulletin. Visits are made every two months to surface stations. In 2008 the IMN stopped paying surface observers and there are now problems with some of the sites. There is a shortage of funds for obtaining vehicles to travel to stations, gas etc. The IMN sells their data, though the price not having been revised in years. The IMN has just finished re-installing an automated weather station on Cocos Island.

From our meeting at the University of Costa Rica, we learned that from the University perspective the most important IASCLIP collaboration would be through joint research and publications coming out of such an activity. They would also be interested in educational opportunities for students. It was recognized by all that the inability of US research project funds to be used to support students or staff in Costa Rica (or any other foreign country) meant that it was more beneficial to seek support from national activities that could provide these tangible benefits. This is not often recognized by US researchers (or NSF and NOAA) as a serious impediment to obtaining international collaborators in programs such as IASCLIP.

Honduras

We presented a several hour series of talks to a diverse group, followed by discussion. Media coverage was conspicuous, with many interviews for the TV and newspapers being given. The heavy rains this summer have seriously affected crop production in western Central America and there was genuine interest in the subject of climate variability.

All Honduran Meteorological Service (SMN) forecasting activities are carried out at their International Airport offices in Tegucigalpa. The SMN has about 60-70 rainfall stations that have 30 or more years of records. Including other institutions there are about 100 rain gauges in the country. There are 14 real-time reporting sites. The SMN has received a set of recommendations from WMO consultants to modernize their meteorological services. They are looking for funding for this activity ($2M USD).

Nicaragua

In Nicaragua the parent organization for meteorology is INETER, which is comprised of many geo-related branches. There are 300 met stations in Nicaragua, including 17 conventional synoptic reporting stations. There are about 20 Campbell automatic stations from post-Hurricane Mitch US AID, but these are not working now. They are trying to install more automatic stations in remote parts of country - vandalism is a problem.

Nicaragua is the country most affected by hurricanes in Central America but they are also interested in seasonal forecasting. It was mentioned that the capacity to do long range forecasts is low. They participate in the foro climatico of Central America, where they receive a map with probability of higher or lower rain. However, their farmers want more precise information. INETER prepares a more detailed report for the farmers. They do not run any numerical forecast models. All weather forecasts are made at the airport.

The meteorology section of INETER includes some individuals with University degrees. They have 8 staff members with Meteorology backgrounds and 16 in all (plus 3 administrators) in the forecasting area. They complained about the difficulty in sending more people abroad to learn Meteorology.

An opinion was voiced that Climate change was gradual and that many non-governmental organizations were obtaining much funding using climate change as an excuse. There was a consensus that it is important to put together a more concrete proposal that would cover what is needed and how people can participate.

There was a complaint from an Agricultural sector participant that the amount of rain was not well forecast this year, which led to large losses in the bean crop. More accurate one to two month forecasts would be useful. One question asked by a participant was: If Nicaragua joined IASCLIP... by what percentage would the forecasts improve?

El Salvador

El Salvador has 40 automatic stations and more than 100 raingauges - 39 conventional and 19 telemetric. Each morning by 7 AM 58 stations send rainfall data. Every three months data from all stations is collected. The data is on the web. The Director of the Met Service also said they have a mix of 170 met stations and ~ 120 stations have records longer than 30 years. We were told that the weather service has 58 members, 12 are forecasters, working 24/7. Two months ago they acquired a marine radar, (Furuno brand) to estimate rainfall, the images are on their web page.

The monetary effects of the recent bad (wet) weather have been significant. It was also mentioned that the Navy has ships that could perhaps be used to go to buoys in the Pacific. The National Electric Company has 4 dams that provide more than 50% of the electricity for El Salvador and it wants better forecasts during the period May-October. A better rainfall forecast would be useful as electricity cost goes up and down depending on the forecast.

The Director stated that people from NOAA rarely visit El Salvador as most of the US interest is in the Atlantic. A list of regional priorities is going to be compiled to get IASCLIP attention. People are very interested in collaborative research and writing papers. A comment was made that it is very hard to go abroad and study. Though there is money to hire meteorologists, there are not many to be found within El Salvador. Training is a problem. The government won't pay the person's salary while he/she is gone. It is preferable to have a course in El Salvador. More people would understand if the courses would be given in Spanish. It was asked if NOAA could sponsor something like this.

4. Summary

Travel has been carried out to six countries to describe the IASCLIP scientific plan and to seek input and collaboration in development of an effective climate monitoring and research program in the region. The response has generally been very positive, with strong interest expressed in participating in any educational activities related to the program as well as promoting use of existing observations and developing additional observing capabilities. Most interest has been shown by the operational sectors in most countries, with the exception of Colombia where there was general interest from the research community. Most other countries, as expected, had relatively small research communities.

A number of countries remain to be visited in the first part of 2011, so that a more complete picture of the IASCLIP community can be developed as well as a realistic operational plan.

Science and Technology Infusion Climate Bulletin
NOAA's National Weather Service
35th NOAA Annual Climate Diagnostics and Prediction Workshop
Raleigh, NC, 4-7 October 2010

Caribbean Precipitation Variability in Observations and IPCC AR4 Models

Elinor R. Martin and Courtney Schumacher

Department of Atmospheric Sciences, Texas A&M University, College Station, Texas

1. Introduction

The Caribbean is one of many regions of the world where it is vital to understand precipitation patterns, variability and extremes. The low-lying coastal regions of Caribbean islands are densely populated with development pressure increasing. The region is also vulnerable to many natural hazards that are related to and exacerbated by precipitation, such as hurricanes, earthquakes, mudslides and drought. There is also evidence that precipitation patterns can influence the spread of Dengue fever in the region (Jury, 2008). Planning, policy and management of these events are extremely dependent on knowledge of the precipitation of the region. These social and economic reasons provide considerable motivation for increasing and expanding current knowledge of precipitation in the Caribbean.

Precipitation in the Caribbean varies spatially and has a bimodal annual cycle with an initial maximum in May, a minimum around July-August, and a second maximum in September-October (*e.g.* Jury *et al.*, 2007). Precipitation in this region has variability on a variety of timescales. Interannually, precipitation is influenced by the El Niño-Southern Oscillation and the North Atlantic Oscillation (NAO) (Chen and Taylor, 2002; Giannini *et al.*, 2001). Intraseasonally, precipitation (including extremes) is influenced by the Madden-Julian Oscillation (Martin and Schumacher, 2010). The region is also affected on shorter timescales (days to weeks) by the propagation of easterly waves, which can mature into tropical storms and hurricanes.

Most models from the 4th Assessment Report (AR4) of the Intergovernmental Panel on Climate Change (IPCC) predict a decrease in precipitation across the Caribbean region whilst also underestimating current precipitation amounts and sea surface temperatures (SSTs) of the Atlantic warm pool in the region (Christensen *et al.*, 2007; Neelin *et al.* 2006). However, the ability of these global climate models to capture the variability of precipitation in the region has not been fully investigated.

It is the aim of this paper to explicitly investigate the representation of precipitation variability, on a variety of time scales, in the Caribbean region by the IPCC AR4 models in comparison to observed variability.

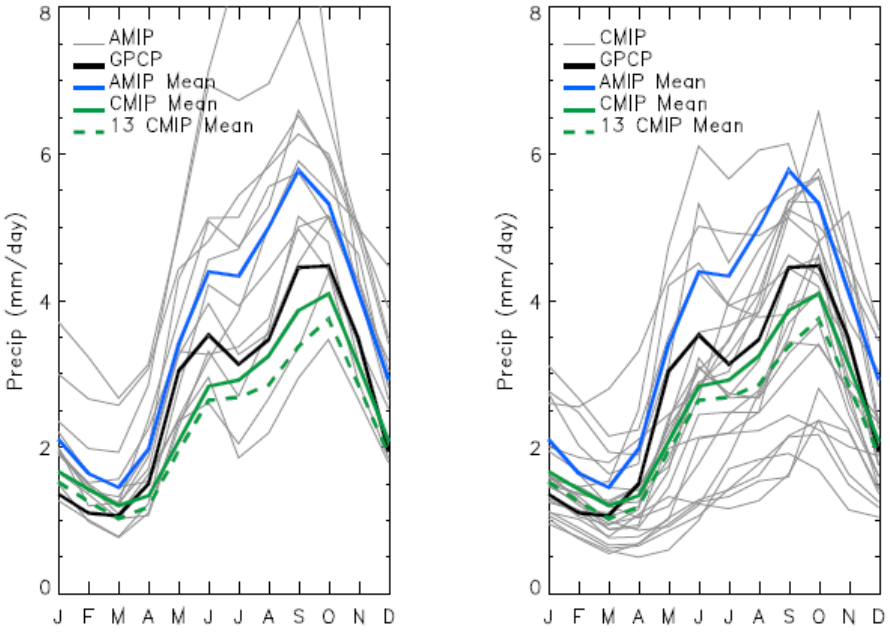

Fig. 1 Annual cycle of monthly Caribbean area averaged (55-90 W, 10-25N) precipitation from observations (black), AMIP model mean (blue), AMIP models (grey, left), CMIP model mean (green solid), CMIP models (grey, right) and the mean of the 13 CMIP models that match the AMIP simulations (green dashed).

Correspondence to: Elinor R. Martin, Department of Atmospheric Sciences, Texas A&M University, College Station, Texas; E-mail: ermartin@tamu.edu

2. Data

This study uses both monthly (1979-2008, 2.5°) and daily (1997-2008, 1°) data from the Global Precipitation Climatology Project (Huffman et al. 2001). Both daily (last 12 years) and monthly (last 30 years) precipitation from the IPCC AR4 models are used. Only one ensemble for each model is used to avoid biasing the model mean towards models with a large number of ensembles. Both coupled 20th century simulations (CMIP) and AMIP-like uncoupled simulations (AMIP, only 1979-1999 available) are investigated. Parameters of interest are precipitation, SST, vertical velocity (ω in hPa/s), and 925 hPa winds. Wind from the models is compared to NCEP II reanalysis (Kanamitsu et al. 2002) and SSTs are compared to the HadISST dataset (Rayner *et al.* 2003).

3. Results

3.1 Annual Cycle

The bimodal nature of the observed annual cycle of Caribbean area-averaged (55-90ºW, 10-25ºN) precipitation is shown in Fig. 1 along with the annual cycle from the models. Large differences between AMIP and CMIP simulations are obvious with the AMIP model mean overestimating and CMIP model mean underestimating precipitation throughout the majority of the year (except January-March where both AMIP and CMIP means overestimate).

The representation of the Mid-Summer Drought (MSD) (Magaňa *et al.*, 1999), which occurs in July and August and separates the two rainfall maxima, is poor in the majority of models. Many of the CMIP models have an annual cycle with a single peak in September or October, which is represented in the model mean.

The AMIP simulations, however, show an improvement in simulating the MSD with a reduction of precipitation in the model mean in July, although this reduction is often not as large as in observations. This suggests that the models are misrepresenting a key process in the climatology of the region, even when forced with observed SSTs. Investigation into the processes (e.g. location and strength of the North Atlantic subtropical high and the Caribbean low-level jet) that are preventing the models ability to accurately capture the MSD are ongoing, with the representation of the Caribbean Low-Level jet (CLLJ) examined in Section 3.4.

3.2 Relationship with vertical motion

To examine the relationship between precipitation and circulation/vertical motion variability on monthly timescales, a regression analysis was performed. Global anomalies of ω at 500 hPa were regressed onto the

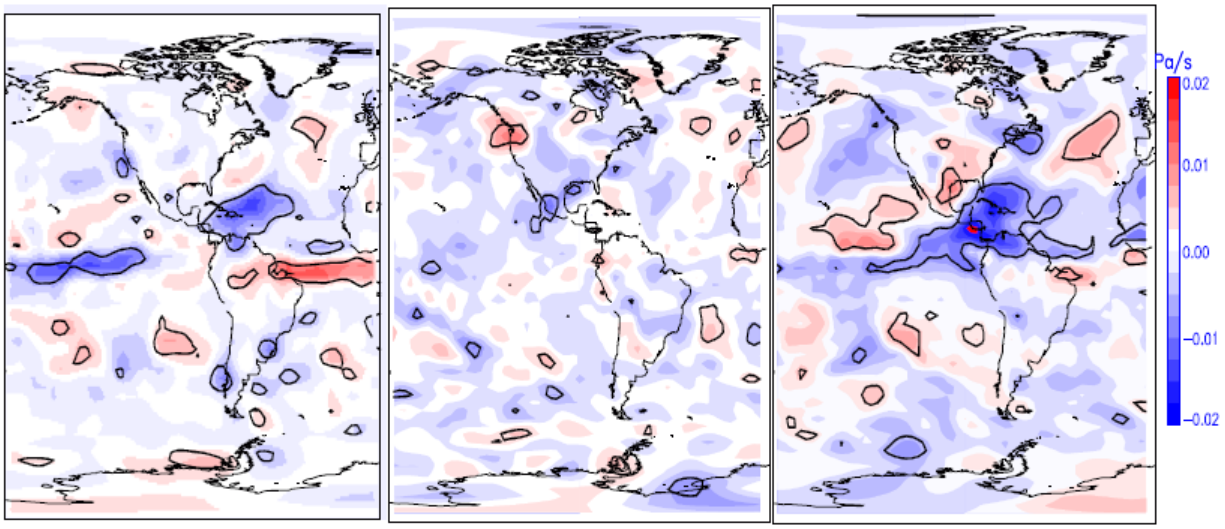

Fig. 2 Regression of MAM monthly 500 hPa omega onto Caribbean area-averaged precipitation for observations (left), miroc_hi CMIP model (center) and miroc_hi AMIP model (right). Thick black lines show 95 % significance of correlation.

simultaneous Caribbean area-averaged precipitation anomaly time series. Anomalies were calculated as differences from the annual cycle. This was done for all four seasons and the results of the March, April, May (MAM) regression are shown in Fig. 2. For purposes of brevity only one representative model is shown.

As expected, the observational regression analysis (Fig. 2, left panel) shows a large and significant region of negative regression coefficients over the Caribbean region, indicating that as precipitation anomalies increase upward vertical motion anomalies increase. A region of negative regression coefficients are also seen in the East Pacific due to the relationship between ENSO and Caribbean precipitation (Chen and Taylor, 2002). A third interesting feature is the region of positive regression coefficients over the Atlantic ITCZ and South America, suggesting that when Caribbean precipitation anomalies are positive, vertical motion over the Atlantic ITCZ and South America is anomalously subsiding.

The CMIP models (*e.g.* Fig. 2, center panel), however, do a very poor job of representing the relationship between Caribbean precipitation and vertical motion, even locally. The example mode in Fig. 2 shows that the negative regression coefficients we would expect to see in the Caribbean are not captured, suggesting that the precipitation that develops in the models is incorrectly related to vertical motion at 500 hPa. The AMIP models (e.g. Fig. 2, right panel) capture the negative regression coefficients in the Caribbean domain, but they are often too strong and too extensive. These incorrect relationships between precipitation and ω may be a manifestation of the known problem that tropical convection is too strongly coupled to local SST (Dai 2006) and CMIP models severely underestimate SST in the Caribbean. All the models do poorly at capturing the remote relationships in both the Pacific and Atlantic.

3.3 Daily Precipitation

Day to day variability in precipitation is essential to understand and correctly model due to its importance for extreme rainfall amounts. Daily data from observations and models were used to calculate the percent contribution to the total rainfall for six different precipitation categories (non zero but less than 1 mm, 1-5 mm, 5-10 mm, 20-50 mm and greater than 50 mm). The distribution was calculated for each grid point and then averaged over the entire Caribbean domain, with the results for the observations and all 16 CMIP models shown in Fig. 3.

Similar to Dai's (2006) analysis between 50ºS-50ºN, the CMIP models severely overestimate the contribution to the total precipitation by low rainrates (< 5 mm) and underestimate the contribution by

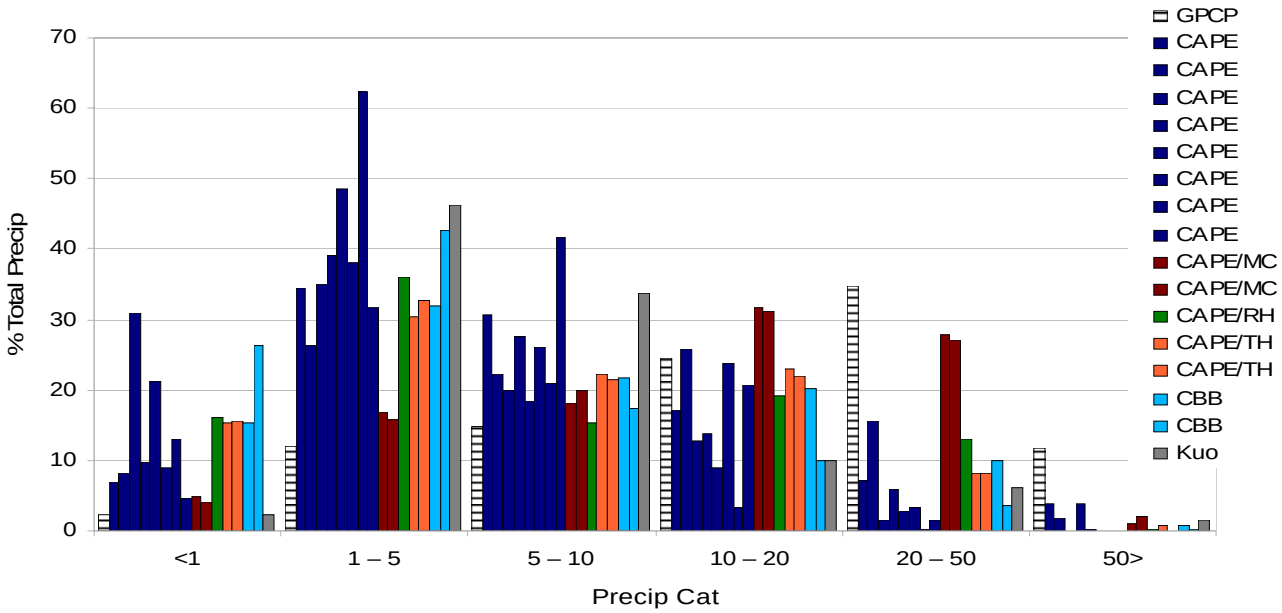

Fig. 3 Percentage contribution to the total Caribbean precipitation in six different precipitation categories for all 16 CMIP models with daily output. Colors indicate type of closure/moisture trigger scheme. MC: moisture convergence, RH: relative humidity, TH: threshold, CBB: cloud base buoyancy.

extreme high rainrates (> 20 mm) in the Caribbean. In the majority of the models, the bias to low precipitation rates is worse in the Caribbean than the large domain shown in Dai (2006). Although not shown here, the AMIP models also show a similar bias, towards low precipitation rates, but not as strong as the CMIP models (i.e. For 1-5 mm, the CMIP median is ~35 % and the AMIP median is ~28 % compared to the observed value of 12 %).

To investigate how the model properties affected this precipitation distribution, models were first categorized by the type of convective parameterization; spectral, bulk or Zhang and McFarlane (for details see Dai 2006). No group of parameterizations produced obviously better or worse distributions of daily precipitation (not shown). The models were then categorized by the type of closure assumption/moisture trigger scheme and shown in Fig. 3. What is most notable is that the two models that use CAPE closure and a moisture convergence trigger outperform all others (except at > 50 mm where all models do poorly).

3.4 Caribbean low-level jet

The CLLJ is a prominent feature of the southern Caribbean. It is an easterly jet maximizing at 925 hPa between 70 and 80ºW at approximately 14ºN and has a semi-annual cycle with maxima in February and July as seen in the reanalysis winds in Fig. 4 (left panel) (Amador 1998; Wang 2007, Muňoz *et al.* 2008). The CLLJ influences precipitation in the Caribbean by affecting moisture divergence (strong CLLJ leads to low Caribbean precipitation) and in the central United States (Cook and Vizy 2010). It is therefore an important feature that needs to be well represented in models.

Figure 4 (left panel) shows reanalysis wind speeds reaching 11 m/s at 925 hPa in July, with a strong weakening seen during September and October. All models were capable of producing a jet in the Southern Caribbean. However, the CMIP models tended to produce a CLLJ that was excessively strong (*e.g.* Fig. 4 center) and had a weak annual cycle (similar strength throughout the year). The location of the CLLJ was also shifted slightly southwards (by 1-2º) in many of the models.

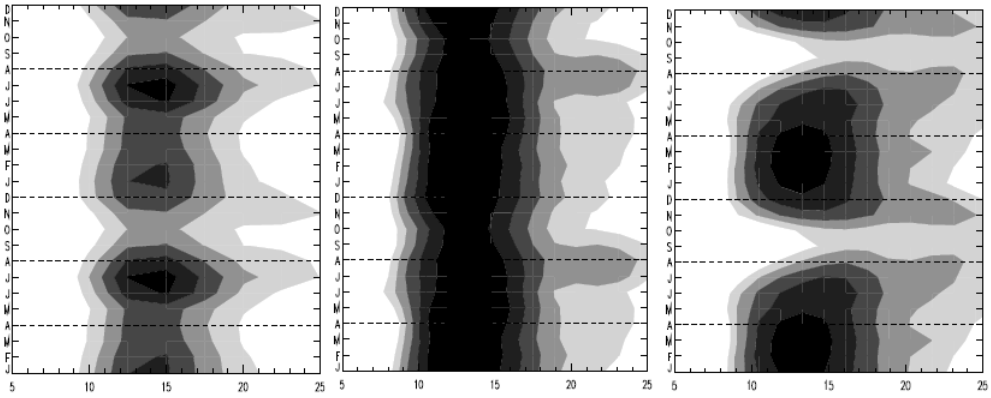

Fig. 4 Annual cycle of 925 hPa zonal wind at 75W for reanalysis (left), ncar_ccsm CMIP model (center) and ncar_ccsm AMIP model (right). Shading interval is 2 m/s beginning at -3 m/s. Annual cycle is repeated twice with month increasing upwards.

The AMIP simulations lead to a weaker jet than the CMIP simulations (*e.g.* Fig. 4 right), but CLLJ speeds were still higher than reanalysis values. AMIP simulations also produced an improved annual cycle in the majority of models, especially the weakening in September and October, perhaps highlighting the importance of correct SSTs and SST gradients to the CLLJ. The relationship between the ability of the models to capture the CLLJ and their representation of the MSD is ongoing, as is the investigation into the mechanisms behind the simulation of the CLLJ in the climate models.

4. Summary

The initial results from this study suggest that the IPCC AR4 CMIP and AMIP models are not accurately capturing many aspects of the Caribbean precipitation variability.

The precipitation annual cycle amplitude and mean is too large in AMIP simulations and too unimodal in CMIP simulations. The ability of the AMIP models to better capture the MSD may relate to their better ability

of capturing the annual cycle of the CLLJ. AMIP and CMIP models are not capturing the month-to-month relationship between Caribbean precipitation and vertical motion (both local and remote). The lack of a correlation between local precipitation and vertical motion is a significant problem for the CMIP simulations and requires further investigation.

The daily precipitation distribution for the Caribbean is shown to be similar to that of a much larger region (Dai 2006), but the bias towards low precipitation rates is accentuated in the Caribbean region. The AMIP models perform better than the CMIP models, but the bias is still large. In essence, the models are raining too frequently (81-100 % of the days) compared to only 42 % in the observations. Models that use the same convective parameterizations do not have the same precipitation distributions; however, models that use CAPE closure with a moisture convergence trigger outperform other types of closure/trigger schemes.

References

Amador, J., 1998: A climatic feature of the tropical Americas: The trade wind easterly jet. *Top. Meteor. Oceanogr*., **5**, 91–102.

Chen, A., and M. Taylor, 2002: Investigating the link between early season Caribbean rainfall and the El Nino + 1 year. *Int. J. Climatol*., **22**, 87–106.

Christensen, J.H., B. Hewitson, A. Busuioc, A. Chen, X. Gao, I. Held, R. Jones, R.K. Kolli, W.-T. Kwon, R. Laprise, V. Magaña , Rueda, L. Mearns, C.G. Menéndez, J. Räisänen, A. Rinke, A. Sarr, and P. Whetton, 2007: Regional Climate Projections. *Climate Change 2007: The Physical Science Basis*. Contribution of Working Group I to the Fourth Assessment Report of the Intergovernmental Panel on Climate Change, Solomon, S., D. Qin, M. Manning, Z. Chen, M. Marquis, K.B. Averyt, M. Tignor and H.L. Miller (eds.), Cambridge University Press, Cambridge, United Kingdom and New York, NY, USA.

Cook, K.H., and E.K. Vizy, 2010: Hydrodynamics of the Caribbean low-level jet and its relationship to precipitation. *J. Climate,* **23**, 1477-1494.

Dai, A. 2006: Precipitation characteristics in eighteen coupled climate models. *J. Climate*, **19**, 4605-4630.

Giannini, A., M. Cane, and Y. Kushnir, 2001: Interdecadal changes in the ENSO teleconnection to the Caribbean region and the North Atlantic oscillation. *J. Climate*, **14**, 2867–2879.

Huffman, G., R. Adler, M. Morrissey, D. Bolvin, S. Curtis, R. Joyce, B. McGavock, and J. Susskind, 2001: Global precipitation at one-degree daily resolution from multisatellite observation. *J. Hydrometeorol*., **2**, 36–50.

Jury, M., B. Malmgren, and A. Winter, 2007: Subregional precipitation climate of the Caribbean and relationships with ENSO and NAO. *J. Geophys. Res*., **112**, D16107, doi:10.1029/2006JD007541.

Jury, M., 2008: Climate influences on dengue epidemics in Puerto Rico. *Int. J. Environ. Heal. R*., **18**, 323–334.

Kanamitsu, M., W. Ebisuzaki, J. Woollen, S-K Yang, J.J. Hnilo, M. Fiorino, and G. L. Potter: 2002: NCEP-DEO AMIP-II Reanalysis (R-2). *Bul. Atmos. Met. Soc*., **83**, 1631-1643.

Magaňa, V., J.A. Amador, and S. Medina, 1999: The midsummer drought over Mexico and Central America. *J. Climate*, **12**, 1577-1588.

Martin, E.R., and C. Schumacher, 2010: Modulation of Caribbean precipitation by the Madden-Julian Oscillation. *J. Climate*, in press.

Muňoz, E., A. Busalacchi, S. Nigam, and A. Ruiz-Barradas, 2008: Winter and summer structure of the Caribbean low-level jet. *J. Climate*, **21**, 1260–1276.

Neelin, J.D., M. Munnich, H. Su, J.E. Meyerson, and C.E. Holloway, 2006: Tropical drying trends in global warming models and observations. *Proc. Nat. Acad. Sci*., **103**, 6110-6115.

Rayner, N.A, D.E. Parker, E.B. Horton, C.K. Folland, L.V. Alexander, D.P. Rowell, E.C. Kent, and A. Kaplan, 2003: Global analyses of sea surface temperature, sea ice, and night marine air temperature since the late nineteenth century. *J. Geophys. Res.*, **108**, No. D14, 4407 10.1029/2002JD002670.

Wang, C., 2007: Variability of the Caribbean low-level jet and its relations to climate. *Clim. Dyn*., **29**, 411–422.

Science and Technology Infusion Climate Bulletin
NOAA's National Weather Service
35th NOAA Annual Climate Diagnostics and Prediction Workshop
Raleigh, NC, 4-7 October 2010

Predicting Caribbean Basin Tropical Cyclone Activity

Philip Klotzbach

Department of Atmospheric Science, Colorado State University, Fort Collins, CO

1. Introduction

The Tropical Meteorology Project (TMP) at Colorado State University (CSU) has been issuing Atlantic basin seasonal tropical cyclone (TC) forecasts in early June with an update in early August since 1984 (Gray 1984). These forecasts have shown moderate skill in real-time (Klotzbach and Gray 2009). The success of these forecasts for the entire Atlantic basin has motivated additional research to see if similar forecast skill can be achieved for portions of the Atlantic basin. This topic is of relevance, because, just because the entire Atlantic basin is active does not guarantee that all portions of the basin will be equally active. For example, 2007 was only an average hurricane season for the entire Atlantic basin, however, Caribbean basin activity was very high, including two Category 5s tracking across the region (Dean and Felix). In this study, the Caribbean basin, defined as 10-20°N, 60-88°W, was examined for predictability (Figure 1).

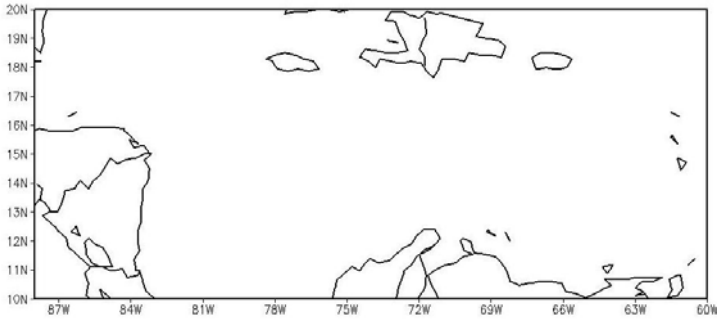

Fig. 1 The Caribbean basin as defined in this study.

2. Data

Caribbean basin tropical cyclone statistics from 1949-2008 were calculated from the "best track" dataset generated by the National Hurricane Center (Jarvinen *et al.* 1984). The forecast metric that is hindcast using the "best track" data was the Accumulated Cyclone Energy (ACE) index, which is defined to be accumulating the maximum sustained wind (in 10^4 knots^2) for all 6-hour period of a TC's existence with at least tropical storm-force winds (>= 34 knots) (Bell *et al.* 2000). ACE was calculated for each storm that tracked through the Caribbean basin. Figure 2 displays the seasonal ACE values for the Caribbean basin from 1949-2008.

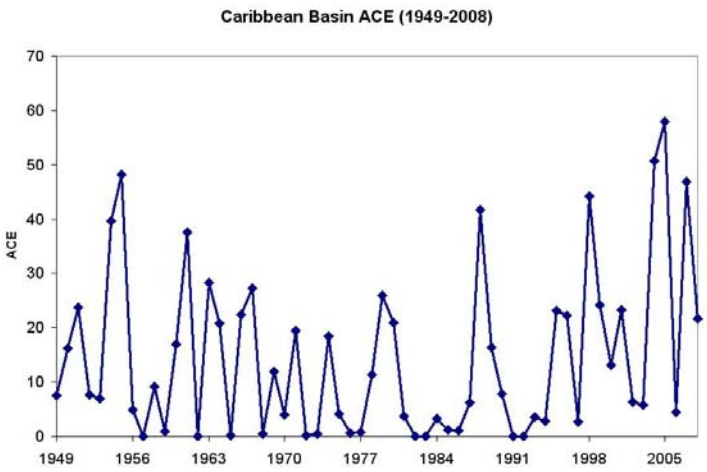

Fig. 2 Caribbean basin ACE from 1949-2008.

The National Centers for Environmental Prediction/National Center for Atmospheric Research (NCEP/NCAR) reanalysis (Kistler *et al.* 2001) was utilized as the source of large-scale atmosphere/ocean data.

3. Predictor Selection Methodology

Predictors were selected from the NCEP/NCAR reanalysis. Firstly, a composite analysis of several large-scale fields (200-mb and 925-mb zonal wind, sea level pressure and sea surface temperature) was conducted to see the differences between active vs. inactive seasons in the Caribbean (Figure 3). In general, active

Correspondence to: Philip Klotzbach, Department of Atmospheric Science, Colorado State University, Fort Collins, CO 80523; E-mail: philk@atmos.colostate.edu.

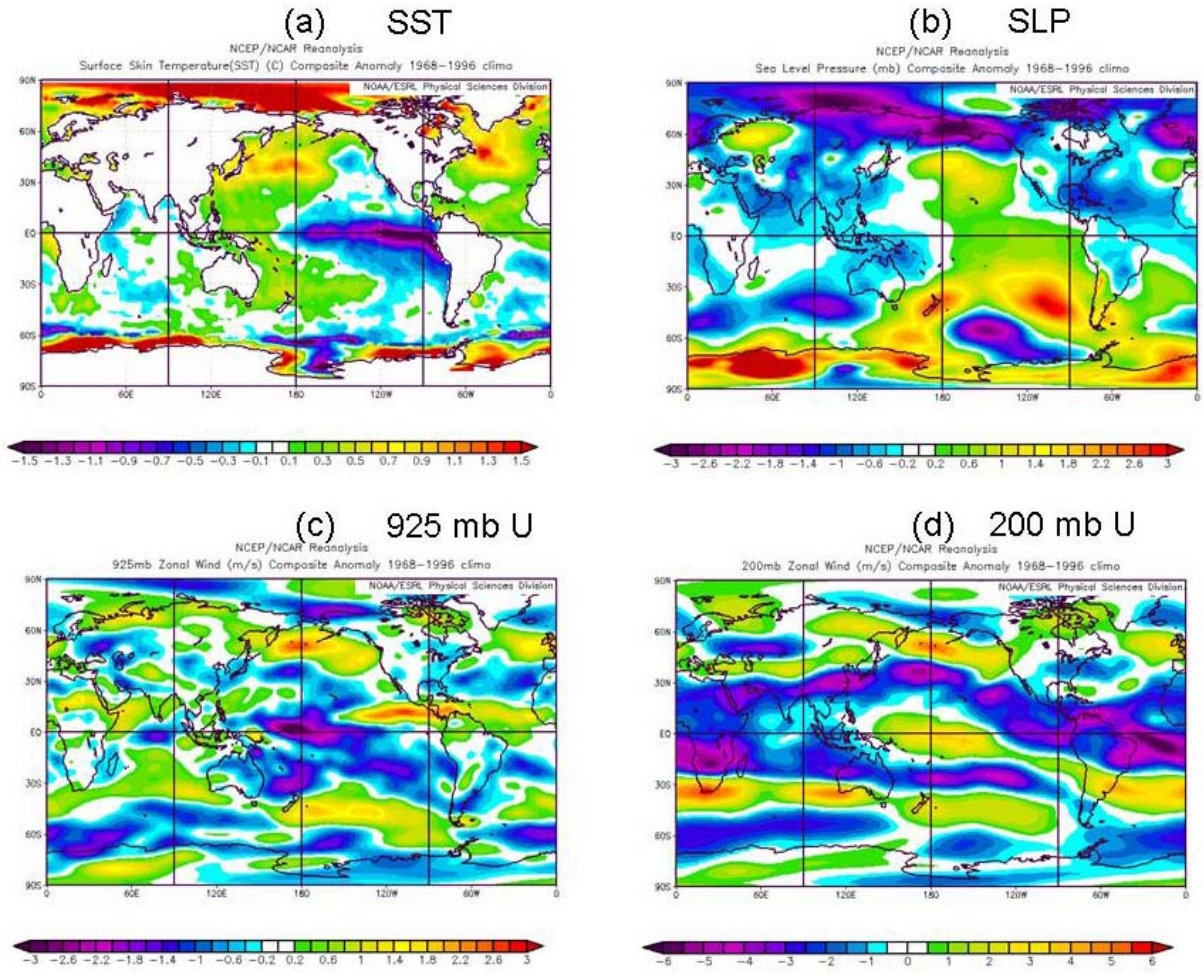

Fig. 3 August-October difference between the ten most active Caribbean basin seasons versus the ten least active Caribbean basin seasons for a) sea surface temperature (SST), b) sea level pressure (SLP), c) 925-mb zonal wind (U), and d) 200-mb zonal wind (U).

seasons are characterized by reduced vertical wind shear, lower-than-normal sea level pressure and warmer-than-normal sea surface temperatures throughout the Caribbean basin and tropical Atlantic. All of these features have been shown in many previous studies to drive more active Atlantic TC seasons (Klotzbach and Gray 2009 and references therein).

Then, precursor signals were sought from the NCEP/NCAR reanalysis using the Linear Correlations website available from the Earth System Research Laboratory at http://www.esrl.noaa.gov/psd/data/correlation/. Two forecast models were constructed, one using April-May data for an early June forecast, while the other model used July data for an early August forecast. Predictors selected had to correlate significantly at the 99% level with Caribbean ACE for the full-time period from 1949-2008 (correlation of at least 0.37) while these predictors had to show stability in correlation by correlating significantly at the 90% level (correlation of at least 0.30) with Caribbean ACE for both the earlier period from 1949-1978 and

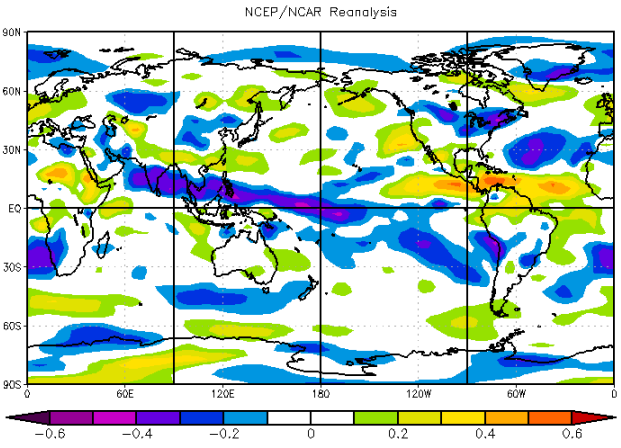

Fig. 4 Linear correlation between July 925-mb zonal wind and post-31 July Caribbean basin ACE.

the latter period from 1979-2008. In addition, each predictor had to show a reasonable qualitative relationship with the physical features in Figure 3 (*e.g.*, the predictors correlated with Caribbean basin and tropical Atlantic August-October values of SST, SLP, 925-mb zonal wind and 200-mb zonal wind). By doing this, the goal is to avoid selecting predictors that correlate by chance. In the real-time forecasts issued by CSU, extensive discussions of the proposed physical relationship between each predictor and Caribbean ACE are discussed in detail (Klotzbach and Gray 2010a, Klotzbach and Gray 2010b). Figure 4 displays a linear correlation map between July 925-mb zonal wind and post-31 July Caribbean ACE. Lastly, each predictor had to add at least three percent to the variance explained of the forecast scheme using a stepwise regression method.

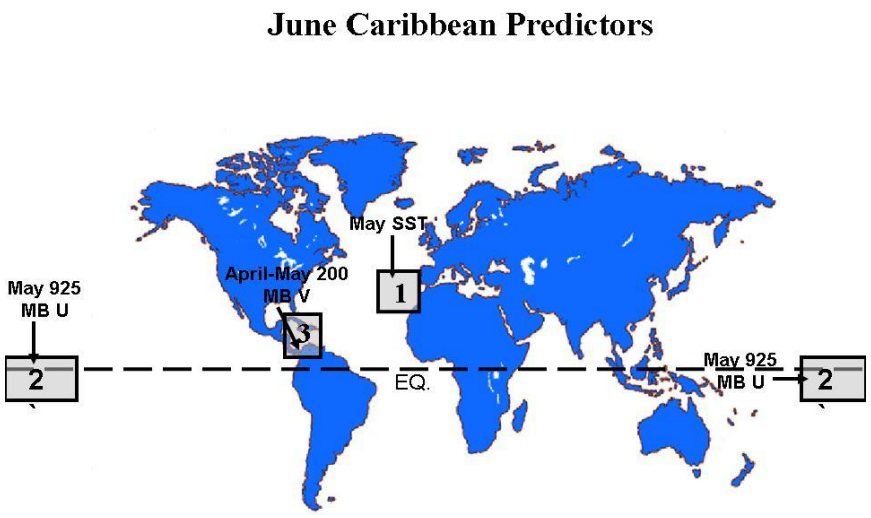

Fig. 5 Location of predictors utilized in the early June forecast of Caribbean basin ACE.

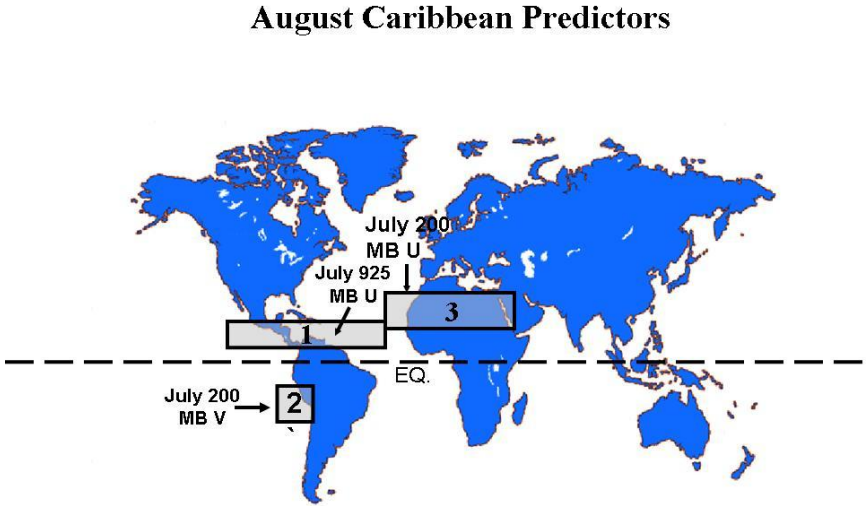

Fig. 6 Location of predictors utilized in the early August forecast of post-31 July Caribbean basin ACE.

4. Results

Figures 5 and 6 display the predictors selected for the early June and early August forecast scheme, respectively. Each forecast scheme uses no more than four predictors, in an effort to reduce over-fitting the forecast. Delsole and Shukla (2009) and Klotzbach and Gray (2009) discuss the danger of over-fitting forecast schemes. By including additional predictors to improve the variance explained in hindcast mode, there is the possibility that the actual prediction scheme's real-time forecast skill may degrade, if the relationship between each predictor and TC activity is not well-understood.

Both of these prediction models show moderate levels of hindcast skill. Figures 7 and 8 display the year-by-year hindcast for the June model and the August model, respectively. Note that the forecast skill improves from the June to the August model, which is to be expected, since the peak of the hurricane season occurs shortly after the August forecast is issued. Also, the variance explained of these forecast schemes is approximately 45-50%, indicating that there is a considerable amount of variability that is not going to be explained by any statistical scheme. There is inherent uncertainty in the atmosphere/ocean system that will always add an unpredictable component to any seasonal forecast.

5. Conclusions and Future Work

There appears to be the potential to issue skillful forecasts for Caribbean basin ACE in early June and early August. These forecasts will likely be of relevance to emergency managers, insurance interests as well as residents of the Caribbean and Central America. Real-time forecasts for Caribbean basin ACE were issued in early June and early August 2010, and these forecasts indicated very high levels of activity in this portion of the Atlantic basin. Activity in the Caribbean has verified at slightly above-average levels through the middle of October. Other portions of the Atlantic basin (*e.g.*, the Gulf of Mexico, the Main Development Region) will be investigated for hindcast skill in the near future.

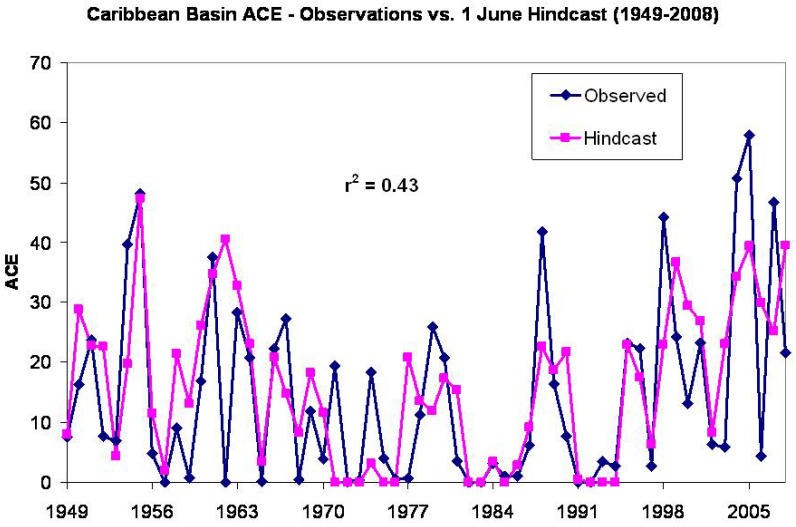

Fig. 7 Observations vs. hindcast Caribbean basin ACE for 1949-2008 for the early June forecast.

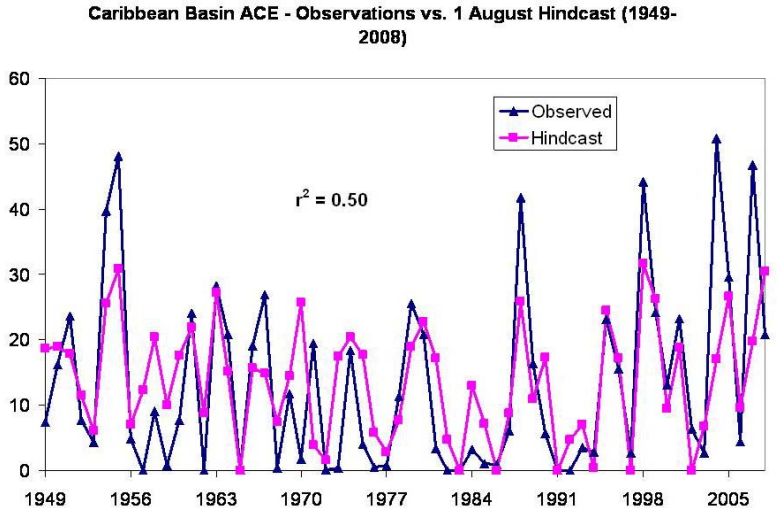

Fig. 8 Observations vs. hindcast post-31 July Caribbean basin ACE for 1949-2008 for the early August forecast.

References

Bell, G. D., and Coauthors, 2000: Climate assessment for 1999. *Bull. Amer. Meteor. Soc.*, **81,** S1-S50.

Delsole, T., and J. Shukla, 2009: Artificial skill due to predictor screening. *J. Climate*, **22,** 331-345.

Gray, W. M., 1984: Atlantic seasonal hurricane frequency. Part II: Forecasting its variability. *Mon. Wea. Rev.*, **112,** 1669-1683.

Jarvinen, B. R., C. J. Neumann, and M. A. S. Davis, 1984: A tropical cyclone data tape for the North Atlantic basin, 1886-1983: Contents, limitations, and uses, 21 pp. *NOAA Tech. Memo.* NWS NHC 22, Miami, FL.

Kistler, R., and Co-Authors, 2001: The NCEP-NCAR 50-year reanalysis: Monthly means CD-ROM and documentation. *Bull. Amer. Meteor. Soc.*, **82,** 247-267.

Klotzbach, P. J. and W. M. Gray, 2009: Twenty-five years of Atlantic basin seasonal hurricane forecasts. *Geophys. Res. Lett.*, **36**, L09711, doi:10.1029/2009GL037580.

___, and W. M. Gray, 2010a: Extended-range forecast of Atlantic seasonal hurricane activity and landfall strike probability for 2010. Issued 2 June 2010. Dept. of Atmospheric Science Report, Colorado State University, Fort Collins, CO, 57 pp. Available online at http://tropical.atmos.colostate.edu/Forecasts/2010/june2010/jun2010.pdf.

___, and W. M. Gray, 2010b: Forecast of Atlantic seasonal hurricane activity and landfall strike probability for 2010. Issued 4 August 2010. Dept. of Atmospheric Science Report, Colorado State University, Fort Collins, CO, 54 pp. Available online at http://tropical.atmos.colostate.edu/Forecasts/2010/aug2010/aug2010.pdf.

Science and Technology Infusion Climate Bulletin
NOAA's National Weather Service
35th NOAA Annual Climate Diagnostics and Prediction Workshop
Raleigh, NC, 4-7 October 2010

Climate Change, Drought, and Jamaican Agriculture: Trends in Crop Suitability

Scott Curtis[1] and Douglas W. Gamble[2]

[1]*East Carolina University, Greenville, NC*
[2]*University of North Carolina at Wilmington, Wilmington, NC*

1. Introduction

The Intra-Americas Seas, including the Caribbean, is projected to experience prolonged droughts in the 21st century according to the most recent climate modeling studies (Dai 2010). The IPCC fourth annual report states that Caribbean nations are very likely to warm in the 21st century and that summer rainfall is likely to decrease over the Greater Antilles, with 40% of seasons being extremely dry (Christensen *et al.* 2007). These projections suggest greater vulnerability to Caribbean small island developing states (SIDS), as summer coincides with the growing season for most agricultural activities. Further, there is a climatological dry spell in the middle of summer (Gamble and Curtis 2008), which may be more sensitive to a changing climate. Rauscher et al. (2008), using CMIP3 model runs for the 21st century suggest that the mid-summer dry spell (MSD) will be stronger and have an earlier onset.

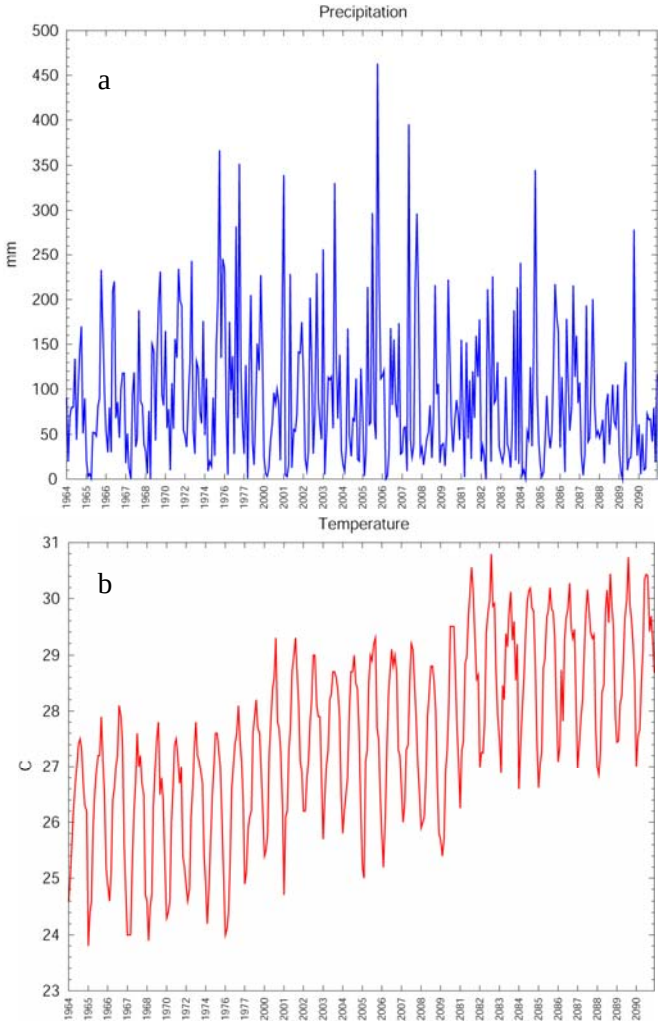

Fig. 1. Monthly weather for Montego Bay, Jamaica for data spanning the 1960s and 70s (past), 2000s (present) and simulated data for the 2080s (future) a) Precipitation (mm) and b) Temperature (°C).

Sixty-five percent of the population of Jamaica is dependent on agriculture as a source of livelihood, yet production is in decline due to trade-related economic pressures (Campbell *et al.* 2010). Agriculture is primarily rain-fed due to limited irrigation and lack of sustainable groundwater resources (Gamble 2004). Because of the presence of the MSD, Jamaican farmers divide their growing season into "early" (April to June), frontal system dependent with high variability, and "primary" (August to November), tropical convection and storm dependent and more consistent. Farmers will often try to bridge the July gap with "quick crops" that mature in less than eight weeks and are popular in tourist markets. If the MSD is weak, then the farmers can "go out big" with cash crops in the primary season, but if the MSD is strong, the farmers may squander precious resources and reduce income for the rest of the year (Gamble *et al.* 2010).

Farmers in St. Elizabeth Parish, Jamaica are very much aware of changes in their environment and 65% detect a trend towards longer, more frequent droughts (Campbell *et al.* 2010). However, they state that the

Correspondence to: Scott Curtis, Department of Geography, East Carolina University, Greenville, NC 27858;
E-mail: curtisw@ecu.edu

timing of drought is more important than its severity (Gamble *et al.* 2010). Gamble *et al.* (2010) found that Global Precipitation Climatology Project (GPCP) data confirms the perceptions, and reveals that the early growing season is becoming drier compared to the primary season, especially since 1991. This divergence of moisture may reinforce the farmer's observation of drought becoming more frequent. While this study is an important step towards the development of drought mitigation and adaptation plans in Jamaica, more work is needed to relate climate change to crop yields. The present study uses monthly temperature and precipitation data for one station in Jamaica to estimate past and future crop water needs and assess crop suitability.

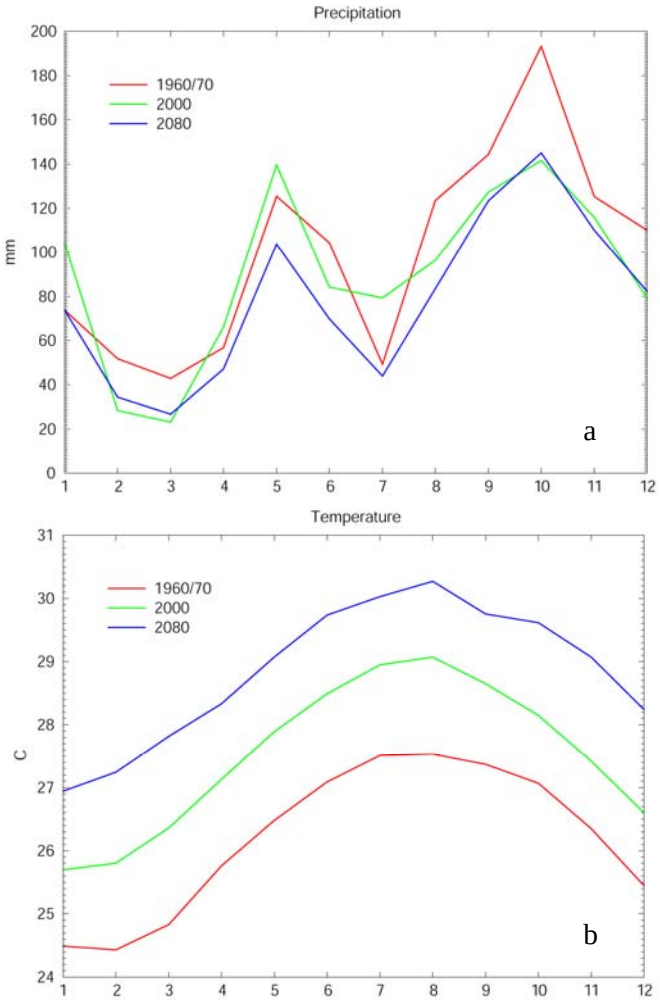

Fig. 2 Annual climatology for Montego Bay, Jamaica for data spanning the 1960s and 70s (past, red curves), 2000s (present, green curves) and simulated data for the 2080s (future, blue curves) a) Precipitation (mm) and b) Temperature (°C).

2. Methods

The intent of this study is to examine the water cycle in Jamaica over two 10-year periods, representing past and present conditions, and simulate the water cycle in the 2080-89 time frame by manipulating observations to match IPCC projections. One drawback to this type of analysis is the lack of sufficient data. The only Jamaica station with a long enough record of precipitation and temperature observations is Montego Bay. Here we assume this station is representative of the variability and change of the country's climate. Due to gaps in the temperature record, the past was defined as the years 1964-68, 1970, 1972, 1974, and 1976-77. The present was defined as 2000 to 2009. To generate the future conditions, we first assumed that only the means would change and not the variances. Temperature data was created with a normal distribution, with monthly means adjusted upward by 2 degrees Celsius from the average of the past and present periods, consistent with the IPCC (Christensen *et al.* 2007). For precipitation, months were selected from the past and present time periods, to ensure that the monthly variability remained unchanged in the future. Then precipitation for each month of the annual cycle was randomly distributed over the 10 years and adjusted downward (again from the mean of the past and present periods) according to the IPCC (Christensen *et al.* 2007). December, January, February, September, October, and November were reduced by 6%, March, April, and May by 13% and June, July, and August by 20%.

Once the temperature and precipitation data was selected, water balances for the three 10-year periods were created with the USGS Thornthwaite Water Balance model. The runoff factor was set at 50% and direct runoff at 5%. Soil moisture storage capacity was determined to be 150 mm according to common United Nations Food and Agriculture Organization soil units in the country. The previous six months (climatological six months for the 2080s) were appended to the beginning of the data sets to spin up the model. From monthly mean temperature and precipitation accumulation, the Thornthwaite model generates potential evapotranspiration, actual evapotranspiration, and soil moisture storage.

Finally, the relative evapotranspiration deficit was used to generate deficit yield (DY) according to Batjes (1987)

$$\mathbf{DY = (1 - Ya/Ym) = ky * (1- AET/ETc)}$$

where Ya = actual yield, Ym = maximum yield, ky is the relational factor, AET = actual evapotranspiration, and ETc = potential evapotranspiration of the crop, which is simply the potential evapotranspiration times the crop coefficient (kc). Agro-climatic suitability classes (Table 1) were developed for each month based upon calculated DY following Batjes (1987).

3. Results

Figure 1 shows the time series of precipitation and temperature for the three time periods. The upward trend in temperature is easier to discern than the downward trend in precipitation. The simulated data seems to have a reasonable variability. The monthly climatologies of the three periods are given in Figure 2. The 2080s are drier in every month compared to the1960s and 70s, but actually wetter than the 2000s in February, March, October, and December. Interestingly, the 2000s had a more muted MSD as compared to the 1960s and 70s. The 2080s agrees with Rauscher (2008), with a more pronounced and longer lasting MSD than the past and present time periods. The temperature graph shows the expected constant trend over the annual cycle.

Suitability Class	DY < 0.2 (out of 10 years)	DY < 0.4 (out of 10 years)
Highly Suitable (HiS)	6+	8+
Moderately Suitable (MoS)	4-5	6-7
Marginally Suitable (MaS)	2-3	4-5
Not Suitable (NS)	0-1	0-3

Table 1 Agro-climatic suitability classes assigned based on deficit yield (DY) values near zero (maximum yield) over x number of years out of ten. For example, Highly Suitable would, in a ten year period, entail six or more years where DY is calculated to be less than 0.2 and eight or more years where DY is less than 0.4.

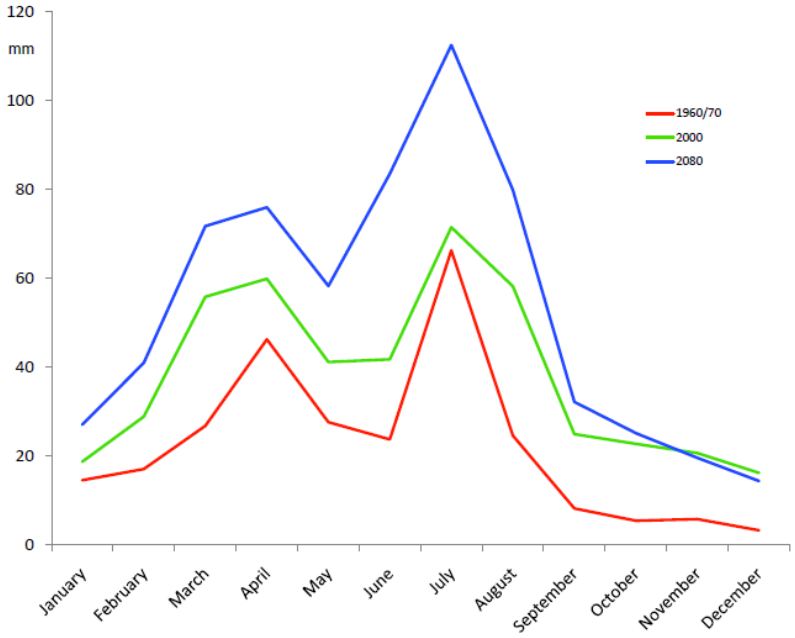

Fig. 3 Annual climatology of actual evapotranspiration minus potential evapotranspiration for Montego Bay, Jamaica for the 1960s and 70s (red curve), 2000s (green curve), and 2080s (blue curve).

After running the temperature and precipitation data through the Thornthwaite model for the past, present, and future scenarios, crop water need was assessed as the difference of the potential evapotranspiration minus the actual evapotranspiration (Fig. 3). While there will be a demand for more water in all months of the year, the months likely to experience the greatest water stress in the future will be June, July, and August. Differences between the 2080s and 1960s-70s are in excess of 45 mm. Also troublesome, is that the moisture deficit appears to be accelerating. In June 70% of the crop water need comes between the 2000s and 2080s, and this number increases to 89% in July during the height of the MSD.

For the agro-climatic suitability analysis, the tomato crop was chosen. The tomato is considered a cash crop, but yield is strongly tied to rainfall amounts and the crop is highly susceptible to drought (Campbell *et al.* 2010). The correlation between annual tomato yield (1000 kg ha^{-1}) for Jamaica as a whole and the closest

GPCP grid node is 0.5 (significant at the 95th percentile) between 1979 and 2007. The tomato has a ky value of 1.05, and it takes three months for the tomato to reach harvest in Jamaica (Campbell *et al.* 2010), when it has a kc value of approximately 0.8. Table 2 shows the Batjes (1987) suitability classes for each month of the year for the three time periods. The month refers to the sowing month, and thus the reaping month would be n+2. With the exception of the primary growing season, which has sufficient moisture supply even in the face of less rainfall and higher temperatures, there is a decline in agro-suitability. April and June, traditionally part of the early growing season, become only marginally suitable for planting in the 2080s. It becomes not suitable to sow in May (with reaping in July) due to the projected strong and extended MSD (Fig. 2a). In fact, in the first half of the year, only March reaches the status of Moderately Suitable in the 2080s, whereas in the 1960s and 70s January, March, April, and June were all considered Highly Suitable.

While not shown here, short maturation crops, like turnip, would demonstrate a similar response as Table 2, except sowing months would be shifted one or two months later. Thus, July would become not suitable for planting, and the potential for "quick crops" to generate income across the MSD would become too risky to attempt.

Time period	JAN	FEB	MAR	APR	MAY	JUN	JUL	AUG	SEP	OCT	NOV	DEC
1960/70	HiS	MoS	HiS	HiS	MaS	HiS	HiS	HiS	HiS	HiS	HiS	HiS
2000	MaS	NS	MoS	MoS	MaS	MaS	HiS	HiS	HiS	HiS	HiS	MoS
2080	NS	NS	MoS	MaS	NS	MaS	MoS	HiS	HiS	HiS	HiS	MoS

Table 2 Agro-climatic suitability classes for planting tomato during the 1960s-70s (past), 2000s (present), and 2080s (future).

4. Discussion

Estimates of past, present, and future crop water needs and suitability are presented for Jamaica. Jamaican farmers and government officials recognize climate change and the threat it poses. As a rural planner in the Jamaican Ministry of Agriculture put it:

> "climate change right now is having an impact. Our problem here in Jamaica is that we have not gotten to the point where we can now predict the growing season…" (July, 2010)

This lack of predictability stems from an increase in temperature and decrease in precipitation, especially during the summer season. If the trend continues, as projected by the IPCC, then by the end of the 21st century crop water needs will be unprecedented, with moisture deficits in March, April, June, July, and August exceeding the present MSD conditions in July (Fig. 3). This would undoubtedly wipe out the early growing season, which would lead to a food crisis. These trends are likely occurring in other Caribbean SIDS, and more data is needed to extend our preliminary findings.

Understanding the interactions between meteorology, hydrology, and land cover over the Caribbean is a challenge that requires an infrastructure of observations that is not presently available. The Intra-Americas Study of Climate Processes (IASCLIP) will likely improve this situation with an intensive field campaign that will help build better drought prediction models and products for the region. Further, it is hoped that IASCLIP will leave a legacy of capacity building, so that Caribbean SIDS will be in a better position to adapt agriculture practices in response to climate change.

References

Batjes, N. H., 1987: CROPRISK: A computerized procedure to assess the agro-ecological suitability of land for rainfed annual crops. Technical Soils Bulletin No. 7, Ministry of Agriculture, Rural Physical Planning Division, Jamaica Soil Survey Unit.

Campbell, D., D. Barker, and D. McGregor, 2010: Dealing with drought: Small farmers and environmental hazards in southern St. Elizabeth, Jamaica. *Applied Geography*, doi:10.1016/j.apgeog.2010.03.007

Christensen, J. H., and co-authors, 2007: Regional Climate Projections. In: *Climate Change 2007: The Physical Science Basis. Contribution of Working Group I to the Fourth Assessment Report of the Intergovernmental Panel on Climate Change*, Solomon, S. *et al.* (eds.), Cambridge University Press, Cambridge, United Kingdom and New York, NY, USA.

Dai, A., 2010: Drought under global warming: A review. *WIREs Climate Change*, doi:20.2002/wcc.81

Gamble, D. W, 2004: Water resource development on small carbonate islands: Solutions offered by the hydrologic landscape concept. In: *WorldMinds:Geographic Perspectives on 100 Problems*, D. J. B. Warf, and L.K. Hansen (eds.), 503-508.

—, D. Campbell, T.L. Allen, D. Barker, S. Curtis, D.F.M. McGregor, and J. Popke, 2010: Climate change, drought, and Jamaican agriculture: Local knowledge and the climate record. *The Annals of the Association of American Geographers*, **100**, 880-893.

—, and S. Curtis, 2008: Caribbean precipitation: Review, model, and prospect. *Progress in Physical Geography*, **32**, 265-276.

Rauscher, S. A., F. Giorgi, N. S. Diffenbaugh, and A. Seth, 2008: Extension and intensification of the Meso-American mid-summer drought in the twenty-first century. *Climate Dynamics*, **31**, 551-571.

Science and Technology Infusion Climate Bulletin
NOAA's National Weather Service
35th NOAA Annual Climate Diagnostics and Prediction Workshop
Raleigh, NC, 4-7 October 2010

The Rendition of the Atlantic Warm Pool in Reanalyses

Ashley Stroman and Vasubandhu Misra
Center for Ocean-Atmospheric Prediction Studies
Department of Earth, Ocean and Atmospheric Sciences
The Florida State University, Tallahassee, FL

1. Introduction

The Intra-America Seas (IAS) region includes the Caribbean Sea, the Gulf of Mexico, the Pacific Ocean west of Central America and northern South America, and the adjacent lands. It hosts the second largest body of warm water, the Western Hemisphere Warm Pool (WHWP). The WHWP lies north of the equator and is characterized by having water temperature equal to or greater than 28.5°C. It can consist of the eastern North Pacific west of Central America, the Gulf of Mexico, the Caribbean Sea, and the western tropical North Atlantic throughout its development (Figure 1). Within the WHWP is the Atlantic Warm Pool (AWP). The AWP is comprised of the Gulf of Mexico, the Caribbean Sea, and the eastern tropical North Atlantic. Wang and Enfield (2001) found that the AWP exhibits intraseasonal variability in that it reaches its maximum size in August-September-October (ASO) and then disappears completely in boreal winter [December-January-February (DJF)]. It also exhibits interannual variability in regards to its size and intensity with years exhibiting large AWPs being roughly three times greater than in small AWP years (Wang *et al.* 2006).

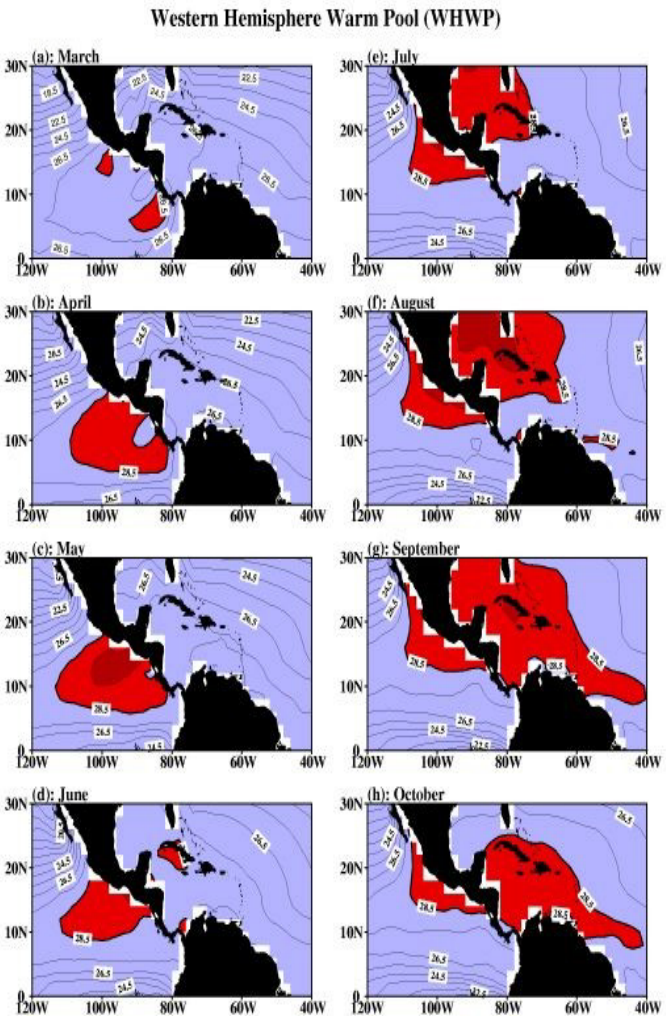

Fig. 1 Monthly variation of WHWP (Wang and Enfield 2001)

The AWP has become a recent topic of interest due to its impact on surrounding areas. Through its interactions with the North Atlantic Subtropical High (NASH), the AWP effects moisture transport to North, Central and South America. It has also been found to have an impact on hurricane activity. Thus, it plays a critical role in the boreal summer climate in the Caribbean and surrounding areas (Wang and Enfield 2001).

The IAS region is one of the most poorly observed locations in the world (Figure 2). It is important to predict the weather and climate in this region as it has an important impact on coastal areas, tropical cyclones, geological and ecological systems, and the climate of North and South America. Therefore, in this study we wish to explain the subsurface evolution of the AWP and discuss the impact of ocean dynamics and thermodynamics that can change it through reanalyses.

Correspondence to: Ashley Stroman, Center for Ocean-Atmospheric Prediction Studies, Department of Earth, Ocean and Atmospheric Sciences, The Florida State University, Tallahassee, FL; E-mail: acs08g@fsu.edu

2. Data and methodology

For this study, the two reanalyses that were used were NCEP GODAS (Global Ocean Data Assimilation System) data with NCEP-DOE Reanalysis 2 and NCEP CFSR (Climate Forecast System Reanalysis). NCEP-DOE R2 data is on a 2.5° by 2.5° global grid mesh with seventeen pressure levels. The GODAS has a model domain from 75°S to 65°N. It has horizontal resolution of 1° by 1°, which is increased to 1/3° in the north-south direction within 10° of the equator, and forty vertical levels. NCEP CFSR is a high resolution, global, coupled atmosphere-ocean-land-surface-sea ice system. The global atmospheric resolution is approximately 38km with sixty-four levels (from surface to 0.26hPa). The latitudinal spacing of the global oceans is 0.25° at the equator and extends to 0.5° beyond the tropics. There are also 40 levels to a depth of 4737m. The CFSR output resolution is at 0.5° by 0.5°.

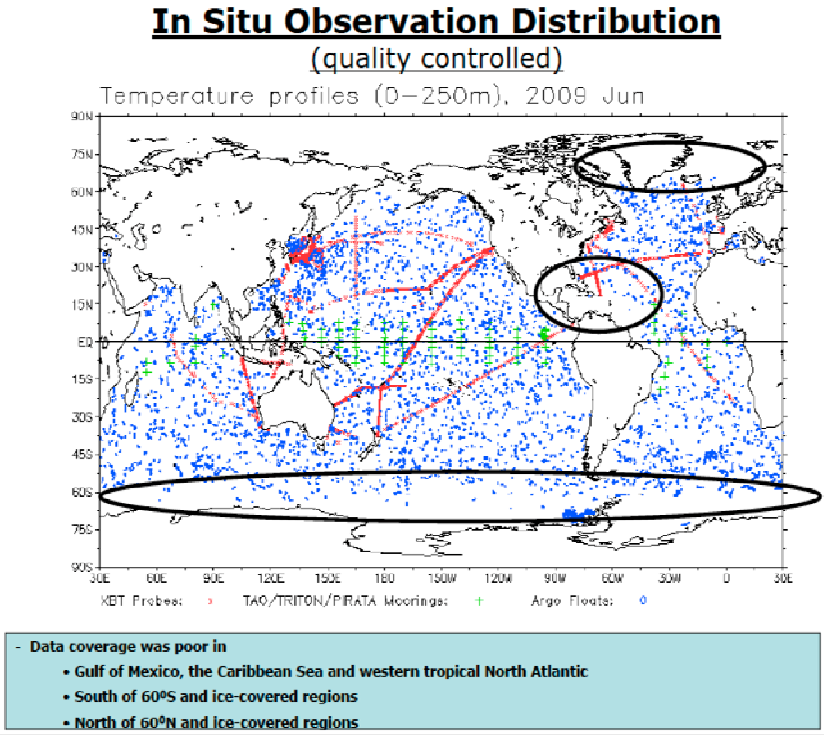

Fig.2 In-situ ocean temperature observation distribution in 2009

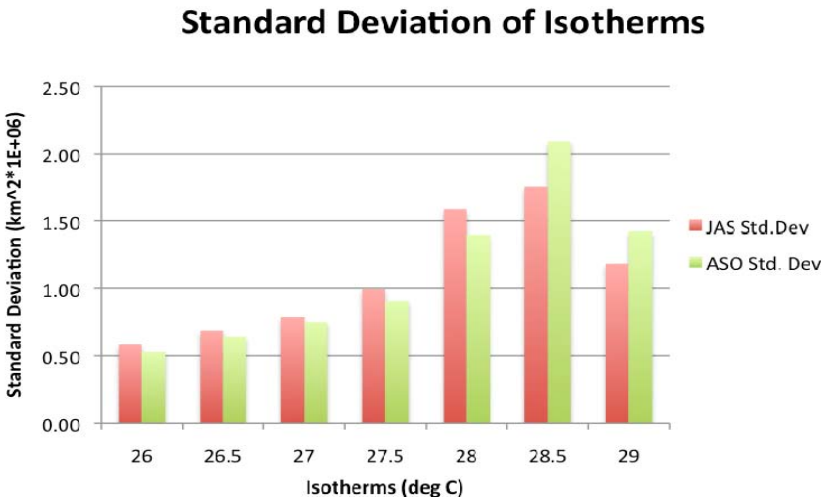

Fig. 3 Standard deviation of isotherms from 26.0°C to 29.5°C. ERSSTv3 data was used from 1854-2009.

We focused on ASO averages from 1980-2007. We chose ASO when the AWP reaches its peak. We computed the size of the AWP using GODAS data and NCEP CFSR data. The area of the AWP was defined as the area where temperature is equal to and greater than 28.5°C. As seen in Figure 3, this isotherm was used since its enclosed area exhibits the largest interannual variability. Correlations were found between the size of the AWP and sea surface temperatures (SSTs) at 0, 3 months lead/lag of AWP. Correlations were also found between the size of the AWP and tropospheric temperature (TT), which is defined as the 850-250mb temperature average. This was to see if the AWP has an effect on heating the troposphere as was found in prior research with the Niño 3 index. (Sobel 2001).

3. Results

Figure 4 shows correlations between the size of the AWP and SSTs. The strongest correlations are between the AWP in ASO and the SSTs in ASO. This suggests that the SSTs in ASO play a large role in the size of the AWP in the Caribbean and the Gulf of Mexico in ASO. SSTs in May-June-July (MJJ) do have an effect on the size of the AWP in the Caribbean portion, however, only CFSR picks up a correlation in the

Gulf of Mexico. Other main differences between GODAS and CFSR are in the Western Pacific and in latitudes larger than 75°N. The latter is due to the domain of the GODAS not including the entire globe.

In Figure 5, correlations between the Sempember-October-November (SON) Niño3 index and TT are shown. This figure is in agreement with the work of Sobel (2001). It was found that the Niño3 region has its highest correlation when it lags at least 3 months due to the fact that the Niño3 region is responsible for warming SSTs in other regions through the atmosphere. This lag is consistent with the ocean mixed layer having a larger heat capacity. This ocean mixed layer also needs to be warmed so that the convective heating anomalies that are associated with the Niño3 anomalies can warm the atmosphere. One of the differences between the GODAS and CFSR is in the Pacific Ocean. The GODAS isn't able to capture the effect that waves have on the SSTs like CFSR is. This is mainly due to the higher resolution of CFSR.

In Figure 6, correlations between the size of the ASO AWP and TT are shown. It is obvious from the figure that size of the AWP has the strongest correlation with TT in the same months, ASO. The AWP does not help warm the TT in the future as shown by the low correlations with TT in November-December-January (NDJ) and February-March-April (FMA). One of the differences between CFSR and the GODAS is shown along the equator.

4. Concluding remarks

The size of the AWP has a stronger correlation with SSTs in the Gulf of Mexico and the Caribbean Sea at an instantaneous time. However, there also exists a correlation between the two for the size of the AWP in ASO and SSTs three months prior. It was found that the AWP does not act in a similar fashion as the Niño3 index. The TT responds to the size of the AWP instantaneously whereas

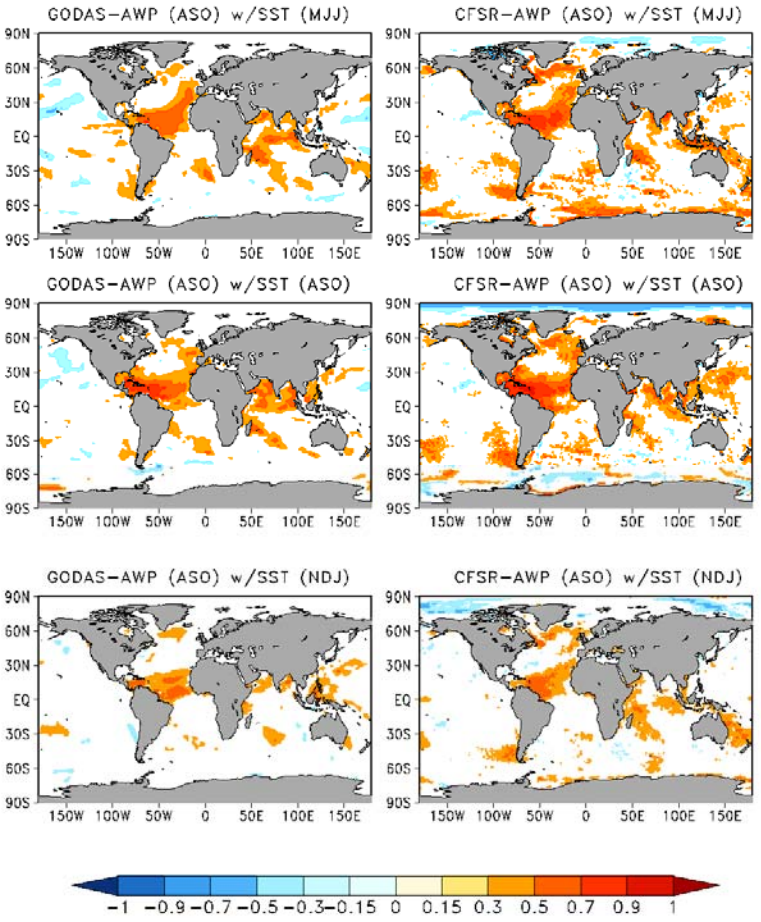

Fig. 4 Correlations between the size of the ASO AWP and SSTs in MMJ (top), ASO (middle) and NDJ (bottom), respectively, at 95% confidence. The left column is for GODAS and the right column is for CFSR.

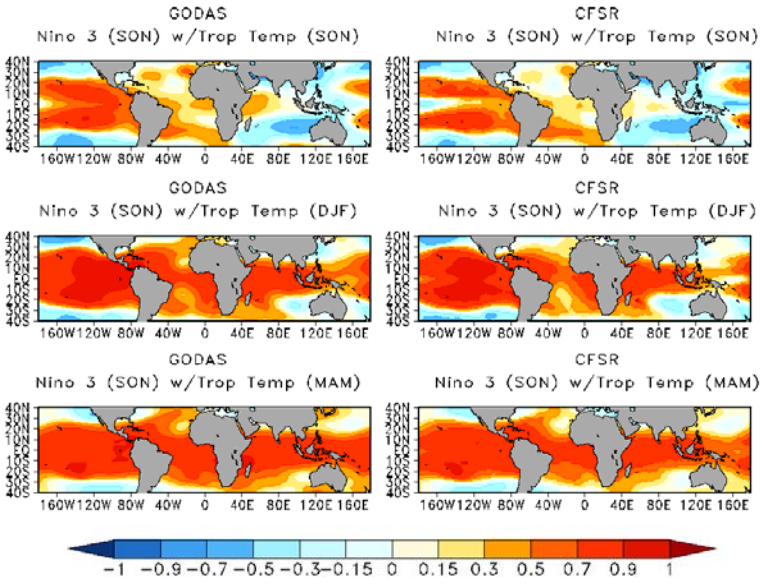

Fig. 5 Correlations between the SON Niño3 index and TT in SON (top), DJF (middle) and MAM (bottom), respectively. The left column is for GODAS and the right for CFSR.

the Niño3 index has a stronger impact on TT at at least a three month lead.

The GODAS and CFSR capture characteristics of the AWP fairly well. Differences arise in higher latitudes and along the equator due to higher resolution of the CFSR and the fact that it uses a coupled atmosphere-ocean model.

References

Wang, C. and D. B. Enfield, 2001: The tropical Western Hemispher warm pool. *Geophys. Res. Lett..*, **28**, 1635-1638.

—, D. B. Enfield, S. K. Lee, and C. W. Landsea, 2006: Influences of the Atlantic warm pool on Western Hemisphere summer rainfall and Atlantic Hurricanes. *J. Climate*, **20**, 5021-5040.

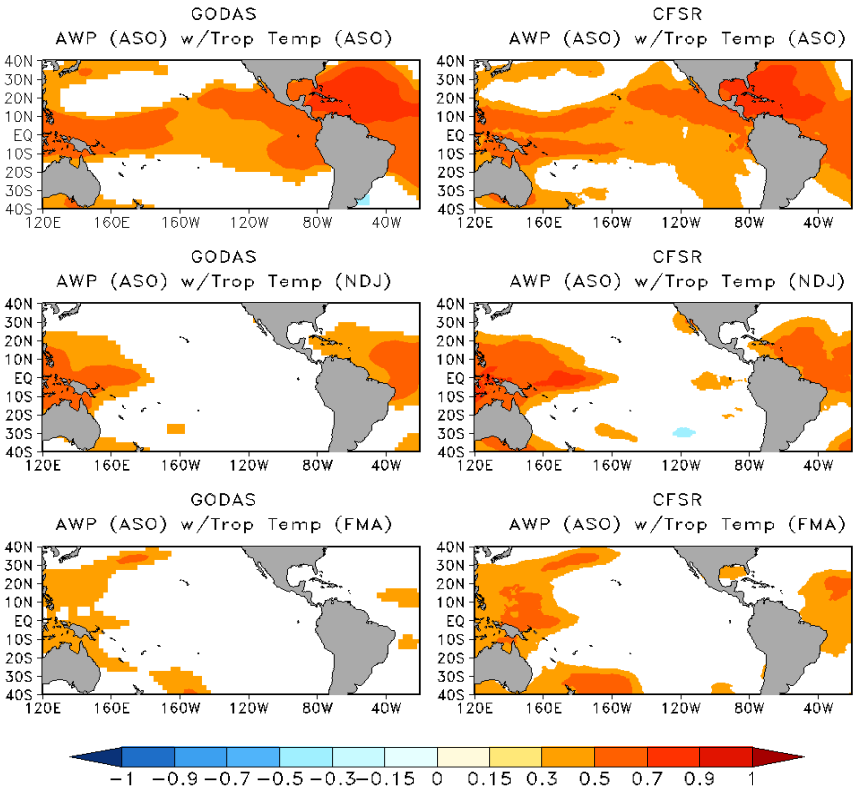

Fig. 6 Correlations between the size of ASO AWP and TT in ASO (top), NDJ (middle) and FMA (bottom), respectively. The left column is for GODAS and the right column is for CFSR.

4. CLIMATE PRODUCTS AND SERVICES

Science and Technology Infusion Climate Bulletin
NOAA's National Weather Service
35th NOAA Annual Climate Diagnostics and Prediction Workshop
Raleigh, NC, 4-7 October 2010

Assessing the Value of Climate Information in Agriculture Using the Stochastic Production Frontier Approach

Daniel Solís and David Letson

Rosenstiel School of Marine and Atmospheric Science, University of Miami, Miami, FL

In the past decades, federal agencies have financed numerous climate research programs aiming to improve the accurately of forecasting techniques and to enhance the dissemination of usable information (NOAA, 2005). While vast amount of resources have been invested to reach these goals, the issue of how to measure the economic value of climate forecasts is still been discussed in the literature.

The value of climate forecasts can be defined and evaluated in different ways. Most published studies on this subject have focused on evaluating the potential effect of climate information on the financial performance (revenues, profit, *etc.*) of a farm (Cabrera *et al.* 2009, Letson *et al.* 2005, among others). However, the use of economic performance measures, such as productivity, input substitution, inefficiency, etc., have received much less attention in the literature.

Consequently, the main goal of this study is to analyze the economic impact of climate information on the technical efficiency of the US agricultural sector. To reach our goal we employ a Stochastic Production Frontier (SPF) framework (Kumbhakar and Lovell, 2003). SPF presents the major advantage of allowing us to estimate simultaneously the production frontier and inefficiency models. Specifically, in this model the impact of climate variability on production is measure by incorporating alternative climatic indexes into the production frontier (*i.e.*, climate zone, annual precipitation and drought index); conversely, the value of climate information is evaluated following Shao and Lin (2001) in which a climate information index (*i.e.*, ENSO signal) is incorporated in the technical inefficiency model.

The geographical region select for this study is the Southeast U.S. (*i.e.*, Alabama, Florida, Georgia, North Carolina and South Carolina). This area is ideal for studying the interaction of climate variability and agricultural production due to the strong influence ENSO in the regional climate. To implement our SPF model we use a balanced panel data, including the economic, production and climate information over approximately a 50-year period from 1960 to 2007. The economic and production data was collected from the USDA Economic Research Service and the USDA National Statistical Service. The climate information was collected from the South East Regional Climate Service.

Preliminary results indicate that variations in climatic conditions affect, directly and indirectly, agricultural production and productivity through interactions, mean output elasticities, economies to scale and technical efficiencies. The included climate variables are not only statistically significant in all estimated models but that their omission could also generate significant inconsistencies on technical efficiency (TE) scores. These results have significant policy implications. Specifically, if the effects of uncontrollable agro-climatic factors on TE are significant, but not accounted for, then agricultural strategies seeking corrective measures to improve productivity would have little impact since the real source of technical inefficiency is the uncontrollable agro-climatic conditions. Lastly, the effect of climate information on the level of technical efficiency of this sector is also positive and significant; suggesting the use of climate information is a good mean for improving agricultural performance.

References

Cabrera, V.E., D. Solís, G.A Baigorria, and D. Letson, 2009: Managing climate variability in agricultural analysis. *Ocean Circulation and El Niño: New Research,* J.A. Long and D.S. Wells (Eds), Nova Science Publishers, Inc., 163-179.

Correspondence to: Daniel Solís, Rosenstiel School of Marine and Atmospheric Science, University of Miami, Miami, FL; E-mail: dsolis@rsmas.miami.edu

Kumbhakar S, Lovell C., 2003: *Stochastic Frontier Analysis*. Cambridge University Press.

Letson, D., G.P. Podestá, C.D. Messina, and R.A. Ferreyra, 2005: The uncertain value of perfect ENSO phase forecasts: Stochastic agricultural prices and intra-phase climatic variations. *Climatic Change*, **69**, 163-196.

NOAA, 2005: New priorities for the 21st century – NOAA's strategic plan, Washington, DC.

Shao, B., and W. Lin, 2001: Measuring the value of information technology in technical efficiency with stochastic production frontiers. *Information & software technology*, **43**(7), 447-456.

Science and Technology Infusion Climate Bulletin
NOAA's National Weather Service
35th NOAA Annual Climate Diagnostics and Prediction Workshop
Raleigh, NC, 4-7 October 2010

Engaging Stakeholders for Conducting Regional Climate Assessments

J. Greg Dobson, Jim Fox, Karin Lichtenstein, and Matt Hutchins

National Environmental Modeling and Analysis Center
The University of North Carolina – Asheville

1. Introduction

Climate variability and change are new challenges that decision makers from across spatial scales and from different sectors are being forced to address and prepare for. These new challenges contain a complexity of issues that include accessing information, assessing uncertainty, and considering vulnerabilities. As our society begins to think about climate variability and climate change impacts, it is critical that such stakeholders as decision and policy makers have a firm understanding of these issues in order to assess risk and develop adaptation strategies at local levels (USGCRP 2009). Simply providing stakeholders with global-scale climate information, models, and products does not equate to successful use and understanding of the information. Traditional climate assessments have primarily used a top-down approach, but rather a bottom-up approach is required (NAST 2001). This will allow for end-users to be engaged from the beginning of the assessment process so that climate experts can better understand specific problems and concerns they face, and ensure that the assessments are user-driven rather than product-driven.

In response to the next National Climate Assessment (NCA), which is currently underway, the University of North Carolina at Asheville's National Environmental Modeling and Analysis Center (NEMAC), with support from NOAA's National Climatic Data Center, and in collaboration with NOAA's Southeast Regional Climate Center and the North Carolina State Climate Office, is developing a unique approach and framework for engaging stakeholders to create comprehensive regional climate assessments for the state of North Carolina and beyond. The approach includes combining climate data with stakeholder values to guide the application of climate information from "global to regional to local levels" and to ensure that local stakeholder knowledge and information can be assessed and integrated at a national level. This approach will lead to better communication with stakeholders across scales and will not only assess the current state of the climate along with associated impacts and vulnerabilities, but take into account other key cross-sector concerns as well as identify data and information gaps.

NEMAC's approach of conducting regional climate assessments through stakeholder engagement is being applied across multiple regions in North Carolina and the Southeastern U.S. This approach has been used for developing climate change adaptation strategies, planning for future transportation infrastructure, and working with local communities to create sustainable initiatives. Issues of how to handle scale and data formats have also been addressed, as climate information is being applied at local levels. Local stakeholders are engaged directly to facilitate proper communication and to guarantee that this group understands how to integrate climate information with other drivers in their communities. While climate is an important factor for decision makers, their decisions are not just climate driven, thus it is important to assess how climate integrates with other factors that they manage.

2. Stakeholder engagement

A recent report from the National Climate Assessment Strategic Planning Workshop stated that as this next NCA moves forward, it is critical that stakeholders from both inside and outside of the government become better involved in the Assessment process, are empowered to create their own sustainable networks, and are provided ongoing support and access to needed climate information (USGCRP 2010a). The report also cited that the needs of stakeholders from across sectors will ultimately drive the questions and goals of the next NCA. This type of engagement ensures the assessment is relevant to the resources the stakeholders

Correspondence to: J. Greg Dobson, National Environmental Modeling and Analysis Center, The University of North Carolina-Asheville, One University Heights, Asheville, NC 28804 ; E-mail: gdobson@unca.edu

manage and results in a certain level of shared ownership and co-production. In addition, there are already a variety of assessment-type activities taking place at local, state, and regional levels that need to be identified, some of which could potentially be integrated into the NCA. However, the capacity for the federal government to do this through its NCA process does not exist, as this level of engagement is a very time consuming and qualitative process. Therefore, it is critical that the NCA include non-federal partners, such as the private sector and universities from across the nation. These non-federal partners could also provide an additional level of engagement cohesiveness and perhaps supply other funding, data, and staffing resources (USGCRP 2010b). Additionally, adaptation efforts will require coordinated efforts across multiple sectors and scales and be built upon existing efforts and knowledge of a wide range of public and private stakeholders (White House Council on Environmental Quality 2010).

One method for engaging stakeholders from multiple sectors within their communities is by the use of small facilitated workshops. Over the past year, NEMAC has been actively involved with the North Carolina Interagency Leadership Team (NCILT) as they and additional agencies seek to develop a climate assessment report and adaptation strategy plan for the state of North Carolina to begin preparing for increased impacts from climate variability and climate change. The NCILT is made up of representatives from all major state agencies, or sectors, including transportation, agriculture, public health, emergency management, commerce, energy, environmental and natural resources, cultural resources, and wildlife. Projected climate change threats to North Carolina include sea level rise, more frequent and intense heat waves, increased air and water temperature, increased storm intensity, and altered rainfall patterns resulting in both droughts and floods. The projected threats from climate change are expected to have substantial impacts on the state's coastal and cultural resources, transportation and other infrastructure, water supplies, agriculture, natural systems, public health, and citizens' homes and livelihoods. Because these threats could have substantial impacts for the state, it is important that North Carolina develop a strategy to reduce its vulnerability and enhance its resilience. Failure to develop and implement such a strategy will leave the communities of the state at risk from current climate impacts and impacts that are projected to increase into the future.

A similar effort to the NCILT work is being undertaken with the Southeast Natural Resources Leadership Group (SENRLG). The effort will allow NEMAC to see if the proposed framework is robust across a larger, regional scale. SENRLG is committed to the common purpose of fulfilling federal agency mandates in ways that promote conservation and restoration of important natural resources, wise management and sound stewardship of natural resources, and ecologically sustainable development. SENRLG recognizes that climate variability and change currently affects and has the potential to further impact ecosystems and human communities. Thus, the intention is to assess the vulnerability of these resources and do so in a manner that is consistent across the southeastern U.S., and ensure that the process can be scaled to support local implementation of adaptation practices. The work with SENRLG will also make certain that the framework can work at not only a state scale, but across state lines. This scalable ability is critical since many water and coastal resource issues are region-wide and not restricted by political boundaries.

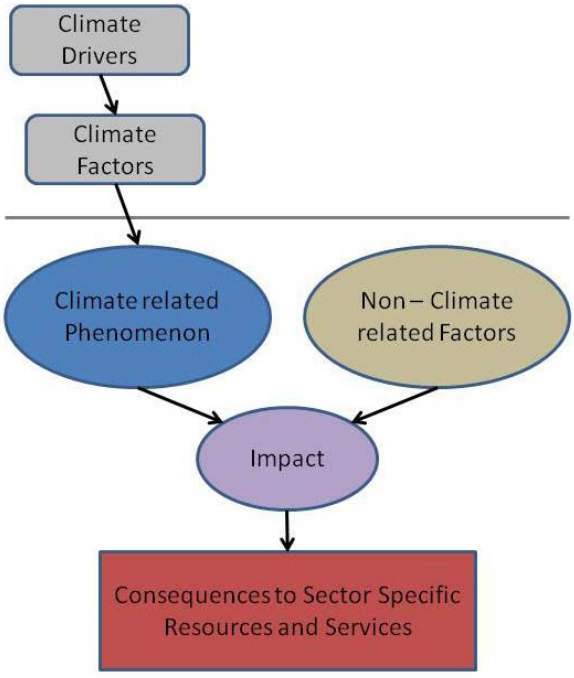

Fig. 1. A conceptual model of NEMAC's framework for creating a regional climate

3. A framework for climate assessments

By working directly with such diverse stakeholder groups as the NCILT and SENRLG, NEMAC, as previously mentioned, is developing an approach and framework that will allow stakeholder values to be fully

integrated with other climate data and information. The framework operates from the bottom-up, across sectors, and is scalable. The use of appropriate vocabulary is also an important issue to consider and is taken into account in this framework. With such a broad range in climate assessment related terms that currently exists from such groups as the International Panel of Climate Change (IPCC), the Pew Center on Global Climate Change, and the White House Council on Environmental Quality, it is critical that stakeholders are able to agree on a standard set of vocabulary and develop a clear understanding of what these terms mean. Finally, the development and use of a web application tool will allow for access to the regional climate assessments for a particular sector or scale and will be built upon a robust database structure.

More specifically, NEMAC's framework will combine climate related drivers and factors with climate related phenomenon and other non-climate related factors, and will identify key impacts that might affect the system (Fig. 1). The term "system" refers to any system-based resource and/or service that might be impacted, and would include the natural, built, and human systems. The framework has been designed to be easily populated and allows for the inclusion of multiple climate and non-climate related factors. Essentially it consists of four key components, first including a conceptual model or series of models similar to that referenced in Figure (1). The second component is an inventory that summarizes all of the data and information that would be needed to make the assessment, and that is shown in the conceptual model. Third is a narrative that provides an overview of the sector and scale being assessed, the climate impacts/stressors, and what affects they would have on the system services and resources. Finally, a map or series of maps further highlights and describes the climate impacts/stressors and provides a visual for communicating vulnerability.

The framework in action

NEMAC's framework for creating a regional climate assessment was recently used to help a regional Council of Governments in western North Carolina update the long range transportation plan and specifically include a section on potential climate variability and change impacts to the transportation sector. In this example, the sector of interest is transportation and the scale is regional, or multi-county. Identified climate impacts/stressors included flooding, landslides, and wildfire. The primary system resource that could be affected was transportation mobility. Potential climate related factors included variable precipitation and temperatures and an increase in intense rainfall events. Non-climate related factors included future transportation demands, land use change, steep slopes, and an increase in impervious surfaces. Specific vulnerability to multiple climate impacts/stressors included an increase in flooding that intersect roadways, landslides that block major highways, and wildfires that close entire areas of road networks (Fig. 2). The transportation sector's system resources and services could be negatively impacted by the interruption of public transportation, movement of products, rail and vehicular traffic, and lost tourism revenue.

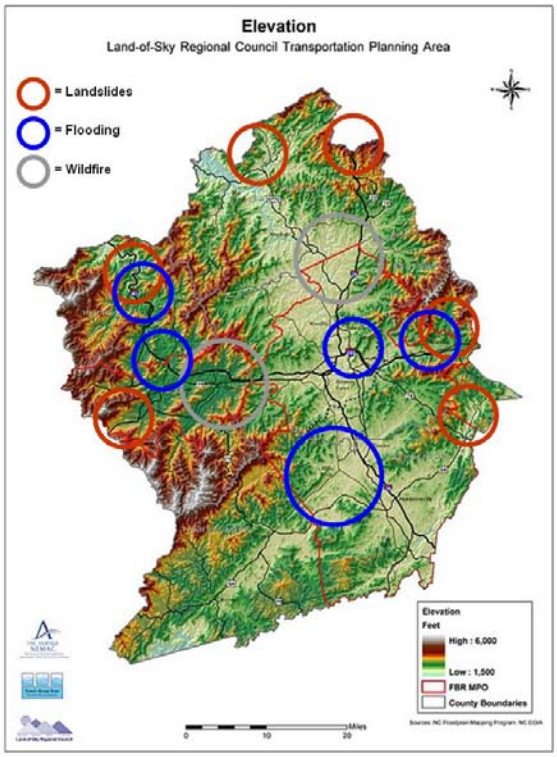

Fig. 2 A map depicting areas that would be vulnerable to increases of landslides, flooding, and wildfires due to climate variability and change.

4. Summary and future work

Regional climate assessments should be a value-based assessment that incorporates a bottom-up approach while identifying system resources by scale and sector. Vulnerabilities to climate variability and change should be identified. Specifically, decision makers at a variety of scales should be able to use these climate assessments to recognize resources that are most vulnerable and discuss how to set priorities for building resiliency in these areas. Strategies and decisions developed from regional climate assessments must also be

solution oriented. Climate scientists and policy makers must understand that climate is only one part of assessment and that the non-climate factors and values must also be integrated. NEMAC's approach for addressing these and other climate assessment related issues involves the engagement of stakeholders through small workshops and other facilitated group decision making venues. Through this type of stakeholder engagement, a framework is being developed that has the ability to guide regional climate assessments throughout North Carolina and beyond.

NEMAC's future work on its regional climate assessment approach will include a continued refinement of the framework with various partners. In addition, new groups and partners will be indentified to gather additional content and useful data for the assessments. Additional impacts and stressors that might affect multiple sectors also need to be highlighted. Finally, descriptive narratives need to be generated that clearly explain each assessment. Other work will include database development for the climate assessments that will allow archival and efficient retrieval of the climate assessments by sector and/or scale through an interactive web interface.

References

National Assessment Synthesis Team, 2001: Climate Change Impacts on the United States: The Potential Consequences of Climate Variability and Change. Report for the US Global Change Research Program, Cambridge University Press, Cambridge UK, 620pp. (http://www.gcrio.org/NationalAssessment/aIntro.pdf)

The United States Global Change Research Program, 2009: Global Climate Change Impacts in the United States, Thomas R. Karl, Jerry M. Melillo, and Thomas C. Peterson, (eds.). Cambridge University Press, 188pp. (http://downloads.globalchange.gov/usimpacts/pdfs/climate-impacts-report.pdf)

—, National Climate Assessment, 2010a: The United States National Climate Assessment, NCA Report Series, Volume 2, Strategic Planning Workshop, February 24th – 25th, 2010, Chicago, IL. (http://www.globalchange.gov/images/NCA/strategic%20planning%20workshop_final.pdf)

—, —, 2010b: National Climate Assessment Draft Strategy. Washington, D.C. (http://www.globalchange.gov/images/NCA/nationalassessmentdraftstrategy.pdf)

The White House Council on Environmental Quality, 2010: Progress Report of the Interagency Climate Change Adaptation Task Force: Recommended Actions in Support of a National Climate Change Adaptation Strategy. Washington, D.C. (http://www.whitehouse.gov/sites/default/files/microsites/ceq/Interagency-Climate-Change-Adaptation-Progress-Report.pdf)

Science and Technology Infusion Climate Bulletin
NOAA's National Weather Service
35th NOAA Annual Climate Diagnostics and Prediction Workshop
Raleigh, NC, 4-7 October 2010

Use of the Early Warning Information in the Field of Agriculture

Shoji Notsuhara and Shingo Ushida

Japan Meteorological Agency

1. Introduction

The Japan Meteorological Agency (JMA) began issuing meteorological information named "Early Warning Information on Extreme Weather" on an operational basis in March 2008. This information is issued every Tuesday and Friday by reference to the result of the numerical prediction model. When seven-day averaged temperature is expected to be very high or low with a certain possibility (30% or more) in the week starting from five to eight days ahead of the date of announcement (Figure 1), JMA provides early warning information on extreme weather on high or low temperature for concerned regions. The terms very high and very low refer to high or low seven-day averaged temperatures that are in the top 10% of all samples (Figure 2). We expect this information will be used in various fields of industry, particularly in agriculture in order to mitigate serious damage to farm products.

Date of Issue					Target days									
Mar 21	22	23	24	25	26	27	28	29	30	31	Apr 1	2	3	4

Fig. 1 Target days when 21 March is the date of issue

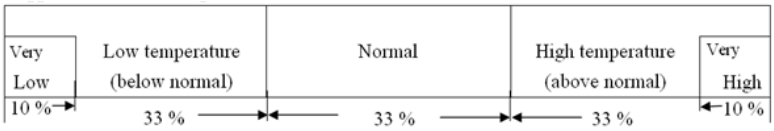

Fig. 2 Appearance rate of temperature

2. Accuracy of early warning information

Table 1 shows the result of early warning information issued from March 2008 to August 2010. In a total of 3072 opportunities in this period, JMA issued early warning information 654 times on "very high" temperature and 203 times on "very low" temperature. The rates that predicted extreme events actually happened were 64% for "very high" temperature and 56% for "very low" temperature. Even if observed temperatures did not reach "very high" or "very low" category, observed temperatures were classified into "high" or "low" category in more than 90% cases. Thus, there were few cases that seven-day averaged temperatures became normal or they were classified into opposite category when early warning information was issued. On the other hand, when observed temperatures were "very high" and "very low", the rates that early warning information was issued in advance were 48% and 40%, respectively. Though almost half of extreme events could be predicted, we should make more efforts to predict extreme events.

Opportunities for issuing			3072				
Very High Temperature				Very Low Temperature			
Number of forecast			654	Number of forecast			203
	Forecast	Observation			Forecast	Observation	
①	Yes	Yes	421	①	Yes	Yes	115
②	Yes	No	233	②	Yes	No	88
③	No	Yes	460	③	No	Yes	172
Hit Rate (=①/(①＋②))			64%	Hit Rate (=①/(①＋②))			56%
Catch Rate (=①/(①＋③))			48%	Catch Rate (=①/(①＋③))			40%

Table 1 Result of issued early warning information

3. Cases in which the information was used effectively

Figure 3 shows time series of daily temperature of Tohoku region in April 2010. Daily temperatures fluctuated around normal until mid-April. From 14 April, daily temperatures greatly fell and seven-day mean

Correspondence to: Shoji Notsuhara, Japan Meteorological Agency;
E-mail: notsuhara@met.kishou.go.jp

temperatures starting from 11 to 24 were “very low”. JMA issued early warning information on “very low” temperature on 6 April for the period from 11 to 20 April and on 9 April for the period from 14 to 23 April. In response, the Tohoku Regional Agricultural Administration Office issued agricultural information for fruit growers to prepare against the frost damage from cold weather. As in this case, with the use of early warning information, agricultural administration offices and farmers could secure enough time to prepare against extreme weather. Furthermore, they can take measures against extreme weather more effectively with the combined use of weekly forecast up to 7 days ahead.

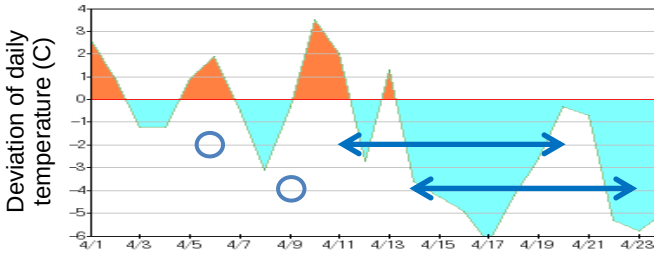

Fig. 3 Time series of daily temperatures of Tohoku region in April 2010. Circle indicates a date of issue. Left and right arrow means target days.

4. Approaches for further use of information

JMA started a research in collaboration with the National Agricultural Research Center for Tohoku Region (NARCT) to advance the use of temperature forecast for the second week that is used for early warning information. The object of the research is to mitigate damage to rice crops from cold weather during summer. There are three main reasons for starting the research. First, damage to rice crops has a big social impact. Second, there are effective measures to mitigate damage from cold weather. Third, it takes one week or more to prepare measures. In this research, we are planning to produce new information that is comprehensible and easy-to-use to farmers, to help their “decision making” by providing index that specializes in use of agriculture with high geographical resolution. We will continue to work for early practical use.

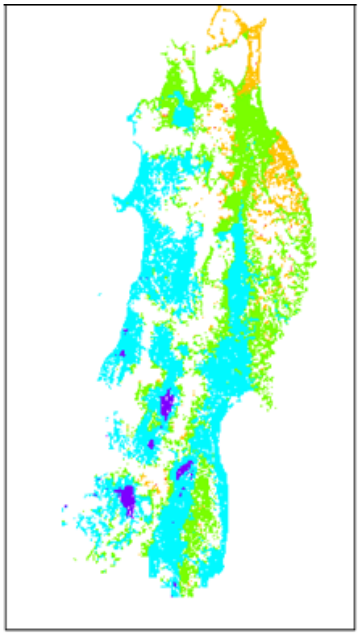

Fig. 4 Sample of agricultural information in Tohoku region. Risk of cold weather is shown by color that signifies value of index.

5. Summary

As shown in section 3, early warning information has been utilized well in the field of agriculture and obtained good evaluation. In the future, JMA will also make an effort for the development of new information specializing in agriculture.

Science and Technology Infusion Climate Bulletin
NOAA's National Weather Service
35th NOAA Annual Climate Diagnostics and Prediction Workshop
Raleigh, NC, 4-7 October 2010

Climate Prediction Application Science Priorities and Issues - Contributions from 2010 CPAS Workshop

Jiayu Zhou, S&TI Climate Mission, Office of Science and Technology
Marina Timofeyeva and Michelle D. Hawkins, Climate Service Division/OCWWS
NOAA's National Weather Service

Introduction

The 8th NOAA Climate Prediction Applications Science (CPAS) Workshop, a sister workshop parallel to the NOAA Climate Diagnostics and Prediction Workshop but focusing on identifying new climate prediction application research, assessing the impact of climate forecast on environmental societal activities and promoting interactions between the climate sensitive integrated research, service, and user communities, was held in San Diego, CA, from 2 to 4 March 2010, co-hosted by the National Weather Service Climate Services Division, the California Department of Water Resources, the National Integrated Drought Information System, and the Water Education Foundation. The special theme for this workshop was Managing Water Resources and Drought in a Changing Climate. A diverse group of 75 people from a variety of sectors including federal and local government, academia, and the private sector gathered to exchange ideas, build mutually beneficial collaborations, and share best practices within this specific climate sensitive sector. Aside from recurring issues, *e.g.* communication and outreach, engagement, decision support, *etc.*, discussions gave prominence to application science priorities and related issues to improve climate service products.

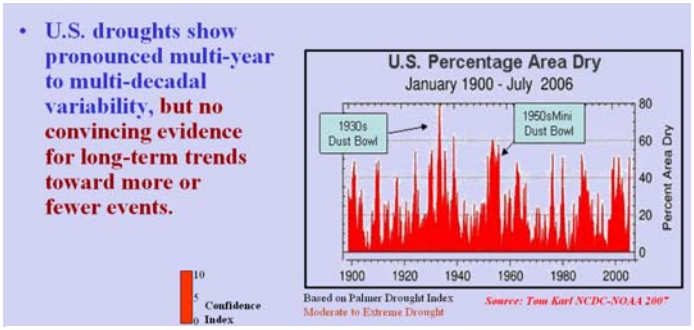

Fig. 1 Observed drought activity during the 20th and early 21st century. (Presented by Sorooshian)

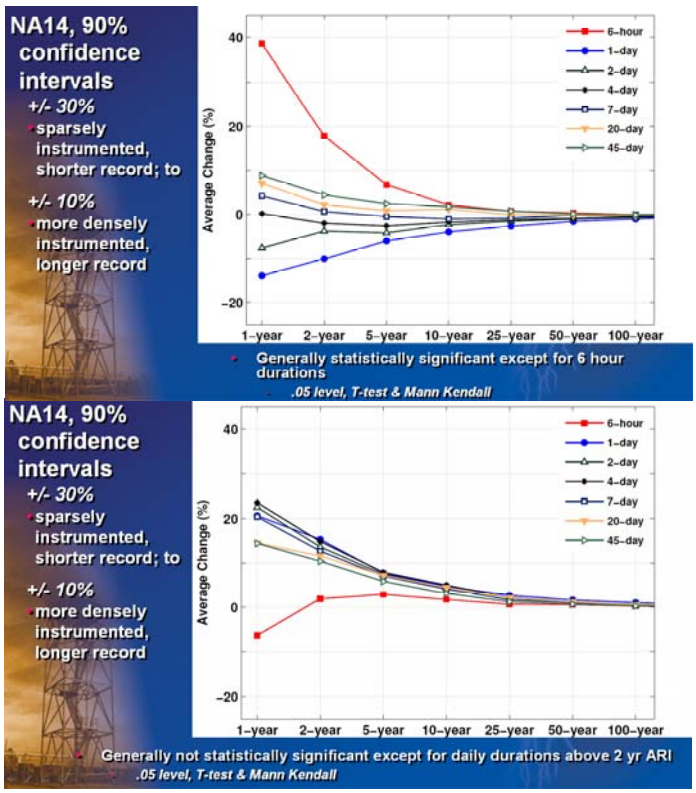

Fig. 2 Trends in exceedances. Average percentage change in number of rainfall exceedances per station per century for semiarid Southwest (top) and Ohio Basin (bottom). (Presented by Bonnin)

1. Improving forecast skill and reliability is crucial to increase users' confidence in climate prediction products.

For IPCC prediction of more arid climate toward a warmer environment in the future, hydrometeorology expert participants looked at historical records (1900-2006) and showed pronounced multi-year to multi-decadal U.S.

Correspondence to: Jiayu Zhou, Office of Science and Technology, NOAA's National Weather Service, Silver Spring, MD 20910; E-mail: jiayu.zhou@noaa.gov.

drought variability, but no convincing evidence of long-term trends toward more or few events from the observation (Figure 1). Non-stationarity of design rainfalls, in the ranges used by civil engineers, was also examined. It was shown that historical trends in the number of rainfall exceedances over key areas of the U.S. were small compared to the uncertainty of intensity, frequency, duration (IFD) values used by civil engineers (Figure 2).

In discussions, there was a general consensus that more research needed to be done to address non-stationarity because of climate change and assess the added value of downscaling over traditional stochastic hydrology methods.

2. Though regional climate services are highly demanded by users in all geographical locations, the predictability is not evenly distributed in space and time. There are gaps between what is known and the knowledge needed in regional applications.

By assessing current 'state of the art' of climate forecasting teleconnection research, no clear link was found between California multi-year droughts and either ENSO or PDO phase. The dominance of ENSO teleconnection research to improve ISI forecast should not dwarf other efforts (i.e. detecting the linkage between summer trends in SLP near Azores and runoff in Sacramento and San Joaquin basins, the impact of the Indian Ocean dipole etc.). A good fraction of annual precipitation from 'atmospheric river' events, which could be linked to MJO and ENSO, are still poorly understood and requires more research. Research needs were also identified for detecting sensitivities of regional impacts to the projected changes of temperature and precipitation.

Studies showed high sensitivity of the Colorado River flows to the projection of warming (Figure 3). It is important to know the underlying mechanisms for the flow changes in order to provide meaningful information that incorporates uncertainties in future climate change projections for water managers and policy makers.

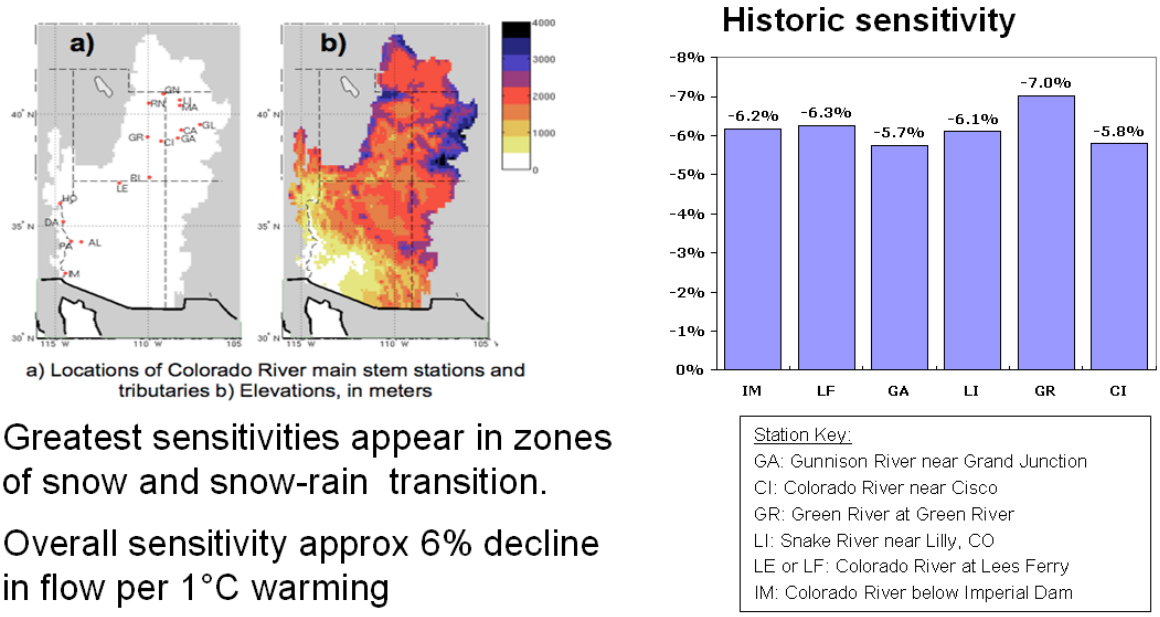

Fig. 3 Colorado River flows highly sensitive to warming. (Presented by Cayan)

3. Coupling of climate science advancement with water resource practices has been shown as a key mechanism to develop needed tools and products for applications.

For climate information products to be considered useful by the civil engineering community, products should address the frequencies and durations used for designing civil infrastructure. Because of different cultures, values, languages, as well as the loading dock method used for information transfer with little

interaction with practitioners during climate research, the climate community's statements on trends in rainfall frequency do not adequately address the concerns of civil engineers.

4. Enhancing partnerships with social scientists to maximize the benefits of climate information for users with statistically unsophisticated climate knowledge and providing training opportunities was another prominent S&T aspect of the workshop.

Lessons learned from past and current practices emphasized the importance of sharing goals and resources, leveraging expertise and fostering extension networks to identify and understand specific information needs, relate these to the design and function of operational tools, and communicate information back to stakeholders. (See the inset of Simplistic Model of CLIMAS presented by Ferguson).

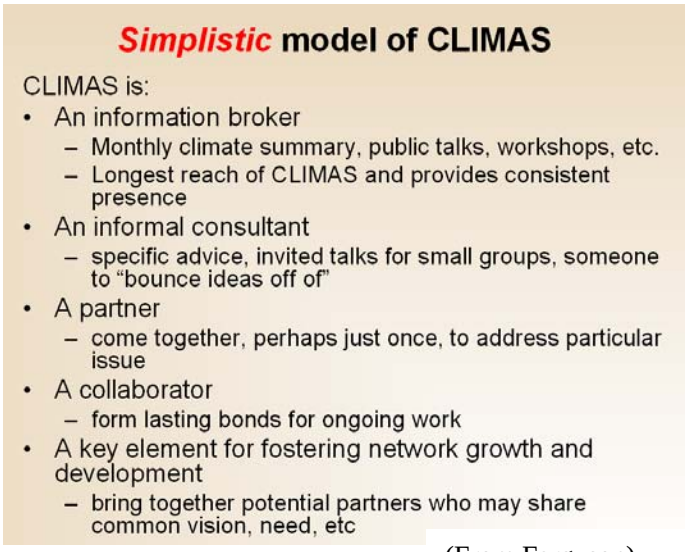

(From Ferguson)

5. From the user perspective, water resource managers need actionable climate information.

Looking forward to the future planning methods (Figure 4), this community emphasized the importance of climate model agreement on change in key parameters, narrowing the uncertainty range of model output, increasing resolution at a spatial and temporal scale that matches water utility current systems, and improving projections within water utility planning horizons. It was also suggested that the development of priorities needs to be more focused on the enhancement of global and regional climate model ensembles, development of regional climate model components, improved use of observations to constrain climate model projections, improved modeling of the tropical Pacific, improved decadal prediction, and development of probabilistic downscaling for extremes and daily data.

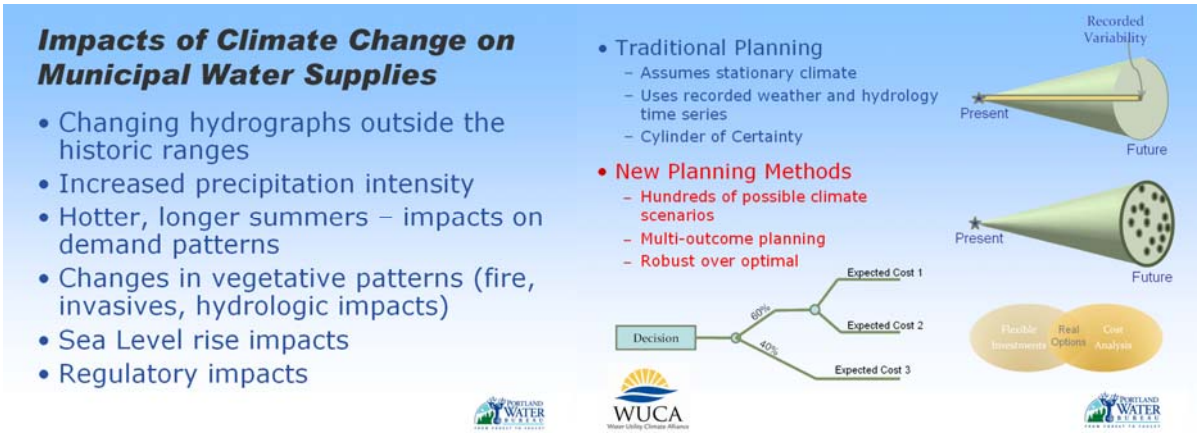

Fig. 4 Impact of climate change and advancement of planning for municipal water supply decision support. (Presented by Stickel)

References

Climate Service Division, NOAA/NWS/OCWWS, 2010: The 8th Climate Prediction Applications Science Workshop Summary. (http://www.joss.ucar.edu/events/2010/cpasw/meeting_report.pdf)

5. CLIMATE FOR COASTAL APPLICATIONS

Science and Technology Infusion Climate Bulletin
NOAA's National Weather Service
35th NOAA Annual Climate Diagnostics and Prediction Workshop
Raleigh, NC, 4-7 October 2010

Potential Future Effects of Sea Level Rise in Northeastern North Carolina

Thomas Shay
Institute for the Environment and Department of Marine Sciences
Brian Blanton
Renaissance Computing Institute
Richard Luettich
Institute of Marine Sciences
University of North Carolina at Chapel Hill

1. Introduction

The coastal area of North Carolina comprises a large system of sounds and estuaries protected by a complex of barrier islands (the Outer Banks). The islands are very low and narrow, and vulnerable to sea-level rise (SLR). With projections of 0.5m to 2.0m of global sea-level rise over the next couple of centuries (*e.g.*, Vermeer and Rahmstorf, 2009), we decided to investigate the potential effects of SLR on the islands as well as on the sounds and estuaries. We studied this problem using numerical simulation of the response of the ocean to both tides, and combined tides and wind in the form of a hurricane. In addition, we ran simulations for a range of SLR from 0m to 2.0m, and for the present topography of the Outer Banks and a partially eroded version of the islands.

2. Numerical simulations

We did the simulations with the fully coupled, parallel, 2D depth-integrated version of the ocean circulation model ADCIRC (Luettich *et al*. 1992) and the surface gravity wave model SWAN (Booij *et al*. 1999) described by Dietrich *et al*. (2011). The coupled model employs an unstructured grid to achieve high resolution in coastal areas. In this case, the grid consisted of approximately 267,000 nodes with minimum and maximum inter-nodal spacing of about 30m and 100km, respectively (Fig. 1). The time step for ADCIRC was 1sec and the time step for SWAN was 600sec.

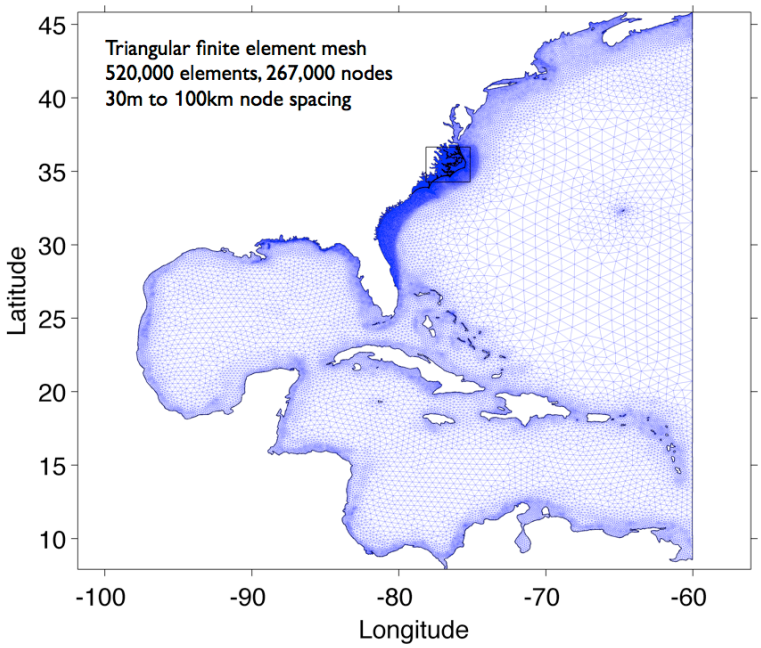

Fig. 1 The full domain and finite-element mesh used for all simulations. The small rectangle in coastal North Carolina delimits the subdomain displayed in subsequent plots.

We did simulations for SLR of 0.0m, 0.5m, 1.0m, and 2.0m in two Outer Banks configurations. The first configuration was the topography of today's Outer Banks, with coastlines changing due to inundation with rising sea level. The second configuration consisted of the Outer Banks altered according to the results of Culver *et al*. (2007). The alterations consisted of collapsing the relief of some of the islands and opening some of the tidal inlets between islands. We will call this configuration the collapsed Outer Banks. The coasts of the islands were changed by inundation with rising sea level as well.

Correspondence to: Thomas Shay, Institute for the Environment and Department of Marine Sciences, University of North Carolina, Chapel Hill, NC; E-mail: tom_shay@unc.edu

All simulations include the effects of tides. We included eight tidal constituents, and preliminary runs of 45 days were done with ADCIRC alone to spin up the tides, both to be used as tide-only results and to serve as hot-start input to initiate wind-forced runs.

The wind-forced runs were done for an extreme case: the passage of hurricane Isabel through the domain and across the North Carolina coastline and coastal plain. The wind input consisted of sea-surface atmospheric pressure and 10m winds in the Oceanweather Inc. (OWI) format, interpolated onto the unstructured grid. The wind-forced runs were hot started with the tidal spin-up output, and these simulations also included tides and surface gravity waves, all computed with the coupled model.

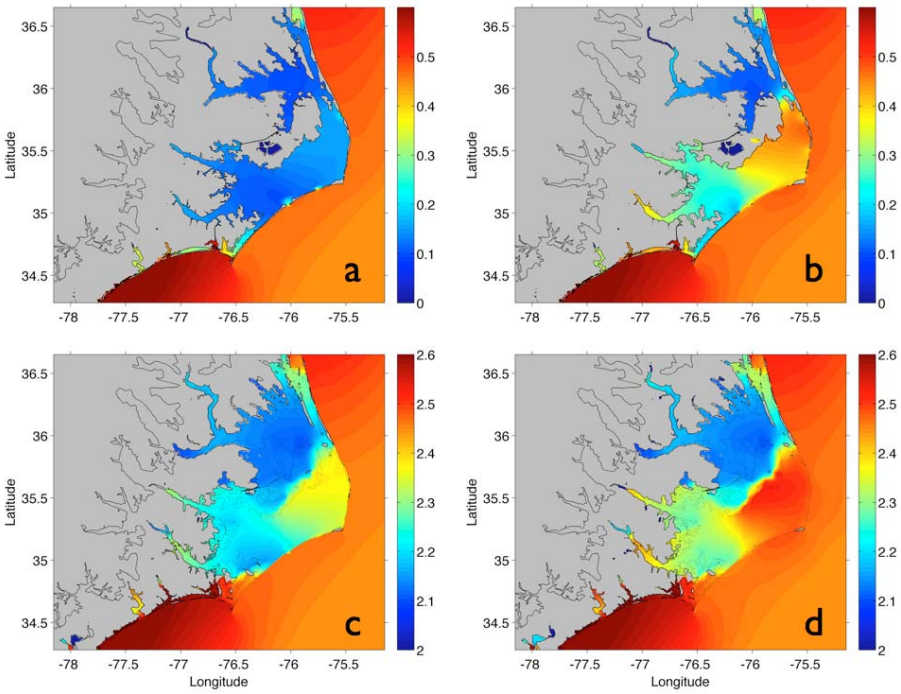

Fig. 2 Maximum tidal elevation (m) for (a) 0m SLR, current Outer Banks; (b) 0m SLR, collapsed Outer Banks; (c) 2.0m SLR, current Outer Banks; (d) 2.0m SLR, collapsed Outer Banks. Note that the minimum elevation in each figure corresponds to the mean SLR, so the colors isolate the effects of the tides.

3. Results

Tides-only simulations

In the current Outer Banks configuration, the maximum tidal range in the sounds and estuaries is low, on the order of 0.1m. The maximum elevation increases with rising sea level because of widening of the inlets and overtopping the islands, which results in the sounds and estuaries being more intimately coupled with the coastal ocean (Figs. 2a and 2c)., and the maximum elevation in the sounds increasing by about a factor of 3. The collapsed Outer Banks configuration amplifies this effect (Figs. 2b and 2d) with the maximum tidal elevation increasing by more than a factor of 5 with 2m of SLR. In addition to the elevations, the

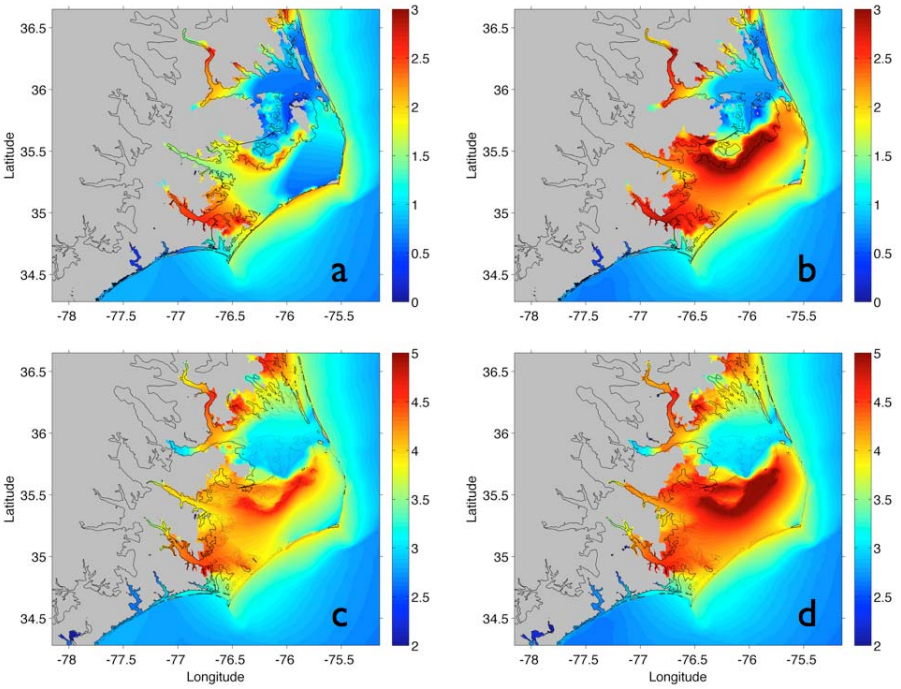

Fig. 3 Maximum surface elevation during the passage of hurricane Isabel for (a) 0m SLR, current Outer Banks; (b) 0m SLR, collapsed Outer Banks; (c) 2.0m SLR, current Outer Banks; (d) 2.0m SLR collapsed Outer Banks.

tidal velocities also increase throughout the sounds and estuaries (not shown) owing to the combined effects of SLR and alteration of the Outer Banks.

Hurricane Isabel

Hurricane Isabel made landfall on the coast of North Carolina east of Cape Lookout on Sept 18, 2003. The storm continued across Pamlico Sound before moving into Virginia. We forced the coupled ADCIRC+SWAN with OWI hindcast pressure and wind fields in addition to continuing the tidal forcing. We ran the Isabel simulations for 5.5 days, starting with the wind fields corresponding to 00Z on September 14, 2003.

Fig. 3 shows the maximum sea-surface elevation during the passage of hurricane Isabel, *i.e.*, the storm surge. Because the storm center crossed the Outer Banks east of Cape Lookout in a northward direction, strong winds from the east tended to lower the water level in the eastern sound and raise it in the western sound and Neuse River estuary. This effect is particularly evident in the current Outer Banks, 0m SLR case (Fig. 3a), where the maximum storm surge elevations in the Neuse and the shore of the Albemarle-Pamlico Peninsula (APP) are 2.5 to 3.0m. In the current Outer Banks configuration and 2.0m SLR, the dewatering of the eastern sound is reduced because of easier overtopping of the islands, and the area of high storm surge in the western sound is increased (Fig. 3c). In the collapsed Outer Banks configuration, the height of the storm surge is increased throughout the Pamlico Sound and on the APP in both the 0m SLR (Fig.

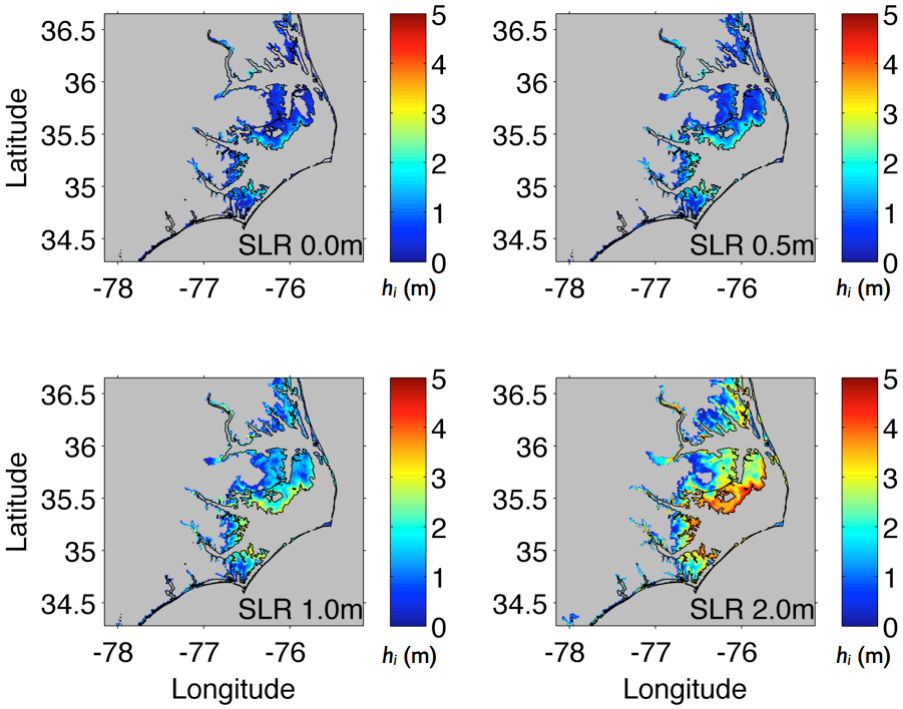

Fig. 4 Inundation of otherwise dry land during the passage of Isabel for current Outer Banks configuration and the four SLR scenarios.

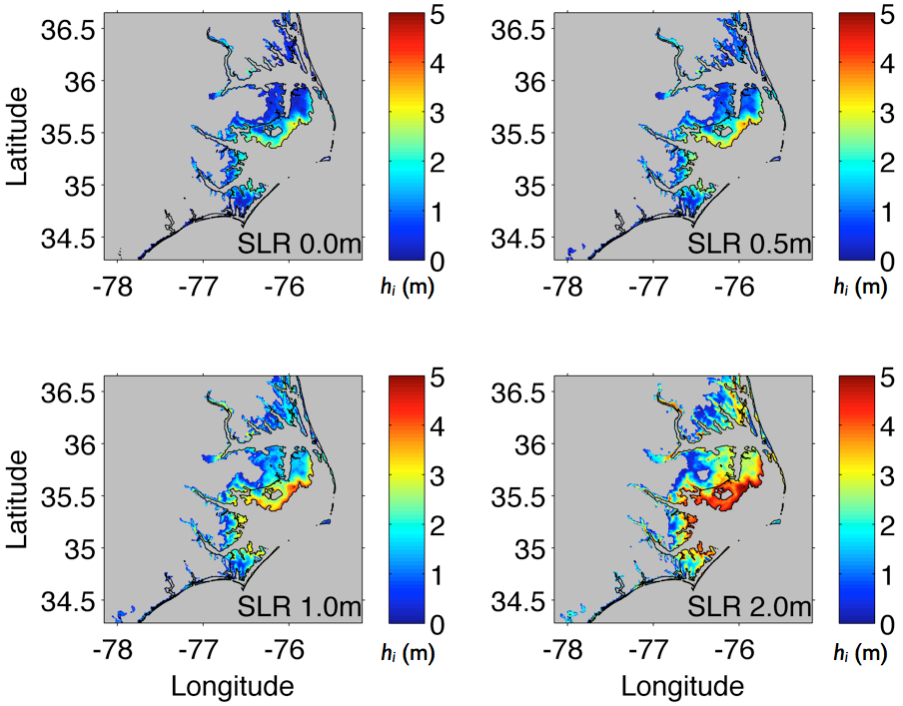

Fig. 5 Inundation of otherwise dry land during the passage of Isabel for the collapsed Outer Banks configuration and the four SLR scenarios.

3b) and 2.0m SLR (Fig. 3d) cases. In these two cases, the maximum storm surge elevation (relative to the mean SLR) is greater than 3.0m along the southern shore of the APP.

The storm-surge inundation of the barrier islands and the land adjacent to the sounds increases with SLR and also with the collapse of the Outer Banks. Figs. 4 and 5 show the degree of inundation (defined as the elevation of the sea surface over land that is dry at 0m SLR) for the current and collapsed Outer Banks, respectively, and for all four SLR scenarios. The area and depth of maximum inundation both increase as SLR increases, owing to both the mean SLR and the enhanced tides and storm surge. These effects are increased in the collapsed Outer Banks configuration because as the islands are submerged, they provide a less effective barrier against tides and storm surge, and the waters of the sounds and estuaries are more directly connected to the shelf waters.

References

Booij, N., R.C. Ris, and L.H. Holthuijsen, 1999: A third-generation wave model for coastal regions, Part I, Model description and validation. *Journal of Geophysical Research*, **104**, 7649–7666.

Culver, S.J., C.A. Grand Pre, D.J. Mallinson, S.R. Riggs, D.R. Corbett, J. Foley, M. Hale, L. Metger, J. Ricardo, J. Rosenberger, C.G. Smith, C.W. Smith, S.W. Snyder, D. Twamley K. Farrell, and B. Horton, 2007: Late Holocene barrier island collapse: Outer Banks, North Carolina, USA. *The Sedimentary Record*, **5**(4), 4–8.

Dietrich, J.C., M. Zijlema, J.J. Westerink, L.H. Holthuijsen, C. Dawson, R.A. Luettich Jr., R.E. Jensen, J.M. Smith, G.S. Stelling, and G.W. Stone, 2011: Modeling hurricane waves and storm surge using integrally-coupled, scalable computations. *Coastal Engineering*, **58**(1), 45–65.

Luettich, R.A., J.J. Westerink, and N.W. Scheffner, 1992: ADCIRC: An advanced three-dimensional circulation model for shelves, coasts, and estuaries. Report 1. Theory and methodology of ADCIRC-2DDI and ADCIRC-3DL. *Technical Report (U. S. Army Engineer Waterways Experiment Station) DRP-92-6 rept. 1*, 137pp.

Vermeer, Martin, and Stefan Rahmstorf, 2009: Global sea level linked to global temperature. *Proceedings of the National Academy of Sciences of the United States of America*, **106**(51), 21527–21532.

NWS Science and Technology Infusion Climate Bulletin
Featured Special Collections

NOAA Climate Test Bed Joint Seminar Series Extended Summaries Collection Volume

1. Assessment of Improvement in Climate Prediction with Outstanding R&D Needs (2009-2010)
   http://www.weather.gov/ost/climate/STIP/FY10CTBSeminars/CollectionVol_FY10CTBJS.pdf
2. Research to Operation and Operation to Research (2008-2009)
   http://www.weather.gov/ost/climate/STIP/FY09CTBSeminars/CollectionVol_FY09CTBJS.pdf
3. CFS as a Prediction System and Research Tool (2007-2008)
   http://www.weather.gov/ost/climate/STIP/CTB-COLA/ctb-cola_seminar_summaries.pdf

Climate Prediction Science and Technology Digest

1. 34th Annual Climate Diagnostics and Prediction Workshop Digest
   http://www.nws.noaa.gov/ost/climate/STIP/34CDPW/34cdpw-CollectionVol.pdf
2. 33rd Annual Climate Diagnostics and Prediction Workshop Extended Summaries
   http://www.nws.noaa.gov/ost/climate/STIP/33cdpw.htm